MODE–MATCHING METHOD IN OPTICAL CORRUGATED WAVEGUIDES WITH LARGE RECTANGULAR GROOVE DEPTH

A thesis submitted to the
Faculty of Engineering of the
University of Glasgow for the degree of
Doctor of Philosophy

by

Woo–Hu Tsai

November 1995

ACKNOWLEDGEMENTS

The author wish to express his sincere gratitude to:

Professor S. P. Beaumont and Professor P. J. R. Laybourn and the staff of the Department of Electronics and Electrical Engineering of the University of Glasgow, for the use of the facilities and materials provided by the Department.

His supervisor, Professor J. M. Arnold, for his guidance, help, and useful suggestions throughout the duration of this research.

Professor R. M. De La Rue, for his enlightenment and suggestions at the beginning of this study.

Professor M.–S. Wu of the Department of Physics, Tatung Institute of Technology, Taiwan, R. O. C., for his valuable suggestions and practical support.

His wife, H. L. Yu, for her encouragement and loving support during his studying in U. K..

Tatung Institute of Technology for its financial support.

ABSTRACT

Corrugated structures have been of great interest and importance in many applications. Recently, aperiodic waveguide gratings have played a significant role in distributed feedback (DFB) lasers and in integrated optical devices. The operating characteristics of such structures (periodic and aperiodic cases) have been investigated and discussed intensively during the past two decades. Most of the studies in this field have been carried out using either approximate analytical techniques or simple numerical methods in the analysis for sinusoidal gratings or other types of gratings with small groove depth (or tooth height), in which the reflection coefficients are very small and the radiation losses can be ignored in the calculation.

With the help of the latest lithography and etching techniques, the fabrication of rectangular gratings with large groove depth can be realised for many applications. Deep rectangular gratings contribute high, broad, and flat frequency responses at the centre stopband, and have a compact size suitable for on–line and on–chip implementation. However, simple approximate methods are no longer valid in the analysis because the depth of these gratings is too large.

The difficulties in the analysis of such a deep rectangular grating follow from the fact that the method which is used in the analysis not only is required to treat each mode produced by every step–junction of the grating with accuracy but also demands that the algorithm of the method be not too cumbersome when applied to an aperiodic grating with a great number of periods and multiple phase shifts. According to the author's knowledge, such a proper method for deep rectangular aperiodic gratings has still not been fully seen in the literature.

In this thesis, a mode–matching procedure and a transfer matrix approach are used and modified to analyse waveguides with rectangular gratings with large groove depth. A systematic investigation has been carried out for several discontinuous structures, including single step discontinuities, double–step discontinuities, periodic gratings, and

aperiodic gratings with single and multiple phase shifts. In addition, comparisons of our results and those of existing methods are presented. It is shown that the method proposed in this thesis, having minimal approximation in the formulation and using a simple matrix algorithm, is suitable for the analysis of deep rectangular gratings and also for computer processing. Furthermore, applications of deep linearly chirped grating filters, including dispersion compensation and chirped pulse compression in the femtosecond regime, will be discussed, and very good performances are demonstrated.

List of Tables

List of Figures

Contents

1

CHAPTER 1

INTRODUCTION

Corrugated thin film optical waveguides have been of great interest and more and more importance in integrated optics [1]–[4]. It is known that two special properties make these structures so unique and important. The first property is that the periodic structure has an inherent wave vector ($k = 2\pi/\Lambda$, where Λ is the period of the structure) that can be adjusted to conserve the momentum (or the wave vector) and to exchange energy in the coupling between any two guided modes. The second property is that in certain frequency bands the propagation wave vector satisfies Bragg's condition. Therefore, a wave propagating in the structure with a frequency in the stopband will exhibit distributed feedback and the longitudinal mode can be controlled by this mode selection [2]. Applications include distributed feedback (DFB) lasers [5]–[7], DBR lasers [8][9], bistable switches [10], demultiplexers and frequency filters [11]–[16], grating input, output and directional couplers [17]–[23], phase matching in nonlinear materials [24][25], and so on. Hence, the knowledge of their propagation and coupling characteristics is an important aspect of designing such devices. This problem has been extensively discussed in the literature during the past two decades. Many works in this field have been carried out both for the collinear cases [6][11][13] [27]–[29] and for oblique incidence onto the grating [30]–[36]. For oblique incidence, the propagation direction does not coincide with $\vec{k}$, and has been used in applications such as Bragg deflectors [37], chirped–grating demultiplexers [38][39], and tunable DFB lasers [40].

In collinear cases, the wave propagates in the guiding layer with a periodic variation

along the guide. There exist codirectional and contradirectional TE or TM modes coupled by the corrugation. These fields appear either as guided waves, which travel parallel to the structure, or as leaky waves, which are also guided by the structure but are radiated continuously into the exterior regions [41]–[43]. Many investigations about such problems have employed approximations that are too restrictive for many practical cases. One simpler approximation has been the assumption that the grating periodicity acts as only a small perturbation in a configuration that, in the absence of the grating, appears as a planar multilayered medium [44]–[48]. In this case, the total electric field of the perturbed structure is written as a linear combination of the modes of the corresponding unperturbed structure, and the total field must satisfy Maxwell's equations using the perturbed dielectric permittivity. This approximation yields good results only if the depth of the periodic structure is sufficiently small, and the method may produce erroneous results in many practical cases, such as thick corrugated gratings having groove depths comparable to the wavelength [49][50]. Another approximation has been the use of the Rayleigh assumption, which incorrectly neglects the presence of incoming waves in the grating region [51]–[53]. It has been shown that this Rayleigh approximation may also result in serious errors if the periodic variation is not sufficiently small [54]. A detailed treatment was given by *Marcuse* [27] and *Kogelnik* [28], both using the coupled–mode analysis (both the ideal–mode and local–mode approaches). In these methods, a set of generalized transmission–line equations as well as coupled wave equations are derived directly from Maxwell's equations, which give identical results on the form of the coupling constants for TE incidence. However, the results differ for TM incidence because the boundary conditions are not satisfied [32][35][55], and the results also have an obvious error in deep grating structures because the neglect of the backward radiation modes no longer holds there [57].

Several effects in oblique incidence, such as conversion of the mode polarization (strong coupling between TE and TM modes) [30][33][34][56], and the appearance of leakage and resonance effects [58][59], have been discussed. The oblique incidence

treatment will be more difficult and more complicated than the analysis used in collinear cases. The difficulties in oblique incidence follow from the fact that this case is three–dimensional with a set of Maxwell equations which must be considered for all possible modes. Further, for oblique incidence, the number of boundary conditions at the grating will increase to five vector components for each TE and TM polarization (in collinear cases only three vector components for each TE and TM modes have been considered) and this needs more sophisticated analysis [32][58].

A grating with large rectangular groove depth (or tooth height) may contribute high reflectivity, strong coupling, broad frequency response, and more compact size. Such structures are suitable for DFB or DBR lasers requiring large coupling coefficient, grating input and output couplers, and aperiodic gratings with phase shifts in the structure. In particular, deep linearly chirped grating filters have very good performance for dispersion compensation and chirped pulse compression in the femtosecond regime. But, the simple approximation methods described above are no longer valid in the analysis because the depth of the grating is too large.

It has been shown that the mode–matching analysis, which was broadly used to analyse a discontinuous structure in both microwave and optical waveguides, is a more accurate and more comprehensive method than others to solve such problems. In the mode–matching analysis, an expansion of the field in a set of real field distributions in different regions is given and the mode matching procedure is applied at the step boundary to obtain a set of equations for the mode amplitudes. One of the guided waves incident onto the step discontinuity will produce a finite number of reflected and transmitted guided modes with a certain discrete spectrum, the number being dependent on the waveguide structure and the index profile, as well as forward– and backward–moving radiation modes with a continuous spectrum, the transverse wavenumbers ranging from 0 to infinity.

Owing to singular integral equations in the analysis, it is difficult to obtain a closed–form solution; one has to use either numerical methods, (such as the finite element

method FEM [60][61], the boundary element method BEM [62][63], a combination of finite and boundary elements method CFBEM [64]), or approximate techniques, (like the residue calculus technique [65], the integral equation method IEM [66], the beam propagation method BPM [67][68]. *Popov and Mashev* used the mode–matching method containing the angular dependence in an explicit form for both TE and TM incidences [32][69], or like *Rozzi* [70] used Laguerre polynomials in a Ritz–Galerkin variation solution to truncate and to discretise the continuous spectrum), to treat step discontinuous problems. All of the numerical methods require extensive computations in multiple–step and corrugated structures. Only the weakly guiding structure is considered in the IEM, also, the BPM is limited in its applications to cases with small refractive index variations and small reflected fields. Both methods are not suitable to analyse waveguide gratings. The residue calculus technique will become too tedious for multiple–step structures. *Popov and Mashev's* method only considered the first order approximation in the expansion of all quantities in series of the step height d; it is obviously not suitable for the analysis of deep corrugated structures. Although *Rozzi's* technique has been successfully used to deal with TE–mode scattering by a single step discontinuity in a symmetric planar dielectric waveguide, it does not appear to be as readily applied to the TM mode case [71] and an incorrect result was found in a double step (rib) structure [72][73].

A simple numerical method for analysing step and step–tapered waveguide structures was proposed by *Suchoski Jr. and Ramaswamy* [74]. They used Simpson's rule to discretise the continuous radiation spectrum and also neglected the evanescent modes, which are not very important for most practical applications, to develop a number of linearly independent equations with the same number of unknown amplitude coefficients. This method offers two distinct advantages over existing techniques. First, the discretised method is easily applied to both symmetric and asymmetric slab waveguides despite the type of radiation modes. Second, the linearly independent equations can be arranged in matrix form, and this transfer matrix approach is a well–known technique

to treat corrugated structures in the coupled–mode analysis [75]–[77].

In this thesis, the mode–matching technique associated with Simpson's rule, in essence, similar to that used by *Suchoski Jr. and Ramaswamy*, will be employed to analyse the discontinuous structures. But, the radiation spectrum is subdivided into a number of panels over the radiation angles instead of the spectrum of k_s (transverse propagation constant in the substrate region)

in the calculation in order to obtain better convergence. Besides, the simultaneous equations with the same number of unknown coefficients have also been rearranged as a matrix form. Combining with the transfer matrix approach, it is shown that the method introduced in this thesis is very suitable to treat waveguide gratings with large groove depth. To minimize the details, a TE_0 mode with normal incidence is considered in the major part of this thesis. But, the extension to the TM mode has no difficulties. Furthermore, extending the application of this method to double–step discontinuities such as groove and rib structures, a ten–to–one transformer, and gratings especially to the grating with aperiodic corrugated structure, will be carried out in this thesis, such as:

1. grating with single or multiple phase shifts.

2. chirped grating with variable period $\Lambda(z)$.

The first case has been used in the quarter–wave ($\lambda/4$) shift, two $\lambda/8$ phase shifts [78]–[83], and corrugation pitch modulated distributed feedback lasers [84]–[86] in order to obtain high coupling coefficients and a narrow spectral linewidth for lowering the chromatic dispersion for long–distance and wide–band optical communication in the 1.5 μm wavelength region. Multiple phase–shifted gratings have been used in DFB lasers for obtaining a uniform longitudinal field distribution, increasing the single longitudinal mode stability, and reducing the influence of spatial hole burning [85]–[92]. Spatial hole burning arises by the inhomogeneous field intensity distribution along the laser cavity,

and it degrades the single–mode properties of the laser. Further, the linewidth and frequency chirp can be reduced if an appropriately designed phase–shifted grating is used [80][81][84]. Frequency chirping in DFB or DBR lasers is unwanted since it causes signal degradation, which limits the modulation speed and the transmission distance of the optical communication systems. Recently, linearly chirped grating filters have been used to compensate the group velocity dispersion (GVD) in single–mode fibre mainly caused by material dispersion [93]–[99] and also to compress a linearly chirped pulse produced by self–phase modulation in an optical fibre [100]–[102].

A systematic investigation about discontinuous and corrugated structures will be presented and discussed in this thesis, beginning with the investigation of a single–step discontinuity, double–step structures, then gratings, and finally the applications of linearly chirped gratings to dispersion compensation and chirped pulse compression. The thesis is organized as follows: in Chapter 2 the mode–matching procedure and transfer matrix approach are introduced and formulated to treat the modes coupled by rectangular gratings with large groove depth. A set of real field distributions for symmetric and asymmetric planar waveguides is shown in Chapter 3. General mode distributions for multiple–layer planar waveguides will also be presented in this chapter. Reflection and transmission coefficients, as well as the radiation power produced by a single–step discontinuity in planar waveguides, are computed using the method proposed in this thesis, and comparisons of our results and others from different methods are shown and discussed in Chapter 4. In Chapter 5 and 6 extensions of this method to double–step discontinuities, periodic gratings, and aperiodic gratings with phase shifts are investigated and discussed. In Chapter 7 the applications of deep linearly chirped gratings for dispersion compensation and pulse compression in the femtosecond regime are demonstrated and analysed. Finally, a general conclusion of the main results and knowledge obtained from this work are given at the end of the thesis.

2

CHAPTER 2

MODE–MATCHING METHOD

2.1 INTRODUCTION

The mode–matching method provides a powerful tool for the analysis of surface waves scattered by a step discontinuity in planar waveguides. With the applications of Maxwell's equations in each region and boundary conditions at all junctions, a set of simultaneous equations is formulated for the mode amplitudes produced by the step junction. Several numerical methods and approximate analytical techniques have been proposed to solve such equations (see Chapter 1). Recently, the mode matching procedure has been used to treat other discontinuous structures, for example a step–discontinuity on microstrip structures [103], step discontinuities in graded–index dielectric slab waveguides [104], and multiple discontinuities on circular structures [105].

In this chapter we apply the mode matching procedure to both step–up and step–down discontinuities in planar waveguides, and use Simpson's rule to subdivide the radiation angles for obtaining a number of linearly independent equations in terms of same number of unknown mode coefficients. These independent equations will be arranged in matrix form and combined with the transfer matrix approach for the analysis of corrugated waveguides. Besides, the problem of singular integral equations in the inner product of two radiation modes and the evanescent modes in the continuous radiation spectrum are also investigated and discussed in this chapter.

2.2 MODE–MATCHING PROCEDURE AT STEP DISCONTINUITIES

The problem of mode scattering caused by a step discontinuity in planar waveguides can be solved very explicitly by the mode–matching procedure. A step discontinuous structure in a planar optical waveguide (see Fig. 1) is a two dimensional structure, in which the fields do not depend on the x coordinate, with a refractive index profile where refractive indices n_i and a step height d are given. The refractive index n_c of the cover above the guide (film) is smaller than or equal to the index n_s of the substrate below the guide as $n_f > n_s \geq n_c$.

All the media in each layer are lossless. A TE or TM guided mode normally incident onto the discontinuity not only produces a finite number of reflected and transmitted guided modes but also generates radiation modes with a continuous spectrum. At the step boundary, the components of these mode distributions must satisfy the following conditions [32]:

1. Maxwell's equations in each region.

2. The boundary conditions between layers I(cover), II(film). and III(substrate),

3. The boundary conditions between regions 1 and 2.

All possible mode couplings have been considered, and all of the above boundary conditions have also been satisfied in the calculation. The transverse fields, satisfying conditions 1 and 2, can be written as a superposition of normalised mode distributions with the constant amplitude coefficients of a_ν for TE modes and b_ν for TM modes, given by:

for TE modes

$$\begin{aligned} \mathcal{E}_x &= \sum_\nu a_\nu \mathcal{E}_{\nu_x} + \sum \int_0^\infty a_r(k_s)\mathcal{E}_{r_x}(k_s)dk_s \\ \mathcal{H}_y &= \sum_\nu a_\nu \mathcal{H}_{\nu_y} + \sum \int_0^\infty a_r(k_s)\mathcal{H}_{r_y}(k_s)dk_s \end{aligned} \tag{1}$$

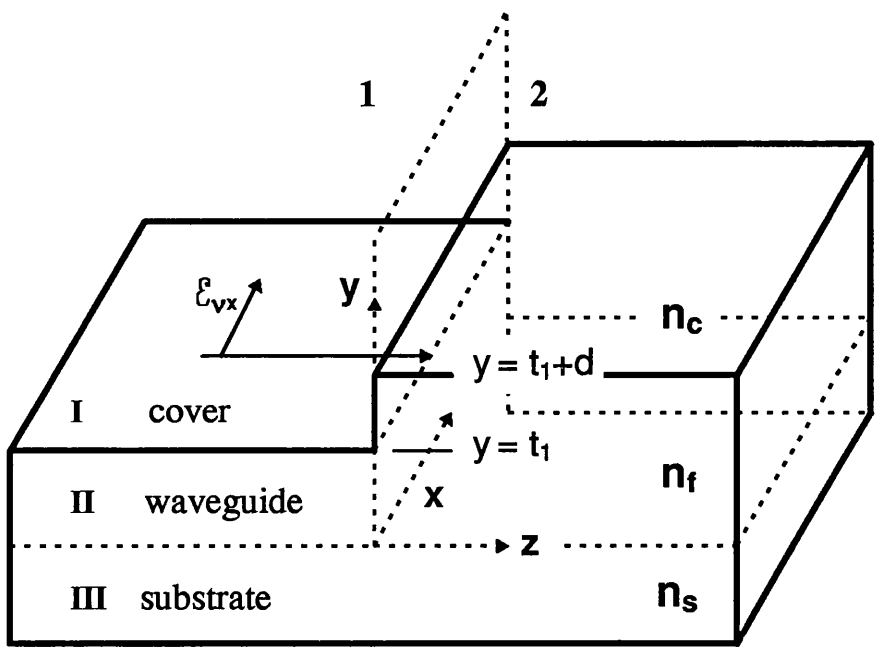

Fig. 1 *Planar optical waveguide with a step discontinuity on the surface.*

for TM modes

$$\mathcal{H}_x = \sum_{\nu} b_\nu \mathcal{H}_{\nu_x} + \sum \int_0^\infty b_r(\bar{k}_s)\mathcal{H}_{r_x}(\bar{k}_s)d\bar{k}_s$$
$$\mathcal{E}_y = \sum_{\nu} b_\nu \mathcal{E}_{\nu_y} + \sum \int_0^\infty b_r(\bar{k}_s)\mathcal{E}_{r_y}(\bar{k}_s)d\bar{k}_s \tag{2}$$

where k_s is the transverse propagation constant of TE modes in the substrate region and the overbar refers to TM modes. Because the values of k_s and $\bar{k}_s$ range from 0 to infinity, it is convenient to use k_s and $\bar{k}_s$ as the continuous mode spectrum. The superposition of modes contains a sum over discrete guided modes and an integral over continuous radiation modes. The real mode distributions guided by such waveguides will be presented and discussed in Chapter 3. According to Maxwell's equations, the field components satisfy the following relations:

for TE guided modes

$$\mathcal{H}_{\nu_y} = \frac{\beta_\nu}{\omega\mu_0}\mathcal{E}_{\nu_x}(y), \qquad \mathcal{H}_{\nu_z} = \frac{1}{j\omega\mu_0}\frac{d\mathcal{E}_{\nu_x}(y)}{dy} \tag{3}$$

for TM guided modes

$$\mathcal{E}_{\nu_y} = -\frac{\bar{\beta}_\nu}{\omega\varepsilon_0 n^2(y)}\mathcal{H}_x(y), \qquad \mathcal{E}_{\nu_z} = -\frac{1}{j\omega\varepsilon_0 n^2(y)}\frac{d\mathcal{H}_{\nu_x}(y)}{dy} \tag{4}$$

where ω is the angular frequency, ε_0 and μ_0 are the vacuum permittivity and permeability, and β, $\bar{\beta}$ are the propagation constants for TE and TM modes respectively.

The next step is to apply the condition 3 (see page 8) to the field components for the incident TE and TM modes. A coordinate system connected with the direction of propagation (see Fig. 1) is used to represent the field components at the boundary between regions 1 and 2. The transverse mode spatial distributions ($\mathcal{E}_{\nu_x}$, $\mathcal{H}_{\nu_y}$) and ($\mathcal{H}_{\nu_x}$, $\mathcal{E}_{\nu_y}$) are the field components related to this coordinate. Furthermore, in the derivation of the mode–matching procedure, the following orthogonality relations have been used [27][32] [106][107] for the mode fields:

for TE guided modes

$$\int_{-\infty}^{\infty} \mathcal{E}^*_{\mu_x}(y)\mathcal{E}_{\mu'_x}(y)dy = \frac{2\omega\mu_0}{|\beta_\mu|}\delta_{\mu\mu'} \tag{5}$$

for TE radiation modes

$$\int_{-\infty}^{\infty} \mathcal{E}^*_{r_x}(y,k_s)\mathcal{E}_{r'_x}(y,k_{s'})dy = \frac{2\omega\mu_0}{|\beta_r|}\delta(k_s - k_{s'}) \tag{6}$$

for TM guided modes

$$\int_{-\infty}^{\infty} \frac{\mathcal{H}^*_{\mu_x}(y)}{n^2(y)}\mathcal{H}_{\mu'_x}(y)dy = \frac{2\omega\varepsilon_0}{|\bar{\beta}_\mu|}\delta_{\mu\mu'} \tag{7}$$

for TM radiation modes

$$\int_{-\infty}^{\infty} \frac{\mathcal{H}^*_{r_x}(y,\bar{k}_s)}{n^2(y)}\mathcal{H}_{r'_x}(y,\bar{k}_{s'})dy = \frac{2\omega\varepsilon_0}{|\bar{\beta}_\mu|}\delta(\bar{k}_s - \bar{k}_{s'}) \tag{8}$$

where the subscript symbol of r is used to label the radiation modes, $\delta_{\mu\nu}$ is the Kronecker symbol and $\delta(x)$ is the Dirac delta function, and the absolute value of β assures that the value of power is always positive. The condition 3 requires that the electric and magnetic tangential components are continuous at the step junction. The results of the mode amplitudes coupled at the step discontinuities shown in Fig. 2(a) and 2(b) can be written as:

for TE modes at step junction 12

$$\sum_{\mu}(\mathrm{a}^{1+}_{\mu} + \mathrm{a}^{1-}_{\mu})\mathcal{E}^1_{\mu_x}(y) + \sum\int_0^{\infty}[\mathrm{a}^{1+}_r(k_s) + \mathrm{a}^{1-}_r(k_s)]\mathcal{E}^1_{r_x}(y,k_s)dk_s$$
$$= \sum_{\nu}(\mathrm{a}^{2+}_{\nu} + \mathrm{a}^{2-}_{\nu})\mathcal{E}^2_{\nu_x}(y) + \sum\int_0^{\infty}[\mathrm{a}^{2+}_r(k_s) + \mathrm{a}^{2-}_r(k_s)]\mathcal{E}^2_{r_x}(y,k_s)dk_s \tag{9}$$

$$\sum_{\mu}(\mathrm{a}^{1+}_{\mu} - \mathrm{a}^{1-}_{\mu})\mathcal{H}^1_{\mu_y}(y) + \sum\int_0^{\infty}[\mathrm{a}^{1+}_r(k_s) - \mathrm{a}^{1-}_r(k_s)]\mathcal{H}^1_{r_y}(y,k_s)dk_s$$
$$= (\mathrm{a}^{2+}_{\nu} - \mathrm{a}^{2-}_{\nu})\mathcal{H}^2_{\nu_y}(y) + \sum\int_0^{\infty}[\mathrm{a}^{2+}_r(k_s) - \mathrm{a}^{2-}_r(k_s)]\mathcal{H}^2_{r_y}(y,k_s)dk_s \tag{10}$$

at step junction 23

$$\sum_{\nu}(\mathrm{a}^{2+}_{\mu} + \mathrm{a}^{2-}_{\mu})\mathcal{E}^2_{\nu_x}(y) + \sum\int_0^{\infty}[\mathrm{a}^{2+}_r(k_s) + \mathrm{a}^{2-}_r(k_s)]\mathcal{E}^2_{r_x}(y,k_s)dk_s$$
$$= \sum_{\mu}(\mathrm{a}^{3+}_{\mu} + \mathrm{a}^{3-}_{\mu})\mathcal{E}^2_{\mu_x}(y) + \sum\int_0^{\infty}[\mathrm{a}^{3+}_r(k_s) + \mathrm{a}^{3-}_r(k_s)]\mathcal{E}^3_{r_x}(y,k_s)dk_s \tag{11}$$

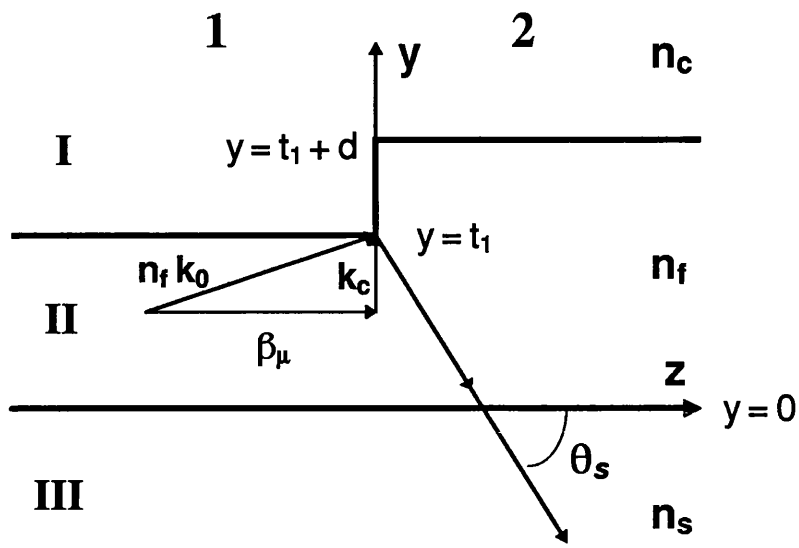

(a) Junction 12

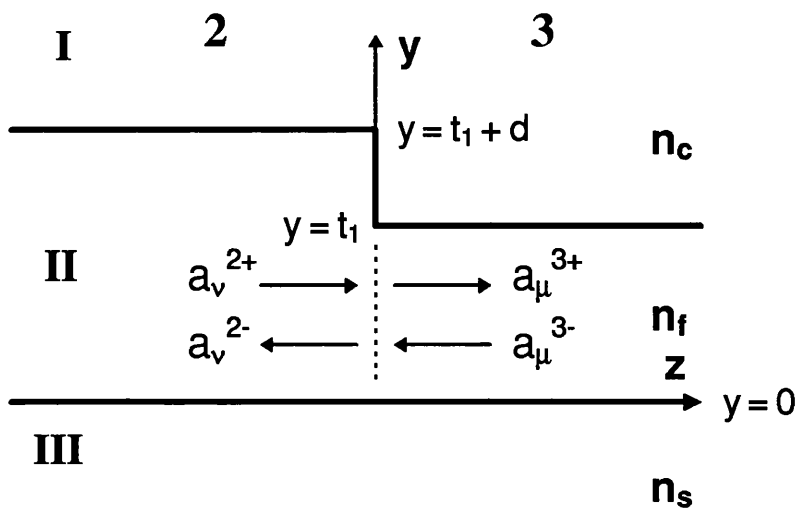

(b) Junction 23

Fig. 2 *Step junctions (a) step-up (b) step-down, and the radiation angle of one of the substrate radiation modes.*

$$\sum_{\nu}(a_{\nu}^{2+}-a_{\nu}^{2-})\mathcal{H}_{\nu_y}^{2}(y)+\sum\int_0^{\infty}[a_r^{2+}(k_s)-a_r^{2-}(k_s)]\mathcal{H}_{r_y}^{2}(y,k_s)dk_s$$
$$=\sum_{\mu}(a_{\mu}^{3+}-a_{\mu}^{3-})\mathcal{H}_{\mu_y}^{3}(y)+\sum\int_0^{\infty}[a_r^{3+}(k_s)-a_r^{3-}(k_s)]\mathcal{H}_{r_y}^{3}(y,k_s)dk_s \tag{12}$$

with

$$\begin{aligned}&\mathcal{E}_{\mu_x}^{1}=\mathcal{E}_{\mu_x}^{3},\quad \mathcal{E}_{r_x}^{1}(k_s)=\mathcal{E}_{r_x}^{3}(k_s)\\&\mathcal{H}_{\mu_y}^{1}=\mathcal{H}_{\mu_y}^{3},\quad \mathcal{H}_{r_y}^{1}(k_s)=\mathcal{H}_{r_y}^{3}(k_s)\end{aligned} \tag{13}$$

where $a_{\mu}^{1\pm}$, $a_{\nu}^{2\pm}$, $a_{\mu}^{3\pm}$ and $a_r^{1\pm}$, $a_r^{2\pm}$, $a_r^{3\pm}$ are the amplitude coefficients for the guided and radiation modes in the region 1, 2, and 3, respectively, while the superscripts $+$ and $-$ indicate the modes which correspond to the positive and negative direction of propagation with respect to the z axis. The negative sign appears in (10) and (12) because the transverse magnetic field changes sign on changing its propagation direction. Junction 12 is a step–up discontinuity and junction 23 is the step–down case. The same process can also be used to formulate a set of equations for TM modes, in which the electric and magnetic tangential components of $\mathcal{H}_x(y)$ and $\mathcal{E}_y(y)$ are also continuous at the junction. In this chapter we concentrate the analysis and the discussion on TE modes and assume that only the lowest guided TE mode can propagate along two dielectric planar waveguides in regions 1 and 2. Omitting the summation symbol in (9)–(12) and multiplying (9), (11) by $\mathcal{H}_{\mu_y}^{1*}(y)$ and $\mathcal{H}_{r_y}^{1*}(y,k_{s'})$, and (10), (12) by $\mathcal{E}_{\nu_x}^{2*}(y)$ and $\mathcal{E}_{r_x}^{2*}(y,k_{s'})$, then integrating over y from $-\infty$ to ∞ we obtain: at step junction 12

$$\begin{cases}a_{\mu}^{1+}+a_{\mu}^{1-}=(a_{\nu}^{2+}+a_{\nu}^{2-})K_{\mu\nu}+\int_0^{\infty}[a_r^{2+}(k_s)+a_r^{2-}(k_s)]K_{\mu r}dk_s\\(a_{\mu}^{1+}-a_{\mu}^{1-})K_{\mu\nu}^{*}+\int_0^{\infty}[a_r^{1+}(k_s)-a_r^{1-}(k_s)]K_{r\nu}^{*}dk_s=a_{\nu}^{2+}-a_{\nu}^{2-}\end{cases} \tag{14}$$

$$\begin{cases}a_r^{1+}(k_{s'})+a_r^{1-}(k_{s'})=(a_{\nu}^{2+}+a_{\nu}^{2-})K_{r\nu}+\int_0^{\infty}[a_r^{2+}(k_s)+a_r^{2-}(k_s)]K_{rr}(k_{s'},k_s)dk_s\\(a_{\mu}^{1+}-a_{\mu}^{1-})K_{\mu r}^{*}+\int_0^{\infty}[a_r^{1+}(k_s)-a_r^{1-}(k_s)]K_{rr}^{*}(k_s,k_{s'})dk_s=a_r^{2+}(k_{s'})-a_r^{2-}(k_{s'})\end{cases} \tag{15}$$

at step junction 23

$$\begin{cases}(a_{\nu}^{2+}+a_{\nu}^{2-})K_{\mu\nu}+\int_0^{\infty}[a_r^{2+}(k_s)+a_r^{2-}(k_s)]K_{\mu r}dk_s=a_{\mu}^{3+}+a_{\mu}^{3-}\\a_{\nu}^{2+}-a_{\nu}^{2-}=(a_{\mu}^{3+}-a_{\mu}^{3-})K_{\mu\nu}^{*}+\int_0^{\infty}[a_r^{3+}(k_s)-a_r^{3-}(k_s)]K_{r\nu}^{*}dk_s\end{cases} \tag{16}$$

$$\begin{cases} (a_\nu^{2+}+a_\nu^{2-})K_{r\nu}+\int_0^\infty [a_r^{2+}(k_s)+a_r^{2-}(k_s)]K_{rr}(k_{s'},k_s)dk_s = a_r^{3+}(k_{s'})+a_r^{3-}(k_{s'}) \\ a_r^{2+}(k_{s'})-a_r^{2-}(k_{s'}) = (a_\mu^{3+}-a_\mu^{3-})K_{\mu r}^*+\int_0^\infty [a_r^{3+}(k_s)-a_r^{3-}(k_s)]K_{rr}^*(k_s,k_{s'})dk_s \end{cases} \tag{17}$$

with the inner products between two modes

$$K_{\mu\nu} \equiv \frac{1}{2}\langle \mathcal{H}_{\mu_y}^1, \mathcal{E}_{\nu_x}^2 \rangle = \frac{\beta_\mu}{2\omega\mu_0}\int_{-\infty}^{\infty} \mathcal{E}_{\mu_x}^{1*}(y)\mathcal{E}_{\nu_x}^2(y)dy \tag{18}$$

$$K_{r\nu} \equiv \frac{1}{2}\langle \mathcal{H}_{r_y}^1(k_s), \mathcal{E}_{\nu_x}^2 \rangle = \frac{\beta(k_s)}{2\omega\mu_0}\int_{-\infty}^{\infty} \mathcal{E}_{r_x}^{1*}(y,k_s)\mathcal{E}_{\nu_x}^2(y)dy \tag{19}$$

$$K_{rr}(k_s,k_{s'}) \equiv \frac{1}{2}\langle \mathcal{H}_{r_y}^1(k_s), \mathcal{E}_{r_x}^2(k_{s'}) \rangle = \frac{\beta(k_s)}{2\omega\mu_0}\int_{-\infty}^{\infty} \mathcal{E}_{r_x}^{1*}(y,k_s)\mathcal{E}_{r_x}^2(y,k_{s'})dy \tag{20}$$

where the propagation constant β is real, and normalised mode distributions with real amplitudes are chosen for the analysis. Thus, the values of $K_{\mu\nu}$, $K_{r\nu}$, and $K_{rr}(k_s,k_{s'})$ are also real, and we have $K_{\mu\nu}=K_{\mu\nu}^*$ and $K_{r\nu}=K_{r\nu}^*$. In addition, (14), (15) and (16), (17) are similar, so we can use the same mode–matching equations (14) and (15) to treat both step–up and step–down discontinuities.

It is difficult to get a closed–form solution from (14) and (15), because the equations in (15) are singular integral equations. This problem has been solved by some approximate methods, for example by means of the Wiener–Hopf technique [108], using the first kind of Chebyshev polynomial [109], or with an asymptotic approach [110][111].

2.3 SINGULARITY PROBLEM IN THE OVERLAP INTEGRATION

As previously mentioned, the singular kernel in (15) arises from the inner products of two radiation modes. The inner products can be obtained by substituting mode

distribution functions of $\mathcal{E}^1_{r_x}(k_s, y)$ and $\mathcal{E}^2_{r_x}(k_{s'}, y)$ into (20), and the result is

$$
\begin{aligned}
&K_{rr}(k_s, k_{s'}) = \\
&\frac{\beta^1(k_s)}{2\omega\mu_0}\left\{\frac{\pi}{2}\left[E_c E_{c'}\cos[(\phi_c-\phi_{c'})+k_{c'}d]\frac{k_c}{k_s}+E_s E_{s'}\cos(\phi_s-\phi_{s'})\right]\delta\,(k_s-k_{s'})\right. \\
&\quad -\frac{1}{\beta(k_s)^2-\beta(k_{s'})^2}\left[\frac{d\mathcal{E}^{1*}_{r_x}(k_s,y)}{dy}\mathcal{E}^2_{r_x}(k_{s'},y)-\mathcal{E}^{1*}_{r_x}(k_s,y)\frac{d\mathcal{E}^2_{r_x}(k_{s'},y)}{dy}\right]_{t_1}^{t_2} \\
&\quad \left.+\frac{1}{{k_{f'}}^2-{k_c}^2}\left[\frac{d\mathcal{E}^{1*}_{r_x}(k_s,y)}{dy}\mathcal{E}^2_{r_x}(k_{s'},y)-\mathcal{E}^{1*}_{r_x}(k_s,y)\frac{d\mathcal{E}^2_{r_x}(k_{s'},y)}{dy}\right]_{t_1}^{t_2}\right\}
\end{aligned}
\tag{21}
$$

where t_1, t_2 are the thickness of the guided layers in region 1 and 2 with $t_2 = t_1 + d$, and the subscript symbols with prime indicate the values belonging to region 2. If the step height of d is equal to zero, (21) will lead to the orthogonality relation of the radiation modes with given k_s and $k_{s'}$. For the case of $d \neq 0$, Cauchy–type singularities appear in the kernels (at $\beta(k_{s'}) = \beta(k_s)$). *Rulf* [111] and *Gelin* et al [112] show that the coefficients of $a_r^{1\pm}(k_s)$ and $a_r^{2\pm}(k_s)$ in (15) exhibit singularities weak enough to be integrated. *Erdogan and Gupta* [109] used Gauss–Chebyshev integration formula for such singular integrals at a discrete set of n expansion terms, but high accuracy can be obtained only by choosing n sufficiently large. However, (21) is related to the magnitude of two radiation modes coupled at the step junction, and the energy exchange of such a coupling is very small in many practical cases. Thus, we assume that the radiation modes of region 1 and 2 are approximately orthogonal to each other to avoid too cumbersome an algorithm in the analysis of corrugated structures, with

$$
K_{rr}(k_{s'}, k_s) = \delta(k_{s'} - k_s), \qquad \text{and} \qquad K^*_{rr}(k_s, k_{s'}) = \delta(k_s - k_{s'}) \tag{22}
$$

This assumes that the radiation modes of k_s do not couple energy to a radiation mode of $k_{s'}$, if the value of k_s is not equal to $k_{s'}$. Thus, in the analysis of a corrugated structure with a series of step discontinuities, it is necessary to determine only the energy coupled among the guided modes and between guided and radiation modes.

Besides, (14)–(17) are integrated over $0 \leq k_s < \infty$. Before starting to solve these equations, the spectrum of k_s in the integrals has to be limited to a finite range.

Table 1:
The range of β and k_s [28]

Modes	β	k_s
guided modes	$k_0 n_f \rightarrow k_0 n_s$	imaginary
substrate rad.	$k_0 n_s \rightarrow k_0 n_c$	$0 \rightarrow k_0\sqrt{n_s^2 - n_c^2}$
substrate–cover rad.	$k_0 n_c \rightarrow 0$	$k_0\sqrt{n_s^2 - n_c^2} \rightarrow k_0 n_s$
evanescent	imaginary	$k_0 n_s \rightarrow \infty$

2.4 TRUNCATION OF THE RADIATION SPECTRUM

The value of k_s is used as the spatial frequency for the continuous mode spectrum. Table 1 shows the ranges of k_s and the propagation constants β with respect to the various mode types.

The evanescent modes with k_s in the range of $k_0 n_s \leq k_s < \infty$ are considered to form a complete set of orthogonal modes to satisfy Maxwell's equations, and are not very important for most practical applications [27]. The evanescent modes have also been ignored in calculations by other authors [27][68][74]. Thus, (14)–(17) are integrated only over $0 \leq k_s \leq k_0 n_s$ as follows

$$\begin{cases} a_\mu^{1+} + a_\mu^{1-} = (a_\nu^{2+} + a_\nu^{2-})K_{\mu\nu} + \int_0^{k_0 n_s} [a_r^{2+}(k_s) + a_r^{2-}(k_s)]K_{\mu r}\, dk_s \\ (a_\mu^{1+} - a_\mu^{1-})K_{\mu\nu}^* + \int_0^{k_0 n_s} [a_r^{1+}(k_s) - a_r^{1-}(k_s)]K_{r\nu}^*\, dk_s = a_\nu^{2+} - a_\nu^{2-} \end{cases} \tag{23}$$

$$\begin{cases} a_r^{1+}(k_{s'}) + a_r^{1-}(k_{s'}) \\ \qquad = (a_\nu^{2+} + a_\nu^{2-})K_{r\nu} + \int_0^{k_0 n_s} [a_r^{2+}(k_s) + a_r^{2-}(k_s)]\delta(k_{s'} - k_s)\, dk_s \\ (a_\mu^{1+} - a_\mu^{1-})K_{\mu r}^* \\ \qquad + \int_0^{k_0 n_s} [a_r^{1+}(k_s) - a_r^{1-}(k_s)]\delta(k_s - k_{s'})\, dk_s = a_r^{2+}(k_{s'}) - a_r^{2-}(k_{s'}) \end{cases} \tag{24}$$

The above equations can be applied to both step–up and step–down discontinuities. Several methods have been proposed to solve the above equations (see Chapter 1). In

the next section, Simpson's rule is used to discretise the continuous spectrum, and the above equations are rearranged as a number of linear equations with the same number of unknown coefficients.

2.5 DISCRETISATION OF THE RADIATION SPECTRUM

A radiation mode propagates through the interface into the substrate region at an angle θ_s to the z axis (Fig. 2(a)). The value of θ_s related to k_s is given by

$$k_s = k_0 n_s \sin\theta_s = \sqrt{k_0^2 n_s^2 - \beta^2} \tag{25}$$

For a symmetric slab waveguide with $n_s = n_c$ in Fig. 2(a) and 2(b), the radiation mode of k_s will be scattered by the step junction and goes into upper and lower regions outside the guide with the same radiation angle. In this case, only one type of radiation mode is necessary to be considered in the analysis. But, for an asymmetric structure with $n_s \neq n_c$, two types of radiation modes are produced at the junction. One of the radiation modes is called a *substrate radiation mode* (Table 1) with the value of k_s ranging from 0 to $k_0\sqrt{n_s^2 - n_c^2}$. It radiates energy into the substrate with a radiation angle from $\theta_s = 0$ to $\theta_s = \cos^{-1}(n_c/n_s)$, but suffers total internal reflection at the interface of the guide and cover layers. The other radiation mode is called a *substrate–cover radiation mode* with $k_0\sqrt{n_s^2 - n_c^2} \leq k_s \leq k_0 n_s$. This type of radiation mode leaks energy out of the guide into both regions, and the radiation angles in the substrate and in the cover obey the relation

$$n_c \cos\theta_c = n_s \cos\theta_s \tag{26}$$

where θ_s and θ_c are the radiation angles in the substrate and in the cover respectively. The range of θ_s is $\cos^{-1}(n_c/n_s) \leq \theta_s \leq \pi/2$, and $0 \leq \theta_c \leq \pi/2$ for θ_c.

For an asymmetric slab waveguide with $n_s \neq n_c$, the integral terms in (23) and (24) can be separated into two parts, one for the substrate radiation mode and the other for the substrate–cover radiation mode. In this case, two types of radiation

modes have to be treated individually. Firstly, we consider a symmetric monomode slab waveguide, in which the step discontinuity appears on both sides of the guiding layer; the structure only supports one guided mode and one type of radiation mode. We subdivide the radiation angle from 0 to θ_η into m equally spaced panels to generate $(m+1)$ discrete points including two endpoints ($\theta = 0$ and θ_η), where the angle θ_η (slightly less than $\pi/2$) is introduced here in order to avoid the singular point $\theta = \pi/2$ in the computation. Considering the radiation losses precisely in the vicinity of $\pi/2$ for the mode–matching procedure has the following advantages: it can improve the convergence condition in the region of small m, and the accuracy of computation can be improved in the analysis of second order gratings for vertical output coupling because most of radiation losses leak into the interior region with radiation angle about 90°. The unknown coefficients of $a_{r_i}^{2+}(\theta_i)$ and $a_{r_i}^{1-}(\theta_i)$ at the $(m+1)$ discrete points can be used to calculate the coupling coefficients of the transmitted radiation mode and the reflected radiation mode. To determine these $2(m+1)$ unknown coefficients and other two unknown coefficients a_ν^{2+} and a_μ^{1-} of guided modes, it is necessary to develop $(2m+4)$ linearly independent equations in terms of these unknown coefficients. No radiation mode exists for $k_s = 0$ ($\theta = 0$), so the number of linearly independent equations as well as the unknown coefficients are reduced to $2(m+1)$ with m radiation panels as well as m radiation modes for forward and backward propagating each. (23), (24) can be approximated by

$$
\begin{aligned}
a_\mu^{1+} + a_\mu^{1-} &= (a_\nu^{2+} + a_\nu^{2-})K_{\mu\nu} + \frac{4\Delta\theta}{3}\sum_{\substack{i=1\\ odd}}^{m-1} a_{r_i}^{2+}(\theta_i)K_{\mu r_i} + \frac{2\Delta\theta}{3}\sum_{\substack{i=2\\ even}}^{m-2} a_{r_i}^{2+}(\theta_i)K_{\mu r_i} \\
&+ \frac{\Delta\theta}{3}a_{r_m}^{2+}(\theta_\eta) + \frac{4\Delta\theta}{3}\sum_{\substack{i=1\\ odd}}^{m-1} a_{r_i}^{2-}(\theta_i)K_{\mu r_i} + \frac{2\Delta\theta}{3}\sum_{\substack{i=2\\ even}}^{m-2} a_{r_i}^{2-}(\theta_i)K_{\mu r_i} + \frac{\Delta\theta}{3}a_{r_m}^{2-}(\theta_\eta) \\
(a_\mu^{1+} - a_\mu^{1-})K_{\mu\nu}^* &+ \frac{4\Delta\theta}{3}\sum_{\substack{i=1\\ odd}}^{m-1} a_{r_i}^{1+}(\theta_i)K_{r_i\nu}^* + \frac{2\Delta\theta}{3}\sum_{\substack{i=2\\ even}}^{m-2} a_{r_i}^{1+}K_{r_i\nu}^* + \frac{\Delta\theta}{3}a_{r_m}^{1+}(\theta_\eta) \\
&- \frac{4\Delta\theta}{3}\sum_{\substack{i=1\\ odd}}^{m-1} a_{r_i}^{1-}(\theta_i)K_{r_i\nu}^* - \frac{2\Delta\theta}{3}\sum_{\substack{i=2\\ even}}^{m-2} a_{r_i}^{1-}K_{r_i\nu}^* - \frac{\Delta\theta}{3}a_{r_m}^{1-}(\theta_\eta) = a_\nu^{2+} - a_\nu^{2-}
\end{aligned}
\tag{27}
$$

$$
\begin{aligned}
&a^{1+}_{r_{i'}}(\theta_{i'}) + a^{1-}_{r_{i'}}(\theta_{i'}) = (a^{2+}_{\nu} + a^{2-}_{\nu})K_{r_{i'}\nu} + \sum_{i=1}^{m}[a^{2+}_{r_i}(\theta_i) + a^{2-}_{r_i}(\theta_i)]\delta(\theta_{i'} - \theta_i) \\
&(a^{1+}_{\mu} - a^{1-}_{\mu})K^{*}_{\mu r_{i'}} + \sum_{i=1}^{m}[a^{1+}_{r_i}(\theta_i) - a^{1-}_{r_i}(\theta_i)]\delta(\theta_i - \theta_{i'}) = a^{2+}_{r_{i'}}(\theta_{i'}) - a^{2-}_{r_{i'}}(\theta_{i'}) \qquad (28) \\
&\qquad\qquad\qquad\qquad \text{with} \quad i' = 1, 2, 3, \ldots, m
\end{aligned}
$$

where

$$
k_s = n_s k_0 \sin\theta, \qquad \Delta\theta = \frac{1}{n_s k_0 \cos\theta}\Delta k_s \qquad (29)
$$

The coefficients a^{2-}_{ν} and $a^{2-}_{r_i}$ of the reflected waves moving along the $-z$ direction in region 2 are equal to zero in the case with a single step discontinuity, but they must be considered in the analysis of corrugated structures. However, (27) and (28) are $2(m+1)$ linearly independent equations (two from (27) and $2m$ from (28)) in terms of the $2(m+1)$ unknown coefficients (a^{1-}_{μ,r_i} and a^{2+}_{ν,r_i}) with the assumption that the incident electric field is normalised to 1 (*i.e.* $a^{1+}_{\mu} = 1$ and others equal zero). We introduce a transfer matrix method in this treatment with the same sequence of numbers for both guided and radiation modes ($a^{1-}_{\mu_i}$, $a^{2+}_{\nu_i}$, with $i = 1, 2, 3, \ldots, m+1$; $i = 1$ for the guided mode, and the rest are for the radiation modes). Then (27) and (28) can be written in matrix form

$$
\left[\begin{array}{c|c}
\begin{bmatrix} 1 & 0 & \cdots \\ 0 & 1 & \cdots \\ \vdots & \vdots & \ddots \end{bmatrix} & \begin{bmatrix} 1 & 0 & \cdots \\ 0 & 1 & \cdots \\ \vdots & \vdots & \ddots \end{bmatrix} \\
\hline
\begin{bmatrix} \sigma_{\mu_1} K^{*}_{\mu_1\nu_1} & \sigma_{\mu_2} K^{*}_{\mu_2\nu_1} & \cdots \\ K^{*}_{\mu_1\nu_2} & 1 & \cdots \\ \vdots & \vdots & \ddots \end{bmatrix} & \begin{bmatrix} -\sigma_{\mu_1} K^{*}_{\mu_1\nu_1} & -\sigma_{\mu_2} K^{*}_{\mu_2\nu_1} & \cdots \\ -K^{*}_{\mu_1\nu_2} & -1 & \cdots \\ \vdots & \vdots & \ddots \end{bmatrix}
\end{array}\right]
\left[\begin{array}{c} a^{1+}_{\mu_1} \\ a^{1+}_{\mu_2} \\ \vdots \\ \hline a^{1-}_{\mu_1} \\ a^{1-}_{\mu_2} \\ \vdots \end{array}\right]
$$

$$
= \left[\begin{array}{c|c}
\begin{bmatrix} \sigma_{\nu_1} K_{\mu_1\nu_1} & \sigma_{\nu_2} K_{\mu_1\nu_2} & \cdots \\ K_{\mu_2\nu_1} & 1 & \cdots \\ \vdots & \vdots & \ddots \end{bmatrix} & \begin{bmatrix} \sigma_{\nu_1} K_{\mu_1\nu_1} & \sigma_{\nu_2} K_{\mu_1\nu_2} & \cdots \\ K_{\mu_2\nu_1} & 1 & \cdots \\ \vdots & \vdots & \ddots \end{bmatrix} \\
\hline
\begin{bmatrix} 1 & 0 & \cdots \\ 0 & 1 & \cdots \\ \vdots & \vdots & \ddots \end{bmatrix} & \begin{bmatrix} -1 & 0 & \cdots \\ 0 & -1 & \cdots \\ \vdots & \vdots & \ddots \end{bmatrix}
\end{array}\right]
\left[\begin{array}{c} a^{2+}_{\nu_1} \\ a^{2+}_{\nu_2} \\ \vdots \\ \hline a^{2-}_{\nu_1} \\ a^{2-}_{\nu_2} \\ \vdots \end{array}\right] \qquad (30)
$$

with

$$\sigma_{\mu_i},\ \sigma_{\nu_i} = \begin{cases} 1, & \text{for the guided mode with } i = 1 \\ \dfrac{4\Delta\theta}{3}, & \text{for radiation modes with } i = even \\ \dfrac{2\Delta\theta}{3}, & \text{for radiation modes with } i = odd,\ i > 1 \\ \dfrac{\Delta\theta}{3}, & \text{for radiation modes with } i = m+1 \end{cases} \tag{31}$$

(30) is also suitable for the case with multiple–mode incidence. For convenience, It may be rewritten as

$$\left[M^1\right]\left[A^1\right] = \left[M^2\right]\left[A^2\right] \tag{32}$$

or

$$\begin{aligned} \left[A^1\right] &= \left[M^{12}\right]\left[A^2\right], \qquad [M^{12}] = [M^1]^{-1}[M^2] \\ \left[A^2\right] &= \left[M^{21}\right]\left[A^1\right], \qquad [M^{21}] = [M^2]^{-1}[M^1] \end{aligned} \tag{33}$$

where $[M^1]$ and $[M^2]$ are two nonsingular matrices, $[A^1]$ and $[A^2]$ are the coefficient column matrices of the modes in the regions 1 and 2 respectively, $[M^{12}]$ is the transfer matrix for the step–up discontinuity, and $[M^{21}]$ $(=[M^{23}])$ is the transfer matrix for the step–down case which has the same form as $[M^{12}]^{-1}$. But, for the case of a single step discontinuity only on one side of the guiding layer, two degenerate radiation modes (even and odd) will be generated at the junction, because the orthogonality relation between even and odd modes no longer holds as the symmetry of the structure disappears. And, both degenerate modes have to be considered in the calculation. Thus, the number of linearly independent equations and also of the unknown coefficients becomes as many as $(4m+2)$. For asymmetric waveguides, two types of radiation modes have to be treated in the analysis. If we subdivide the substrate radiation angle $0 \leq \theta_\nu < \cos^{-1}(n_c/n_s)$ into n equally spaced panels, and also subdivide the substrate–cover radiation angle $\cos^{-1}(n_c/n_s) \leq \theta_\nu < \pi/2$ in the substrate region into m equally spaced panels for both even and odd degenerate radiation modes, this generates $(m+2n+3)$ discrete points

and the same number of unknown coefficients of $a_{r_i}^{1-}$ and $a_{r_i}^{2+}$ to be determined. By ignoring the points $k_s = 0$ and $k_c = 0$ in both sets of discrete points, and including the two unknown coefficients a_{μ}^{1-} and a_{ν}^{2+}, the total number of unknown coefficients is summed up to $2(m+2n+1)$. Using the same procedures described above, we can develop $2(m+2n+1)$ linearly independent equations in terms of these unknowns coefficients.

The advantage of using the transfer matrix in the mode–matching method is in the analysis of periodic gratings, and can be extended to treat aperiodic corrugated structures. A transfer matrix approach is introduced in the next section for this analysis.

2.6 THE TRANSFER MATRIX APPROACH

Let us consider one period of a grating (Fig. 3) consisting of two discontinuities and two sections of planar waveguides, each section between two adjoining step–junctions with thickness $t_1 (= t_3)$ and t_2, respectively. A wave propagating in these regions experiences a phase delay $\exp(\mp j\beta_{\nu}^{i}\Lambda_i)$, where $\mp$ refers to waves propagating in the $\pm z$ directions. This can be represented as a propagating matrix

$$[T^i] = \left[\begin{array}{c|c} \begin{bmatrix} e^{-j\beta_{\nu_1}^{i}\Lambda_i} & 0 & \cdots \\ 0 & e^{-j\beta_{\nu_2}^{i}\Lambda_i} & \cdots \\ \vdots & \vdots & \ddots \end{bmatrix} & 0 \\ \hline 0 & \begin{bmatrix} e^{+j\beta_{\nu_1}^{i}\Lambda_i} & 0 & \cdots \\ 0 & e^{+j\beta_{\nu_2}^{i}\Lambda_i} & \cdots \\ \vdots & \vdots & \ddots \end{bmatrix} \end{array}\right] \tag{34}$$

and

$$[A^{i\prime}] = [T^i]\,[A^i]\ , \qquad [A^i] = [T^i]^{-1}\,[A^{i\prime}] \tag{35}$$

where Λ_i is the length of the section i, and β_{ν_i} is the propagation constant of each mode in this region. We can describe the effect of a mode or modes propagating through a

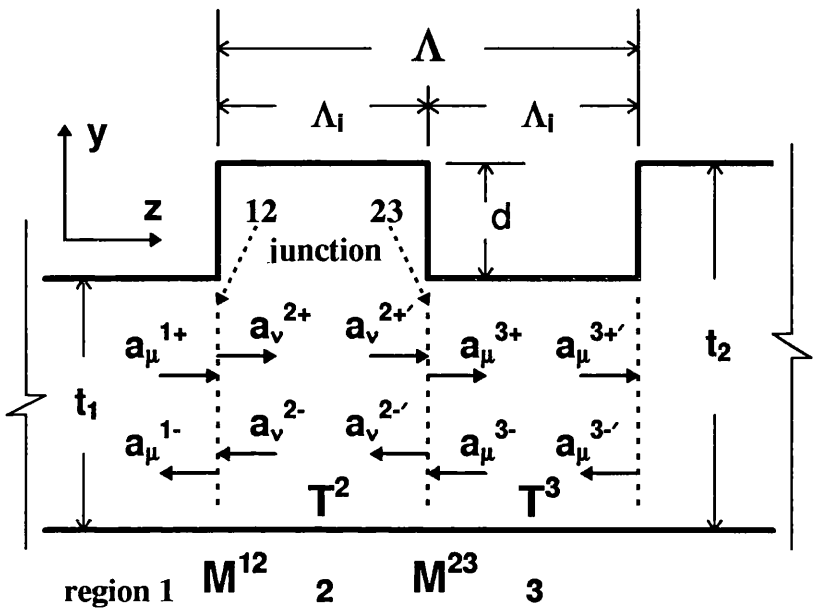

Fig. 3 *Schematic diagram for the* ith *period and coefficients at each boundary.*

single period by using a combination of the transfer matrix and the propagating matrix in the analysis. The total transfer matrix at the end of a period is of the form

$$\left[A^1\right] = \left[M^{12}\right]\left[T^2\right]^{-1}\left[M^{23}\right]\left[T^3\right]^{-1}\left[A^{3\prime}\right] \tag{36}$$

or

$$\left[A^{3\prime}\right] = \left[T^3\right]\left[M^{32}\right]\left[T^2\right]\left[M^{21}\right]\left[A^1\right] \tag{37}$$

We define a total transfer matrix $[M]$ that links the mode amplitudes of one period; then (36) and (37) reduce to

$$\begin{aligned} [A^1] &= [M]\,[A^{3\prime}]\ , \qquad [M] = [M^{12}]\,[T^2]^{-1}\,[M^{23}]\,[T^3]^{-1} \\ [A^{3\prime}] &= [M]^{-1}\,[A^1]\ , \qquad [M]^{-1} = [T^3]\,[M^{32}]\,[T^2]\,[M^{21}] \end{aligned} \tag{38}$$

For a periodic grating consisting of N periods, the total transfer matrix equation is given by

$$[A^1] = [M]^N\,[A^o] \tag{39}$$

where $[A^o]$ is the coefficient column matrix of the modes at the end of the grating (output port). For linearly chirped gratings with constant grating depth, the transfer matrices $[M^{12}]$ and $[M^{21}]$ for step discontinuities have the same form as for periodic gratings but the propagating matrix $[T^i]$ is variable due to the different value of Λ_i. The perturbation of variable period $\Lambda+\Delta\Lambda(n)$ can be adjusted for special applications. Thus, (39) becomes

$$[A^1] = [M^1][M^2][M^3]\cdots[M^N][A^o] \tag{40}$$

where $[M^i]$ is the total transfer matrix of the ith period with the section length Λ_i. The transfer matrix of (39) can be modified flexibly for the analysis of special phase–shifted grating, for example, single $\lambda/4$ phase–shifted gratings, multiple phase–shifted gratings, and more complicated structures such as super structure gratings (SSG) and chirped

gratings. These extended applications will be discussed and carried out in the following chapters.

The resultant transfer matrix equation (39) or (40) is also a system of $2(m+1)$ linearly independent equations with $2(m+1)$ unknown coefficients that can be solved numerically. They can be rewritten in a general form such as

$$\begin{bmatrix} a_{\mu_i}^{1+} \\ a_{\mu_i}^{1-} \end{bmatrix} = \begin{bmatrix} M_{11} & M_{12} \\ M_{21} & M_{22} \end{bmatrix} \begin{bmatrix} a_{\nu_i}^{o+} \\ a_{\nu_i}^{o-} \end{bmatrix}, \qquad i = 1, 2, 3, \ldots, m+1 \tag{41}$$

where $a_{\mu_i}^{1+}$ are normalised amplitudes of the incident modes from the left side of the grating, $a_{\mu_i}^{1-}$, $a_{\nu_i}^{o+}$ are the $2(m+1)$ unknown amplitude coefficients of the reflected and transmitted modes in the left and right sides of the grating, respectively. Since the waveguide becomes a homogeneous structure beyond the grating, the coefficients of reflected modes beyond the grating $a_{\nu_i}^{o-}$ should equal zero. (41) can be rearranged as

$$\begin{bmatrix} a_{\nu_i}^{o+} \\ a_{\mu_i}^{1-} \end{bmatrix} = \begin{bmatrix} -M_{11} & 0 \\ -M_{21} & U \end{bmatrix}^{-1} \begin{bmatrix} -U & M_{12} \\ 0 & M_{22} \end{bmatrix} \begin{bmatrix} a_{\mu_i}^{1+} \\ a_{\nu_i}^{o-} \end{bmatrix} \tag{42}$$

or as

$$\begin{bmatrix} a_{\nu_i}^{o+} \\ a_{\mu_i}^{1-} \end{bmatrix} = \begin{bmatrix} S_{11} & S_{12} \\ S_{21} & S_{22} \end{bmatrix} \begin{bmatrix} a_{\mu_i}^{1+} \\ a_{\nu_i}^{o-} \end{bmatrix} \tag{43}$$

In (42), matrix U is an $(m+1)$th order $[(m+1)\times(m+1)]$ unit matrix with $(u)_{ij}=\delta_{ij}$. The $[S]$ matrix as well as the $2(m+1)$ unknown coefficients $a_{\mu_i}^{1-}$ and $a_{\nu_i}^{o+}$ can be determined by evaluating the necessary overlap integrals (18)–(20).

2.7 CONCLUSION

A method was developed in this chapter based on the mode–matching procedure and transfer matrix approach. With minimal approximation and all-significant mode couplings in the analysis, this method may be used to treat corrugated waveguides with large groove depth. In particular, the numerical algorithm of matrix algebra presented in this chapter is suitable for computer processing.

3

CHAPTER 3

MODE DISTRIBUTIONS IN PLANAR WAVEGUIDES

3.1 INTRODUCTION

A complete orthonormal set of modes supported by the slab waveguide (Fig. 1) is necessary to be introduced for the inner product calculation. *Morishita* et al. [57] and *Rozzi* [70] used the normalised Laguerre functions for the expansions of guided and radiation modes, and it is shown that the normalised Laguerre functions have good convergence because Laguerre functions decrease exponentially as the value of k_s increases. Other authors [68][113] used the well-known normalised field distributions which are obtained from Maxwell's equations and boundary conditions for the analysis. Since normalised field distributions have real amplitudes in each region, these field functions are suitable for the mode-matching calculation described in Chapter 2.

A set of normalised field distributions from *Kogelnik* [28] is presented in this chapter for the analysis of asymmetric planar waveguides, and similar field functions may also be used for symmetric structures after a very small alteration. These field distributions are cast in a simple form with peak amplitudes and phase shift constants in expressions, and they are classified as guided modes, substrate radiation modes, substrate-cover radiation modes, and evanescent modes.

In this chapter we also propose a set of general field distributions for multiple-layer planar waveguides with arbitrary index profile of the guiding layers between the

superstrate and the substrate. It is shown that eigenvalue equations of such structures can be simplified as a form of an equivalent three–layer planar waveguide, and the peak amplitudes and phase shift constants of the field functions are evaluated easily by computer processing. Some comparisons of the results from these field distributions with those obtained by other methods are carried out in order to ensure that field functions as well as the computer programs are accurate.

3.2 MODE DISTRIBUTIONS FOR ASYMMETRIC SLAB WAVEGUIDES

Before starting to analyse the discontinuous structures, it is important to understand the guided and radiated modes propagating in the planar waveguide. Consider TE modes propagating in the structure shown in Fig. 4(a), in which the slab is infinitely extended in the xz plane. The common phase factor of $\exp[j(\omega t - \beta z)]$ is omitted in the field expressions. With $\mathcal{H}_x = 0$, $\mathcal{E}_y = \mathcal{E}_z = 0$, the time independent one–dimensional wave equation obtained from Maxwell's equations for $\mathcal{E}_x$ is

$$\frac{\partial^2 \mathcal{E}_x(y)}{\partial y^2} = (\beta^2 - \omega^2 \mu\varepsilon)\mathcal{E}_x(y) = (\beta^2 - n^2 k_0^2)\mathcal{E}_x(y) \tag{44}$$

where $k_0 = \omega/c = \omega\sqrt{\mu_0 \varepsilon_0}$ and $\mu\varepsilon = n^2 \mu_0 \varepsilon_0$, k_0 is the propagation constant in the free–space. For convenient range, the transverse propagation constant $k_s = \sqrt{n_s^2 k_0^2 - \beta^2}$ in the substrate region will be used as the spatial frequency for the radiation modes (Table 1). As mentioned before, we ignore the evanescent modes in the mode–matching analysis. A set of $\mathcal{E}_x$ components obeying the wave equation (44) and boundary conditions (that $\mathcal{E}_x$ and $\mathcal{H}_z$ should be continuous at $y = 0$, and $y = t$) is described in the following sections

Consider a slab waveguide having refractive indices n_s, n_f, and n_c of the substrate, the film, and the cover, and the film–thickness t. For guided TE modes, the electric

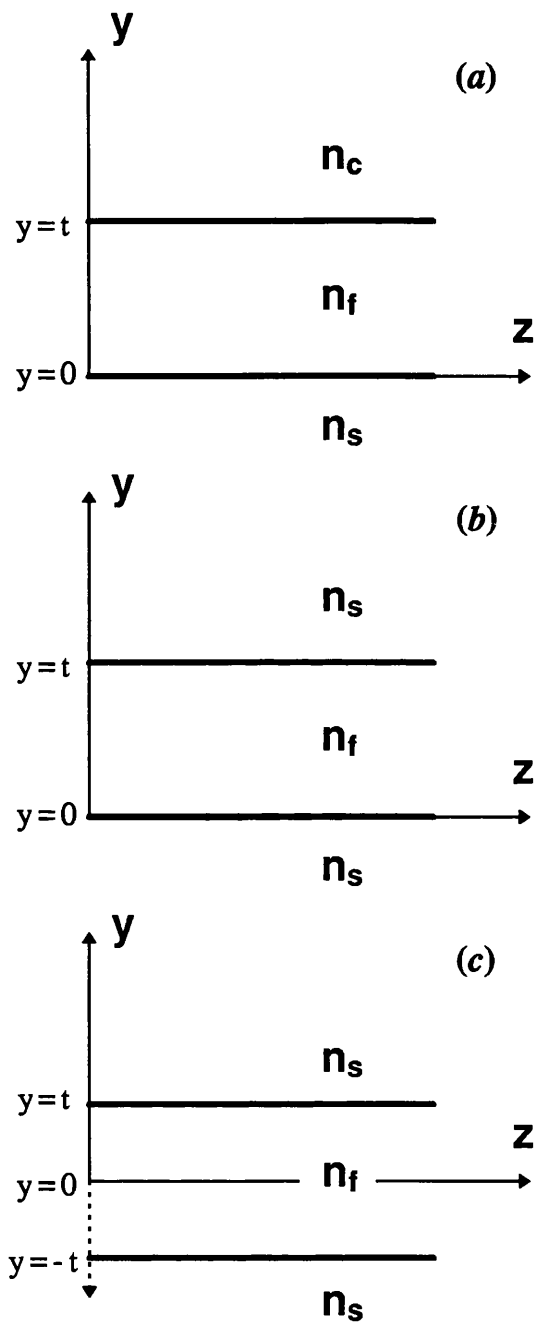

Fig. 4 *(a) A three-layer asymmetric planar waveguide. (b) A symmetric slab waveguide. (c) A symmetric slab waveguide with coordinate adjustment.*

field $\mathcal{E}_x(y)$ is expressed as [28]

$$\mathcal{E}_x(y) = \begin{cases} E_c \exp[-\gamma_c(y-t)], & \text{for} \quad y \geq t\,, & \text{cover} \\ E_f \cos(k_f y - \phi_s), & \text{for} \quad 0 \leq y \leq t\,, & \text{film} \\ E_s \exp(\gamma_s y), & \text{for} \quad y \leq 0\,, & \text{substrate} \end{cases} \tag{45}$$

with

$$\begin{aligned} \gamma_c &= (\beta^2 - k_0^2 n_c^2)^{1/2} \\ k_f &= (k_0^2 n_f^2 - \beta^2)^{1/2} \\ \gamma_s &= (\beta^2 - k_0^2 n_s^2)^{1/2} \end{aligned} \tag{46}$$

where E_c, E_f, and E_s are the peak amplitudes in each layer, and β is the propagation constant of the mode. On application of the boundary condition, these peak amplitudes are related by

$$E_f^2(n_f^2 - n_{\text{eff}}^2) = E_s^2(n_f^2 - n_S^2) = E_c^2(n_f^2 - n_c^2)\,, \qquad \text{with } n_{\text{eff}} = \frac{\beta}{k_0} \tag{47}$$

and the eigenvalue equation

$$k_f t - \phi_s - \phi_c = \nu\pi\,, \quad \text{with} \quad \phi_c = \tan^{-1}\frac{\gamma_c}{k_f} \quad \text{and} \quad \phi_s = \tan^{-1}\frac{\gamma_s}{k_f} \tag{48}$$

where n_{eff} is the effective refractive index of the waveguide for the TE mode with a given β, and the integer ν of $\nu = 0, 1, 2, \ldots$ is the mode order. Demanding the orthogonality relation of the mode, the peak amplitude of E_f can be determined by

$$P = \frac{|\beta|}{2\omega\mu_0}\int_{-\infty}^{\infty} |\mathcal{E}_x|^2(y)dy = \frac{\beta}{4\omega\mu_0} E_f^2\, t_{\text{eff}} \tag{49}$$

where P is the power of the mode per unit cross–section perpendicular to the mode propagation direction and $t_{\text{eff}} = (t + 1/\gamma_s + 1/\gamma_c)$. Because we use the normalised mode distributions in the analysis, the mode amplitudes in each layer are real values. For the substrate radiation mode with $0 \leq k_s \leq k_0\sqrt{n_s^2 - n_c^2}$, the field distribution is

$$\mathcal{E}_x(y) = \begin{cases} E_c \exp[-\gamma_c(y-t)], & \text{for} \quad y \geq t \\ E_f \cos(k_f(y-t) + \phi_c), & \text{for} \quad 0 \leq y \leq t \\ E_s \cos(k_s y + \phi), & \text{for} \quad y \leq 0 \end{cases} \tag{50}$$

where $k_s = (k_0^2 n_s^2 - \beta^2)^{1/2}$.

By applying the boundary conditions, we have

$$\begin{cases} \tan\phi_c = \dfrac{\gamma_c}{k_f} \\ k_s \tan\phi = k_f \tan(\phi_c - k_f t) \end{cases} \tag{51}$$

and

$$\begin{cases} E_f^2(n_f^2 - N^2) = E_c^2(n_f^2 - n_c^2) \\ E_s^2 = E_f^2 \left[1 + \dfrac{n_f^2 - n_s^2}{n_s^2 - N^2} \sin^2(\phi_c - k_f t)\right] \end{cases} \tag{52}$$

The normalisation condition using a Dirac delta function [27] is given as

$$\left(\frac{\beta^*}{2\omega\mu_0}\right) \int_{-\infty}^{\infty} \mathcal{E}_x(y, k_s)\mathcal{E}_x^*(y, k_{s'})dy = \left(\frac{\beta^*}{|\beta|}\right) \delta(k_s - k_{s'}) \tag{53}$$

Substituting the substrate radiation wave function into the normalisation condition, we obtain

$$P = \frac{\pi|\beta|}{4\omega\mu_0} E_s^2 \, \delta(k_s - k_{s'}) \tag{54}$$

For the substrate–cover radiation modes, two mutually orthogonal mode functions will be chosen in the calculation. For the sake of convenience, those modes of $\mathcal{E}_x^{o,e}(y)$ are also called "even" and "odd" modes [28], such as

$$\begin{array}{ll} \text{for odd modes} & \text{for even modes} \\ \begin{cases} E_c^o \sin[k_c(y-t) + \phi_c^o]; \\ E_f^o \sin(k_f y - \phi); \\ E_s^o \sin(k_s y - \phi_s^o); \end{cases} & \begin{cases} E_c^e \cos[k_c(y-t) + \phi_c^e], & y \geq t \\ E_f^e \cos(k_f y - \phi), & 0 \leq y \leq t \\ E_s^e \cos(k_s y - \phi_s^e), & y \leq 0 \end{cases} \end{array} \tag{55}$$

where $k_c = (k_0^2 n_c^2 - \beta^2)^{1/2}$, and the superscript "o", "e" referred to the "odd" and "even" mode, respectively. The peak amplitude relations for odd and even modes are as following:

for the odd modes

$$\begin{cases} k_s \cot \phi_s^o = k_f \cot \phi \\ k_c \cot \phi_c^o = k_f \cot(k_f t - \phi) \\ E_s^{o2} = E_f^{o2}(\sin^2 \phi + \dfrac{k_f^2}{k_s^2} \cos^2 \phi) \\ E_c^{o2} = E_f^{o2} \left[\sin^2(k_f t - \phi) + \dfrac{k_f^2}{k_c^2} \cos^2(k_f t - \phi) \right] \end{cases} \tag{56}$$

for the even modes

$$\begin{cases} k_s \tan \phi_s^e = k_f \tan \phi \\ k_c \tan \phi_c^e = k_f \tan(k_f t - \phi) \\ E_s^{e2} = E_f^{e2}(\cos^2 \phi + \dfrac{k_f^2}{k_s^2} \sin^2 \phi) \\ E_c^{e2} = E_f^{e2} \left[\cos^2(k_f t - \phi) + \dfrac{k_f^2}{k_c^2} \sin^2(k_f t - \phi) \right] \end{cases} \tag{57}$$

and the normalised power can be expressed as

$$P = \frac{\pi |\beta|}{4\omega\mu_0} \left(\frac{k_c}{k_s} E_c^2 + E_s^2 \right) \delta(k_s - k_{s'}) \,, \quad \text{for both odd and even modes} \tag{58}$$

According to the orthogonality between odd and even modes, the phase shift ϕ can be written as

$$\tan\ 2\phi = \sin(2k_f t) \left[\cos(2k_f t) + \frac{k_s}{k_c} \frac{(1 - k_f^2/k_s^2)}{(1 - k_f^2/k_c^2)} \right]^{-1} \tag{59}$$

3.3 MODE DISTRIBUTIONS FOR SYMMETRIC SLAB WAVEGUIDES

In the limit $n_c = n_s$, the structure as shown in Fig. 4(b) become a symmetric planar waveguide, and only one type of radiation modes need be considered in the calculation. For guided modes, the field functions $\mathcal{E}_x(y)$ have the same form as (45) but with subscript "c" replaced by "s". In general, these guided modes can be categorised

into two types "even" and "odd" mode which correspond to the even and odd mode number respectively. The mode distributions can be rearranged as:

for odd modes

$$\begin{cases} E_s \exp[-\gamma_s(y-t)]; \\ E_f \sin[k_f(y-\frac{t}{2})]; \\ E_s \exp(\gamma_s y); \end{cases}$$

for even modes

$$\begin{cases} E_s \exp[\gamma_s(y-t)], & y \geq t \\ E_f \cos[k_f(y-\frac{t}{2})], & 0 \leq y \leq t \\ E_s \exp(\gamma_s y), & y \leq 0 \end{cases} \tag{60}$$

and for the radiation modes

for odd modes

$$\begin{cases} E_s^o \sin[k_s(y-t)+\phi_s^o]; \\ E_f^o \sin[k_f(y-\frac{t}{2})]; \\ E_s^o \sin(k_s y - \phi_s^o); \end{cases}$$

for even modes

$$\begin{cases} E_s^e \cos[k_s(y-t)+\phi_s^e], & y \geq t \\ E_f^e \cos[k_f(y-\frac{t}{2})], & 0 \leq y \leq t \\ E_s^e \cos(k_s y - \phi_s^e), & y \leq 0 \end{cases} \tag{61}$$

with

$$\begin{cases} k_s \cot\phi_s^o = k_f \cot(k_f\frac{t}{2}) \\ E_s^{o2} = E_f^{o2}\left[\sin^2(k_f\frac{t}{2}) + \frac{k_f^2}{k_s^2}\cos^2(k_f\frac{t}{2})\right] \end{cases} \quad \text{for odd radiation modes} \tag{62}$$

$$\begin{cases} k_s \tan\phi_s^e = k_f \tan(k_f\frac{t}{2}), \\ E_s^{e2} = E_f^{e2}\left[\cos^2(k_f\frac{t}{2}) + \frac{k_f^2}{k_s^2}\sin^2(k_f\frac{t}{2})\right] \end{cases} \quad \text{for even radiation modes} \tag{63}$$

and

$$P = \frac{\pi|\beta|}{2\omega\mu_0} E_s^2\, \delta\,(k_s - k_{s'}), \quad \text{for both odd and even modes} \tag{64}$$

For the waveguide with a single junction on both sides of the guide, we usually shift the coordinate (see Fig. 4(c)) to simplify the field expressions to the forms:

for the odd guided modes

$$\mathcal{E}_x(y) = \begin{cases} E_f \sin k_f y, & |y| \leq t \\ \frac{y}{|y|} E_s \exp[-\gamma_s(|y|-t)], & |y| > t \end{cases} \tag{65}$$

for the even guided modes

$$\mathcal{E}_x(y) = \begin{cases} E_f \cos k_f y, & |y| \leq t \\ E_s \exp[-\gamma_s(|y| - t)], & |y| > t \end{cases} \tag{66}$$

for the odd radiation modes

$$\mathcal{E}_x^o(y, k_s) = \begin{cases} E_f^o \sin k_f y, & |y| \leq t \\ \dfrac{y}{|y|} E_s^o \sin[k_s(|y| - t) + \phi_s^o], & |y| > t \end{cases} \tag{67}$$

for the even radiation modes

$$\mathcal{E}_x^e(y, k_s) = \begin{cases} E_f^e \cos k_f y, & |y| \leq t \\ E_s^e \cos[k_s(|y| - t) + \phi_s^e], & |y| > t \end{cases} \tag{68}$$

3.4 MODE DISTRIBUTIONS FOR GENERAL MULTIPLE–LAYER WAVEGUIDES

The field distributions of three–layer planar waveguides can be modified to analyse general multiple layers structures. We consider a planar waveguide consisting of L layers with symbols n_i and d_i to label the refractive index and thickness of the ith–layer (shown in Fig. 5). The guided modes are assumed to propagate in the z direction with a phase term $\exp[j(\omega t - \beta z)]$, where β is the propagation constant. All the media of the waveguide are lossless. Obeying the wave equation and boundary conditions, the guided mode distributions $\mathcal{E}_x(y)$ and $\mathcal{H}_x(y)$ are given as:

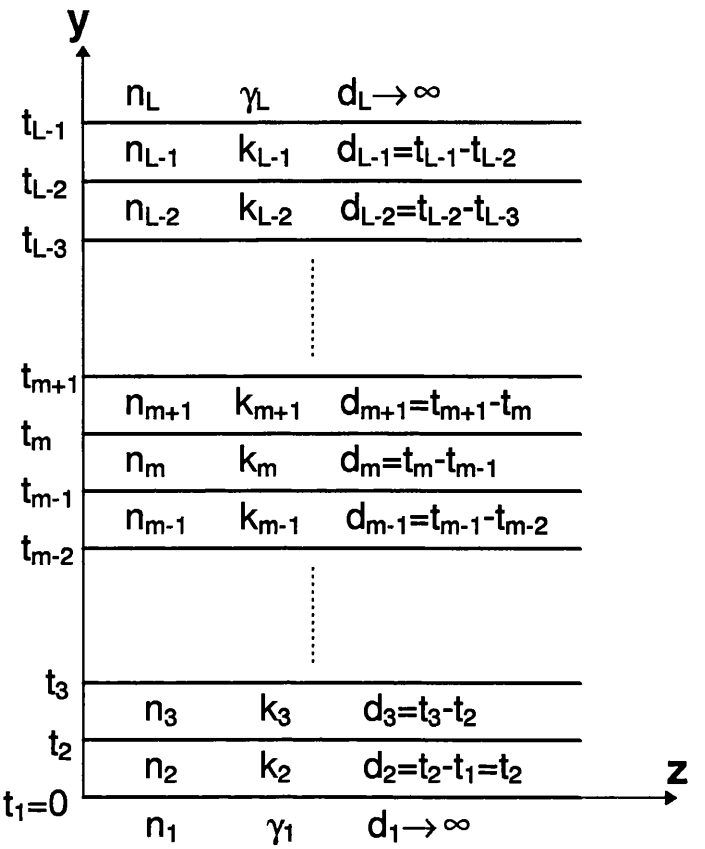

Fig. 5(a) *An L-layer planar wavegide structure, where n_i and d_i are the refractive index and the thickness of the* ith*-laye. The z coordinate is taken as the direction of propagation and parallels to the interfaces. The y coordinate is perpendicular to layers, where k_i and γ_1 , γ_L are the transverse propagation constant and decays of the* ith*-layer, cover, and substrate, respectively.*

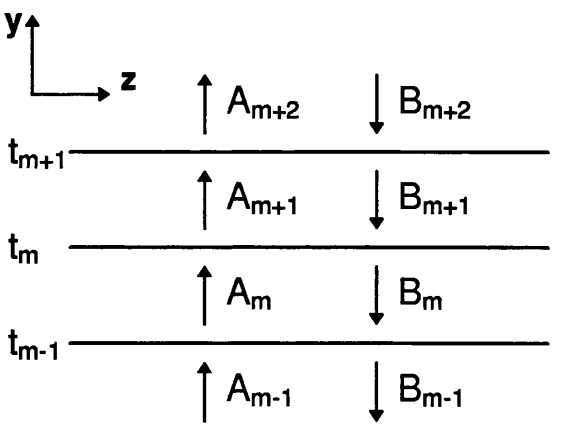

Fig. 5(b) *Scheme of the forward- and backward-propagation field amplitudes.*

for the guided TE modes

$$\mathcal{E}_x(y) = \begin{cases} E_L \exp[-\gamma_L(y - t_{L-1})], & y \geq t_{L-1} \\ E_{L-1} \cos k_{L-1}[(y - t_{L-2}) - \xi_{L-1}], & t_{L-2} \leq y \leq t_{L-1} \\ \quad \vdots & \quad \vdots \\ E_{m+1} \cos k_{m+1}[(y - t_m) - \xi_{m+1}], & t_m \leq y \leq t_{m+1} \\ E_m \cos k_m[(y - t_{m-1}) - \xi_m], & t_{m-1} \leq y \leq t_m \\ E_{m-1} \cos k_{m-1}[(y - t_{m-2}) - \xi_{m-1}], & t_{m-2} \leq y \leq t_{m-1} \\ \quad \vdots & \quad \vdots \\ E_2 \cos k_2(y - \xi_2), & 0 \leq y \leq t_2 \\ E_1 \exp(\gamma_1 y), & y \leq 0 \end{cases} \tag{69}$$

for the guided TM modes

$$\mathcal{H}_x(y) = \begin{cases} H_L \exp[-\bar{\gamma}_L(y - t_{L-1})], & y \geq t_{L-1} \\ H_{L-1} \cos \bar{k}_{L-1}[(y - t_{L-2}) - \bar{\xi}_{L-1}], & t_{L-2} \leq y \leq t_{L-1} \\ \quad \vdots & \quad \vdots \\ H_{m+1} \cos \bar{k}_{m+1}[(y - t_m) - \bar{\xi}_{m+1}], & t_m \leq y \leq t_{m+1} \\ H_m \cos \bar{k}_m[(y - t_{m-1}) - \bar{\xi}_m], & t_{m-1} \leq y \leq t_m \\ H_{m-1} \cos \bar{k}_{m-1}[(y - t_{m-2}) - \bar{\xi}_{m-1}], & t_{m-2} \leq y \leq t_{m-1} \\ \quad \vdots & \quad \vdots \\ H_2 \cos \bar{k}_2(y - \bar{\xi}_2), & 0 \leq y \leq t_2 \\ H_1 \exp(\bar{\gamma}_1 y), & y \leq 0 \end{cases} \tag{70}$$

where L is the total number of layers, $k_i\xi_i$ is the phase constant, and k_i, γ_i are the transverse propagation constants and decay of the ith–layer for TE modes and the overbar refers to TM modes, with

$$\begin{array}{ll} \text{for } TE \text{ modes} & \text{for } TM \text{ modes} \\ k_i^2 = k_0^2 n_i^2 - \beta^2 = -\gamma_i^2 \,, & \bar{k}_i^2 = k_0^2 n_i^2 - \bar{\beta}^2 = -\bar{\gamma}_i^2 \end{array} \tag{71}$$

where the value of k_i (or $\bar{k}_i$) may be real or imaginary which is determined by the refractive index n_i of the ith–layer and the propagation constant β (or $\bar{\beta}$) of the incident

mode, and the field distribution in the ith–layer decays exponentially (as a hyperbolic function) as the value of k_i (or $\bar{k}_i$) is imaginary. The requirement of the boundary conditions leads to the following system of equations for the phase shifts at the interfaces

$$
\begin{aligned}
&\tan k_{(L-1)}\xi_{c(L-1)} = \Gamma_{(L-1)L}(\frac{\gamma_L}{k_{(L-1)}}),\\
&\tan k_{(L-2)}\xi_{c(L-2)} = -\Gamma_{(L-2)(L-1)}(\frac{k_{(L-1)}}{k_{(L-2)}})\tan k_{(L-1)}(d_{(L-1)} - \xi_{c(L-1)}),\\
&\qquad\vdots\\
&\tan k_{(m+1)}\xi_{c(m+1)} = -\Gamma_{(m+1)(m+2)}(\frac{k_{(m+2)}}{k_{(m+1)}})\tan k_{(m+2)}(d_{(m+2)} - \xi_{c(m+2)}),\\
&\tan k_m\xi_{cm} = -\Gamma_{m(m+1)}(\frac{k_{(m+1)}}{k_m})\tan k_{(m+1)}(d_{(m+1)} - \xi_{c(m+1)}),\\
&\tan k_m\xi_{sm} = -\Gamma_{m(m-1)}(\frac{k_{(m-1)}}{k_m})\tan k_{(m-1)}(d_{(m-1)} - \xi_{s(m-1)}),\\
&\tan k_{(m-1)}\xi_{s(m-1)} = -\Gamma_{(m-1)(m-2)}(\frac{k_{(m-2)}}{k_{(m-1)}})\tan k_{(m-2)}(d_{(m-2)} - \xi_{s(m-2)}),\\
&\qquad\vdots\\
&\tan k_3\xi_{s3} = -\Gamma_{32}(\frac{k_2}{k_3})\tan k_2(d_2 - \xi_{s2}),\\
&\tan k_2\xi_{s2} = \Gamma_{21}(\frac{\gamma_1}{k_2}),
\end{aligned}
\tag{72}
$$

with

$$
\begin{aligned}
\xi_{ci} &= d_i - \xi_i, \quad \text{for} \quad m < i < L,\\
d_i &= t_i - t_{i-1}, \quad \text{for} \quad i = 1, 2, \cdots, L-1,\\
\xi_{si} &= \xi_i, \quad \text{for} \quad 1 < i < m,
\end{aligned}
$$

and

$$
\Gamma_{lk} = \begin{cases} 1, & \text{for } TE \text{ modes},\\ \dfrac{n_l^2}{n_k^2}, & \text{for } TM \text{ modes}, \end{cases}
$$

where the subscripts c and s indicate the layer in the cover side ($i > m$) and in the substrate side ($i < m$), respectively. For TM modes, k_i and ξ_i are replaced by $\bar{k}_i$ and $\bar{\xi}_i$ in the above equations and also in the rest part of this section. If we set the m–layer

as the dominant guiding layer, then, (72) can be rewritten as an equivalent three–layer planar waveguide

$$k_m d_m = \phi_s + \phi_c + \nu\pi \tag{73}$$

where the value of ν is an integer and the phase shifts ϕ_s and ϕ_c are given as

$$\begin{aligned} &\phi_c = k_m \xi_{cm} = -\tan^{-1}\left[\Gamma_{m(m+1)} \frac{k'_{(m+1)}}{k_m}\right] \\ &\text{with} \\ &k'_{(m+1)} = k_{(m+1)} \tan[k_{(m+1)}(d_{(m+1)} - \xi_{c(m+1)})] \end{aligned} \tag{74}$$

and

$$\begin{aligned} &\phi_s = k_m \xi_{sm} = -\tan^{-1}\left[\Gamma_{m(m-1)} \frac{k'_{(m-1)}}{k_m}\right] \\ &\text{with} \\ &k'_{(m-1)} = k_{(m-1)} \tan[k_{(m-1)}(d_{(m-1)} - \xi_{s(m-1)})] \end{aligned} \tag{75}$$

The eigenvalue equation has a similar form on both cover and substrate sides. It means that the propagation constants β of each mode can be obtained easily by the numerical analysis of the preceding transcendental equation (72). In addition, the values of peak fields in each layer of $E_1, E_2, \cdots, E_L$ for TE modes and $H_1, H_2, \cdots, H_L$ for TM modes can be solved with the help of the boundary conditions at each interface and the orthogonality relations of each mode. The power per unit length (in x direction) is

$$\begin{aligned} P = &\\ &\frac{|\beta|}{4\omega\mu_0} E_m^2 \left\{ \left[\cdots [(g_2 \frac{E_2^2}{E_3^2} + g_3)\frac{E_3^2}{E_4^2} + g_4]\frac{E_4^2}{E_5^2} + \cdots + g_{(m-1)} \right] \frac{E_{(m-1)}^2}{E_m^2} + \right. \\ &[d_m + (1 - \frac{k_m^2}{k_{(m-1)}^2})\frac{\sin 2k_m \xi_m}{2k_m} + (1 - \frac{k_m^2}{k_{(m+1)}^2})\frac{\sin 2k_m(d_m - \xi_m)}{2k_m}] + \\ &\left. \frac{E_{(m+1)}^2}{E_m^2} \left[g_{(m+1)} + \cdots + \frac{E_{(L-3)}^2}{E_{(L-4)}^2}[g_{(L-3)} + \frac{E_{(L-2)}^2}{E_{(L-3)}^2}(g_{(L-2)} + \frac{E_{(L-1)}^2}{E_{(L-2)}^2} g_{(L-1)})] \cdots \right] \right\} \end{aligned} \tag{76}$$

with

$$g_2 = (d_2 + \frac{1}{\gamma_1}),$$

$$
\begin{aligned}
g_i &= d_i + (1 - \frac{k_i^2}{k_{(i-1)}^2})\frac{\sin 2k_i\xi_{si}}{2k_i}, \qquad 3 \le i < m \\
&\vdots \\
g_i &= d_i + (1 - \frac{k_i^2}{k_{(i+1)}^2})\frac{\sin 2k_i\xi_{ci}}{2k_i}, \qquad m < i \le L-2 \\
g_{(L-1)} &= (d_{(L-1)} + \frac{1}{\gamma_L}),
\end{aligned}
\tag{77}
$$

and

$$
\begin{aligned}
&\frac{E_1^2}{E_2^2} = (1 + \frac{\gamma_1^2}{k_2^2})^{-1}, \\
&\frac{E_i^2}{E_{(i+1)}^2} = \left[\cos^2 k_i(d_i - \xi_i) + \frac{k_i^2}{k_{(i+1)}^2}\sin^2 k_i(d_i - \xi_i)\right]^{-1}, \\
&\frac{E_L^2}{E_{(L-1)}^2} = (1 + \frac{\gamma_L^2}{k_{(L-1)}^2})^{-1}, \qquad i = 3, 4, \ldots, L-2.
\end{aligned}
\tag{78}
$$

We examined several cases and the results are shown in Table 2 and Table 3. The structures of the cases in Table 2 are multiple quantum wells with periodic refractive indexes profiles, and the total number of layers are from 7 to 19. After comparing with the results of *Streifer* et al. [119], it is shown that the above mode distributions can be applied to analyse the multiple–quantum–well laser structures without introducing any approximate approach in the calculation.

Besides, the field functions are directly derived from the previous sections, so that the field distributions may be used in the mode–matching method for the corrugated structure analysis. The propagation constants β and the relative percentage powers guided in each layer obtained by (73) and (76) for TE and TM modes propagating in a multiple–mode six–layer lossless waveguide, and a comparison of present results with those from *Chilwell and Hodgkinson* [120] using a matrix method is shown in Table 3.

To determine the TE radiation modes, we have applied the same procedure of the treatment described in the previous sections to treat an L–layer planar waveguide with $n_1 = n_L = 1$. On application of the boundary conditions at the interfaces, a complicated

Table 2: Data and results of periodic planar waveguides.

(For a TE_0 mode propagating in a multiple–quantum–well waveguide with $\lambda_0 = 0.80\mu m$, where both the effective index n_{eff} and the confinement factor Γ in N_a layers are obtained from the method described above and compared with the results from [119].)

n_a	n_b	n_c	N_a	N_b	$d_a(\mu m)$	$d_b(\mu m)$	n'_{eff} [119]	n_{eff}	Γ' [119]	Γ
3.6	3.4	3.4	6	5	0.012	0.012	3.4169	3.4169	0.1478	0.1478
3.6	3.4	3.4	6	5	0.008	0.012	3.4083	3.4083	0.0754	0.0754
3.6	3.3	3.3	6	5	0.006	0.024	3.3097	3.3097	0.056	0.0560
3.6	3.4	3.3	3	2	0.01	0.01	3.3115	3.3115	0.058	0.0580
3.6	3.4	3.4	3	2	0.012	0.012	3.405	3.4050	0.0472	0.0473
3.6	3.4	3.4	3	2	0.008	0.012	3.4023	3.4023	0.0219	0.0219
3.6	3.3	3.3	9	8	0.03	0.03	3.4161	3.4161	0.4603	0.4603
3.6	3.3	3.3	6	5	0.06	0.06	3.4308	3.4308	0.4957	0.4957

Table 3: Propagation constants and percentage power in each layer of the planar waveguide with $n_s = 1.50$, $n_2 = 1.66$, $n_3 = 1.60$, $n_4 = 1.53$, $n_5 = 1.66$, $n_c = 1$, and $d_2 = d_3 = d_4 = d_5 = 500nm$, with $\lambda = 0.6328\mu m$, and the mode distributions shown in Fig. 6, and Fig. 7.

The values in the parenthesises are from [120].

	n_{eff}	Percentage relative power (%)					
Mode	(β/k_0)	n_s	n_2	n_3	n_4	n_5	n_c
TE_0	1.622729	3.93	76.34	19.27	0.40	0.06	0.00
	(1.622729)	*(3.9)*	*(76.3)*	*(19.3)*	*(0.4)*	*(0.1)*	*(0.0)*
TE_1	1.605276	0.02	0.20	0.19	11.44	87.13	1.03
	(1.605276)	*(0.0)*	*(0.2)*	*(0.2)*	*(11.4)*	*(87.1)*	*(1.0)*
TE_2	1.557136	6.56	20.74	59.01	12.30	1.35	0.04
	(1.557136)	*(6.6)*	*(20.7)*	*(59.0)*	*(12.3)*	*(1.4)*	*(0.0)*
TE_3	1.503587	32.13	18.58	14.74	27.97	6.27	0.32
	(1.503587)	*(32.1)*	*(18.6)*	*(14.7)*	*(28.0)*	*(6.3)*	*(0.3)*
TM_0	1.620031	3.81	74.34	21.35	0.47	0.04	0.00
	(1.620031)	*(3.8)*	*(74.3)*	*(21.4)*	*(0.5)*	*(0.0)*	*(0.0)*
TM_1	1.594788	0.03	0.28	0.43	15.36	83.38	0.52
	(1.594788)	*(0.0)*	*(0.3)*	*(0.4)*	*(15.4)*	*(83.4)*	*(0.5)*
TM_2	1.554981	7.26	21.26	57.31	11.97	2.17	0.03
	(1.554981)	*(7.3)*	*(21.3)*	*(57.3)*	*(12.0)*	*(2.2)*	*(0.0)*
TM_3	1.501818	45.00	15.09	12.97	22.66	4.17	0.11
	(1.501818)	*(45.0)*	*(15.1)*	*(13.0)*	*(22.7)*	*(4.2)*	*(0.1)*

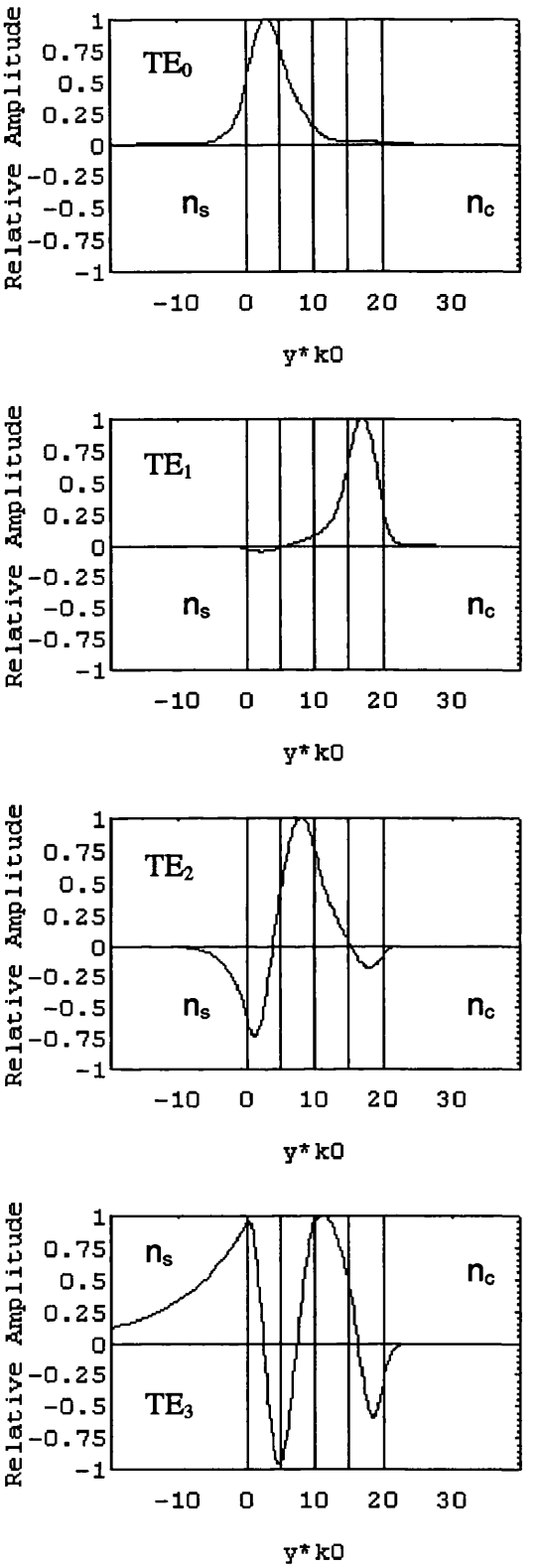

Fig. 6 *Normalized amplitudes of the field distributions for each of the TE modes supported by the waveguide given in Table 3.*

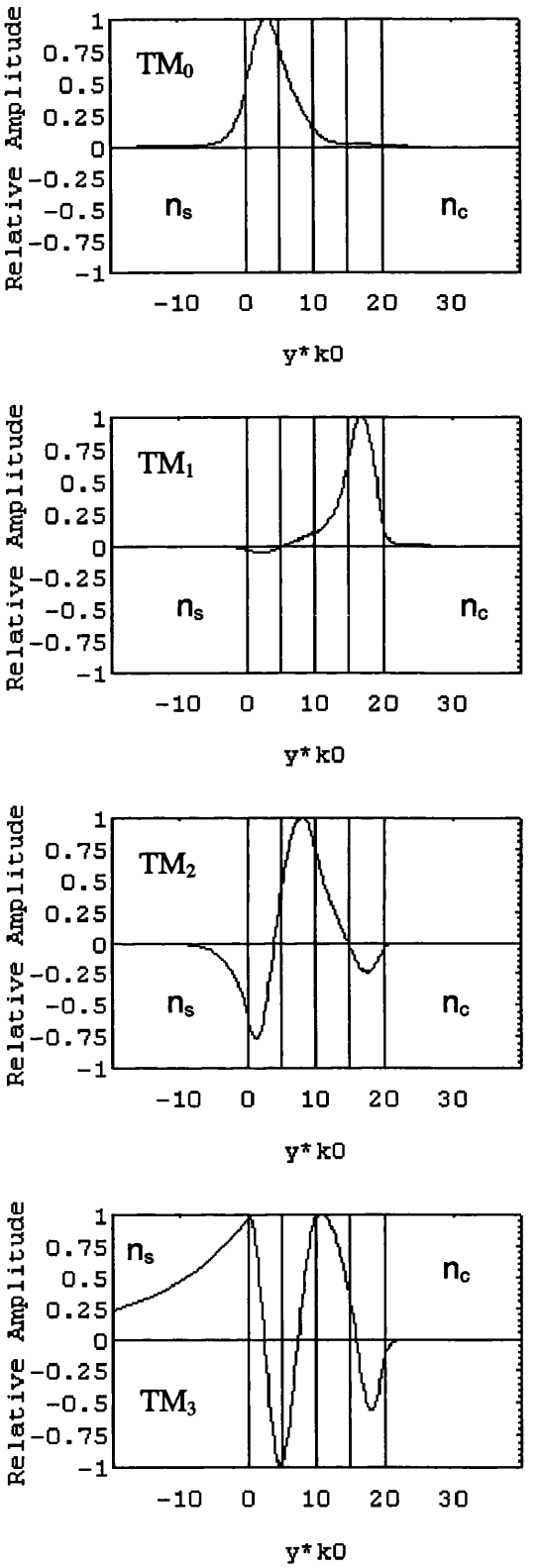

Fig. 7 *Normalized amplitudes of the field distributions for each of the TM modes supported by the waveguide given in Table 3.*

transcendental equation with respect to the phase shifts at the interfaces for each radiation mode can be obtained straightforwardly. The use of a numerical technique is required to solve such a transcendental equation. Transfer matrix analysis techniques can be used to find the propagation constants and the mode distributions of the modes in a multiple-layer optical waveguide without needing to handle the transcendental characteristic equation [121][122].

In an L-layer planar waveguide (Fig. 5(b)), which has the same structure and refractive index profile as shown in Fig. 5(a), the electric field in layer m can be written as

$$\mathcal{E}_x(y)|_m = A_m \exp(-jk_m y) + B_m \exp(jk_m y) \tag{79}$$

where $k_m^2 = k_0^2 n_m^2 - \beta^2$ and A_m and B_m represent the electric field amplitudes of the fields propagating in the forward and backward directions (see Fig. 5(b)), respectively. The transfer matrix which relates the amplitudes of the fields in each layer is given by

$$\begin{aligned} \begin{bmatrix} A_{m+1} \\ B_{m+1} \end{bmatrix} &= M_m \begin{bmatrix} A_m \\ B_m \end{bmatrix} \\ &= \prod_{n=1}^{m} M_n \begin{bmatrix} A_1 \\ B_1 \end{bmatrix} \end{aligned} \tag{80}$$

where $[M_m]$ is a 2×2 matrix and can be determined by applying the boundary conditions and the reflection and transmission coefficients at the interface [122]. All $\{A_m, B_m\}$ are linearly dependent on (A_1, B_1)

$$\begin{aligned} \mathcal{E}_x(y)|_m &= \left(e^{-jk_m y} \quad e^{jk_m y}\right) \prod_{n=1}^{m-1} M_n \begin{bmatrix} A_1 \\ B_1 \end{bmatrix} \\ &= A_1(F_{1m}e^{-jk_m y} + G_{1m}e^{jk_m y}) + B_1(F_{2m}e^{-jk_m y} + G_{2m}e^{jk_m y}) \\ &= A_1\psi_m(y) + B_1\phi_m(y) \end{aligned} \tag{81}$$

where F's and G's are constants and both A_1 and B_1 are arbitrary. The waveguide

modes are assumed to be normalised so

$$P = \int_{-\infty}^{\infty} (A_1\psi + B_1\phi)(A_1^*\psi^* + B_1^*\phi^*)dy \tag{82}$$

where

$$\begin{aligned} \psi &= \psi_m(y), \qquad t_{m-1} < y < t_m \\ \phi &= \phi_m(y), \qquad t_{m-1} < y < t_m \end{aligned} \tag{83}$$

(82) can be written as

$$P = (A_1^* \quad B_1^*) \begin{bmatrix} P_{AA} & P_{AB} \\ P_{BA} & P_{BB} \end{bmatrix} \begin{bmatrix} A_1 \\ B_1 \end{bmatrix} \tag{84}$$

where

$$\begin{aligned} P_{AA} &= \int_{-\infty}^{\infty} |\psi|^2 dy = \sum_{m=1}^{L} \int_{t_{m-1}}^{t_m} |\psi|^2 dy \\ P_{BB} &= \int_{-\infty}^{\infty} |\phi|^2 dy \end{aligned} \tag{85}$$

and

$$\begin{aligned} P_{AB} &= \int_{-\infty}^{\infty} \phi\psi^* dy \\ P_{BA} &= \int_{-\infty}^{\infty} \phi^*\psi dy = P_{AB}^* \end{aligned} \tag{86}$$

If the 2×2 matrix P is diagonalised, the resulting two eigenvectors give the required values of A_1 and B_1 for decoupled radiation modes. This calculation is all algebraic (no transcendental equations). The TM radiation modes can be formulated by changing the boundary conditions at each interface.

3.5 CONCLUSION

Field distributions of planar slab waveguides presented in this chapter will be substituted into (18)–(20) for the inner product calculations and the mode–matching analysis. In order to avoid resulting errors in the transfer matrix calculations, we let

the peak amplitude of the field in the guiding layer be always positive and the value of the field amplitude at the interface between the guide and the surrounding layer is determined by the boundary condition.

The general L–layer field distributions proposed in the last section have a simple form as in the case of three–layer planar waveguides. Therefore, with only very minor modification in the formulating procedure and computer programs, the extension of the application to corrugated structures in multiple–layer waveguides is possible.

4

CHAPTER 4

THEORETICAL APPROACH FOR A SINGLE–STEP DISCONTINUITY IN PLANAR WAVEGUIDES

4.1 INTRODUCTION

The single–step discontinuity in the planar optical waveguide is the important building block for many corrugated structures for integrated circuits and DFB, DBR lasers. In the previous two chapters, we have proposed a method to treat corrugated waveguides with large groove depth, along with a set of field distributions chosen for the numerical calculation. Before starting to analyse more complicated multiple–step discontinuities, we apply this method to a single step discontinuity in planar waveguides firstly, so that we may check the accuracy of this method via the comparison of the results given by this method and others obtained by different techniques.

To understand the behaviour of modes coupled by the step junction, some important properties are introduced and discussed in this chapter, for example the convergence conditions of each coupled mode on the step junction versus the number of radiation panels for Simpson's rule approximation, the comparisons of mode coefficients and the total radiation power of our results and others from several methods, and radiation patterns of the single–step discontinuities in different planar waveguides.

4.2 FORMULATION OF THE NUMERICAL ANALYSIS

Let us consider a single step discontinuity in planar optical waveguides: Fig. 8(a) is for a single step–junction on both sides of the guide, in which the dash-dotted line is the central line of the waveguide; Fig. 8(b) is for a single step–junction on one side of the guide. The behaviour of mode couplings at these step junctions are specified by the mode–matching matrix equation (33). The matrix elements of $[M^{12}]$ and $[M^{21}]$ can be evaluated through calculating the inner products (18)–(20). Substituting the field distributions of regions 1 and 2 into (18)–(20) leads to the following results:
for guided–guided, guided–radiation, and radiation–guided mode coupling

$$K_{\mu\nu} = \frac{\beta_\mu}{2\omega\mu_0} \frac{(n_c^2 - n_f^2)k_0^2}{(k_{f'}^2 - k_f^2)(\gamma_c^2 + k_{f'}^2)} \left[\frac{d\mathcal{E}_{\mu_x}^{1*}(y)}{dy} \mathcal{E}_{\nu_x}^2(y) - \mathcal{E}_{\mu_x}^{1*}(y) \frac{d\mathcal{E}_{\nu_x}^2(y)}{dy} \right]_{t_1}^{t_1+d} \tag{87}$$

and for radiation–radiation mode coupling

$$K_{rr}(k_{s'}, k_s) = \delta(k_{s'} - k_s) \tag{88}$$

where the subscripts ν and f' indicate the values belong to the region 2, and d is the step height. We assume that only the normalised TE_0 mode is incident onto the junction with $a_{\mu_1}^{1+} = 1$, so that the coefficient column matrix $[a_{\mu_i}^{1+}]$ is given as

$$[a_{\mu_i}^{1+}] = (\ 1,\ \underbrace{0,\ 0,\ 0, \ldots,\ 0}_{\text{No. of radiation modes}}\ ) \tag{89}$$

where the number of radiation modes is determined by the number of radiation panels for Simpson's rule and the types of radiation modes generated by the step discontinuity. In addition, the coefficients $a_{\nu_i}^{2-}$ of the reflected modes in region 2 are equal to zero and

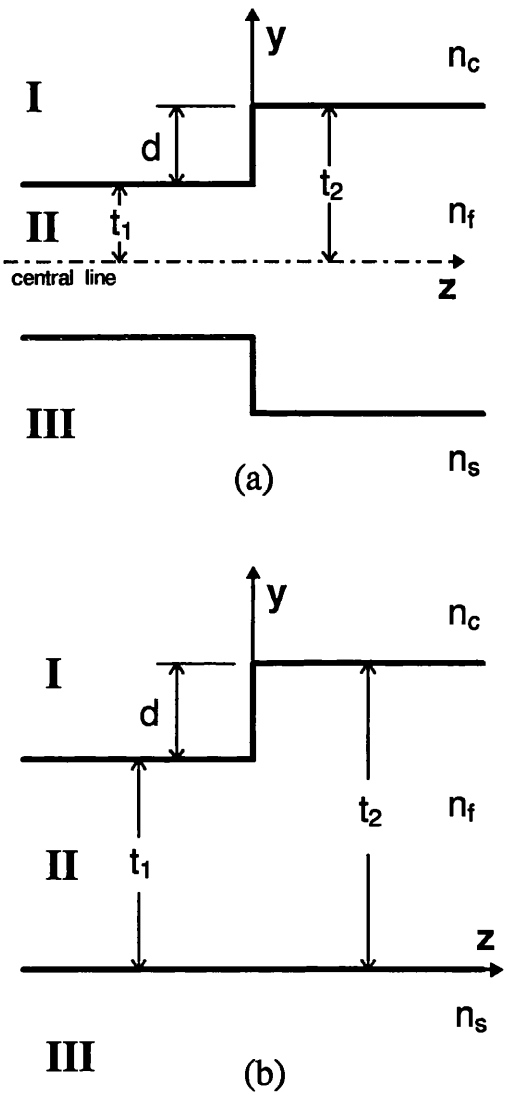

Fig. 8 *A single step discontinuity in planar waveguides: (a) a single step junction on both sides of the guide and (b) a single step junction on one side of the guide. The dash-dotted line in (a) is the central line of the waveguide.*

therefore (43) has the following form

$$\left[\begin{array}{c} a_{\nu_1}^{2+} \\ a_{\nu_2}^{2+} \\ \vdots \\ \hline a_{\mu_1}^{1-} \\ a_{\mu_2}^{1-} \\ \vdots \end{array}\right] = \left[\begin{array}{c|c} & \\ S_{11} & S_{12} \\ & \\ \hline & \\ S_{21} & S_{22} \\ & \end{array}\right] \left[\begin{array}{c} 1 \\ 0 \\ \vdots \\ \hline 0 \\ 0 \\ \vdots \end{array}\right] \tag{90}$$

where matrix $[S]$ can be evaluated from (30) and (42). The coefficients $a_{\mu_i}^{1-}(\theta_i)$ and $a_{\nu_i}^{2+}(\theta_i)$ with $i=2,3,\ldots,m+1$ (for the waveguide shown in Fig. 8(a) with $n_s=n_c$) are the amplitudes of reflected and transmitted radiation modes at the discrete points, and the radiation power carried by each mode at the discrete points are given by $|a_{\mu_i}^{1-}(\theta_i)|^2$ and $|a_{\nu_i}^{2+}(\theta_i)|^2$. By calculating these values at each discrete angle, there results the radiation power pattern ranging from $\theta_i = 0$ to $\theta_i = \theta_\eta(\theta_\eta \to \pi)$ above and below the guiding layer. The total radiation power including all of transmitted and reflected radiation modes is the area under the pattern from 0 to π, which can be evaluated by Simpson's rule

$$P_r = \sum_{i=2}^{m+1} \sigma_i |a_{\mu_i}^{1-}(\theta_i)|^2 + \sum_{i=2}^{m+1} \sigma_i |a_{\nu_i}^{2+}(\theta_i)|^2, \quad \text{with} \quad i = 2,3,\ldots,m+1 \tag{91}$$

where m is the number of radiation panels and σ_i was defined in (31), or we can calculate the value of P_r from

$$P_r = 1 - |a_{\mu_1}^{1-}|^2 - |a_{\nu_1}^{2+}|^2. \tag{92}$$

where $a_{\mu_1}^{1-}$ and $a_{\nu_1}^{2+}$ are the amplitude coefficients of reflection and transmission guided modes, respectively. The total power summed over all modes is equal to 1 in our analysis. It is very important to keep the total power as a constant in the analysis of multiple–step structures such as a grating with a great number of periods. For an asymmetric planar waveguide, the total radiation power must include two types of radiation modes in the calculation.

4.3 CONVERGENCE CONDITIONS

In order to find the adequate number of radiation panels for Simpson's rule approximation, we check the convergence of the reflection and transmission coefficients of guided modes as well as the total radiation power versus the number of radiation panels which have been considered in the calculation.

In Table 4 we list the values of $|R|$, $|T|$, and P_r of symmetric waveguides with respect to the difference angle of $90°-\theta_\eta$ and the number of radiation panels m for $t_2/t_1=0.8$ and $t_2/t_1=0.2$. It is shown that the use of the angle θ_η to approach the singular point $\theta_\nu=90°$ in the analysis instead of assuming the radiation mode $a_r(90°)=0$ at the angle of 90° has good convergence in the region of small m, so that we can avoid subdividing too many radiation panels for Simpson's rule to reduce the number of linear equations without creating conspicuous errors. In this thesis the angle of $90°-\theta_\eta = 0.0001°$ is chosen for the following calculations.

Fig. 9 shows the convergence of the total radiation power obtained by two discretisation methods. It is apparent that the results of our method by dividing over the radiation angle (curve a) have better convergence than that by dividing over the radiation spectrum k_c (curve b).

Fig. 10(a)–(c) shows the convergence of the total radiation power P_r versus the number of radiation panels m for the case of TE_0 mode incidence. Fig. 11(a) and 11(b) show the convergence for a TM_0 mode incidence.

By the convergence test, it is found that the deviations of P_r are $2.2 \times 10^{-8}\%$ in 10(a), $6.7 \times 10^{-9}\%$ in 10(b), and 0.065% in 10(c) for a TE mode with $m=20$, as well as are $2.3 \times 10^{-7}\%$ in 11(a) and 0.088% in 11(b) for the TM mode. The convergence speed depends on the step height and the index profile.

Fig. 12(a) and 12(b) show the convergence of total radiation power P_r for a TE_0 mode incident onto a step junction (shown in inset) with different index profiles. These waveguides are an asymmetric discontinuous structure, so that not only even radiation

Table 4: Data of a single step discontinuity with different θ_η and m with $t_2/t_1=0.8$ and $t_2/t_1=0.2$ in a symmetric planar waveguide with $n_c=1$ and $n_f=2.2361$

		$a_r(90°)=0$			$90° - \theta_\eta = 0.1°$		
t_2/t_1	m	$\|R\|$	$\|T\|$	P_r	$\|R\|$	$\|T\|$	P_r
0.8	m=10	0.023453	0.99954	0.00036196	0.023466	0.99953	0.00038818
	m=20	0.023460	0.99954	0.00037552	466	953	818
	m=30	0.023464	0.99953	0.00038457	466	953	818
	m=40	0.023465	0.99953	0.00038570	466	953	818
0.2	m=10	0.25722	0.94055	0.049202	0.25776	0.93984	0.050253
	m=20	0.25749	0.94020	0.049726	776	984	0.050251
	m=30	0.25758	0.94008	0.049902	776	984	251
	m=40	0.25763	0.94002	0.050000	776	984	251
		$90° - \theta_\eta = 0.01°$			$90° - \theta_\eta = 0.001°$		
t_2/t_1	m	$\|R\|$	$\|T\|$	P_r	$\|R\|$	$\|T\|$	P_r
0.8	m=10	0.023467	0.99953	0.00038900	0.023467	0.99953	0.00038908
	m=20	467	953	900	467	953	908
	m=30	467	953	900	467	953	908
	m=40	467	953	900	467	953	908
0.2	m=10	0.25778	0.93982	0.050284	0.25778	0.93982	0.050287
	m=20	778	982	0.050283	778	982	0.050286
	m=30	778	982	283	778	982	286
	m=40	778	982	283	778	982	286

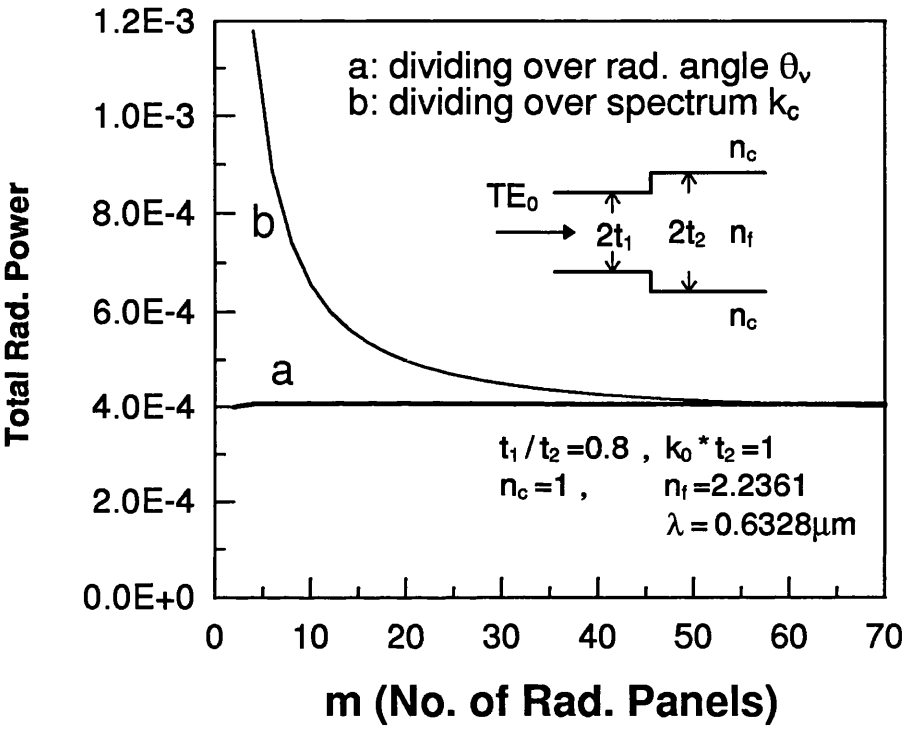

Fig. 9 *A comparison of convergence of the total radiation powers obtained by two discretisation methods for a step-up discontinuity on a slab waveguide ($k_c = k_s$).*

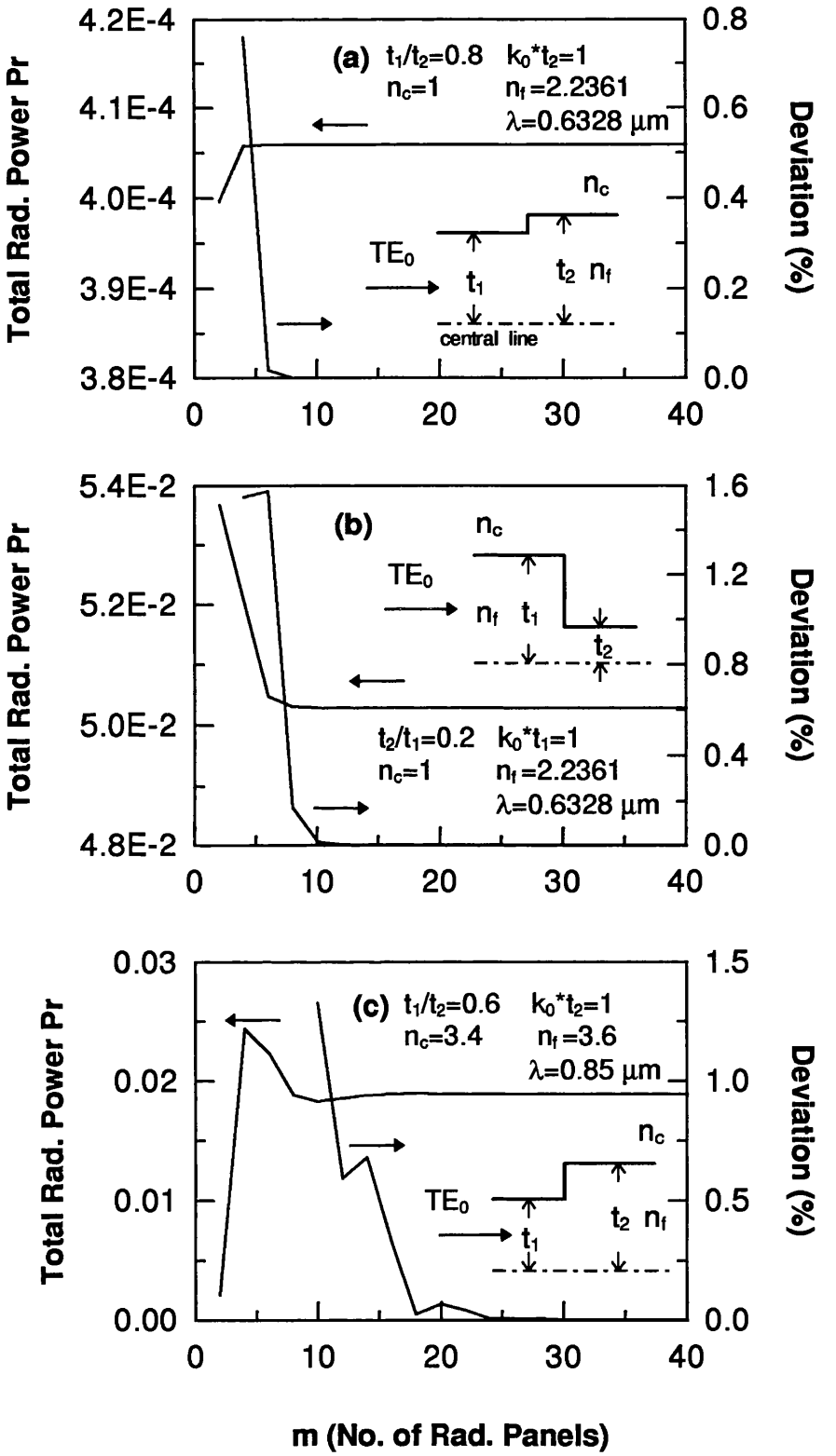

Fig. 10 *Convergence of the total radiation power of a TE_0 mode incident onto a single step discontinuity in symmetric planar waveguides (shown in insets) versus the number of radiation panels with (a) t_1/t_2=0.8, (b) t_2/t_1=0.2, (c) t_1/t_2=0.6.*
(The dash-dotted line is the central line of the waveguide.)

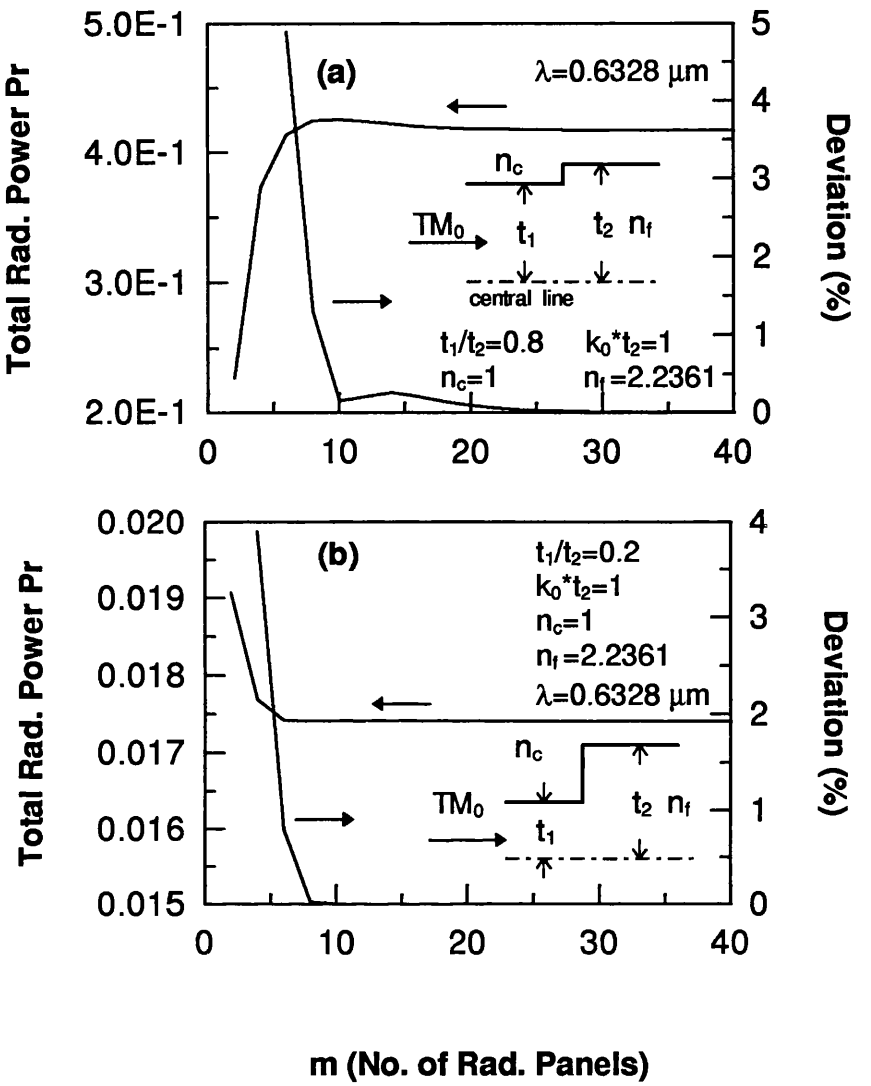

Fig. 11 *Convergence of the total radiation power of a TM_0 mode incident onto a single step discontinuity in the symmetric planar waveguide (shown in inset) versus the number of radiation panels with (a) $t_1/t_2=0.8$, (b) $t_1/t_2=0.2$.(The dash-dotted line is the central line of the waveguide.)*

modes but also odd radiation modes are produced at each discrete angle.

In these cases the total number of radiation modes is $2m$, and the radiation losses of these structures are much more than those of symmetric structures due to the discrepancy of field distributions on the step junction. The deviations on the convergence of P_r are $1.8 \times 10^{-7}\%$ in 12(a) and 0.45% in 12(b) with $m = 20$. For the waveguide (shown in Fig. 12) with small variation of the index profile ($n_c = n_s = 3.4$ and $n_f = 3.6$), we need to consider more radiation modes in the calculation to obtain more accurate results. However, the convergence can be improved by adequately truncating the radiation spectrum because most of the radiation loss of this waveguide is concentrated within a very narrow range of radiation angle (or radiation spectrum).

4.4 NUMERICAL RESULTS AND COMPARISONS

In this section we examine the properties of a step discontinuity on several slab waveguides, and compare our results with others from different methods. All of our results shown in this thesis are obtained by using the *Mathematica* package on *Sun* workstation and PC computers.

In Fig. 13, a symmetric slab waveguide with a single–step discontinuity on both surfaces, we consider a normalised TE_0 mode incident normally from both end ports onto the junction. Reflection coefficients $|R_1|$, $|R_2|$, transmission coefficients $|T|$, and total radiation power P_r have been plotted versus the relative step height. Comparing with the results from *Rozzi* [70] (dashed lines), it is shown that our results have good agreement in the most practical region $0.1 \leq t_1/t_2 < 1$. When the thickness ratio of t_1/t_2 is less than 0.1, the radiation losses become very important (more than 20% of total power), and in this case the power coupling among these radiation modes must be reconsidered in the mode–matching calculation. In Fig. 13, the values of $|T|$ are similar for both left and right incidences, but the discrepancies of $|R|$ and P_r are larger as step height increases.

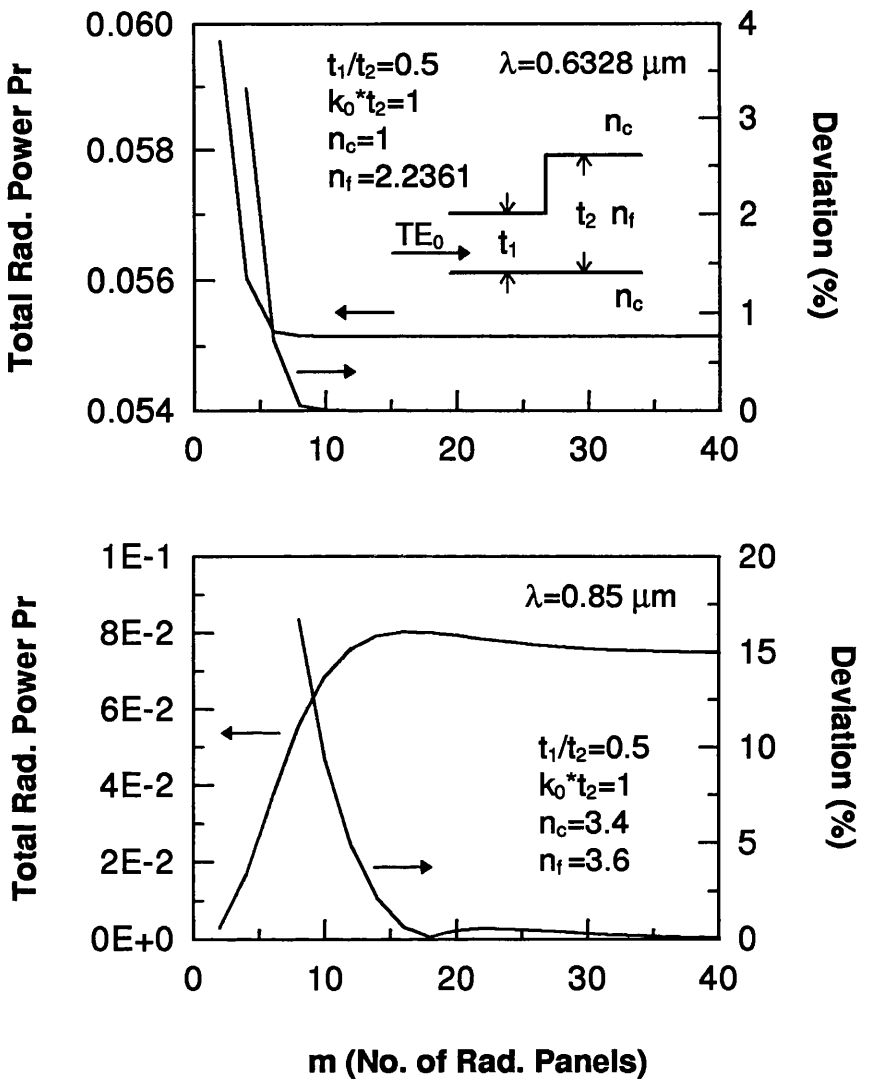

Fig. 12 *Convergence of the total radiation power of a TE_0 mode incident onto a single step discontinuity on one side of the symmetric planar waveguide (shown in inset) versus the number of radiation panels m for even and odd types radiation modes individually with t_1/t_2 =0.5 and (a) n_c=1, n_f=2.2361, (b) n_c=3.4, n_f=3.6 .*

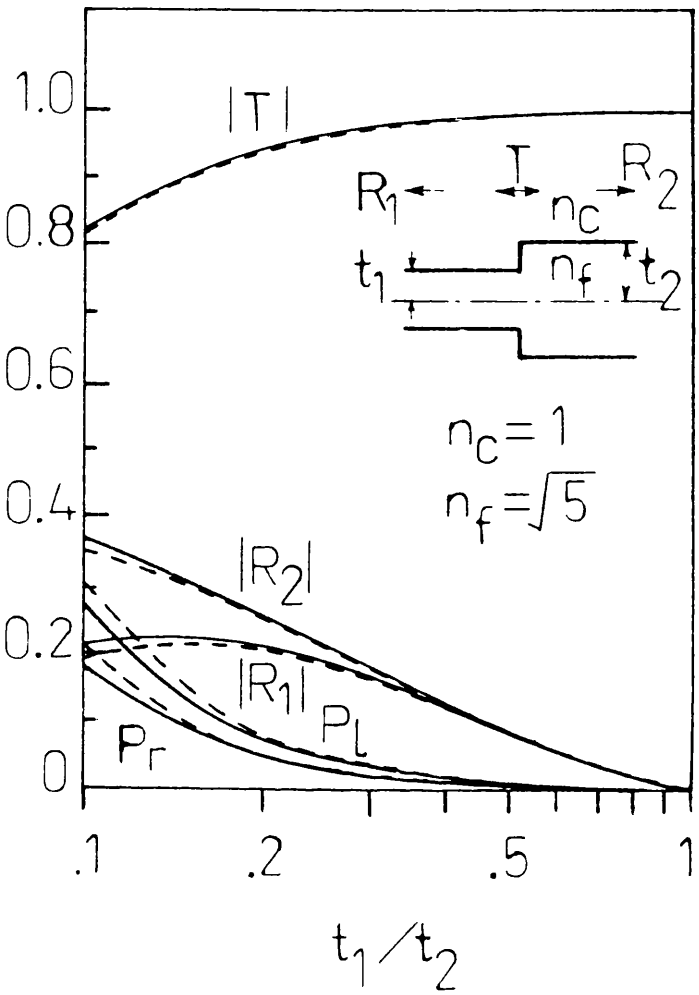

Fig. 13 *Amplitudes of the reflection and transmission coefficients of a step discontinuity between monomode waveguides and the radiation power versus step height.*

..... *Rozzi* [70], ———— *Present.*

Fig. 14 and 15 show the radiation power P_r of a TE_0 mode incident onto a step junction versus the normalised slab thickness $k_0 t_1$ (Fig. 14) and the step height t_2/t_1 (Fig. 15). The step discontinuity for both cases is shown in the inset of Fig. 14. By comparing with other results, it is shown that our results agree well with others. The waveguides described above have small refractive index contrast between the guide and surrounding medium and therefore a large fraction of the incident mode power is carried by the evanescent field outside the guiding layer. Such a waveguide has a tiny reflection coefficients for both guided and radiation modes, so that it is suitable to be treated by simple approximation methods.

Fig. 16 shows the radiation power of both lowest TE and TM modes incident onto a step–down discontinuity (shown in inset) as a function of the thickness of the guiding layer and comparisons of our results and others obtained by both the finite element method (FEM) and the boundary element method (BEM) [62]. For TM at $t_1/\lambda = 0.1$ and for TE at $t_1/\lambda = 0.4$ there is about 5% disagreement between them.

Hardy [114] proposed a method in which he neglected the radiation modes in the mode–matching calculation; thus the reflection and transmission coefficients give

$$R_{12} = \frac{\beta_1 - \beta_2}{\beta_1 + \beta_2} = -R_{21} \tag{93}$$

and

$$t_{12} = \frac{2\beta_1 \int_{-\infty}^{\infty} \mathcal{E}_x^1 \mathcal{E}_x^2 dy}{(\beta_1 + \beta_2) \int_{-\infty}^{\infty} |\mathcal{E}_x^2|^2 dy} \tag{94}$$

We compare our results with those obtained from the above equations in Fig. 17 and 18; they show that with small variation in the index profile (weakly guiding structures) both results are quite similar, but the discrepancy between them becomes larger as the index of the exterior region n_c decreases.

Fig. 19 also shows the values of $|R|$, $|T|$, and P_r versus the relative step height t_1/t_2 of a discontinuity in the planar waveguide with a TE_0 mode incidence and the comparison of our results and those from *Hardy*. It is shown that the approximation can

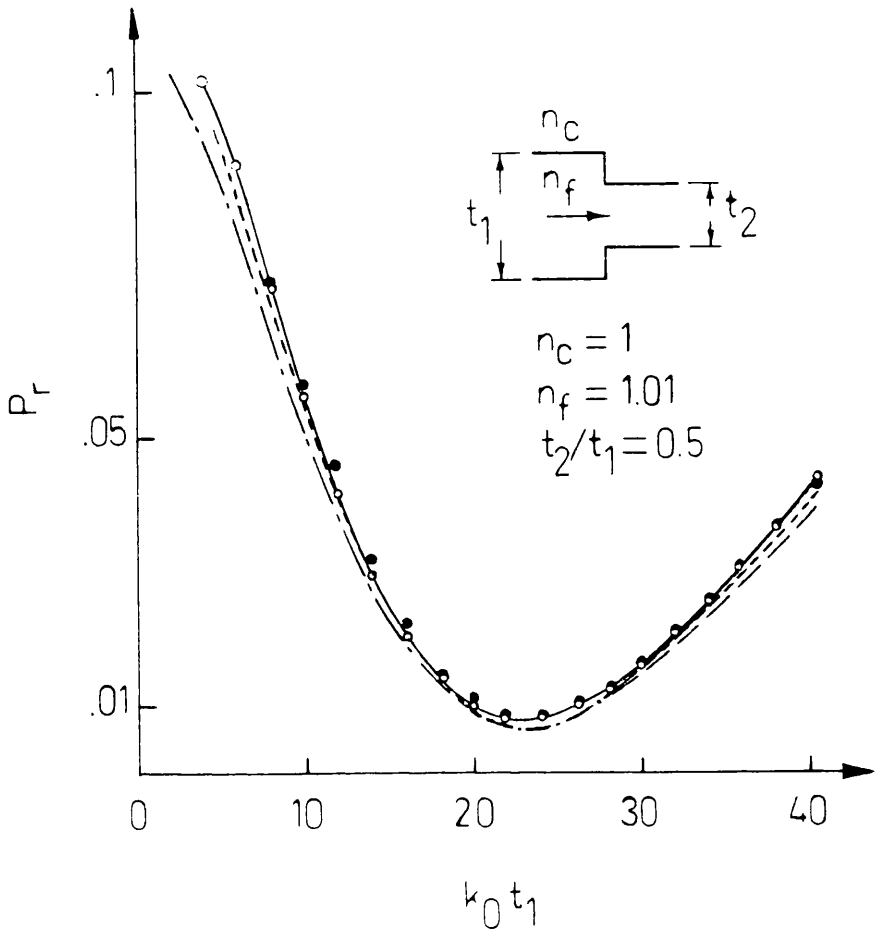

Fig. 14 *TE-mode radiation power of a symmetric step discontinuity as a function of* $k_0 t_1$.

..... *Integral equation method (Nishimura)* [66],
– – – – *Approximate mode matching (Marcuse)* [27],
– – – – – *Residue calculus technique (Ittipiboon)* [65],
• • • • *BPM (Gomma)* [67],
—o——o— *Present results.*

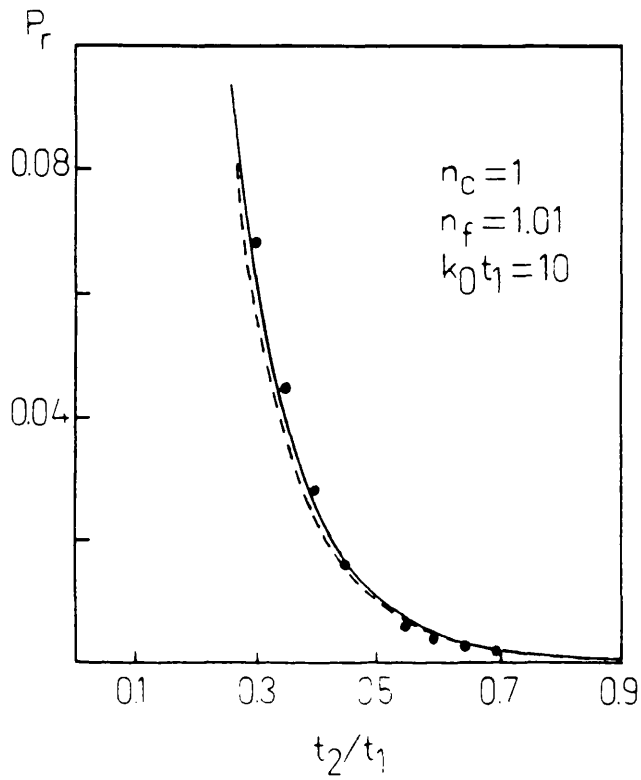

Fig. 15 *Radiation power of TE mode as a function of* t_2 / t_1 .

• • • • *Marcuse's analysis* [27],
---------- *Residue calculus (Ittipiboon)* [65],
———— *Present results.*

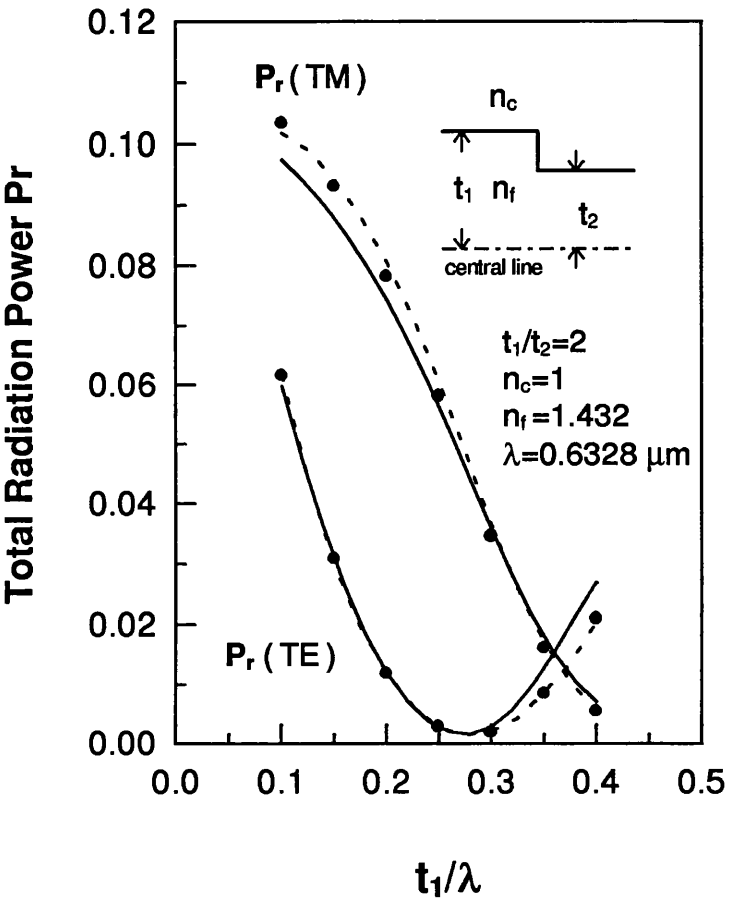

Fig. 16 *Total radiation power P_r of the TE_0 and TM_0 modes caused by a symmetric step discontinuity in the planar waveguide (shown in inset) versus the thickness of the guiding layer.*

..... *BEM,* *(Koshiba,* et. al.*)* [62],
• • • • *FEM,*
——— *Present results.*

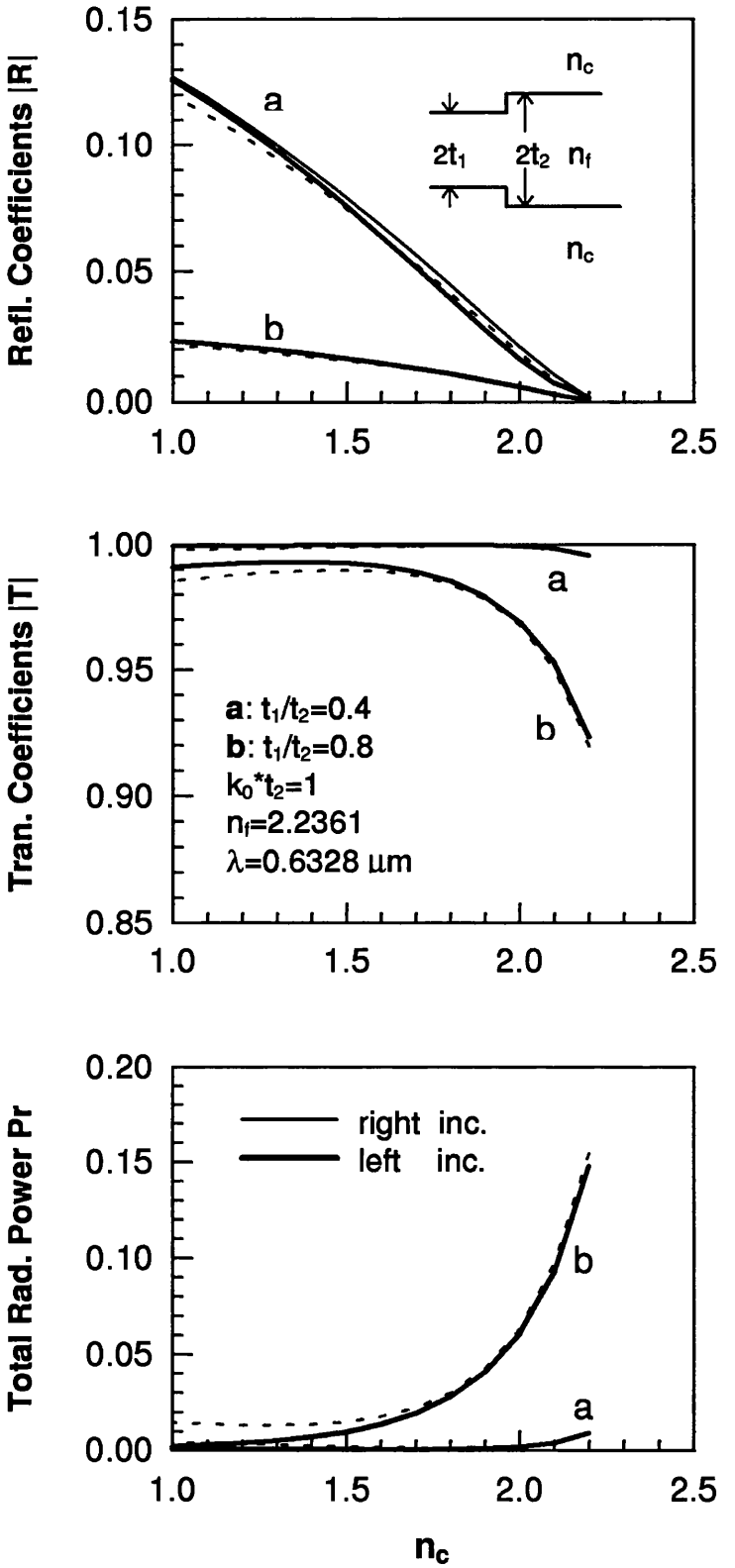

Fig. 17 *Reflection coefficients |R| and transmission coefficients |T| of a step discontinuity in a monomode planar waveguide and the total radiation power P_r versus the values of n_c with λ=0.6328 μm and m=40, where m is the number of radiation panels for Simpson's rule. The dotted lines are obtained from approximation and the solid lines show the present results for (a)t_1/t_2=0.4 and (b)t_1/t_2=0.8 cases.*

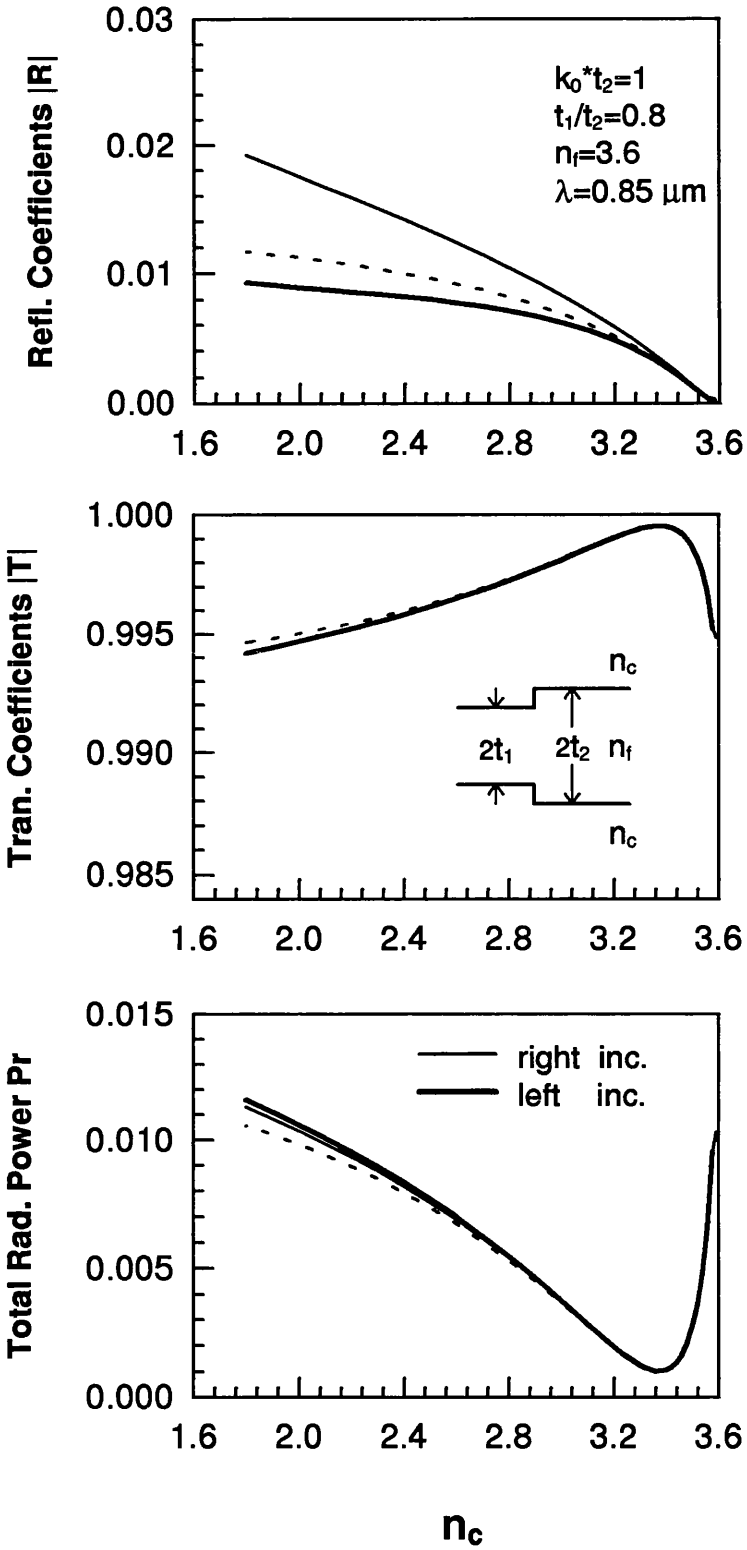

Fig. 18 *Reflection coefficients |R| and transmission coefficients |T| of a step discontinuity between two monomode planar waveguides and the total radiation power P_r versus the values of n_c with λ=0.85 μm and m=40, where m is the number of radiation panels for Simpson's rule. The dotted lines are obtained from approximation and the thin and thick solid lines show present results for left and right incidence, respectively.*

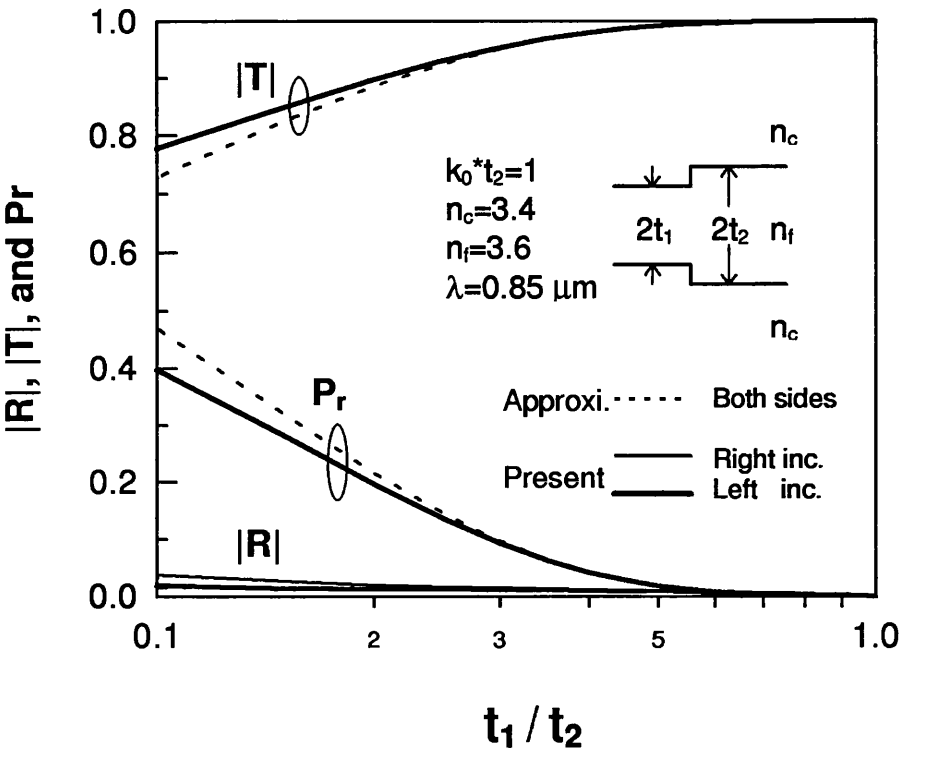

Fig. 19 *Reflection coefficients /R/ and transmission coefficients /T/ of a step discontinuity between two monomode planar waveguides and the total radiation power P_r versus the step thickness with λ=0.85 μm and m=40, where m is the number of radiation panels for Simpson's rule.*

be used to treat discontinuous structures accurately only at the condition with small step height and small index variation.

Similar conclusions are also demonstrated in Fig. 20 and Fig. 21, in which a step–junction is on one side of the guiding layer with large index variation (Fig. 20) and small index variation (Fig. 21). It is shown that the simple approximation method may produce erroneous results if the step height and the index variation are large.

Fig. 22 shows the values of $|R|$, $|T|$, and P_r of a step discontinuity in the planar waveguide (shown in inset) for a TE_0 mode with left incidence versus the normalised thickness of guiding layer $k_0 t_1$, and a comparison of radiation loss obtained from our result and that of *Boyd* et al. [123] is also shown in Fig. 22 and in Fig. 23 with small variation in the index profile.

Fig. 24(a) and (b) show the values of $|R|$, $|T|$, and P_r versus the step height for a single step–junction in the asymmetric planar waveguides with different index profiles. The radiation losses become very significant in these cases because a large amount of radiation power leaks into the substrate region, and the reflection coefficients $|R|$ are obviously different between left and right incidences in the small step height range (shown in Fig. 24). This discrepancy will degrade the reflection coefficients and may change Bragg's frequency in grating structures. It will be investigated and discussed in the next chapter.

4.5 RADIATION PATTERNS AT THE JUNCTION

The radiation pattern of a single step discontinuity in a symmetric planar waveguide evaluated by three methods is shown in Fig. 25. The peak value of the present results is less than those of *Rozzi's* [70] and *Hirayama* et al. [64], but our results show more losses in reflected radiation modes. However, as we can see from Fig. 25, only our radiation pattern is continuous in the vertical direction with radiation angle of $\theta = 90°$.

According to our investigation, the radiation pattern strongly depends on the step

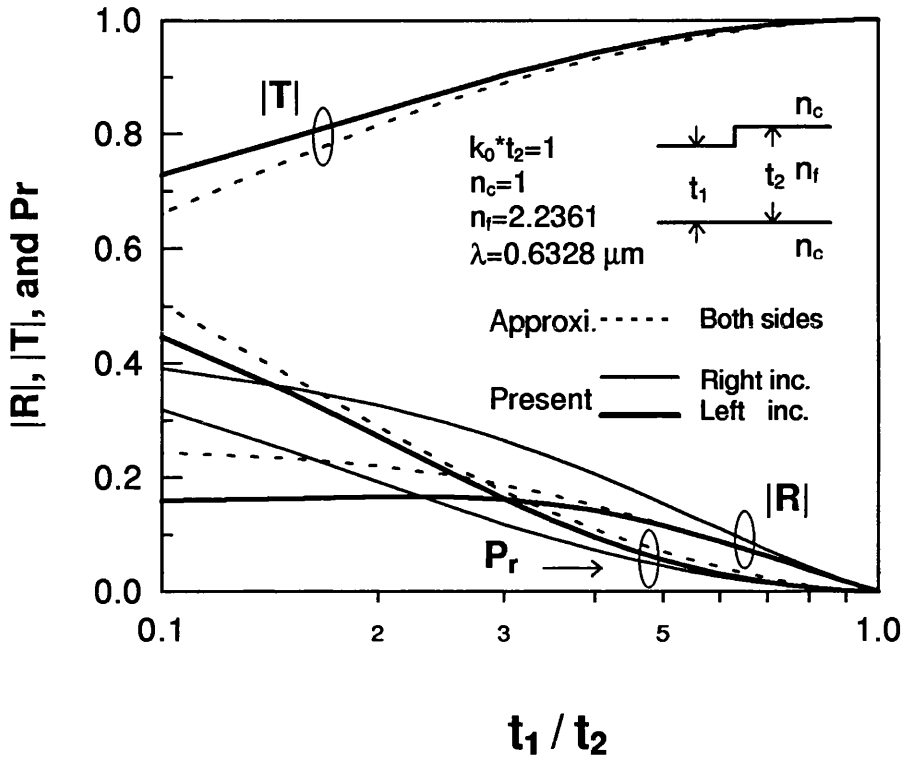

Fig. 20 *Reflection coefficients |R| and transmission coefficients |T| of a step discontinuity between two monomode planar waveguides and the total radiation power P_r versus the step thickness with λ=0.6328 μm and m=40, where m is the number of radiation panels for Simpson's rule.*

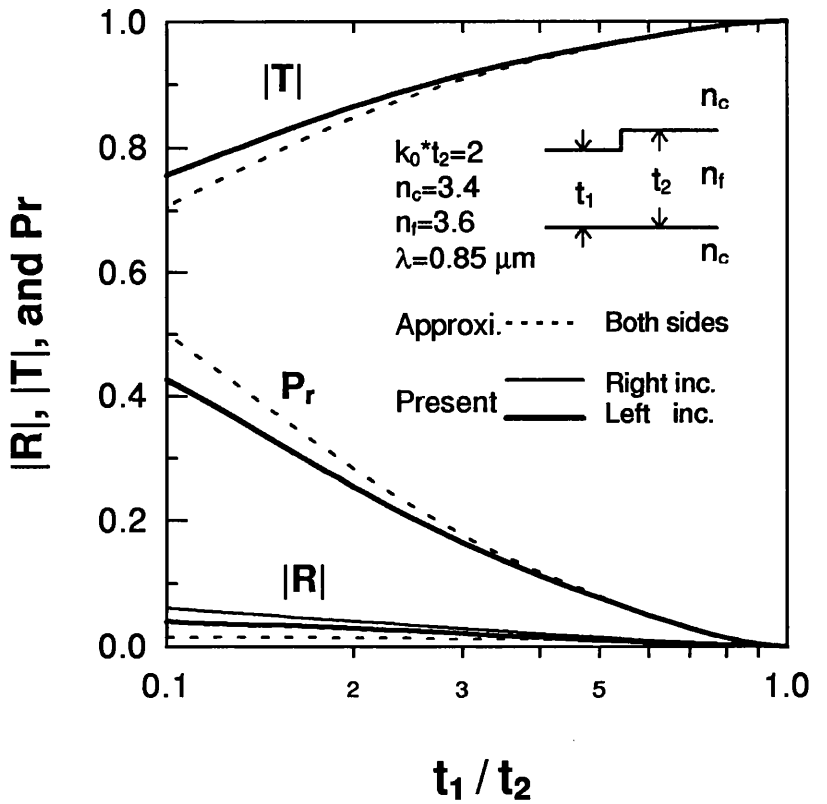

Fig. 21 *Reflection coefficients /R/ and transmission coefficients /T/ of a step discontinuity between two monomode planar waveguides and the total radiation power P_r versus the step thickness with λ=0.85 μm and m=40, where m is the number of radiation panels for Simpson's rule.*

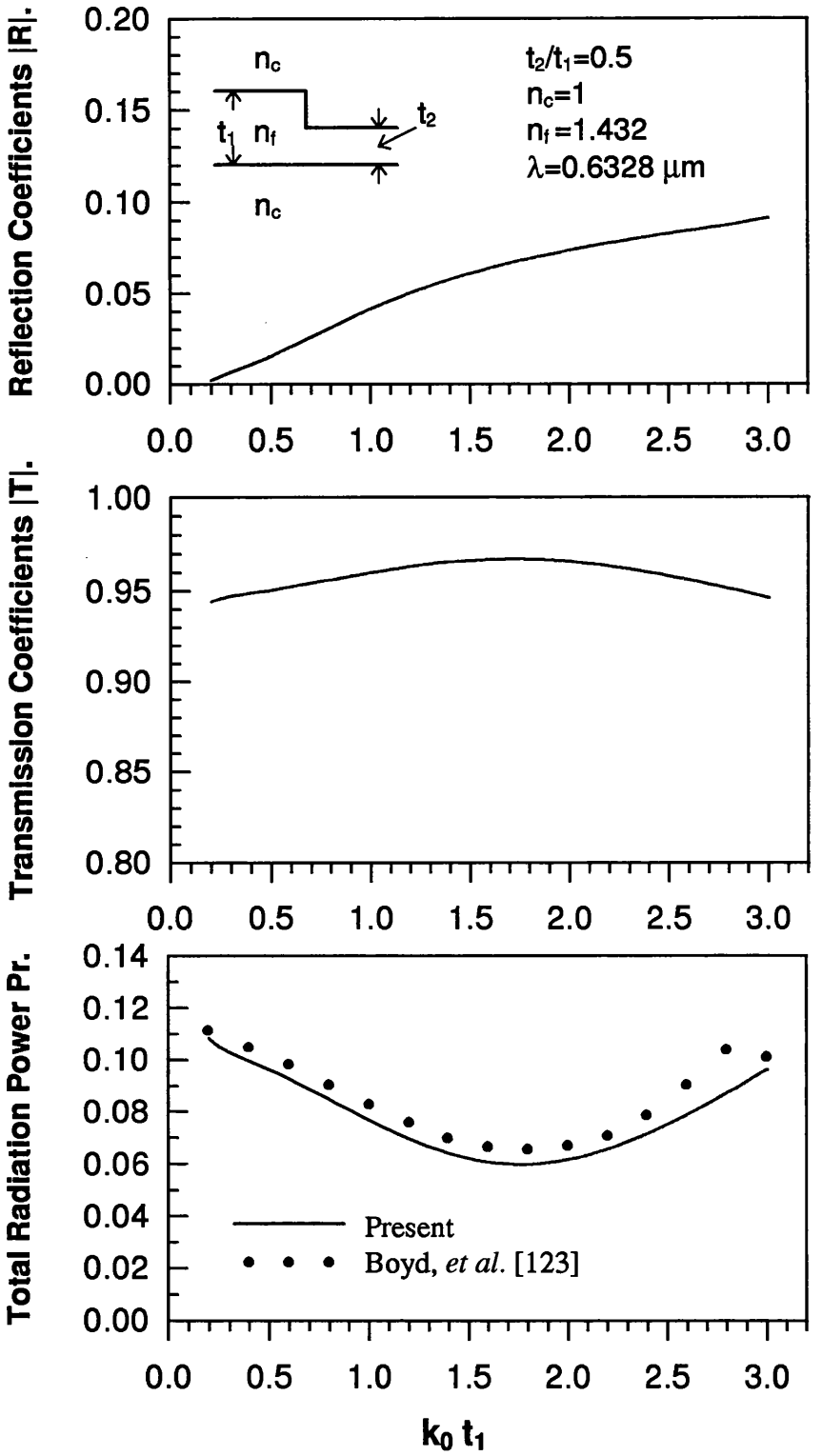

Fig. 22 *Reflection coefficients /R/, transmission coefficients /T/, and the total radiation power P_r of a step discontinuity in the planar waveguide (shown in inset) versus the values of $k_0 t_1$.*

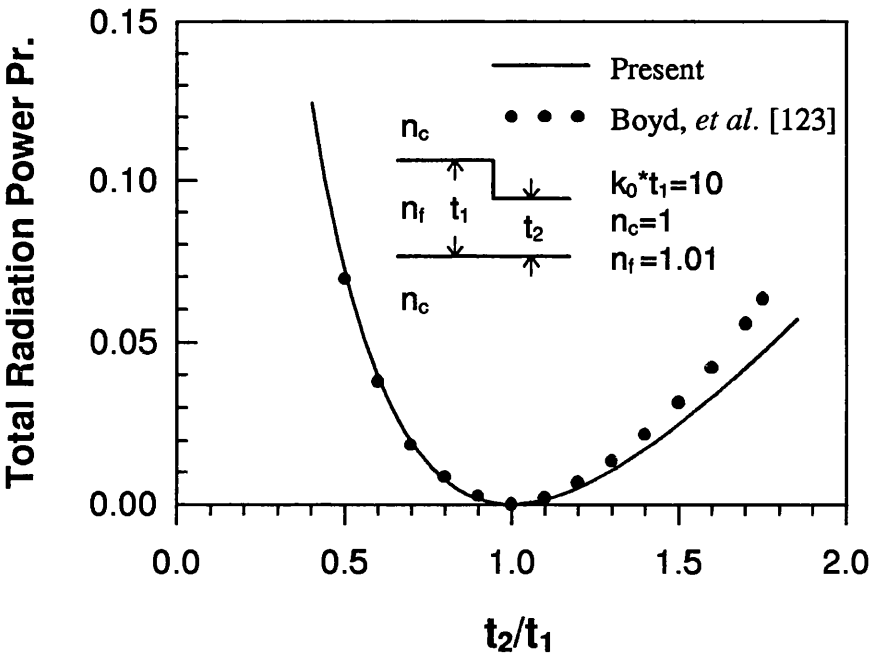

Fig. 23 *Calculated values of the total radiation power P_r caused by the step discontinuity in the planar waveguide (shown in inset) as a function of the relative step height t_2 / t_1 . The solid line shows the present results and the solid circles show the results of Boyd, et al.* [123]. *(λ=0.6328 μm)*

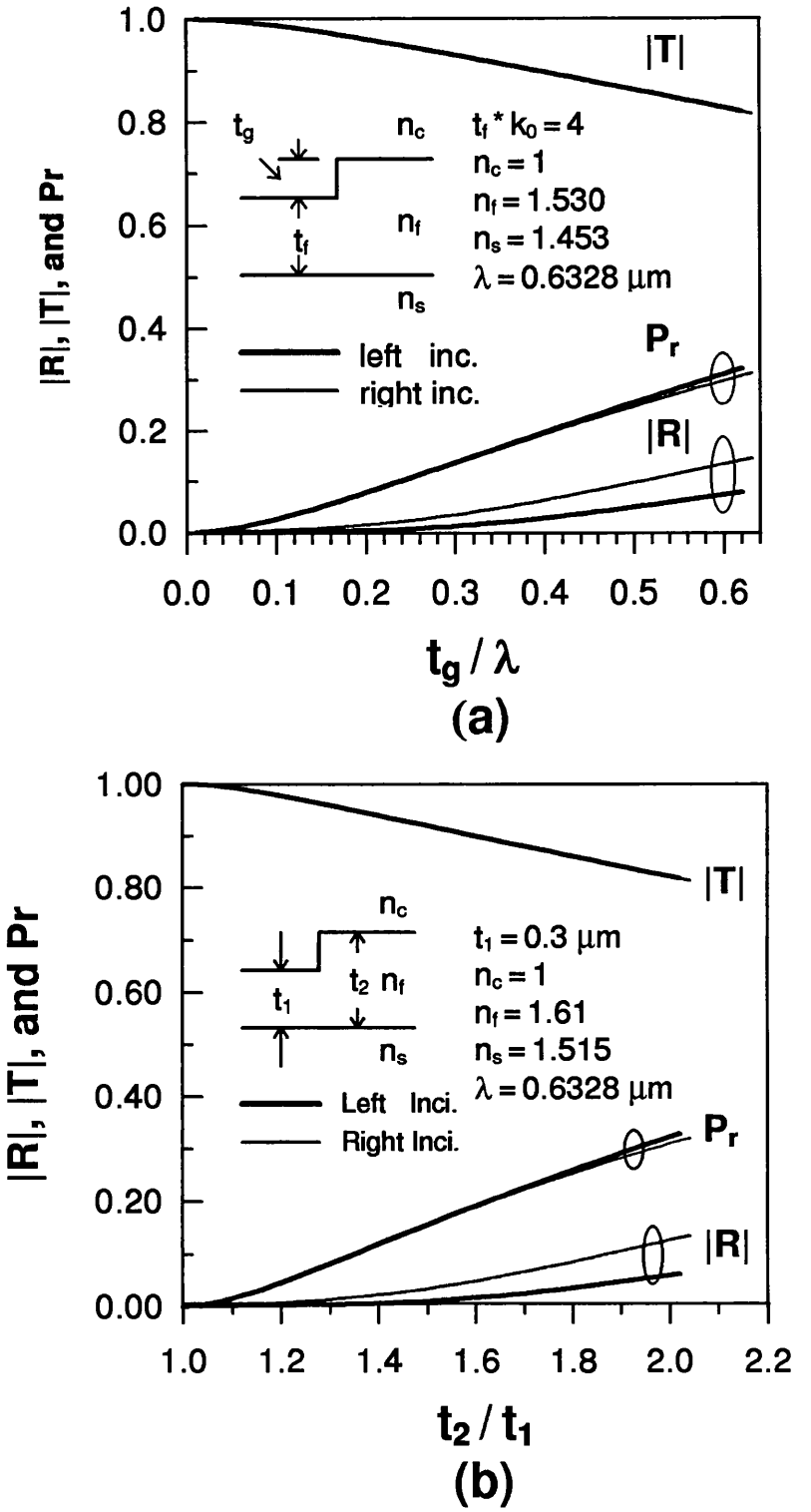

Fig. 24 *Two cases of the reflection coefficients |R| and transmission coefficients |T| of a step discontinuity between two monomode asymmetric planar waveguides and the total radiation power P_r versus step height.*

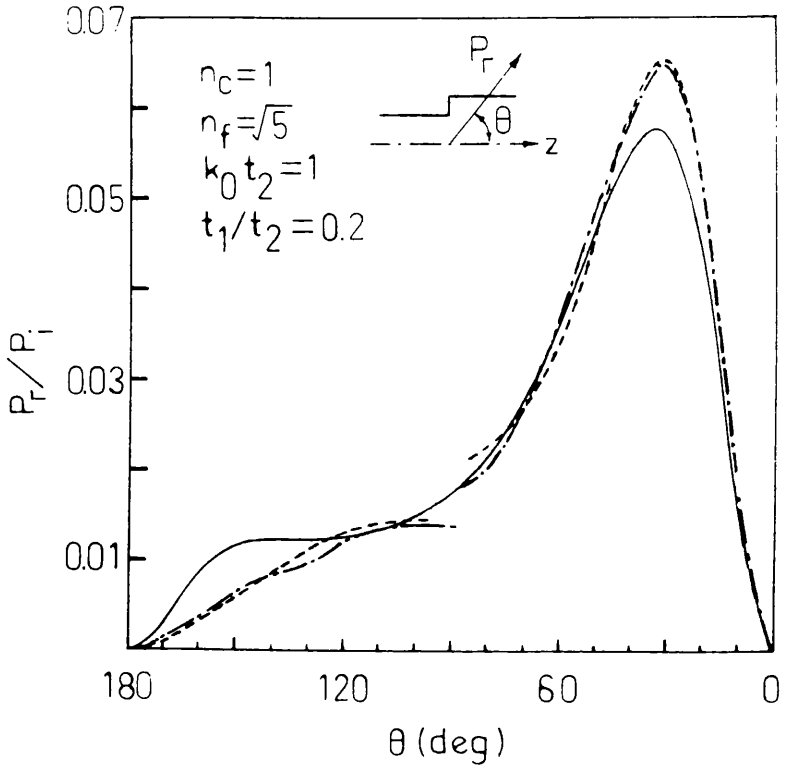

Fig. 25 *Radiation patterns (incidence from left) of a single step discontinuity in a symmetric planar waveguide.*

..... *Rozzi* [70]
– – – – – *CFBEM (Hirayama)* [64]
——— *Present*

height and index profile. In Fig. 26 we have plotted the radiation patterns of a single step discontinuity in the planar waveguide described in inset for different relative step heights t_1/t_2. These figures show that the lobe in the radiation pattern near the waveguide surface (small radiation angle) increases significantly as the step height d $(= t_2 - t_1)$ increases. Fig. 27 shows the radiation patterns for the step discontinuity with small index variation ($n_c = n_s = 3.4$ and $n_f = 3.6$) for different relative step heights. The radiation patterns in this figure are quite different from those in Fig. 26; not only are major radiation losses close to the slab surface within a very narrow angle range, but also the reflected radiation modes are so small as to be ignored. In Fig. 26(c) we have demonstrated the lobe structure in the radiation pattern.

In Fig. 28, both cases of radiation pattern have been shown together for easy comparison, Fig. 28(a), 28(c), and 28(e) for the single step discontinuity on one side of the slab waveguide with large index variation and Fig. 28(b), 28(d), and 28(f) for the single step junction with small index variation. The results show the spanning angle of the major radiation losses more narrow and closer to the slab surface than that of symmetric structures shown in Fig. 26 and 27.

4.6 CONCLUSION

Results on the reflection coefficients, transmission coefficients and total radiation power of the lowest TE mode incident onto a single step discontinuity in planar waveguide were presented in this chapter. The comparisons of present results with those obtained by simple approximation and other methods show that our results have good agreement with others over large range of the step height and the variation in the refractive index profile. It is worth noting that the reflected modes can be neglected in the approximate methods only under the conditions of small step height and small index variation.

By the convergence test, it was found that an adequate number of radiation panels

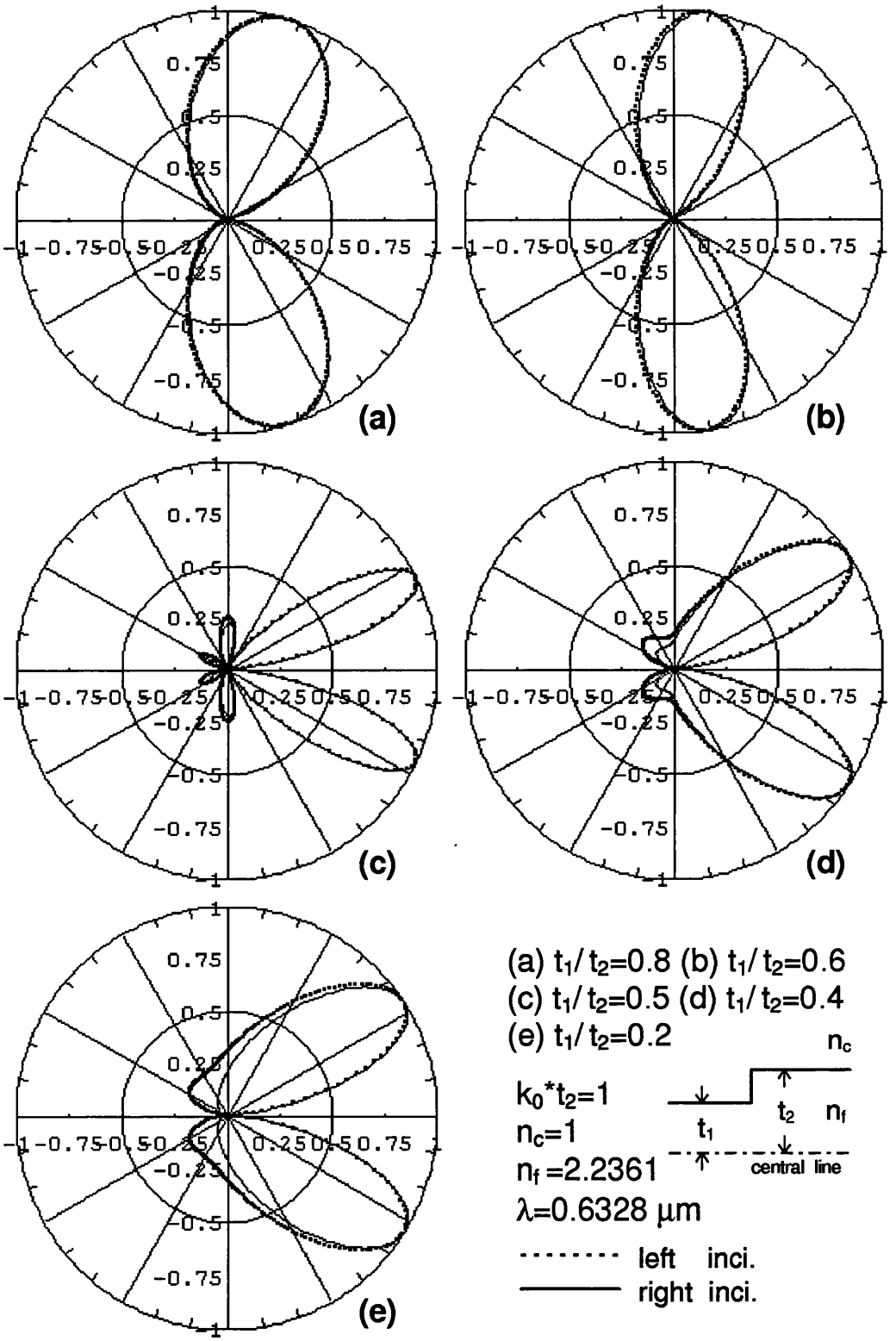

Fig. 26 *Radiation patterns of a step discontinuity in symmetric planar waveguides with different step heights for the TE_0 mode. The dotted lines and solid lines belong to step-up and step-down discontinuities respectively.*

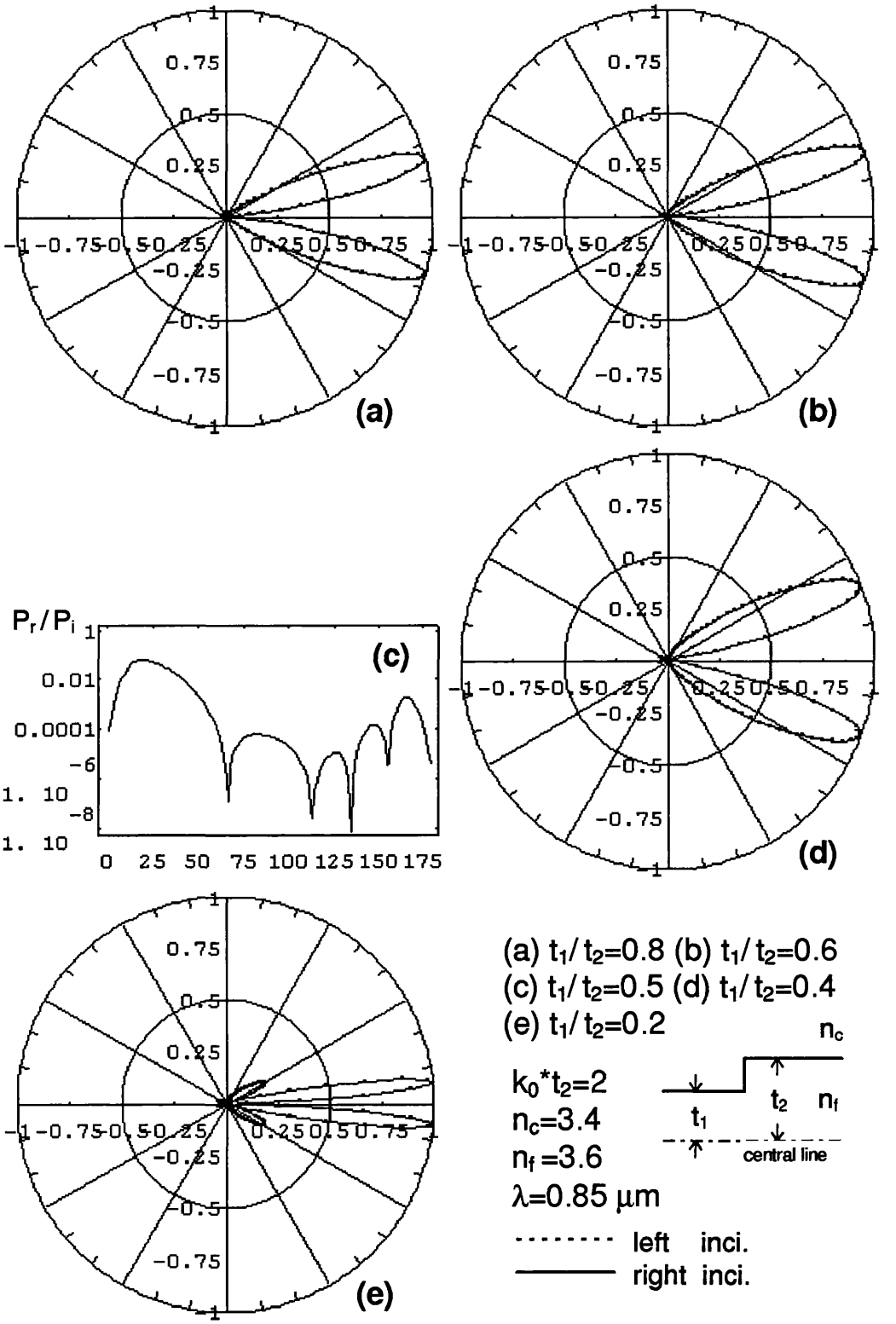

Fig. 27 *Radiation patterns of a step discontinuity in symmetric planar waveguides with different step height for the TE_0 mode. The dotted lines and solid lines belong to step-up and step-down discontinuities respectively.*

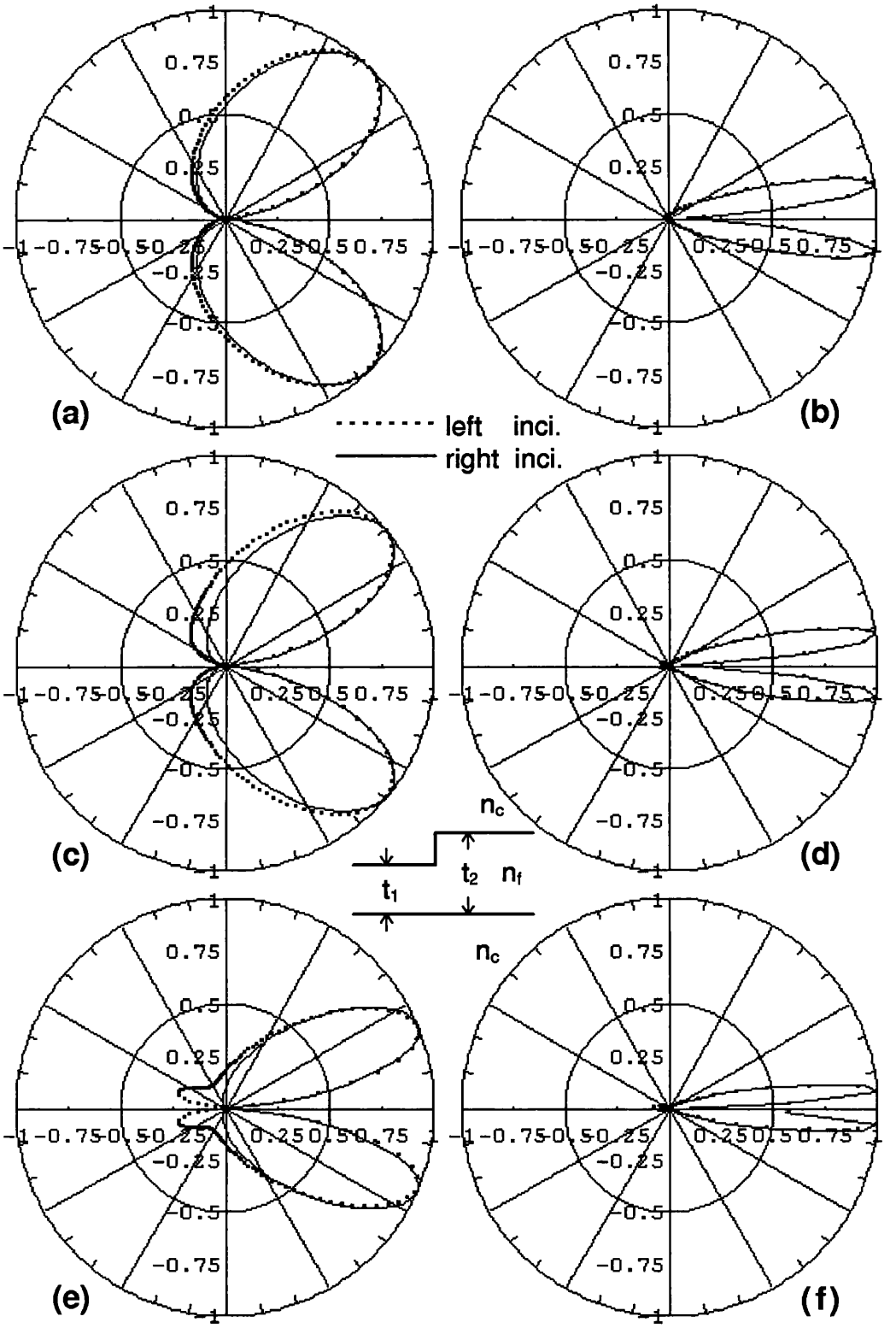

Fig. 28 *Radiation patterns of a single step discontinuity on one side of the slab waveguide with different index profiles for the TE_0 mode. The dotted lines and solid lines belong to step-up and step-down discontinuities respectively.*
n_c=1, n_f=2.2361, $k_0 * t_2$=1, λ=0.6328 μm, (a)t_1/t_2=0.8, (c)t_1/t_2=0.5, (e)t_1/t_2=0.2.
n_c=3.4, n_f=3.6, $k_0 * t_2$=2, λ=0.85 μm, (b)t_1/t_2=0.8, (d)t_1/t_2=0.5, (f)t_1/t_2=0.2.

for Simpson's rule is between 20 and 40 for the mode–matching calculations to ensure accurate results and also to avoid handling too large matrix treatments. But, in the corrugated structure its radiation pattern is more complicated than that of a single discontinuity, so we have to check the convergence carefully when the structure changes. Certainly, using more radiation panels induces more accurate results but also leads to more computer time.

According to the radiation patterns shown in the last section, for the step discontinuity with a small variation in the index profile, its major radiation loss is concentrated in a cigar–shaped lobe with a very narrow range of radiation angles. Therefore, we can truncate the minor radiation modes in order to reduce the matrix dimensions in the algorithm without creating considerable errors in the results.

5

CHAPTER 5

THEORETICAL APPROACH FOR DOUBLE–STEP DISCONTINUITIES AND PERIODIC GRATINGS

5.1 INTRODUCTION

In Chapter 4, we have been concerned with the applications of our method to a single step discontinuity in planar waveguides, in which modes produced by the step junction have been treated in detail. But, for the analysis of multiple–step discontinuities, we have to consider not only modes coupled by each step junction but also the phase response of each mode propagating in such a structure. The amplitude of a mode reaches a maximum as the phase–matching condition is achieved. Especially, the resonance effect of gratings induces distributed feedback in its stopband and can control the longitudinal mode by mode selection in the applications of DFB and DBR lasers. Besides, the wavelength–sensitive phase–matching condition of gratings can be used in the applications of the output couplers [124][125] and the grating–assisted directional couplers [21][22][77][126]. Other applications have been discussed in Chapter 1.

We will investigate and discuss the reflection coefficients and radiation losses of double–step discontinuities as well as the comparison of our results and those from other methods. In grating structures, the convergence, reflection spectra, radiation losses, radiation modes of higher order gratings, and the coupling coefficient will also

be carried out in this chapter for periodic gratings with various groove depths and refractive index profiles.

5.2 DOUBLE–STEP DISCONTINUITIES

We consider a groove and a rib obstacle, as shown in the inset to Fig. 29(a) and Fig. 29(b), in which two step discontinuities are separated by a segment of planar waveguide of length b. When a TE_0 mode is incident on such structures, there are guided and radiation modes reflected from two step discontinuities, and such modes have different phase delays when they travel back to the incident side. The phase delays of these modes are determined by the factor of $\exp(j\beta_{\nu_i}^{(2)}b)$, where $\beta_{\nu_i}^{(2)}$ are the propagation constants of the reflected modes $a_{\nu_i}^{(2)}$ in region 2 between two step junctions. The total transfer matrix for the double–step discontinuities structure is given by

$$[A^1] = [M^{12}][T^2]^{-1}[M^{23}][A^3] \quad \text{with} \quad [M^{23}] = [M^{12}]^{-1} \tag{95}$$

where $[A^1]$ is the coefficients column matrix of the modes in region 1, and $[A^3]$ is for the modes in region 3. M^{12} and M^{23} are the transfer matrices of junction 12 and junction 23 for the rib and the groove structure. Since there are no incoming waves from region 3, (95) may be arranged as

$$\left[\begin{array}{c} \mathrm{a}_{\mu_1}^{3+} \\ \mathrm{a}_{\mu_2}^{3+} \\ \vdots \\ \hline \mathrm{a}_{\mu_1}^{1-} \\ \mathrm{a}_{\mu_2}^{1-} \\ \vdots \end{array}\right] = \left[\begin{array}{c|c} S_{11} & S_{12} \\ \hline S_{21} & S_{22} \end{array}\right] \left[\begin{array}{c} 1 \\ 0 \\ \vdots \\ \hline 0 \\ 0 \\ \vdots \end{array}\right] \tag{96}$$

where matrix $[S]$ can be evaluated from (30) and (42). In Fig. 29(a) and (b), the amplitude coefficients of reflected and transmitted modes are plotted versus the relative separation b/t_1 as well as the comparisons of present results with those of *Suzuki and*

Table 5: Data at minimal amplitude of $|R|$ for the double–step discontinuities (rib) shown in the inset of Fig. 30

n	b/t_1	$\|R\|$	$\beta_\nu^{(2)}b$	$\Delta\%$	P_r
1	1.014	0.01003	3.1765	1.1	0.07420
2	1.993	0.008694	6.2434	0.63	0.03729
3	3.015	0.001723	9.4450	0.21	0.02369

Koshiba [60] calculated by the finite element analysis are also presented. There is a small difference between them in the resonance of the reflected mode in the groove (or rib) region. In the results we presented, apparent oscillation appears in the reflection coefficients $|R|$, and the value of $|R|$ reaches the minimum at $\beta_\nu^{(2)}b=3.07924$. Compared with the phase–matching condition of $\beta_\nu^{(2)}b=\pi$, there is a deviation of about 2% between them because we have considered the radiation losses in the calculation.

Apparent resonance in the reflection coefficient also appears in Fig. 30, in which a rib structure in a symmetric planar waveguide is considered in the analysis with the parameters listed in the inset. The reflection coefficients reach minima obeying the condition given by

$$\beta_\nu^{(2)}b = n\pi, \quad \text{with} \quad n = 1, 2, 3, \cdots \tag{97}$$

and $\beta_\nu^{(2)}b = (n - 1/2)\pi$, with $n = 1, 2, 3, \cdots$ is the condition of maximal reflection coefficient. Table 5 shows data at the minimal $|R|$ and the deviations of the phase–matching points between our results and that of (97). Both the deviation and total radiation power P_r decrease as the order n increases. This effect of losses on the reflection minimum due to the radiation losses has also been discussed by *Rozzi and In't Veld* [72]. The double–step discontinuities shown in the inset to Fig. 30 have been

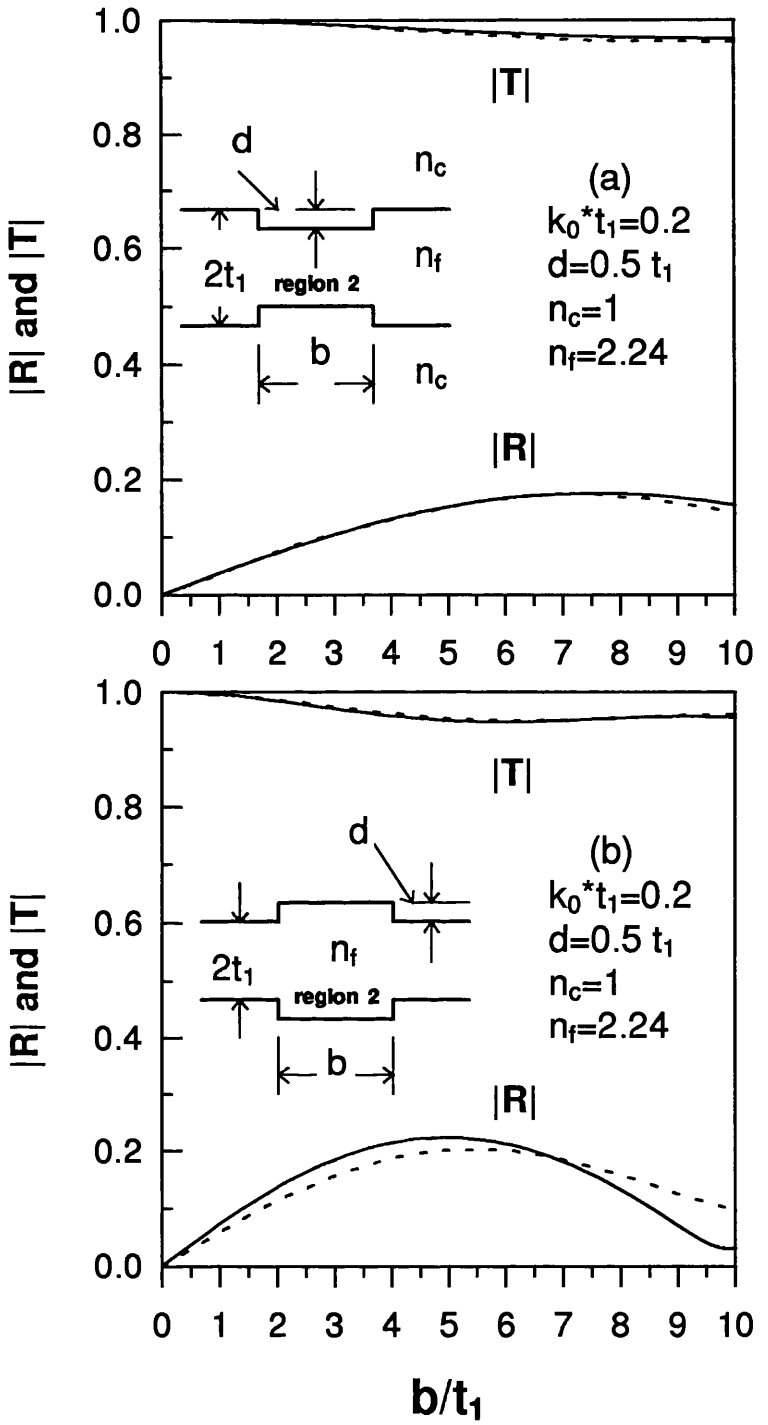

Fig. 29 *Reflection coefficients |R| and transmission coefficients |T| of a symmetric double-step discontinuities, (a) a groove and (b) a rib structure, as a function of the relative separation b/t_1 with λ=0.6328 μm and m=40.*

——— *Present* ····· *Suzuki* et al . [60]

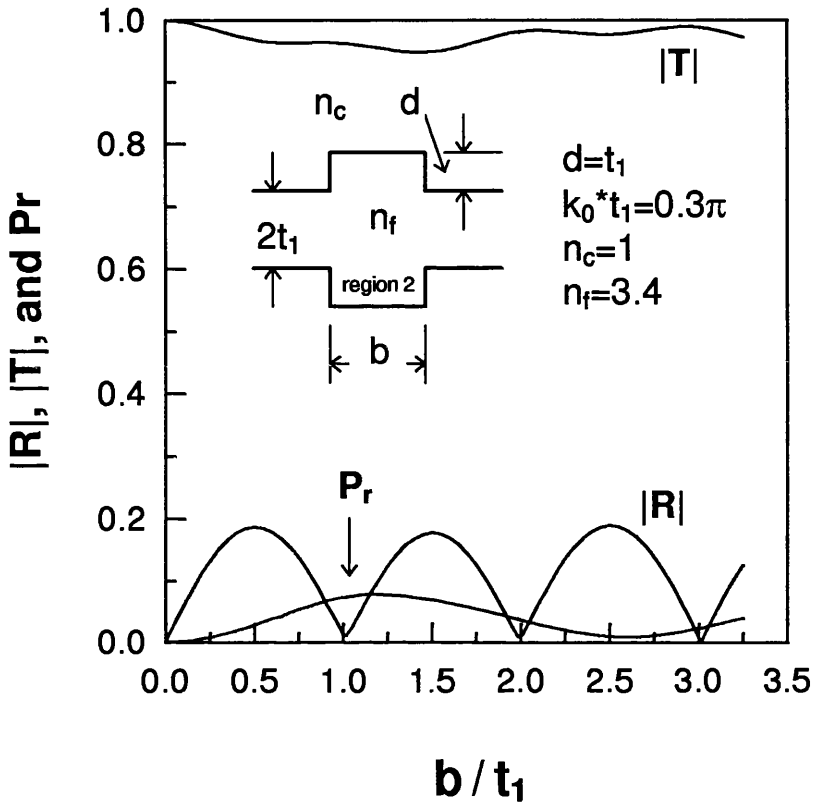

Fig. 30 *Reflection coefficients /R/, transmission coefficients /T/, and the total radiation power P_r of a symmetric double-step discontinuities as a rib versus the relative separation b/t_1 with λ=0.85 μm and m=40.*

Table 6: Data at the impedance matching condition of the staircase transformer shown in the inset of Fig. 31(a)

Propagation	$n=1$		$n=3$	
Directions	b/t_3	$\|R\|$	b/t_3	$\|R\|$
Left Inci.	1.019	0.007581	3.193	0.02364
Right Inci.	1.086	0.05947	3.223	0.04791

investigated by *Rozzi and In't Veld* [72] and by *Hosono* et al. [73]. However, the phase–matching condition of the reflection coefficients did not match (97) in the results of *Rozzi and In't Veld*, and an unreasonable change of the peak reflection coefficients appeared in the results from *Hosono* et al. because a bounded configuration had been introduced in their calculation.

We also check the resonance effect of the waveguide with a staircase structure, namely, a ten–to–one quarter–wave transformer as shown in the inset of Fig. 31(a), in which the parameters of the structure are the same as those that *Hirayama and Koshiba* [64] and *Chung and Chen* [115] had used in their papers. The phase change only arises from the reflected mode propagating through the region between two step junctions, as $\beta_\nu^{(2)} b = n\pi/2$ where $n = 1, 3, 5, \cdots$, the impedance matching condition achieved with minimal reflection coefficients (see Table 6). Comparing with the reflection coefficient reach a minimum near $b/t_3 = 1.08$ and 3.25 predicted by the relation of $\beta_\nu^{(2)} = \sqrt{\beta_\mu^{(1)} \beta_{\mu'}^{(3)}}$, our results have good agreement with them and also with those from other methods [64][115]. Fig. 31(b) shows the radiation patterns for $b/t_3 = 2$ (solid line) and $b/t_3 = 1$ (dotted line) with the main peak of the lobe in the direction about 21°, only 1° difference from the result (20°) of *Hirayama and Koshiba* [64].

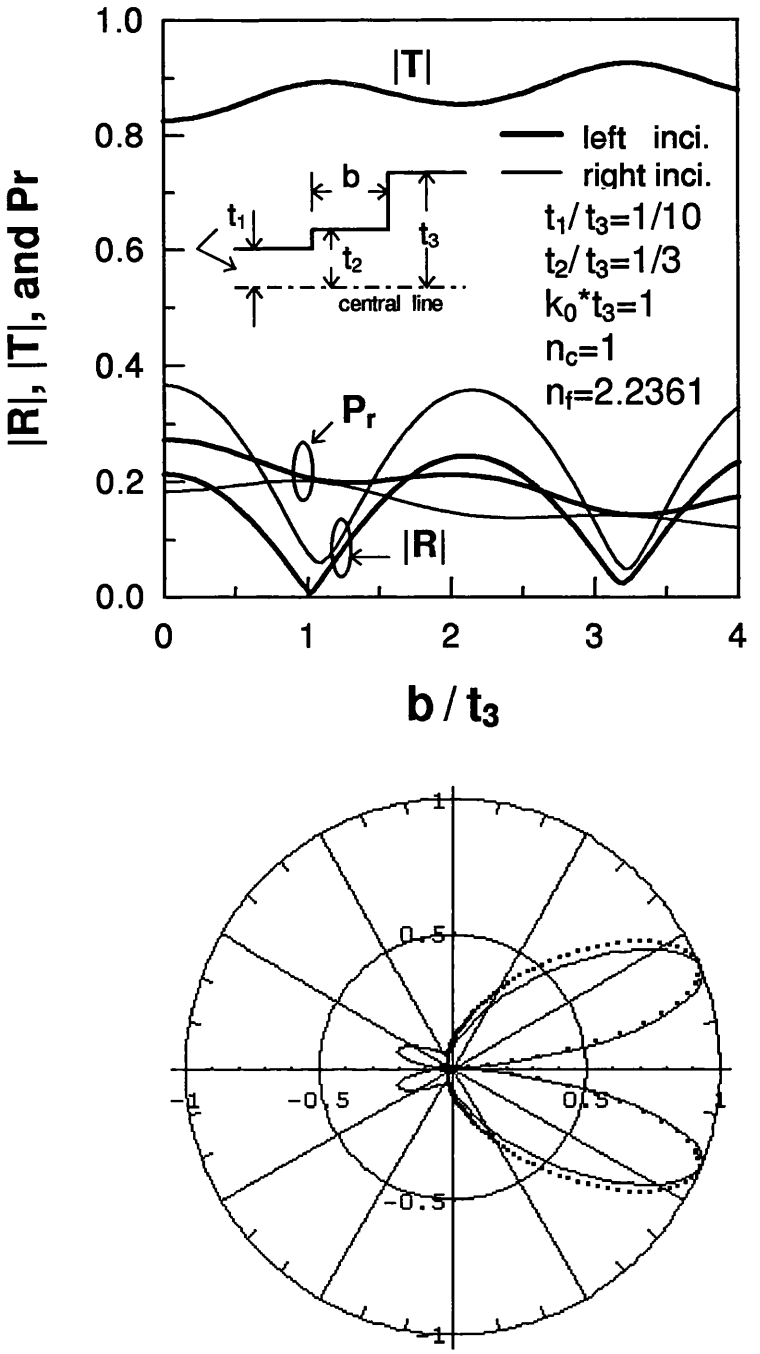

Fig. 31 *(a)Reflection coefficients |R|, transmission coefficients |T|, and the total radiation power P_r of a staircase transformer for both left and right incidences with λ=0.6328 μm. (b) Scattering radiation patterns for left incidence with b/t_3=2 (solid line) and b/t_3=1 (dotted line).*

In Fig. 32 we have plotted the values of $|R|$, $|T|$, and P_r versus the relative separation b/t_1 for a groove and a rib structure in asymmetric planar waveguides shown in each inset to the figures. The phase–matching responses of reflection coefficients $|R|$ in the two cases are apparently different. A good contrast between maximal and minimal amplitudes of the modes reflected from the groove structure is shown in Fig. 32(a), but the contrast of the rib structure (Fig. 32(b)) decreases because much more radiation losses arise from such a structure.

Double step discontinuities such as a groove and a rib are the basic structure of gratings. The resonance effect in waveguide gratings obeys Bragg's law with a higher reflection coefficient in the stopband. This property leads the grating to very broad applications. In the next section, we will investigate the mode behaviour in periodic gratings.

5.3 PERIODIC GRATINGS

Considering a periodic grating in planar dielectric waveguides with N periods, one of such structures is shown in the inset to Fig. 33, in which $t_1(=t_3)$ and t_2 are the thickness of guiding layers in region 1 (rib) and 2 (groove) respectively, and the period Λ is given by $\Lambda = 2\Lambda_1$ as a symmetric rectangular grating. We only consider constant groove depth (or tooth height) in this thesis, but the extension to tapered gratings is straightforward.

5.3.1 General Properties

The phase–matching point of the reflected guided mode satisfies the Bragg condition given by

$$\frac{\beta_\mu^{(1)} + \beta_\nu^{(2)}}{2} = \frac{l\pi}{\Lambda}, \quad \text{with} \quad l = 1, 2, 3, \cdots \tag{98}$$

where $\beta_\mu^{(1)}$ and $\beta_\nu^{(2)}$ are the propagation constants of reflected modes in region 1 and 2 respectively, and l is some integer with respect to the various orders of the grating.

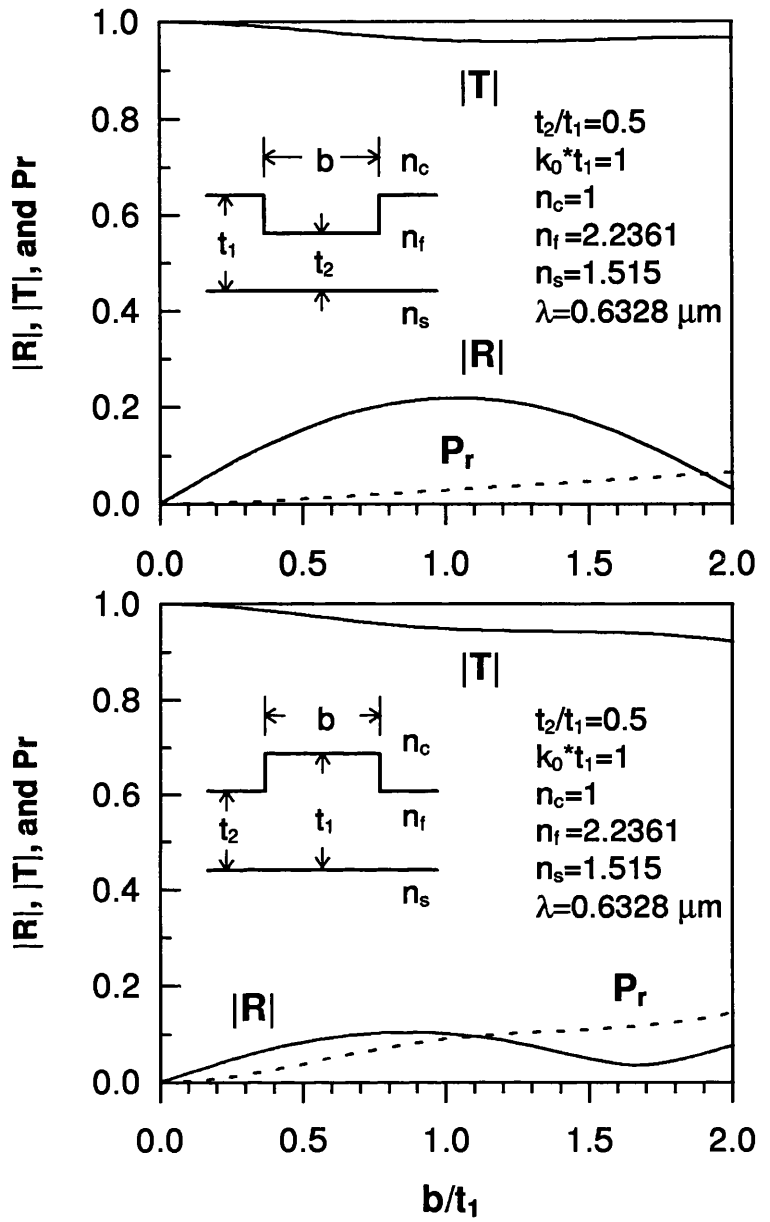

Fig. 32 *Reflection coefficients /R/, transmission coefficients /T/, and the total radiation power P_r of the asymmetric double-step discontinuities, (a) a groove and (b) a rib structure, as a function of the relative separation b/t_1 with λ=0.6328 μm.*

Therefore, the amplitude of the reflected mode reaches a maximum as one of the Bragg conditions is achieved. But according to the discussion given by *Yariv and Nakamura* [3], the condition (98) is necessary but not sufficient. We have checked the case of a symmetric rectangular grating plotted in Fig. 33(a), where the second–order coupling ($l = 2$) vanishes. In Fig. 33(b), the total radiation power P_r becomes very significant as the grating order l is greater than 1. The reason is that the radiation mode with a certain radiation angle θ_ν can reach constructive interference and strong radiation losses arise from higher order gratings. This effect will be discussed later in this chapter.

Fig. 34 and Fig. 35 show the convergence of the total radiation power P_r produced by the gratings versus the number of radiation panels m for Simpson's rule. The curves of P_r show very bad oscillation in the small m region, because a number of small sublobes appear in the radiation patterns. These sublobes arise from the phase response of radiation modes in the grating region. However, the oscillations disappear when the number of panels m is larger than 40. Similar conditions have also been found in Fig. 36 for the gratings on one side of the guiding layer shown in the inset. In this chapter the number of panels of $m = 40$ will be used in the calculation.

In Fig. 37 the power of modes coupled by symmetric gratings with different groove depths have been plotted versus the number of periods N. Unlike shallow or sinusoidal corrugated structures, deep rectangular gratings have very strong coupling effects as shown in the figure so that, after passing only a few periods, the reflected mode reaches its maximum and the transmitted mode approaches zero in the case with $t_2/t_1 = 0.4$.

In Fig. 38 two gratings having the same groove depth but different index profiles as shown; the reflected power of $P^{(-)}$ and transmitted power of $P^{(+)}$ for backward– and forward–propagating guided modes are shown as a function of the position along the grating for (a)$N = 40$ with $n_c = 1$ and $n_f = 2.2361$, (b)$N = 200$ with $n_c = 3.4$ and $n_f = 3.6$. The latter case with small index variation, which has been discussed in Chapter 4, has small reflection coefficients for reflected modes, and is suitable for simple approximate analysis. As shown in Fig. 38(b), the reflected and transmitted power are roughly linear

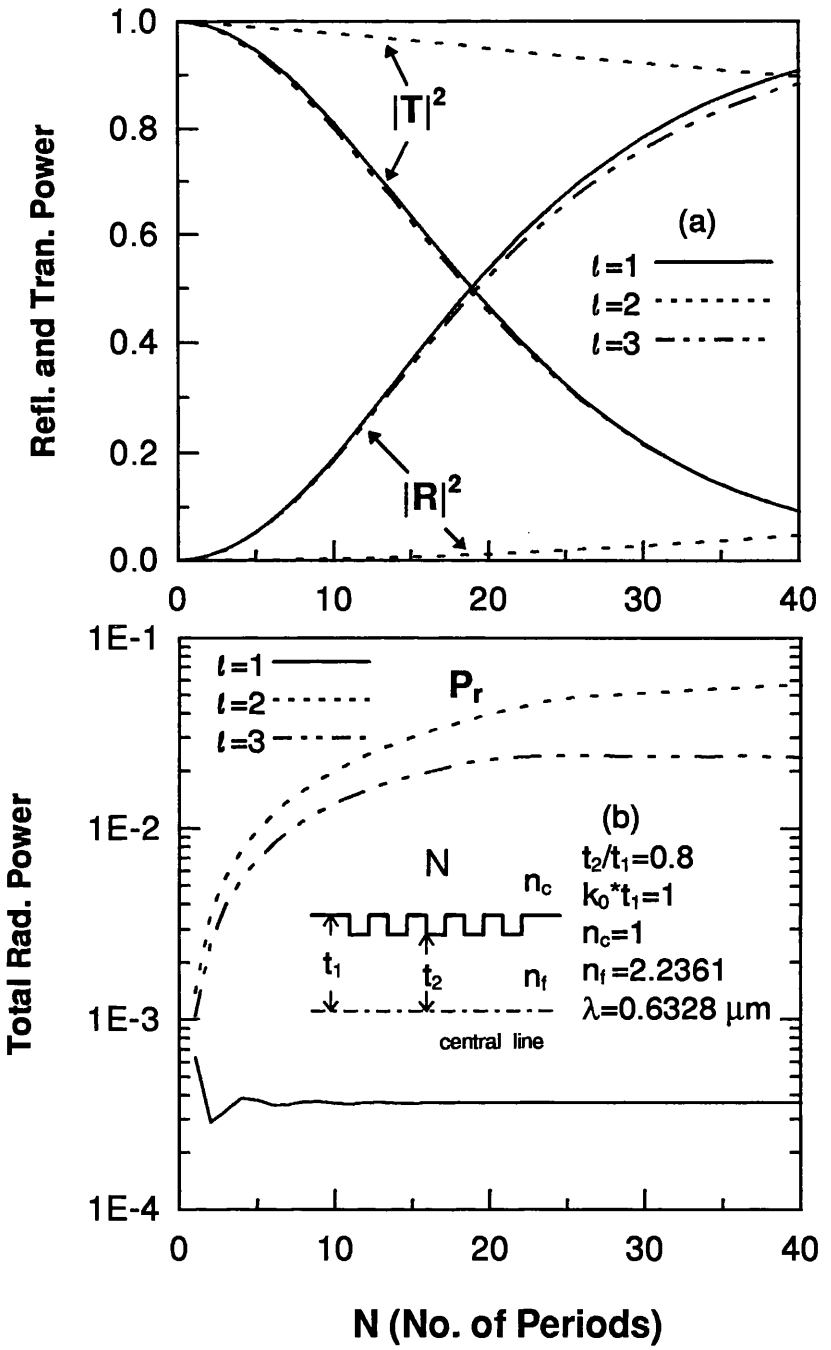

Fig. 33 *The reflected, transmitted, and total radiation power of three symmetric rectangular gratings with the grating order of* l *=1 (solid lines),* l *=2 (dotted lines), and* l *=3 (dash-dotted-dotted lines) versus the number of grating periods N.*

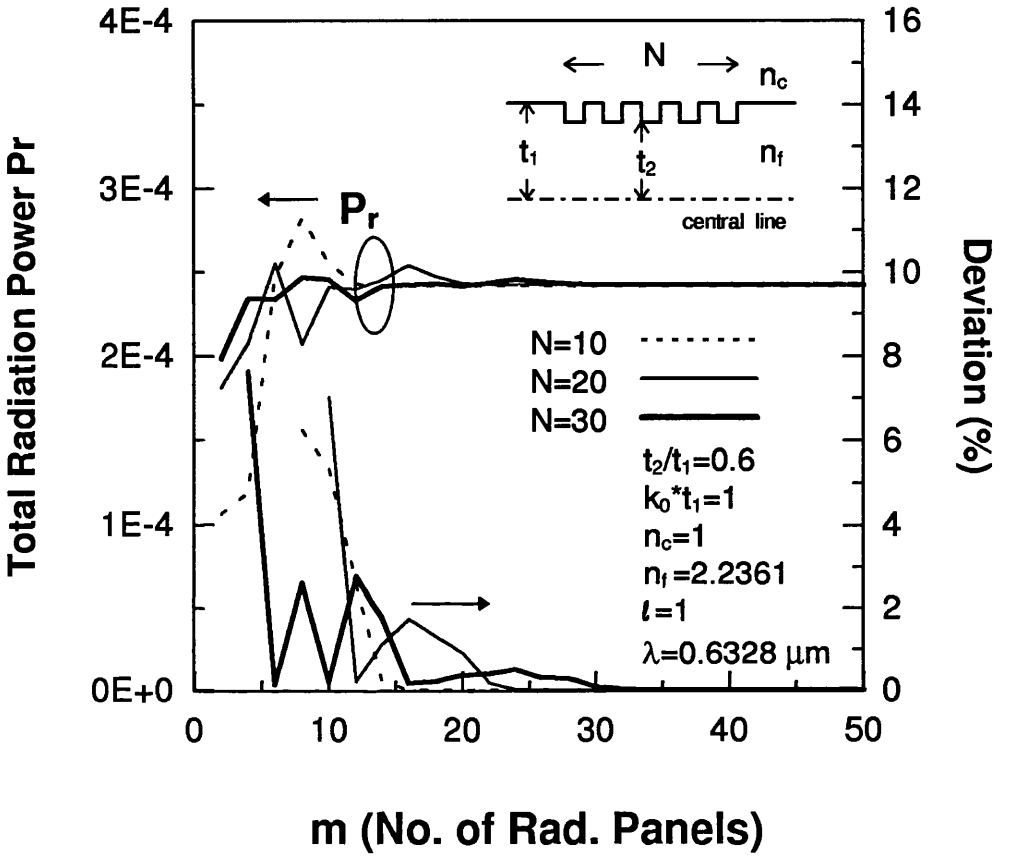

Fig. 34 *Convergence of the total radiation power P_r of a TE_0 mode incident onto three symmetric gratings with the number of grating periods as: N=10 (dotted lines), N=20 (thin solid lines), and N=30 (thick solid lines) versus the number of radiation panels for Simpson's rule.*

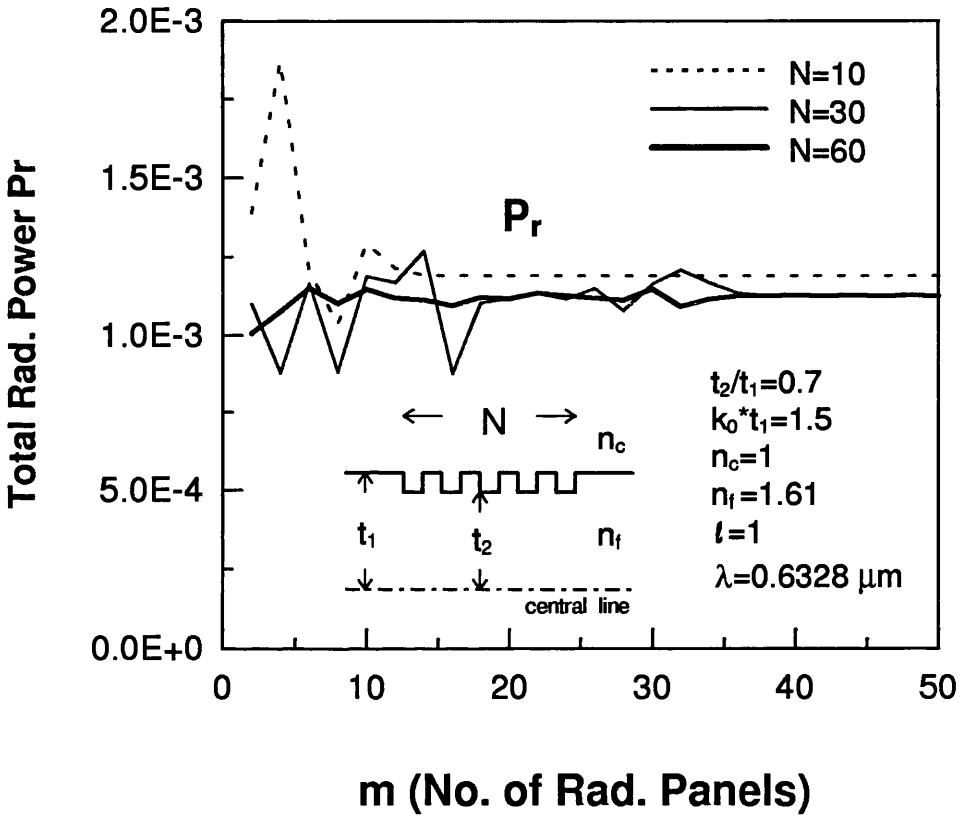

Fig. 35 *Convergence of the total radiation power P_r of a TE_0 mode incident onto three symmetric gratings with the number of grating periods as: N=10 (dotted lines), N=30 (thin solid lines), and N=60 (thick solid lines) versus the number of radiation panels for Simpson's rule.*

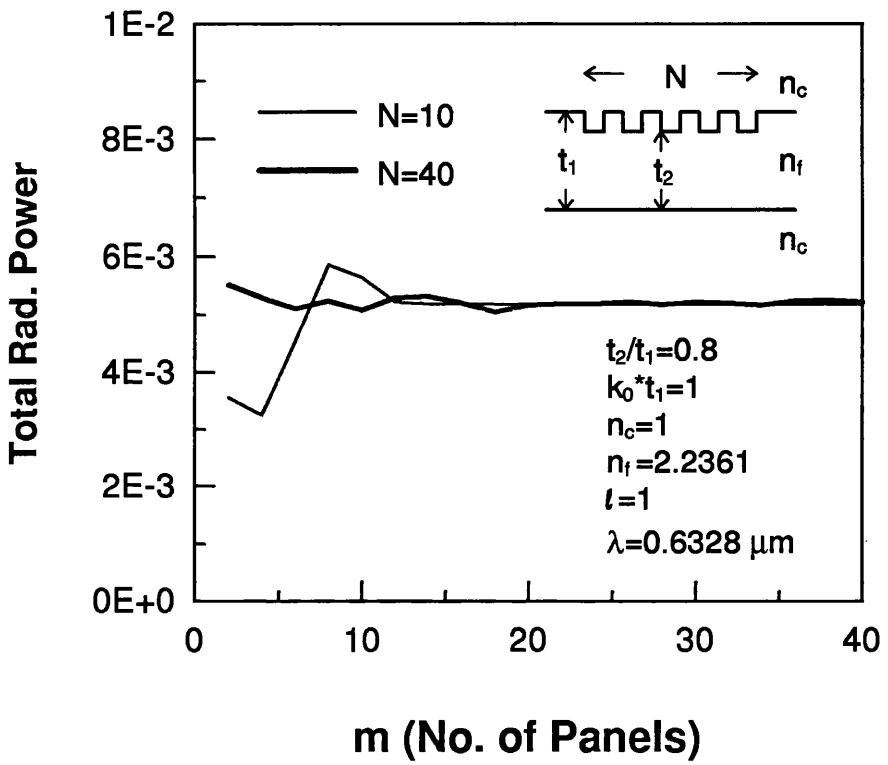

Fig. 36 *Convergence of the total radiation power P_r of a TE_0 mode incident onto two gratings (shown in inset) with the number of grating periods as: N=10 (thin solid lines), N=40 (thick solid lines) versus the number of radiation panels for Simpson's rule.*

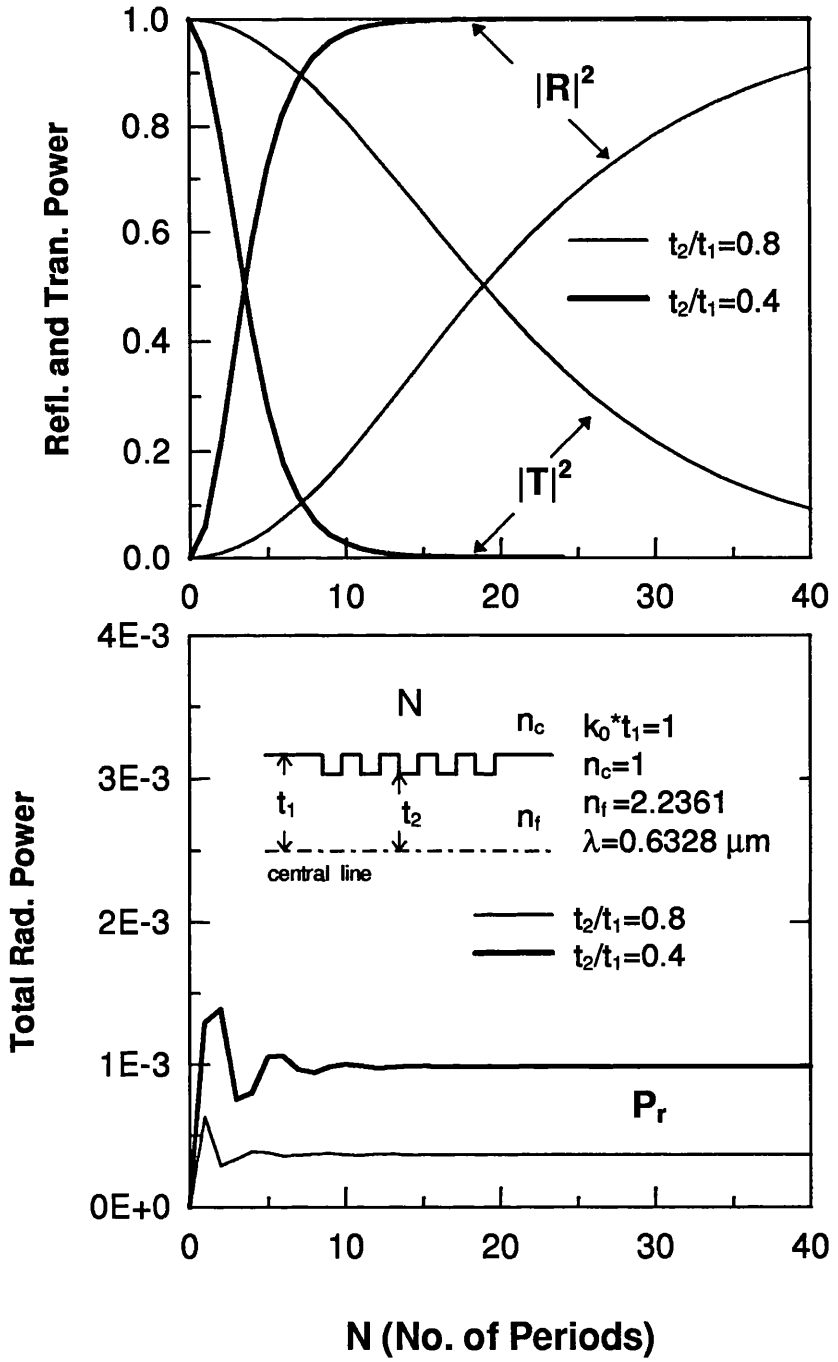

Fig. 37 *The reflected power $|R|^2$, transmitted power $|T|^2$, and the total radiation power P_r of the first order grating (shown in inset) versus the number of grating periods for $t_2/t_1=0.8$ (thick lines) and $t_2/t_1=0.4$ (thin lines) with $m=40$.*

responses over a wide grating region, where the coupling coefficient $|\kappa|$ is a constant.

The values of $|R|^2$, $|T|^2$ and P_r of a grating on one side of the guiding layer (shown in the inset to Fig. 39) have been plotted in Fig. 39 versus the number of periods N. It is shown that the radiation losses of P_r become constant after a few oscillations at first.

Fig. 40(a) and 40(b) show the values of $|R|^2$, $|T|^2$, and P_r of the gratings, as shown in the inset with small index variation as well as (a)$t_2/t_1 = 0.8$ and (b)$t_2/t_1 = 0.5$, versus the number of periods N. In Fig. 40(b) the reflected power only reaches 40% of the input power in the region of $N \geq 100$ because the rest of the power goes to the radiation modes.

5.3.2 Reflection Spectra and Radiation Losses

In this subsection, we investigate the frequency response of gratings by changing the free–space wavenumber $k' = 2\pi/\lambda'$ of the incident mode. Fig. 41 shows the spectra of reflection coefficients and the total radiation power P_r versus the deviation of k'/k_0, where k_0 is the wavenumber of the incident mode satisfying the Bragg condition. The width of the centre stopband of a periodic grating is shown as a function of the number of periods. Results show that the first minimum of the grating with $N = 20$ falls over the second minimum of the grating with $N = 40$ which ensures that the destructive interference of the reflected guided mode obeys the Bragg condition. Besides, the amplitude of sidelobes increases as the number of periods N increases. Similar phenomena also appear in Fig. 42 for the gratings with different index profiles and the number of periods. The peak of the centre stopband increases and its bandwidth becomes more narrow as the number of periods N increases. In Fig. 42(b), the radiation losses increase and oscillate significantly in the higher frequency region just outside the centre stopband of the grating with $N = 160$.

In Fig. 43, we have plotted the spectra of the reflection coefficients for two gratings

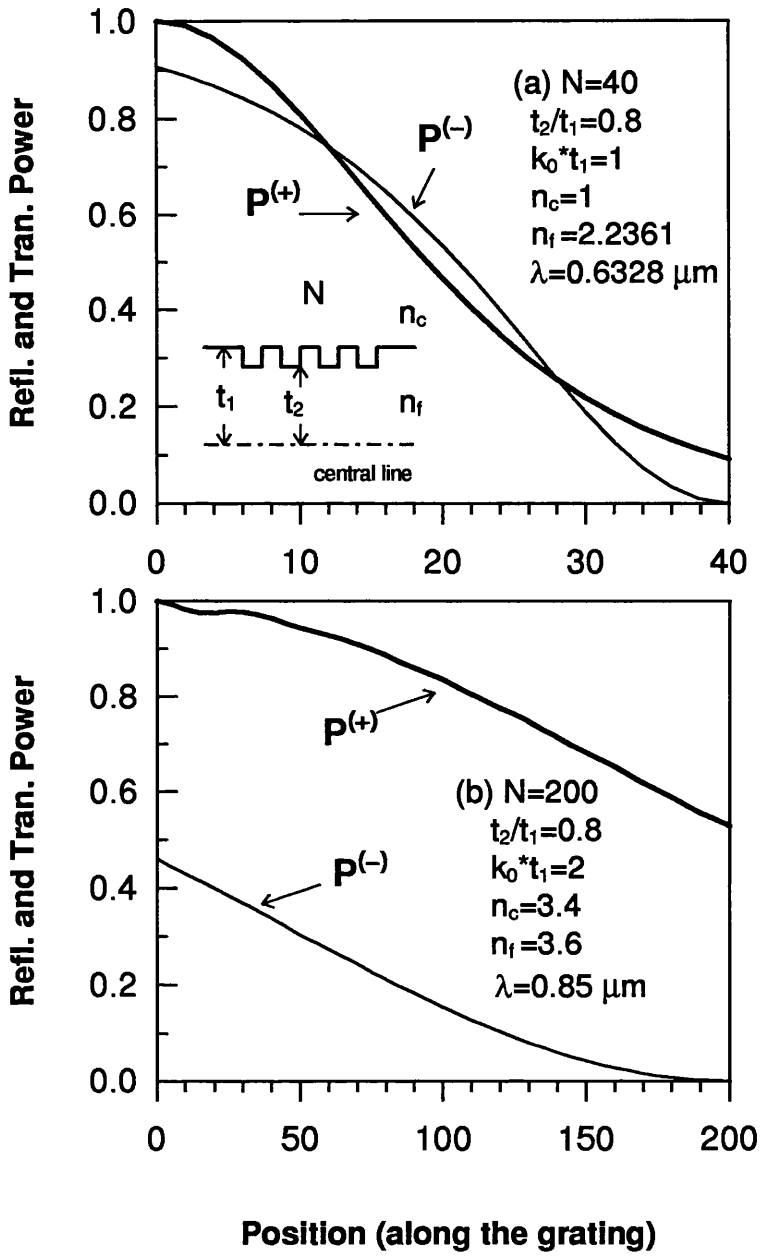

Fig. 38 *The reflected power $P^{(-)}$ and transmitted power $P^{(+)}$ as a function of the position along the grating, where the thick solid lines show the values of transmitted power and the thin solid lines show the values of reflected power for two first-order gratings.*

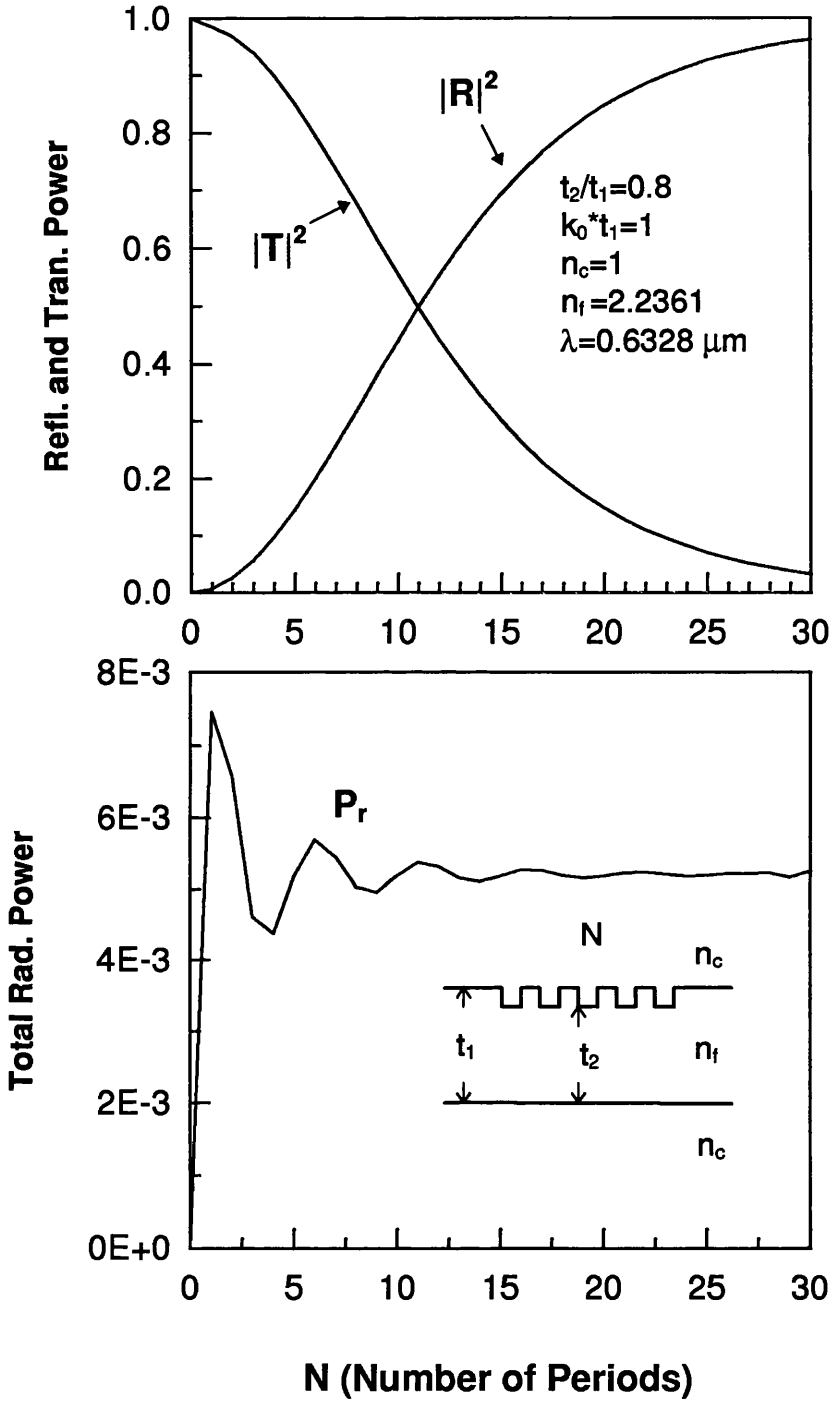

Fig. 39 *The reflected power $|R|^2$, transmitted power $|T|^2$ and the total radiation power P_r of the first order grating (shown in inset) for $t_2/t_1=0.8$ versus the number of periods N with m=40.*

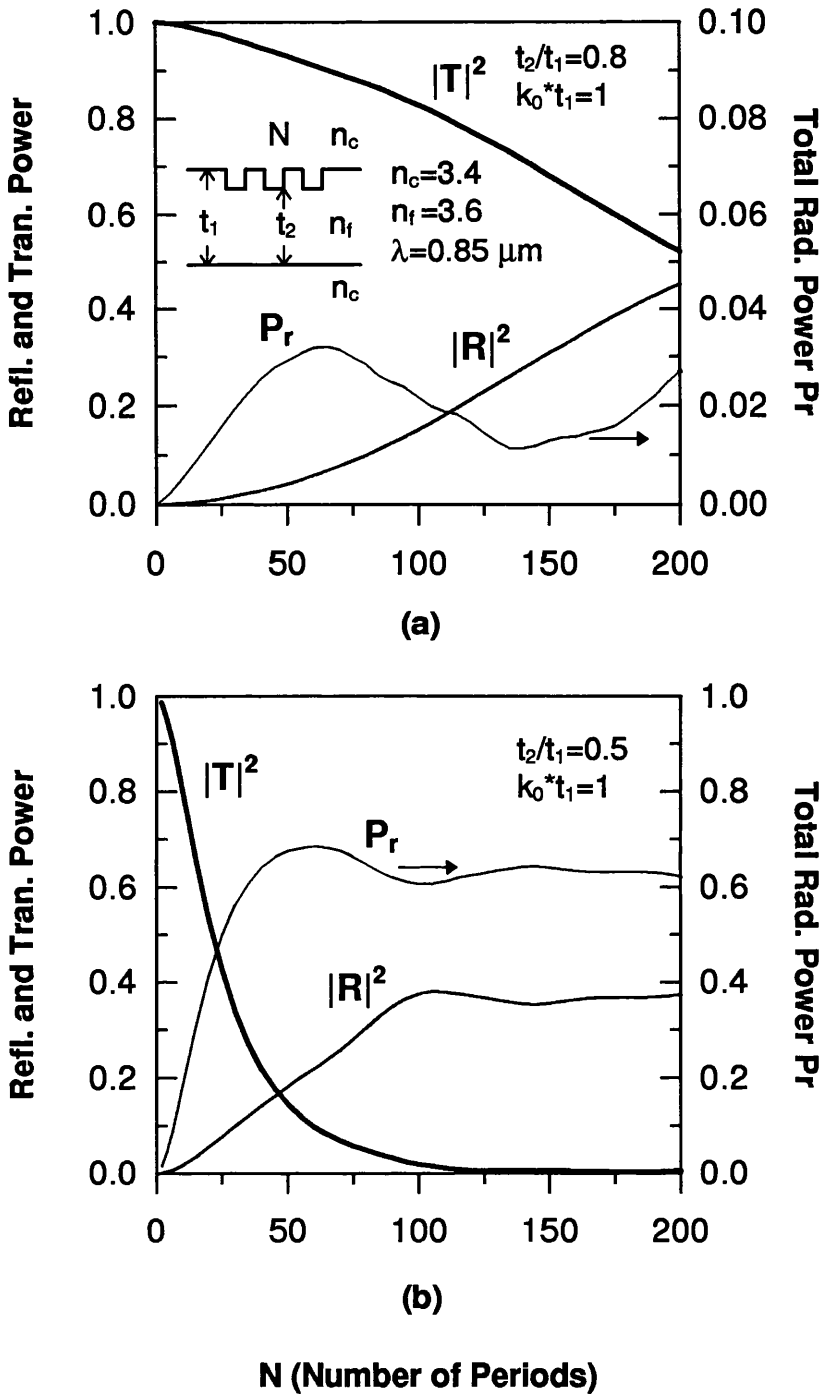

Fig. 40 *The reflected power $|R|^2$, transmitted power $|T|^2$ and the total radiation power P_r of the first order grating (shown in inset) for (a) $t_2/t_1=0.8$ and (b) $t_2/t_1=0.5$ versus the number of periods N with m=40.*

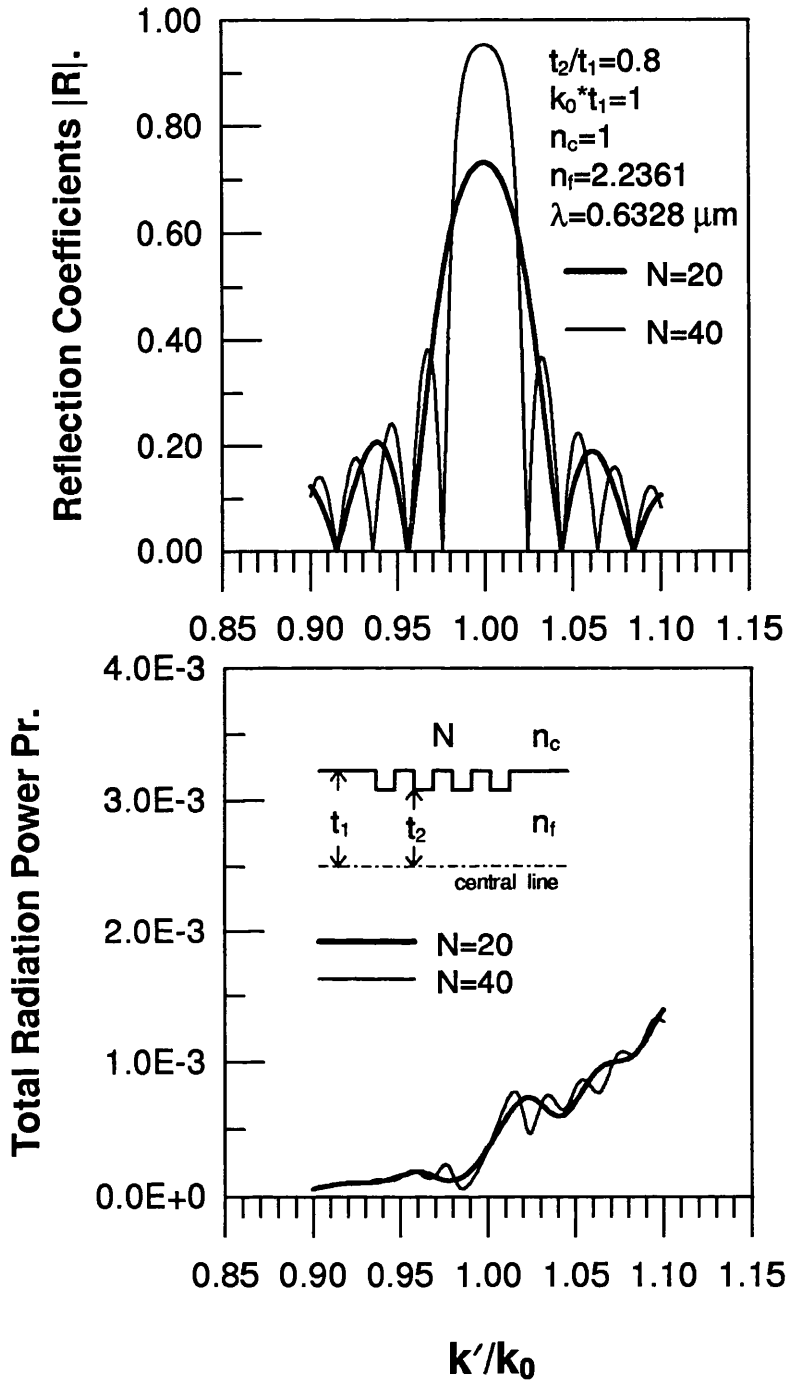

Fig. 41 *Reflection spectra and the total radiation power P_r of the first order grating (shown in inset) plotted as a function of the deviation (k'/k_0) from the Bragg condition with the number of grating periods of N=20 and N=40 .*

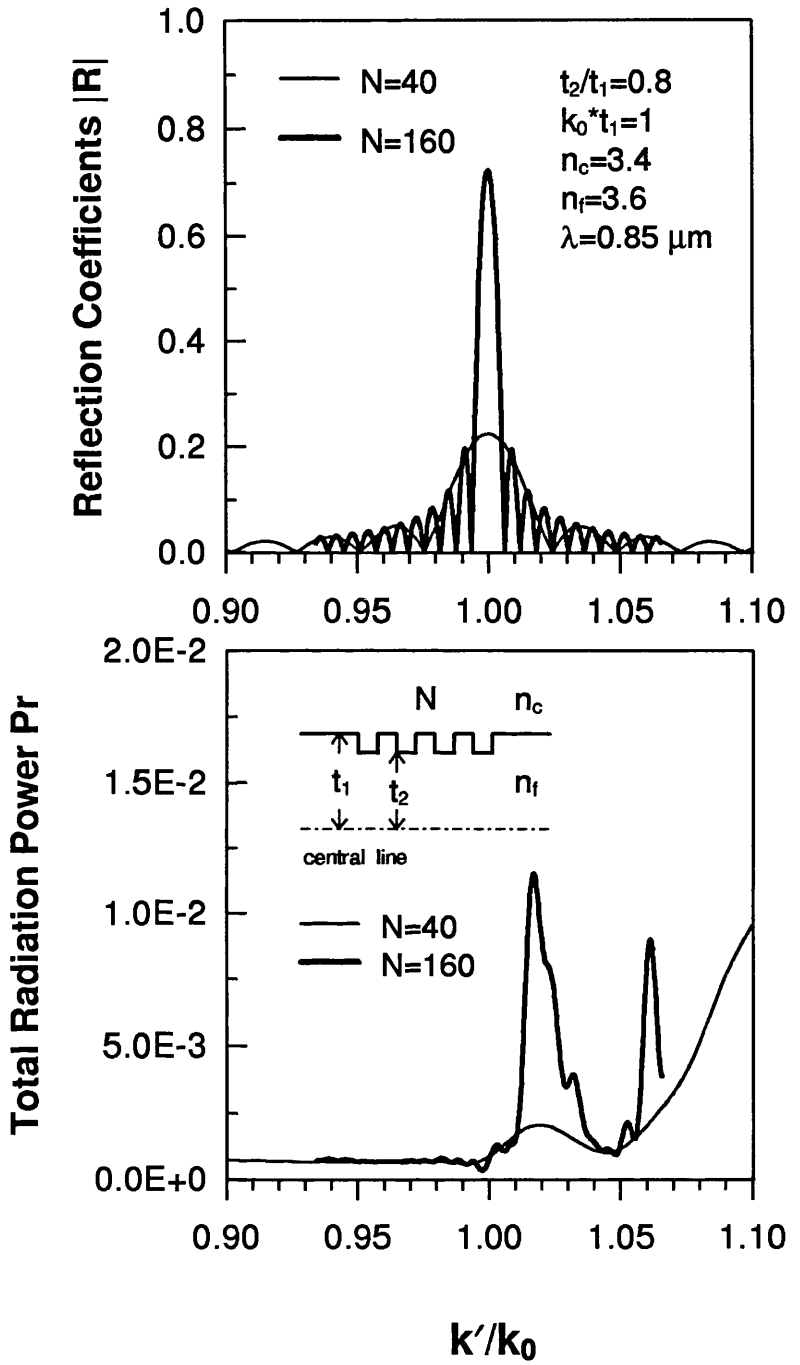

Fig. 42 *Reflection spectra and the total radiation power P_r of the first order grating (shown in inset) plotted as a function of the deviation (k'/k_0) from the Bragg wavenumber k_0 with N=40 and N=160 periods.*

with $t_2/t_1 = 0.8$ and $t_2/t_1 = 0.6$. Both the peak amplitude and the bandwidth of the centre main lobe increase as the groove depth increases. The centre stopband of the deeper grating has a very wide and flat frequency response, but the sidelobes of such a grating are also too significant to be ignored. Unlike the results from simple approximation methods, the spectra of $|R|$ are not completely symmetric over lower and higher frequency regions, because the radiation losses are different in both regions.

Fig. 44 and Fig. 45 show that the broadening of the centre bandwidth, the amplitudes of sidelobes, and the asymmetry appearing in the spectrum curves of such a grating on one side of the guide (shown in insets) is more significant than those of the cases in Fig. 40–Fig. 42. A grating with the corrugated structure on one side of the guide exhibits a stronger coupling effect and larger radiation loss than those of a grating on both sides of the guide.

5.3.3 Radiation Patterns

In this subsection we will calculate the far–field radiation patterns of gratings with different index profiles and grating orders under the phase–matching condition. Fig. 46 shows the radiation patterns of 1st, 2nd, and 3rd order gratings with the number of periods $N=40$. No radiation mode can satisfy the phase–matching condition in the case of the first–order grating and therefore the radiation pattern has similar profile to that of a single–step discontinuity but with considerable backward radiation losses caused by the reflected mode. Strong interference and significant radiation losses appear in the results of 2nd and 3rd order gratings. We have also plotted radiation patterns for the gratings with small index deviation as $n_c=3.4$ and $n_f=3.6$ (shown in Fig. 47), in which radiation modes at the peaks have maximal coupling coefficients as the phase–matching conditions are achieved. Also, many sublobes appear in the radiation patterns, as shown in Fig. 47, because these sublobes arise from the phase response of radiation modes.

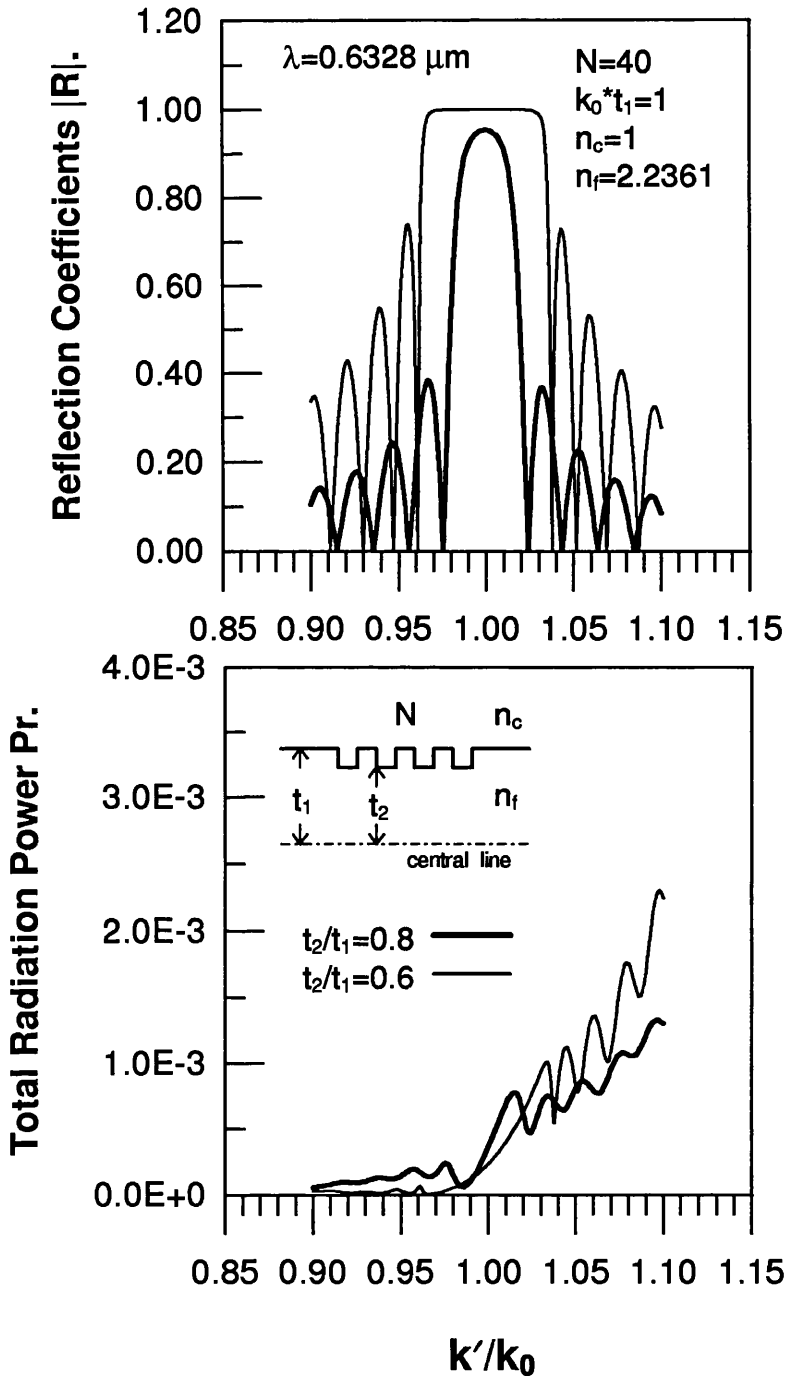

Fig. 43 *Calculated reflection spectra and total radiation power of the first order grating (shown in inset) with different grating depths of (a) $t_2/t_1=0.8$ as the thick solid lines and (b) $t_2/t_1=0.6$ as the thin solid lines.*

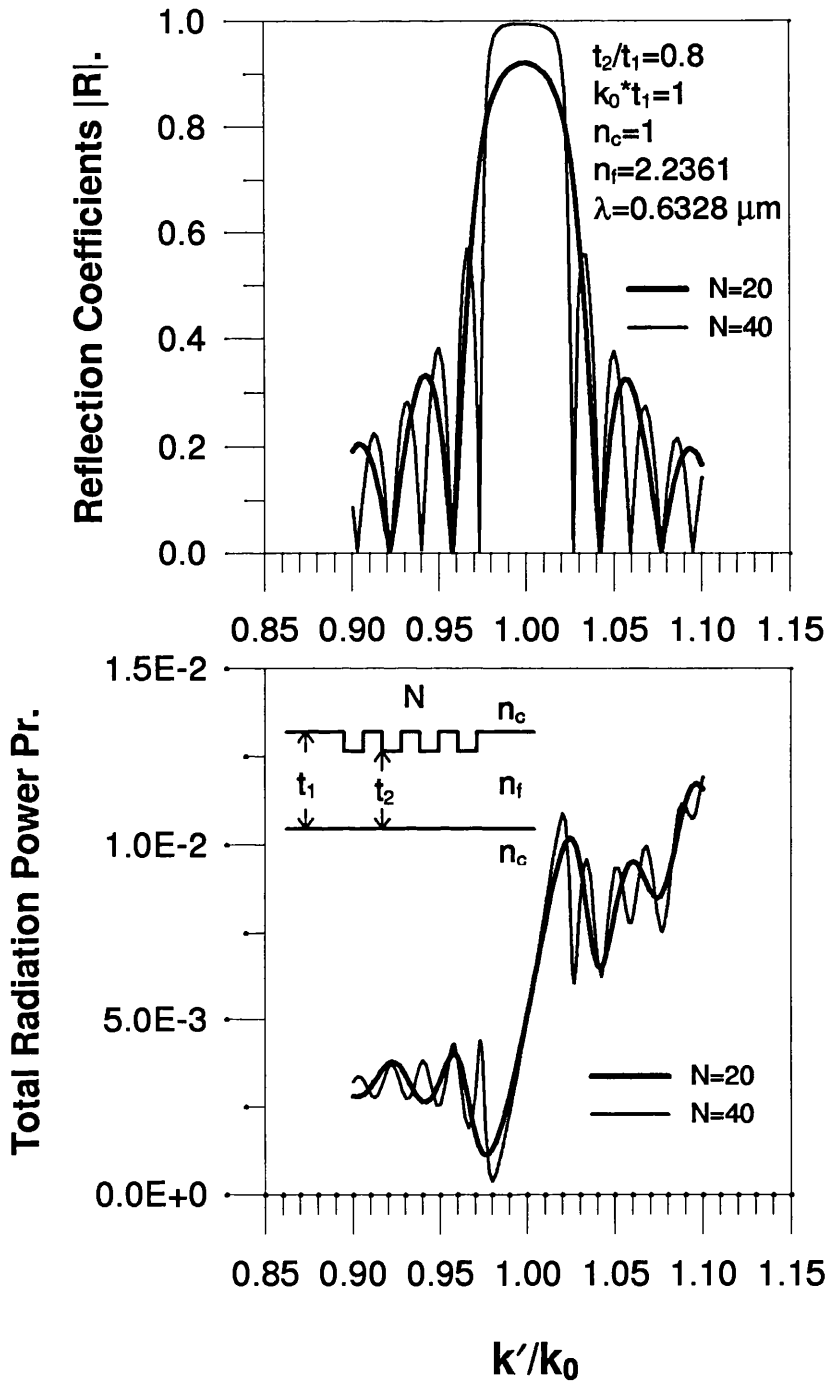

Fig. 44 *Reflection spectra and the total radiation power of the first order grating (shown in inset) versus the deviation of (k'/k_0) with N=20 and N=40 periods.*

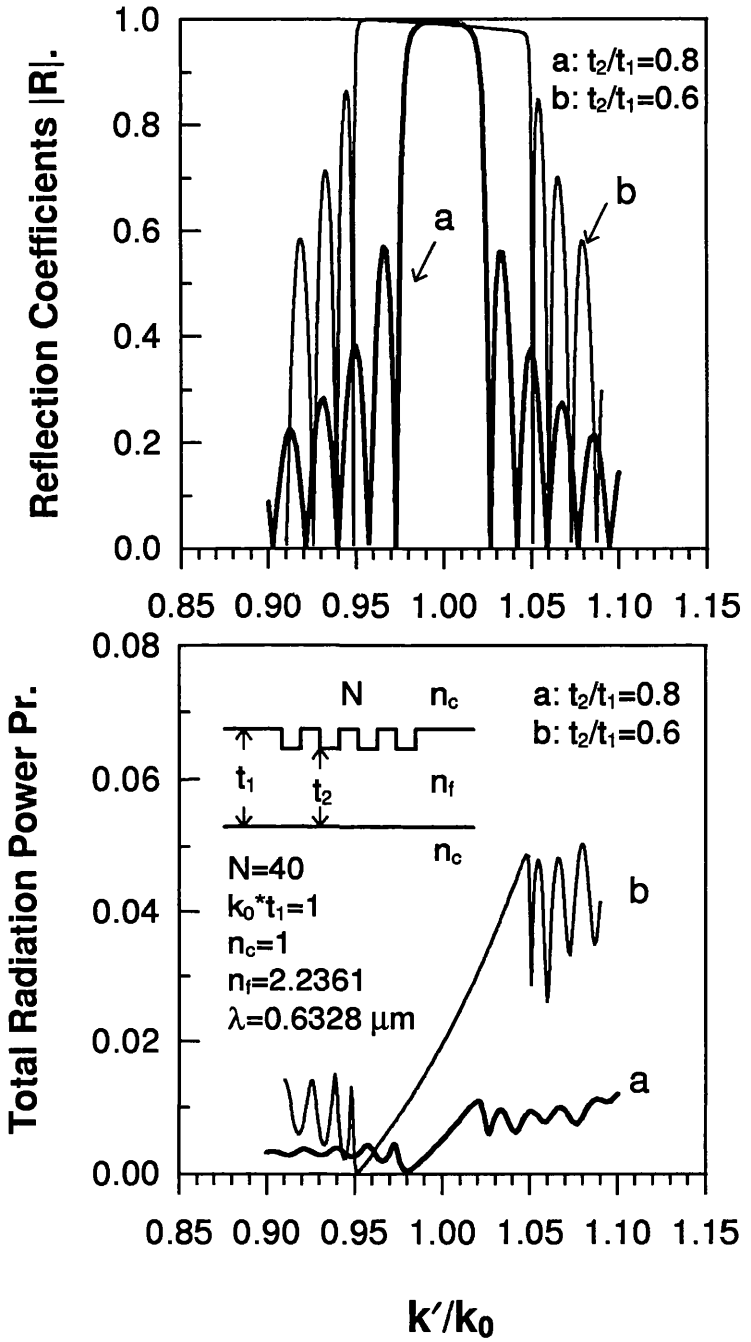

Fig. 45 *Calculated the reflection spectra and the total radiation power of the first order grating with the grating depths of t_2/t_1=0.8 (line a) and t_2/t_1=0.6 (line b).*

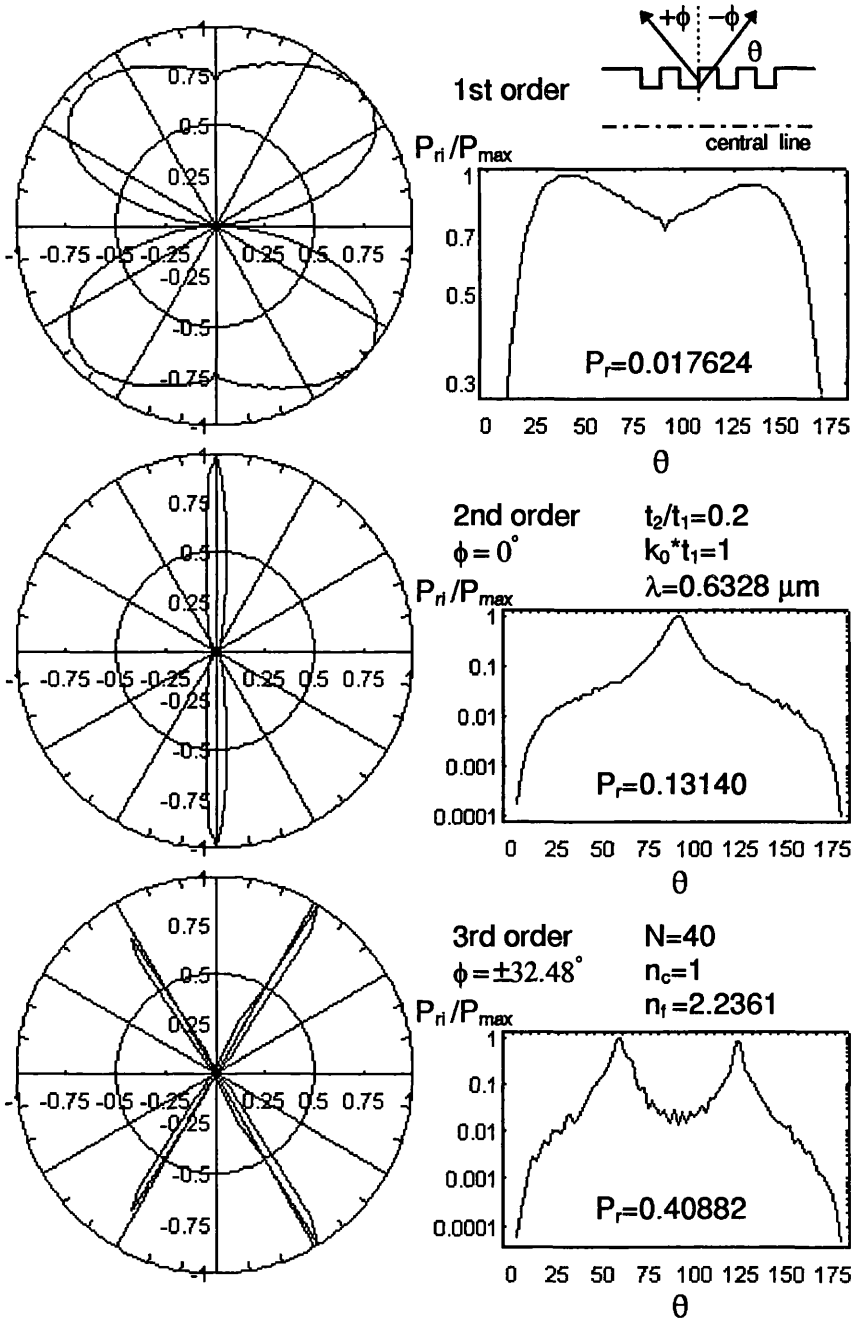

Fig. 46 *Normalised radiation patterns of the 1st, 2nd, and 3rd order waveguide gratings for the TE_0 mode incidence, where P_r is the total radiation power.*

Many sublobes appear in the range of large values of k_c. Fig. 47 also shows that the dominant radiation loss of the 3rd order grating going to the forward direction is caused by the transmitted guided mode because the reflection coefficient of such a grating only reaches $|R| = 0.42222$, far less than the transmission coefficient of $|T| = 0.81048$. But, the dominant radiation loss will change its direction as the power of the reflected guided mode is larger than that of the transmitted guided mode.

The radiation coupling angle ϕ of higher order gratings can be formulated with the help of Bragg conditions and a simple ray–optics approach. A schematic diagram of the radiation modes of a grating is shown in Fig. 48(b). The radiation modes are scattered by each corresponding step junction and reach the same point outside the guiding layer in phase, when the following phase–matching condition is satisfied

$$(\beta_\mu^{(1)} + \beta_\nu^{(2)})\frac{\Lambda}{2} + k_0 n_f b = p\pi \quad \text{with} \quad p = 2, 4, 6, \cdots \tag{99}$$

with $b = \Lambda \sin\phi'$. According to Snell's law $n_f \sin\phi' = n_c \sin\phi$, (99) can be written as

$$\phi = \sin^{-1} \frac{1}{k_0 n_c \Lambda}[\, p\pi - (\beta_\mu^{(1)} + \beta_\nu^{(2)})\frac{\Lambda}{2}\,] \tag{100}$$

where $\beta_\mu^{(1)}$ and $\beta_\nu^{(2)}$ are the propagation constants of the incident mode in the region 1 (rib) and 2 (groove) respectively. If the Bragg condition is also satisfied, the angle ϕ becomes

$$\phi = \sin^{-1} \frac{1}{k_0 n_c \Lambda}(p - l)\pi \tag{101}$$

where l is the grating order. Applying the above equation to the cases shown in Fig. 46 and 47, the results of the angle ϕ listed in the figures are matched fairly well with the radiation patterns obtained from our method. In Fig. 48(a) we have calculated the radiation angle ϕ versus the deviation of $\Delta k/k_0$ for two second–order gratings with the parameters listed in the inset.

Fig. 49(a) shows the angle ϕ versus the variation of the grating period $(\Lambda - \Lambda_0)k_0$, in which we can adjust the period Λ to steer the radiation coupling angle ϕ. Our results

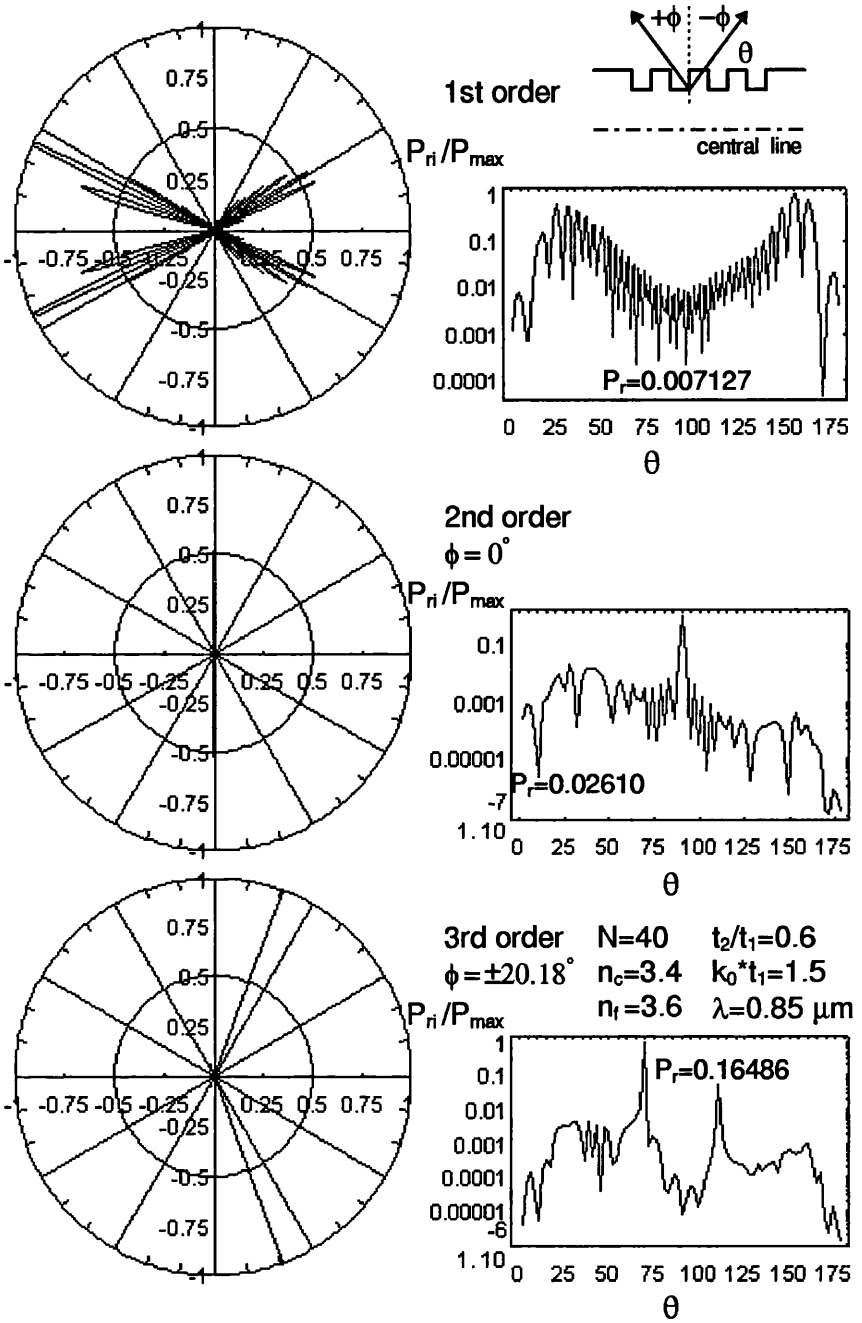

Fig. 47 *Normalised radiation patterns of the 1st, 2nd, and 3rd order waveguide gratings for the TE_0 mode incidence, where P_r is the total radiation power.*

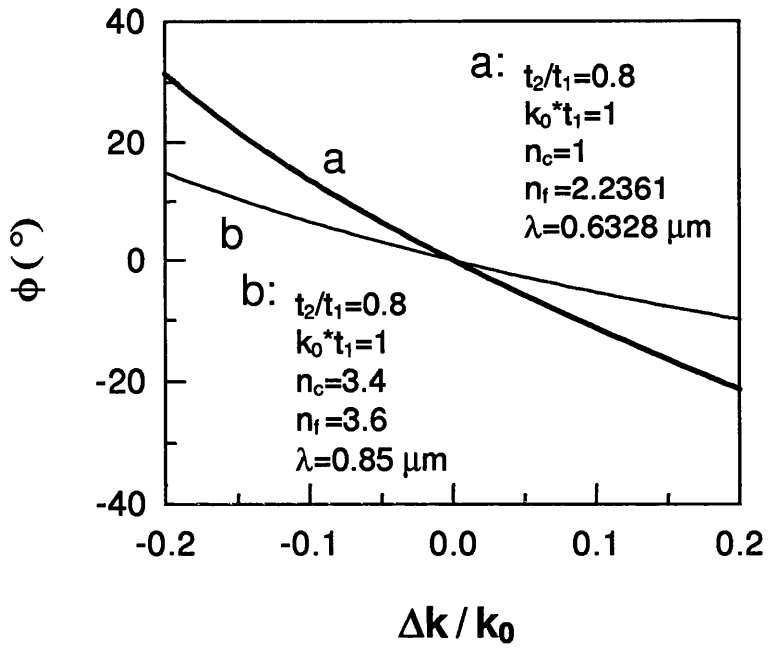

Fig. 48(a) *Radiation angles from the normal direction of the second order grating versus the values of $\Delta k/k_0$ with $\Delta k=k'-k_0$, where k' is the wavenumber of the incident mode and k_0 is Bragg wavenumber.*

Fig. 48(b) *Schematic diagram for the radiation angle ϕ.*

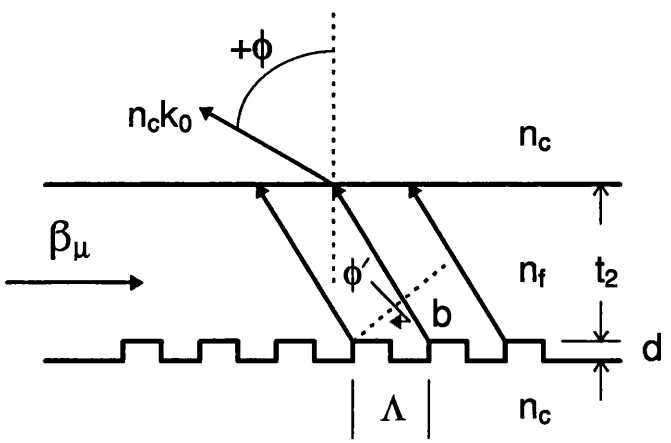

appear very good agreement with that of (99), as shown in Fig. 49(b), for the grating plotted in Fig. 48(b) and with the parameters listed in the inset (case b) to Fig. 49(a).

5.3.4 Coupling Coefficients

Recently, *Hardy* [127][128] proposed a method modified from coupled–mode theory for the analysis of corrugated waveguides, in which he introduced the parameters of wavelength deviation from the Bragg condition and modelled field absorption losses in his calculation, but in essence this method is still based on the coupled–mode theory and only considered two guided modes in the mode–matching procedure. *Winick* [129] used effective–index method theory for almost–periodic waveguide gratings, neglecting radiation modes in the matrix–based technique; however, its results are equivalent to coupled–mode methods for the TE polarization. *Frolik* [130] presented an asymmetric discrete–time approach for the analysis of periodic waveguide gratings, in which a digital signal processing (DSP) theory was used in the numerical algorithm for the purpose of faster computation speed and grating design. Nevertheless, only two guided modes were considered in this method which had similar results to those of the effective–index method [129].

We will compare our results with those obtained by the coupled–mode method in this subsection. Although the coupled–mode theory is older and quite approximate, this method has been applied more widely than others. One of its results is derived by *Yariv* et al. [3], in which the coupling coefficient κ is given by

$$\kappa = \frac{2\pi^2 s^2}{3l\lambda}\frac{(n_2^2 - n_1^2)}{n_2}\left(\frac{a}{t}\right)^3\left[1 + \frac{3}{2\pi}\frac{\lambda/a}{(n_2^2 - n_1^2)^{1/2}} + \frac{3}{4\pi^2}\frac{(\lambda/a)^2}{(n_2^2 - n_1^2)}\right] \tag{102}$$

where all parameters in the above equation are defined in the original paper. An

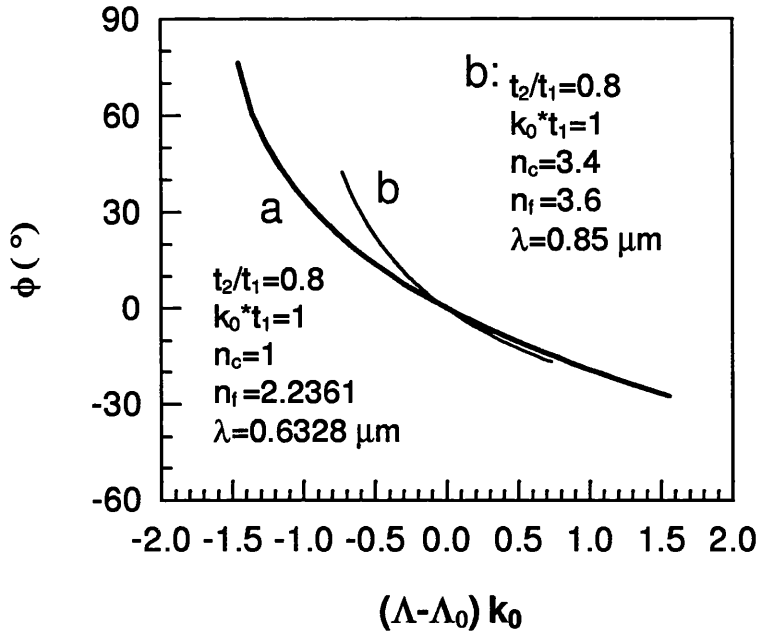

Fig. 49(a) *Radiation angles from the normal direction of the grating versus the deviation of grating period, where Λ_0 is second order period.*

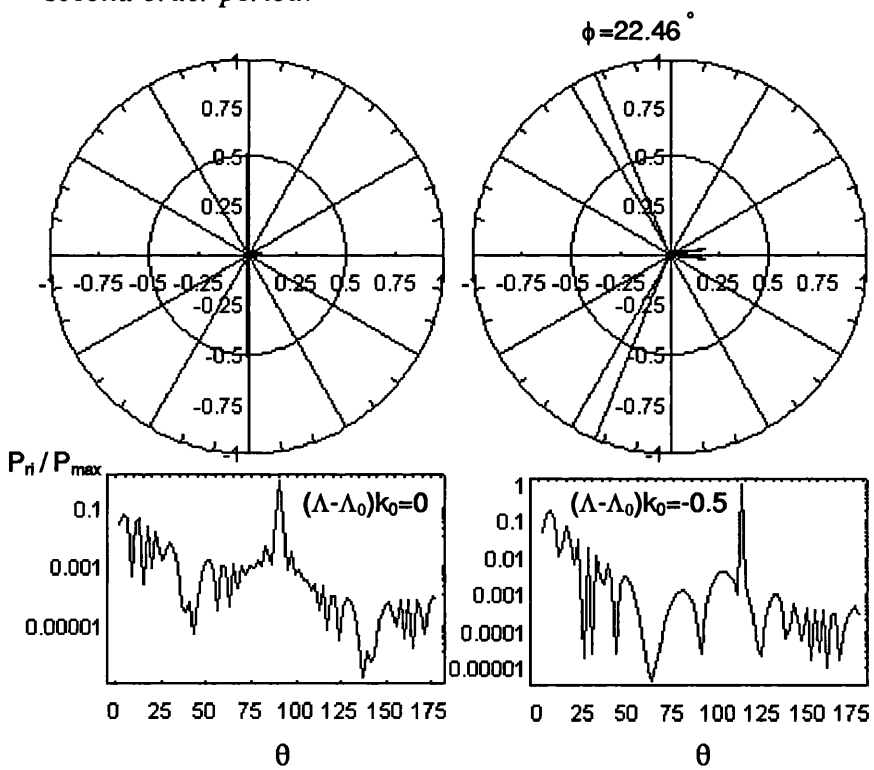

Fig. 49(b) *Radiation patterns of two gratings with $(\Lambda-\Lambda_o)k_0=0$ and $(\Lambda-\Lambda_o)k_0=-0.5$, where Λ_0 is second order period. ($n_c=3.4$, $n_f=3.6$) with $N=40$ and $m=40$.*

alternative to (102) is derived by *Streifer* et al. [6] as

$$\kappa = \frac{k_0^2(n_1^2 - n_2^2)}{4\pi\beta m N^2} \sin(\frac{\pi m w}{\Lambda}) \left\{ g_2 + \frac{\sin(2g_2h)}{2h} + \frac{q}{h^2}[1 - \cos(2g_2h)] + \frac{q^2}{h^2}\left[g_2 - \frac{\sin(2g_2h)}{2h}\right] + \frac{1}{q}[1 - \exp(-2qg_1)] \right\} \tag{103}$$

with $g_1 = wg/\Lambda$ and $g_2 = (1 - w/\Lambda)g$. Both equations (102) and (103) are for rectangular gratings but with different index periodicity for the perturbation calculation. *Streifer* et al. [6] calculated the coupling coefficient by judiciously choosing the unperturbed guide boundary to avoid leading to inaccurate excessively high coupling coefficients. In order to compare easily with those results from (102) and (103), the following definition of the coupling coefficients $|\kappa|$ from the coupled–mode theory is also applied to our results,

$$|\kappa| = \frac{1}{|\mathrm{a}_\mu^{t+}(z)|} \left| \frac{d\mathrm{a}_\mu^{r-}(z)}{dz} \right| \tag{104}$$

where $\mathrm{a}_\mu^{r-}(z)$ is the complex amplitude of the reflected guided mode and $\mathrm{a}_\mu^{t+}(z)$ is the complex amplitude of the transmitted guided mode at the position z along the grating. The increment of a_μ^{r-} and the value of a_μ^{t+} can be obtained from our method, and the results are shown in Fig. 50(a) and 50(b) for first–order gratings. In Fig. 50(a) the coupling coefficient calculated from our results shows good agreement with that of (103) for the grating with small index deviation ($n_f = 3.6$ and $n_c = 3.4$) and small groove depth of $t_2/t_1 = 0.9$, but a discrepancy appears in the case with $t_2/t_1 = 0.8$. Fig. 50(b) illustrates that the coupling coefficient $|\kappa|$ decreases as z (as well as N) increases along the grating for the grating with large index difference between the guiding layer and the exterior medium. The curve of $|\kappa|$ exhibits obvious oscillation as the number of periods reaches $N \geq 30$ for the grating with $t_2/t_1 = 0.8$, as shown in Fig. 50(b), and the reflection coefficient $|R|$ is saturated in the region. In coupled–mode theory, the value of coupling–coefficient–length product κL is a very important parameter which gives the relative amount of power coupled between two modes per unit length, but in our results the value of κ is no longer constant in the deep grating. We note that the

simple coupled–mode theory could produce erroneous results if it is applied to treat the grating with large groove depth. Fig. 51 shows that the coupling coefficients of our results are consistent with those from *Streifer* [6] over wide ranges of $k_0 t_1$ and n_c for a grating with very small relative groove depth such as $t_2/t_1 = 0.99$.

5.4 CONCLUSION

The method we proposed has been applied to double–step discontinuities and gratings in this chapter. These include single rib and groove structures, a staircase structure, and periodic gratings with various groove depths and refractive index profiles. The results show that the spectra of reflection coefficients and the total radiation power as well as the phase responses of guided and radiation modes arise from a series of discontinuities of these structures with respect to the phase–matching condition. We have also compared our results with those from other methods, and good agreements have been found between our results and others for double–step discontinuities, and for periodic gratings with small groove depths. But, the disagreement between the results of simple coupled–mode theory and ours becomes significant as the groove depth increases. For deep gratings, the reflection coefficient reaches saturation and the transmission coefficient approaches zero just propagating through a small number of grating periods, in which the coupling coefficient is a function of the position along the grating. Simple approximation methods are no longer valid in the analysis because the depth of these gratings is too large.

We also demonstrate the radiation modes of higher order gratings under phase–matching condition. It is shown that we can steer the radiation coupling angle by properly adjusting the grating period. A wide tuning range of the radiation coupling angle is presented.

Besides, we have investigated periodic gratings in an asymmetric planar waveguide with $n_c \neq n_s$, and results show that the phase–matching condition (98) of the reflected

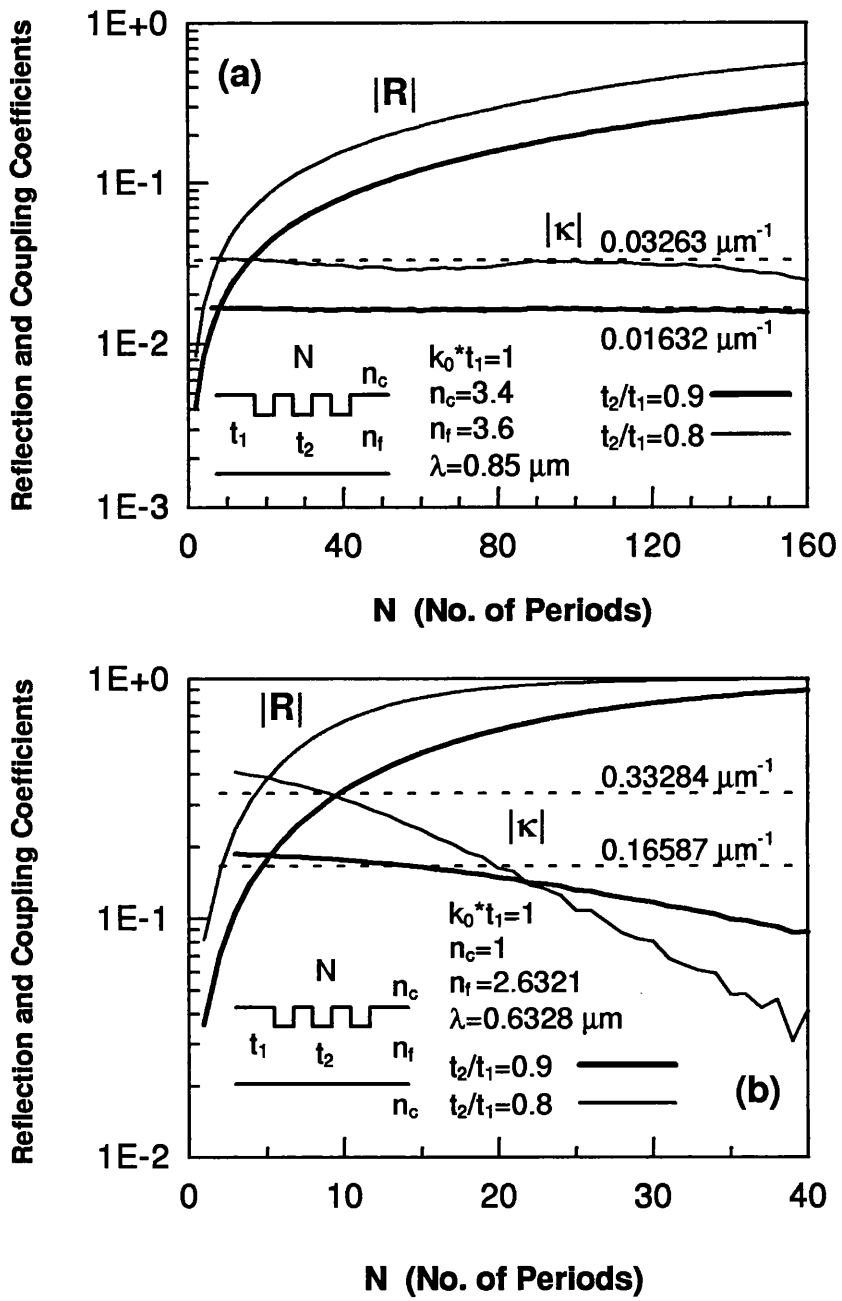

Fig. 50 *Reflection coefficients* |R| *and coupling coefficients* |κ|(μm^{-1}) *versus the number of periods N for the first order gratings with (a)* n_c=3.4, n_f=3.6, *(b)* n_c=1, n_f=2.2361. *The dotted lines with the values of* |κ| *are calculated from Streifer* [6].

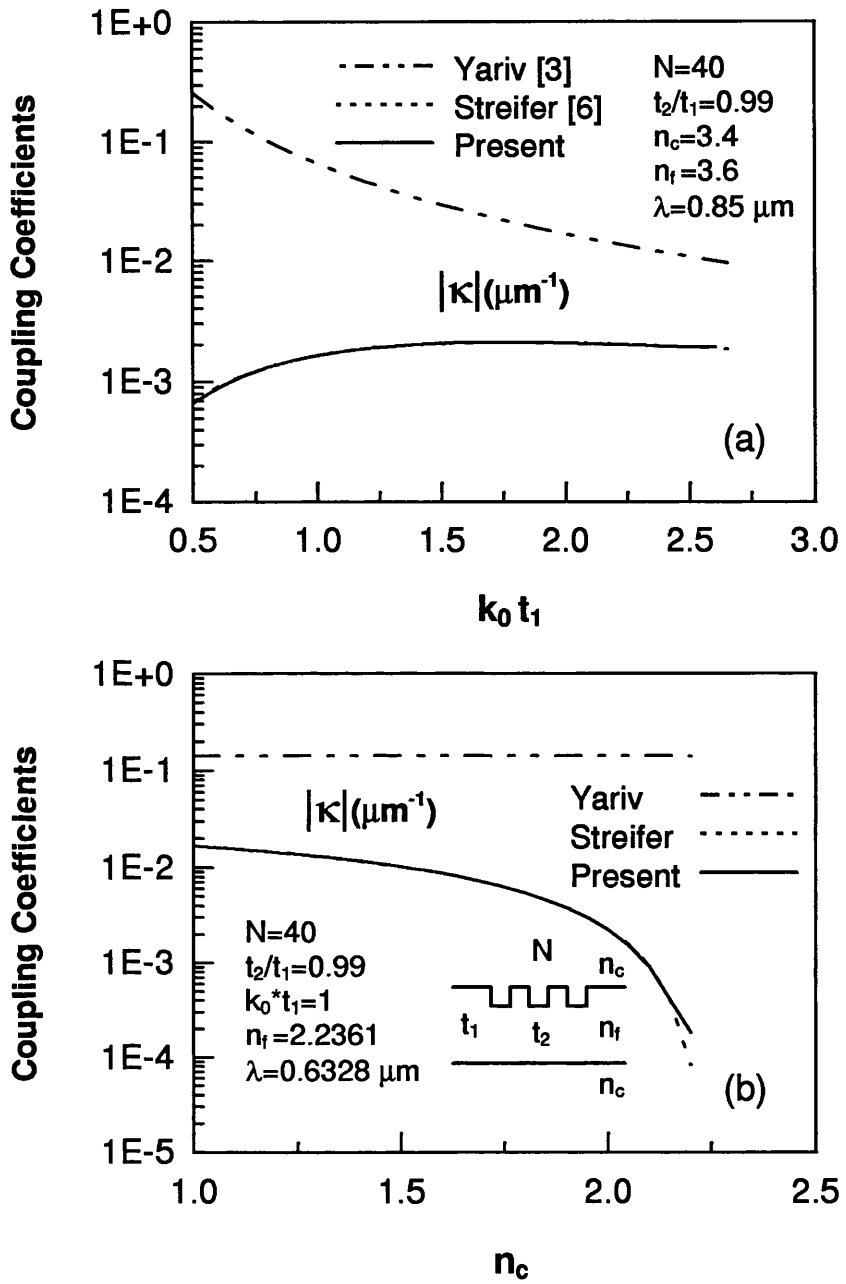

Fig. 51 *(a) Coupling coefficients* $|\kappa|(\mu m^{-1})$ *versus the thickness of the guiding layer* $k_0 t_1$ *for the first order grating. (b) Coupling coefficients* $|\kappa|(\mu m^{-1})$ *versus the refractive index of the cover region* (n_s=n_c) *for the first order grating with parameters listed in inset.*

guided mode was changed as the groove depth was not small enough. The effect of loss on the phase–matching condition is due to a large amount of radiation loss arising from this structure. The major part of the radiation losses are going to the substrate region. In our analysis, both types of radiation modes (substrate and cover–substrate radiation modes) of open dielectric waveguides have continuous spectra and are treated by similar procedures. However, for practical waveguides the thickness of the substrate region is finite or a metallic layer is coated on the substrate surface. Thus, the substrate modes are discrete and the total number is finite in these structures, and only air radiation modes have to be considered in the analysis. An extension of the application of our method for multiple–layer waveguides is suitable to handle these problems.

6

CHAPTER 6

THEORETICAL APPROACH FOR APERIODIC GRATINGS

6.1 INTRODUCTION

Recently, single and multiple phase shifts have been added to grating structures in order to change the spectra of reflection coefficients for special purposes. These include the performance improvement of DFB and DBR lasers and the realisation of broad–range wavelength tuning of optical filters. It is known that $\lambda/4$ shifted DFB LDs have the particular advantages of large gain difference between the main mode and the submodes as well as stable single longitudinal mode operation at high output power, but spatial hole burning in such lasers due to the nonuniform mode intensity distribution along the laser structure will deteriorate the mode properties. Fortunately the light intensity at the $\lambda/4$ phase–shifted region can be reduced by using multiple phase–shifted structures or corrugation–pitch–modulated (CPM) gratings [82]–[84]. Such devices can be thought of as two or multiple periodic gratings in series or as a gradual variation of the grating period.

Several theoretical analyses of the mode behaviours for these devices have been proposed. *Kogelnik* [118] used a Riccati differential equation in the numerical calculation for tapered and chirped gratings, *Kim and Fonstad* [131] proposed an analysis technique based on coupled–mode theory to calculate the reflection spectrum of sinusoidal gratings

with a phase shift in the structure, *Björk and Nilsson* [76] as well as *Yamada and Sakuda* [116] used a matrix approach for the analysis of asymmetric phase–shifted gratings, *Winick* [129] introduced an effective–index/impedance–matching method for almost–periodic waveguide gratings, and *Radic* at al. [132] extended the application of the transfer matrix method for nonuniform nonlinear distributed feedback structures. A very important factor of κL had been used in the above methods, and only two guided modes (reflected and transmitted) were considered in those analyses. However, when the groove depth is deeper, our results show that the value of the coupling coefficient κ is no longer a constant and the radiation modes become too significant to be ignored in the calculation. For such deep gratings, too simple an approximation will result in serious errors.

In this chapter, the method we proposed will be applied to treat single and multiple phase–shifted gratings and linearly chirped gratings operating near the first–order Bragg wavenumber. Because modes coupled by step discontinuities and the phase delays caused by modes propagating in the grating are calculated by the mode–matching procedure and the transfer matrix approach respectively, the total transfer matrix in our method may be rearranged easily for the analysis of non–uniform and aperiodic gratings as the grating structures are adjusted for special purposes.

6.2 $\lambda/4$ AND $\lambda/8$ PHASE–SHIFTED GRATINGS

Consider an extra segment of planar waveguide placed between two periodic gratings (shown in the inset to Fig. 52), all of the modes propagated through this segment have experienced different phase delays of $\exp(\mp j\beta_{\nu_i}\Delta)$, where β_{ν_i} is the propagation constant of the mode ν_i and Δ is the length of the extra segment along the z-axis. A positive Δ indicates both periodic gratings shifted apart by a small length and a negative Δ is for shifting towards each other. Therefore, the total transfer matrix equation can be arranged by inserting the propagation matrix $[T^{ph}]$ defined by (35)

into (39), then we have

$$[A^1] = [M]^{N_1}[T^{ph}]^{-1}[M]^{N_2}[A^o] \quad \text{with} \quad N = N_1 + N_2 \tag{105}$$

where N_1 and N_2 are the number of periods of periodic gratings connected by the extra segment waveguide, and N is the total number of periods. A similar procedure can also be applied to more complicated multiple phase–shifted gratings. Since the mode propagating in the groove region and in the rib region of the grating structure have different propagation constants, the small length Δ has to be calculated precisely in order to keep an accurate phase shift in the analysis.

In Fig. 52 we introduce a $\lambda/8$ phase shift in the rib region between two similar periodic gratings , in which the transmitted guided mode has experienced a $\pi/4$ phase delay when it passes through the extra segment waveguide and a $\pi/2$ phase shift is for the reflected guided mode as it is reflected back to its origin. The results show that a passband appears in the centre stopband and the position of the passband depends on the way we shift the gratings. The total radiation power is a function of the wavenumber of the incident mode, and a small peak appears in the centre stopband region with respect to the position of the passband. For single and multiple phase–shifted gratings, the radiation angle has been subdivided into 40 equally spaced panels for Simpson's rule.

Similar phenomena appear in Fig. 53 for the gratings on one side of guiding layer with a $\lambda/8$ phase shift located in the middle of gratings (shown in the inset). It is shown that a very significant radiation loss caused by the transmitted guided mode appears at the passband position within the lower frequency part of the centre stopband.

In Fig. 54 and Fig. 55 we compare the spectra of reflection coefficients and total radiation power of both a $\lambda/4$ (π) and a $\lambda/8$ ($\pi/2$) phase–shifted grating on slab waveguides (shown in the insets to these figures), in which the movement of the passband in the centre stopband depends on the degree of the phase shift. We have, in further studies, shown that the centre passband width of the $\lambda/4$ phase–shifted grating becomes

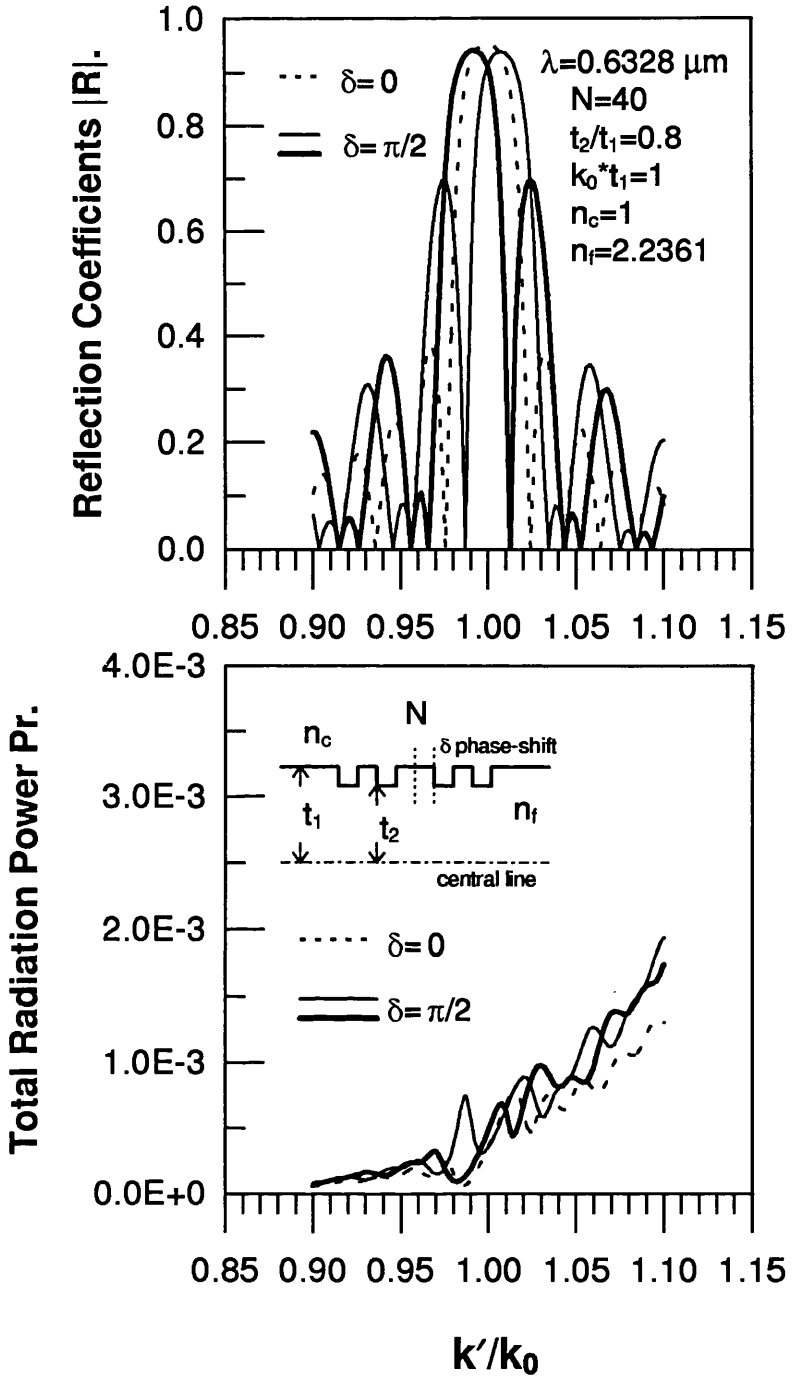

Fig. 52 *Characteristics of the reflection spectra and total radiation power of a periodic grating (dotted line) and a π/2 phase-shift between two periodic gratings (solid lines) by shifting both gratings towards each other (thin solid line) and shifting apart by (thick solid line) a small length.*

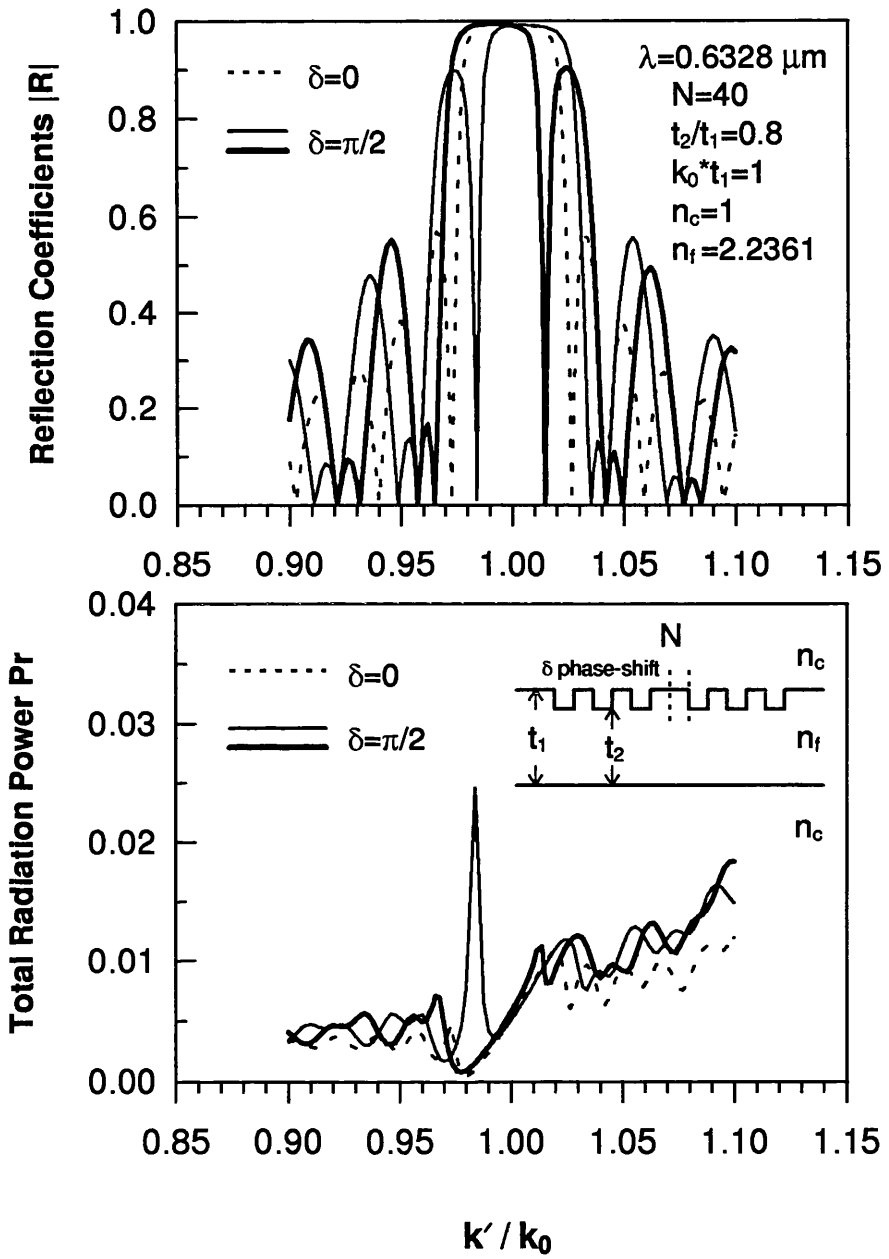

Fig. 53 *Characteristics of the reflection spectra and total radiation power of a periodic grating (dotted line) and a π/2 phase-shift between two periodic gratings (solid lines) by shifting both gratings towards each other (thin solid line) and shifting apart by (thick solid line) a small length.*

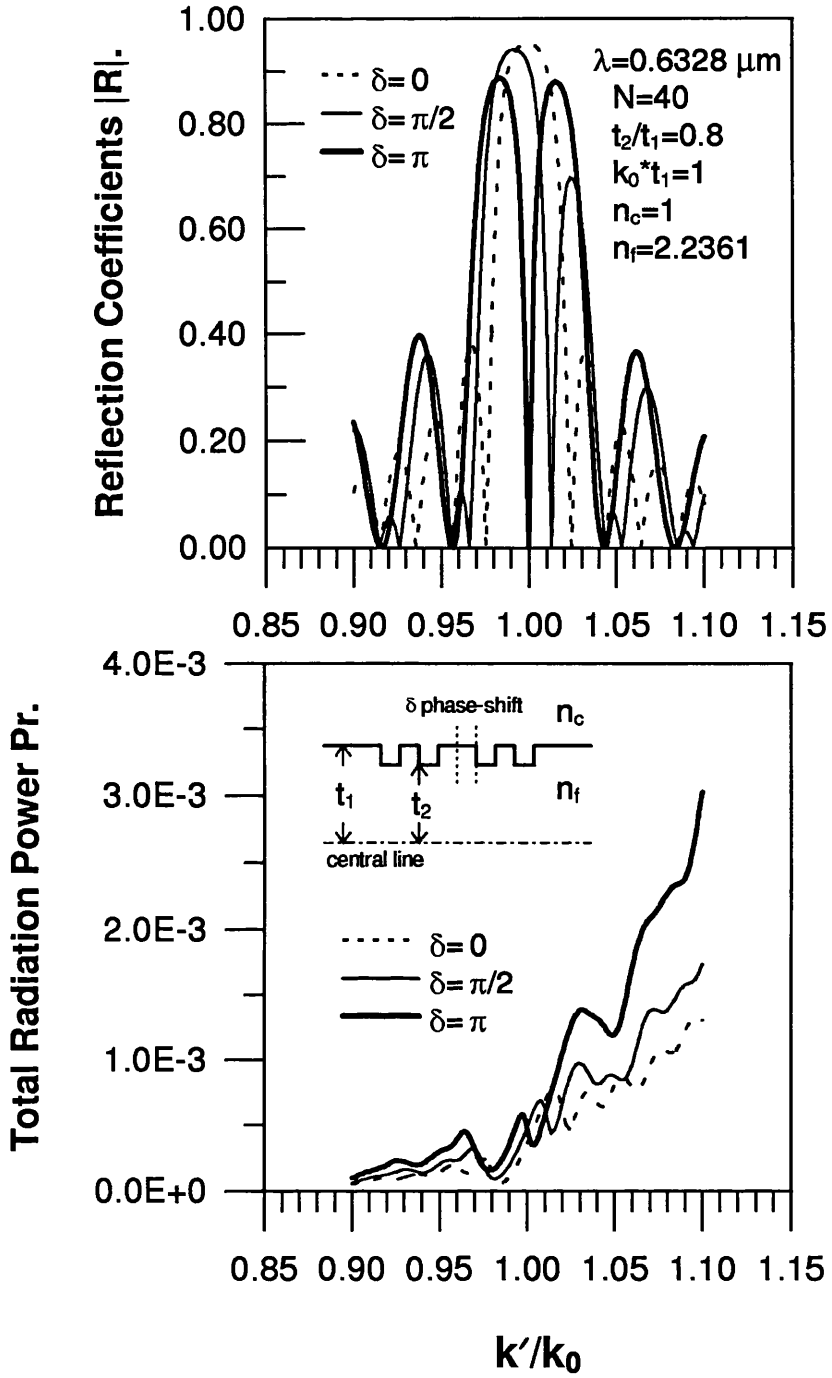

Fig. 54 *Characteristics of the reflection spectra and total radiation power of a periodic grating (dotted line), a π/2 phase-shifted grating (thin solid lines) and a π phase-shifted grating (thick solid line) by inserting an extra length in the rib region.*

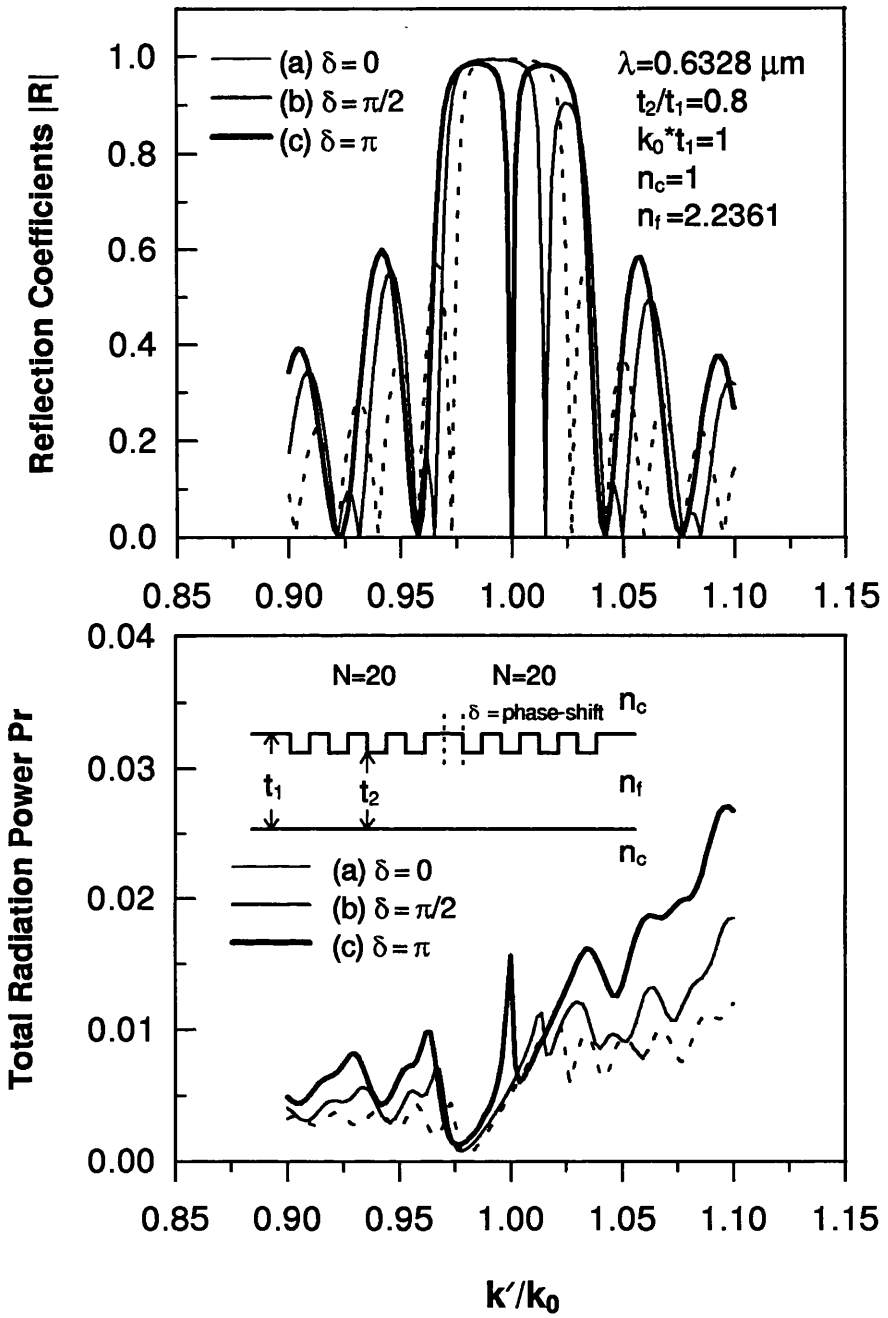

Fig. 55 *Characteristics of the reflection spectra and total radiation power of the grating such as (a) a periodic structure, (b) a π/2 phase-shifted grating, and (c) a π phase-shifted grating with the extra segment in the centre of the grating.*

narrower as the groove depth increases.

Fig. 56 shows the calculated reflection spectra of two $\lambda/4$ phase–shifted gratings with different phase–shifted dispositions (as asymmetric $\lambda/4$ phase–shifted gratings) and the comparison with the results of a symmetric $\lambda/4$ phase–shifted grating. The reflection coefficient at the passband is no longer equal to zero but depends on the relative position of the phase shift. It has been seen that the external differential quantum efficiency can be improved without seriously decreasing the single longitudinal mode yield in such asymmetric $\lambda/4$ phase–shifted DFB lasers [117].

6.3 MULTIPLE PHASE–SHIFTED GRATINGS

Fig. 57(a) shows the schematic diagram of two phase shifts in a grating, in which the grating has three regions separated by two phase shifts with the number of periods of N_1, N_2, and N_3 respectively. We have plotted the reflection spectra for such a structure consisting of two $\lambda/8$–phase–shifts in a grating with different dispositions as shown in Fig. 57(b), and have compared these results with that of a single $\lambda/8$ phase–shifted grating. The sidelobes of the curves appear different as the locations of phase–shifted regions are changed.

Fig. 58 shows the spectra of reflection coefficients and the total radiation power of three corrugation–pitch–modulated gratings with an effective $\lambda/4$ phase shift in the centre phase arranging region (shown in the inset to Fig. 58).

For the sake of geometric symmetry, the length of extra segment of $\lambda/4$ phase shift in such gratings has been subdivided into $(N_2 + 1)$ equally spaced panels and inserted into (N_2+1) grooves of the centre phase arranging region. We note that one of the main lobes of such CPM gratings is suppressed considerably as the number of periods N_2 of the phase arranging region increases. Also, CPM gratings have lower radiation losses than that of a single $\lambda/4$ phase–shifted grating in the higher frequency region. Although the multiple phase–shifted structures are used in DFB lasers in order to reduce the light

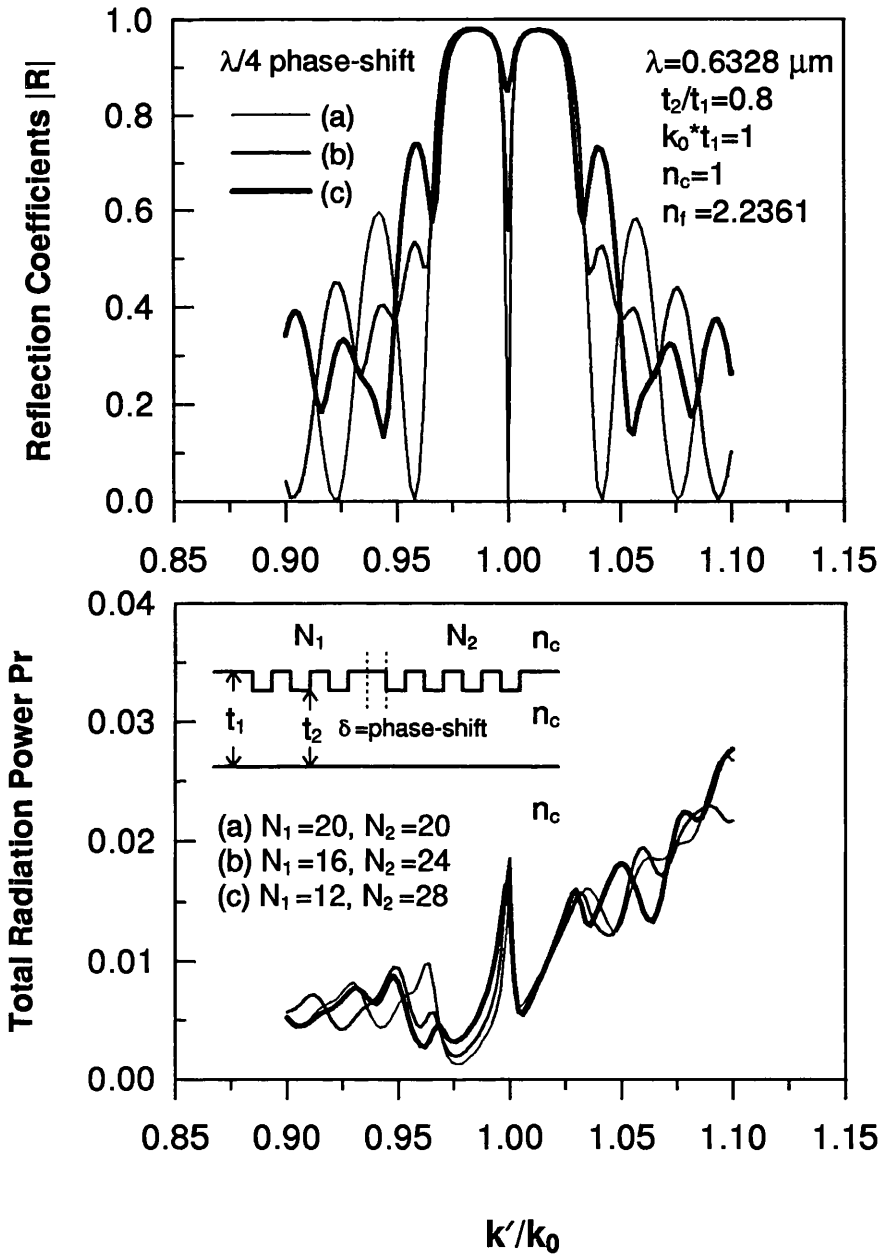

Fig. 56 *Reflection spectra and the total radiation power of three gratings with a λ/4 phase-shift (δ =π) at different locations (shown in inset).*

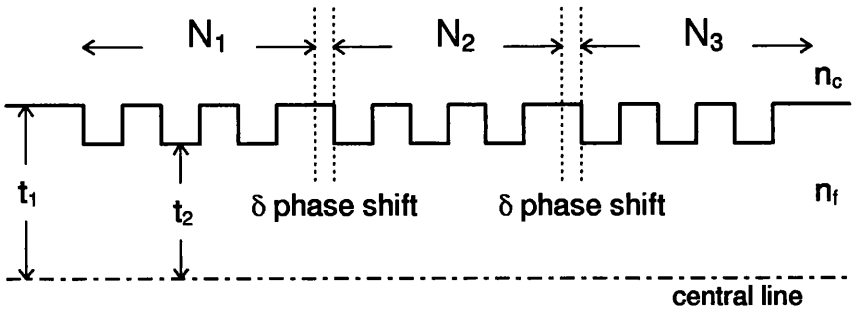

Fig. 57(a) *Schematic diagram for a multiple phase-shifted grating. The dash-dotted line is the central line of the waveguide.*

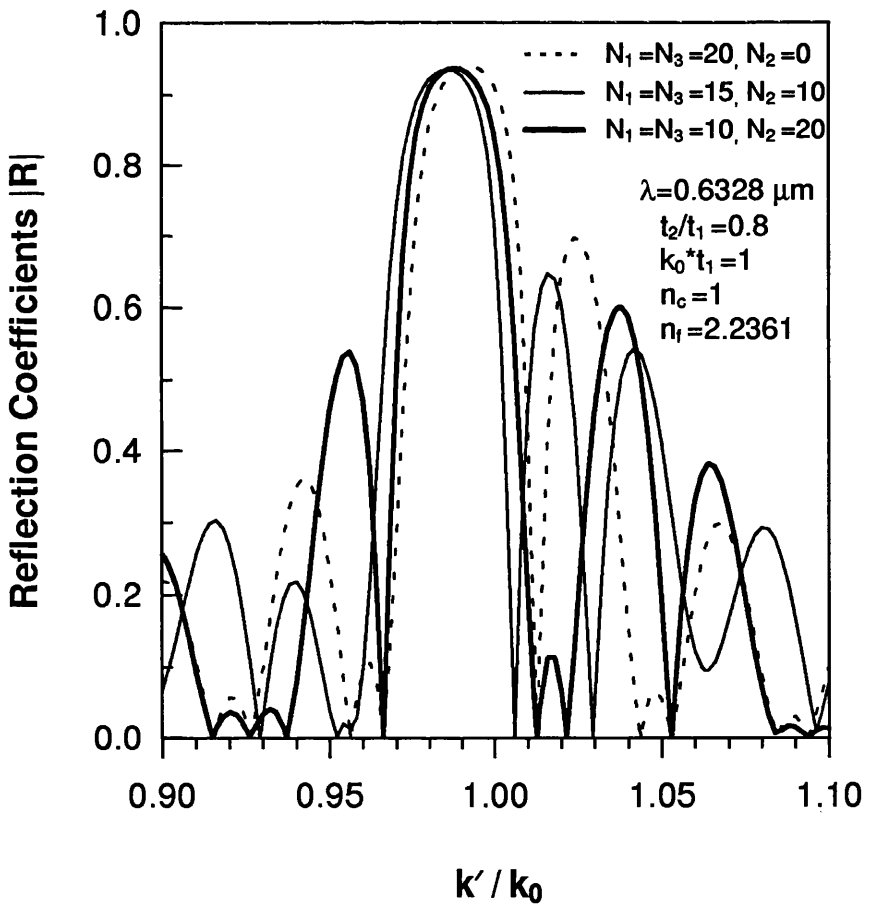

Fig. 57(b) *Characteristics of the reflection spectra of two two-λ/8 phase-shifted gratings with different dispositions (solid lines) and comparing with the results of a single λ/8 phase-shifted grating (dotted line)*

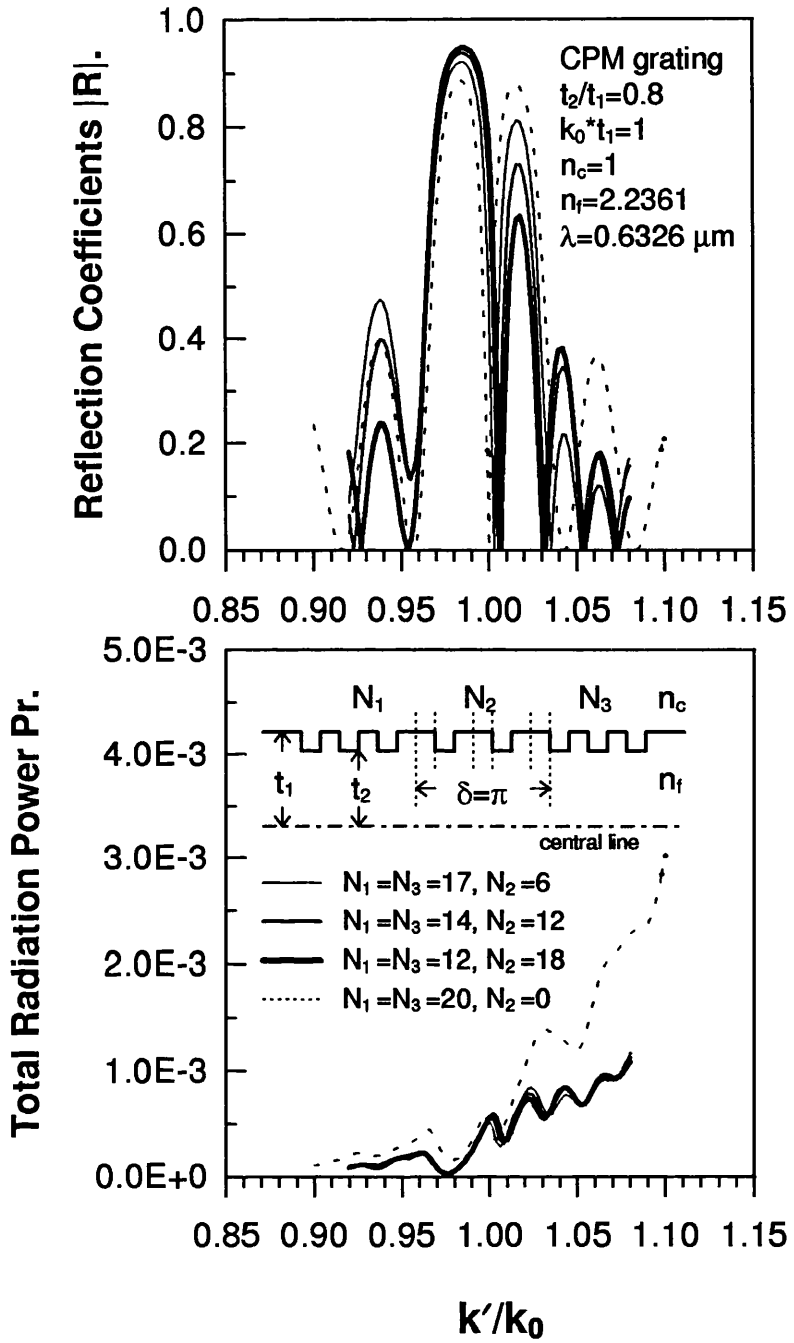

Fig. 58 *Characteristics of the reflection spectra and total radiation power of three CPM gratings (solid lines) with an effective λ/4 phase shift in the centre phase arranging region and comparing with the results of a single λ/4 phase-shifted grating (dotted lines).*

concentration in the phase arranging region, our results also show that the reflection spectra of such gratings may be adjusted by properly designing the structure to improve the stability of single mode operation and output power of DFB lasers.

6.4 CHIRPED GRATINGS

Consider a monomode linearly chirped waveguide grating with rectangular corrugations on both sides of a guide (shown in Fig. 59) and on one side of the guide (shown in Fig. 60), as a two dimensional structure with a strong coupling effect among the modes, in which the fields do not depend on the x–coordinate (see Fig. 3) and all the media in each layer are lossless.

The perturbation of variable period $\Lambda + \Delta\Lambda(n)$ is a linear function of the position along the grating. The linear chirp constant is defined by

$$\begin{cases} \dfrac{F}{2\pi} = (N_{chirp} - 1)\dfrac{\Delta\Lambda}{\Lambda}, & \text{for } N_{chirp}\text{=odd} \\ \\ \dfrac{F}{2\pi} = (N_{chirp} - 2)\dfrac{\Delta\Lambda}{\Lambda}, & \text{for } N_{chirp}\text{=even} \end{cases} \tag{106}$$

where the constant F is a measure for the degree of the chirp, N_{chirp} is the total number of periods, and $\Delta\Lambda$ is the difference of the grating periods at the centre ($n=0$) and the end ($n=(N_{chirp}-1)/2$ for odd N_{chirp} or $n=N_{chirp}/2-1$ for even N_{chirp}). If the number of grating periods N_{chirp} is large enough, the above definition has the same form as that of *Kogelnik*[118].

In this thesis we introduce two types of chirped gratings. One is the perturbation of variable period $\Delta\Lambda(z)$ applied to both groove and rib structures of the chirped grating with odd N_{chirp}, in which the lengths of the groove and of the rib are functions of the position along the grating. Another one is the perturbation of variable period only applied to the rib of chirped gratings with even N_{chirp}, in which we keep the length of groove as a constant and change the length of the rib with respect to the position. A grating with constant length and constant depth of the groove structure is suitable

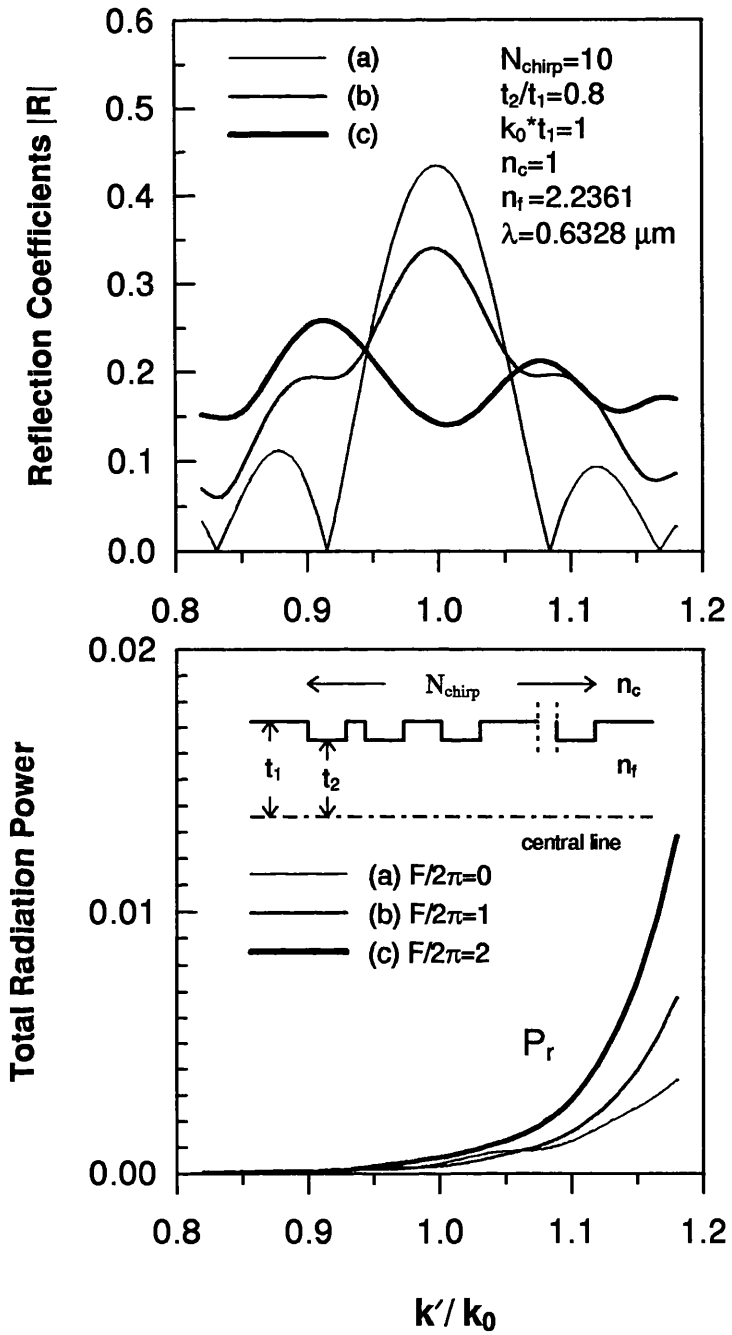

Fig. 59 *Reflection spectra and the total radiation power of the linearly chirped grating (shown in inset) with the chirp constant as (a) F/2π=0 a periodic grating, (b) F/2π=1, (c) F/2π=2.*

for dry etching fabrication. Such gratings consist of a series of step–down and step–up discontinuities. If the depth of the grating is quite large, at the discontinuity the power of each incident mode coupled to the radiation modes and other guided modes becomes very strong and has to be treated explicitly. Owing to the complicated structure of chirped gratings, we have to calculate the phase delays of modes propagating through each period of the grating in detail. The total transfer matrix of linearly chirped gratings has been given by (40).

Fig. 59 shows the reflection spectra and total radiation losses of linearly chirped gratings with different chirp constants $F/2\pi$, in which the length of groove is fixed and the length of rib is determined by (106). Comparing with the results of a periodic grating, it is shown that the peak of the centre stopband decreases, with the zeros washed out, and the frequency response broadens as the chirp constant increases. Similar results are also demonstrated in Fig. 60 for the linearly chirped gratings on one side of the guiding layer (shown in the inset). We note that the total radiation power increases very quickly in the higher frequency region just outside the centre stopband. The characteristics of our results show good agreement with those of weakly coupling chirped gratings (such as sinusoidal chirped gratings) with many periods, but an asymmetric response in the reflection spectrum appears in our results because we have considered the radiation modes in our analysis. For both cases we subdivided the radiation angle into 40 equal panels for the calculation.

We have compared the results of the chirped grating for a TE_0 mode incident from left– and right–hand sides, and we have, in a further study, shown that only a very tiny difference has been seen in the higher frequency region due to the discrepancy of the radiation losses in both cases.

If we increase the groove depth and the number of periods of the linearly chirped grating with a properly chosen chirp constant, the reflection spectrum of this chirped grating will have broader and flatter frequency response in its centre stopband. The reflection spectra of linearly chirped gratings with variable groove and rib lengths de-

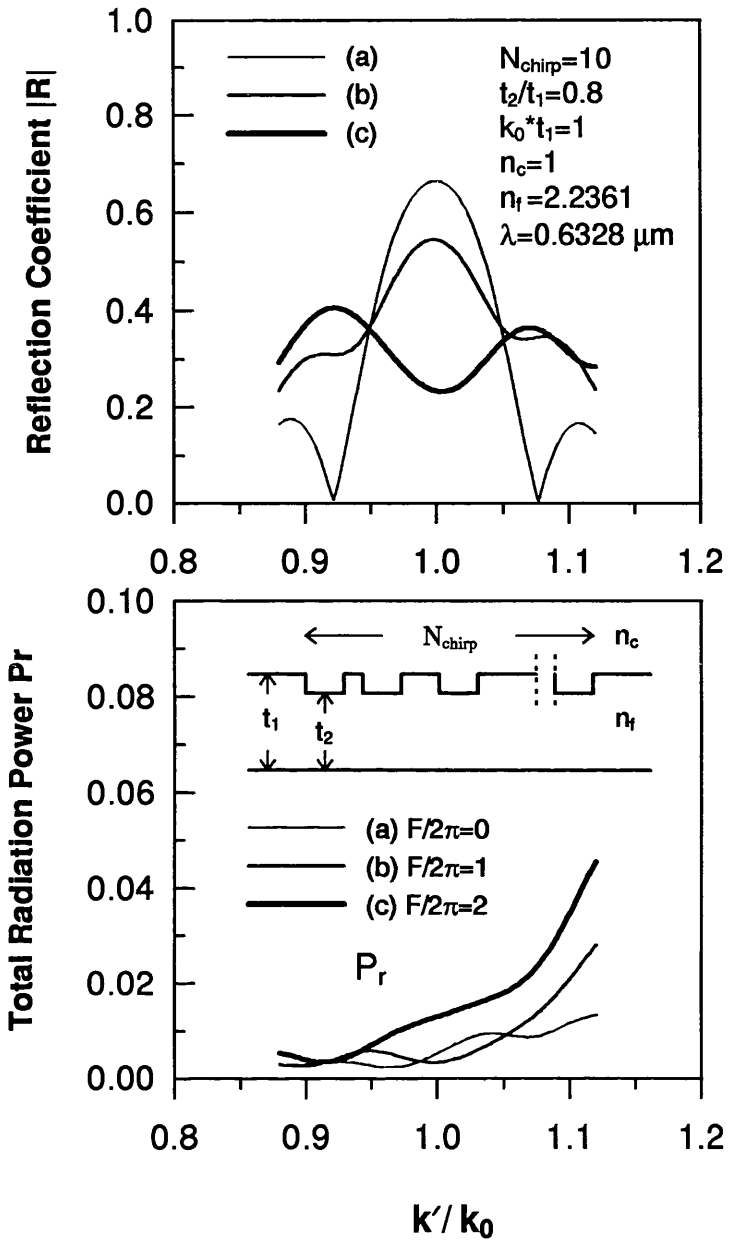

Fig. 60 *Reflection spectra and the total radiation power of the linearly chirped grating (shown in inset) with the chirp constant as (a) F/2π=0 a periodic grating, (b) F/2π=1, (c) F/2π=2.*

termined by (106) can be seen in Fig. 61. A very flat and broad frequency response appears in the centre stopband as shown in Fig. 61(c) for the linearly chirped grating with $t_2/t_1 = 0.5$ and $F/2\pi = 4$. In Fig. 61(c') a small dip appears at the centre frequency, which can be removed by increasing the number of chirped periods N_{chirp} or the groove depth. In this analysis and the next one, we only subdivided the radiation panels into 20 for Simpson's rule with the convergence error less than 1% (comparing with $m = 40$). We note that using more radiation modes induces more accurate results but also leads to more computer time.

Fig. 62(a) shows the schematic diagram for a super–structure grating (SSG) in a symmetric planar waveguide, in which the linearly chirped grating with number of periods N_{chirp} is arranged periodically. Its reflection spectrum contains periodic multiple peaks within the centre envelope profile over a wide range of frequencies. Such devices have been used in the DBR laser to achieve broad wavelength tuning operation [89][90].

In Fig. 62(b) the peak amplitudes and the mode spacing between those peaks can be adjusted by changing the SSG structure, where the centre envelope profile is determined by the chirped grating structure, the mode spacing is determined by the number of periods N_{chirp}, and the amplitude of peaks is determined by the value of $N_{chirp} \times N_{\mathrm{SSG}}$.

6.5 CONCLUSION

In this chapter we have investigated single and multiple phase–shifted gratings by applying our method to the analysis. The total transfer matrix in our method may be rearranged easily to analyse complicated aperiodic gratings designed for special purposes.

Results show that the reflection spectra of such gratings can be adjusted by properly arranging the locations of phase–shifted regions in the grating for the applications of DFB and DBR lasers and optical filters. We also illustrated a deep linearly chirped

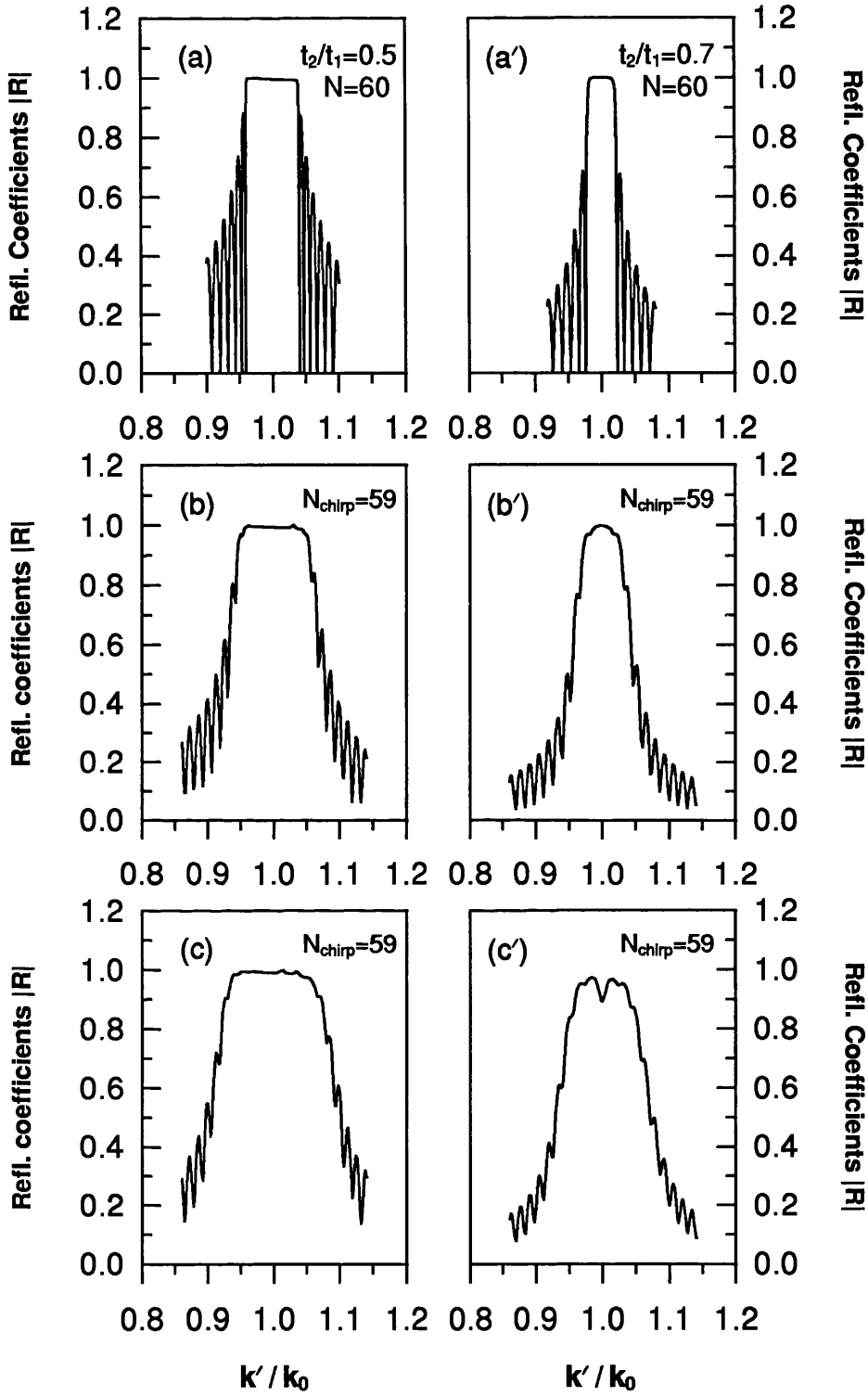

Fig. 61 *Reflection spectra of the linearly chirped gratings with different chirp constants and groove depths, as following:*
t_2/t_1=0.5 with (a) F/2π=0, (b) F/2π=2, (c) F/2π=4,
t_2/t_1=0.7 with (a′) F/2π=0, (b′) F/2π=2, (c′) F/2π=4.
(All with k_0t_1=1, n_c=1, n_f=1.61, λ=1.55 μm).

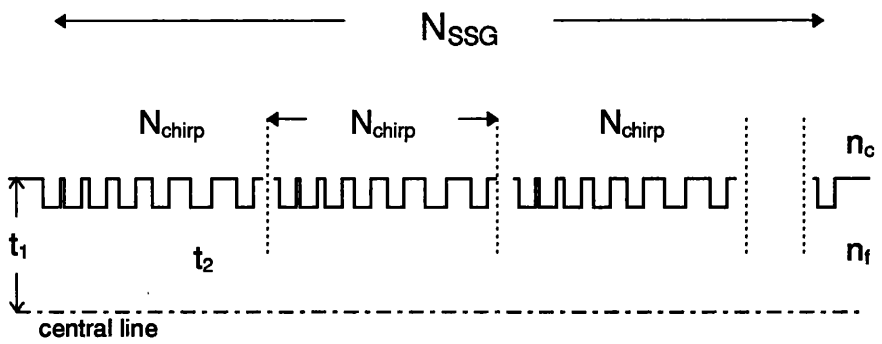

Fig. 62(a) *Schematic diagram for a super-structure grating (SSG) in a symmetric planar waveguide.*

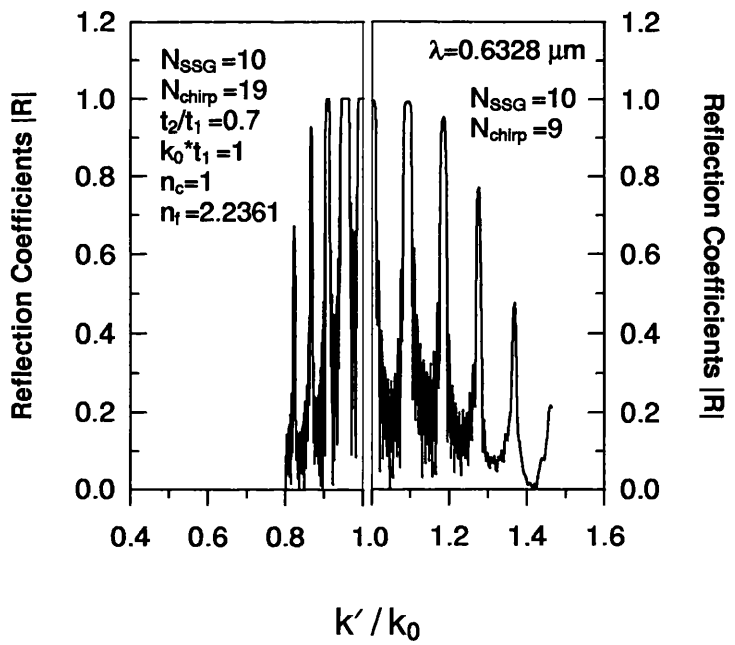

Fig. 62(b) *Reflection spectra of two super-structure gratings (SSG) with a linear chirp constant $F/2\pi=2$ for both cases.*

grating having quite flat and broad frequency response in its centre stopband with an appropriate number of periods and a chirp constant.

In the next chapter we will discuss and investigate applications of deep linearly chirped grating filters with a small number of grating periods. Such filters have high reflection coefficients over a wide frequency range with frequency–dependent nearly quadratic phase response about the centre frequency. It is shown that they may be used for dispersion compensation and pulse compression for the ultrashort pulse in the femtosecond regime.

7

CHAPTER 7

DEEP LINEARLY CHIRPED GRATINGS FOR DISPERSION COMPENSATION AND PULSE COMPRESSION

7.1 INTRODUCTION

Recently, linearly chirped grating filters have been broadly used for dispersion compensation and pulse compression [93]–[102]. Such filters consist of corrugated structures with linearly varying spatial frequency and can be fabricated by lithographic techniques on optical waveguides or by photoinduced methods in photosensitive optical fibres. The varying spatial frequency of this chirped grating is a linear function of the position along the grating; therefore, the phase delay of each frequency component of the incident pulse will depend on its frequency and the chirp. The sign (positive or negative) of the dispersion of the filter refers to the sign of the chirp constant F and can be changed simply by reversing the filter. *Ouellette*[93] considered a linearly chirped Bragg grating filter with a 1–cm–long tapered structure, with a normalised coupling coefficient $\kappa_0 L = 2\pi$ and chirp constant $F/2\pi = 10$, to compensate a broadened pulse with pulsewidth of 34 *ps*. Calculating from the coupled mode theory, the dispersion of this filter is roughly quasi–constant over the pulse bandwidth and is inversely proportional to the chirp constant. *Roman et al.*[95] also proposed using the Gel'fand–Levitan–Marchenko inverse scattering method with coupled mode equations to design a tapered chirped grating filter for

dispersion compensation and pulse compression of a pulse of 60 ps duration. Such a filter has both flat amplitude and nearly perfect quadratic phase response over wide pulse bandwidths. The reflectivity and bandwidth of grating filters strongly depend on the corrugation depth and the index profile, a weakly coupled grating requiring a very long grating length and a large chirp constant to get sufficient reflectivity and bandwidth. Thus, it is impractical to use these filters in the femtosecond regime [95], for example, for ultrashort pulse compression [133],[134] and for intracavity chirp compensation in mode–locked lasers [135],[136]. On the contrary, a deep linearly chirped grating with the relative grating depth t_2/t_1 between 0.4 and 0.8 has high reflection coefficients over a wide frequency range and these high reflection coefficients lead to high, broad, and rather flat frequency response about the centre frequency of chirped gratings. Also a deep chirped grating only consists of a small number of periods from several tens to hundreds with uniform grating depth over the entire structure, so that its compactness and efficiency would make it suitable for on–line or on–chip implementation. However, the simple coupled mode theory is no longer valid in the analysis because the depth of these gratings is too large.

In the previous three chapters, we have applied the method we proposed to treat single and double–step structures as well as periodic and aperiodic gratings. Because at each step discontinuity all of the modes excited by the step–junction and the phase delay for each mode caused by propagating through the segment between two successive steps have been calculated in detail, so our method is suitable to treat very deep gratings. With the help of the discrete Fourier transform, amplitudes of field distributions in the frequency domain obtained from the Fourier transform of an input Gaussian pulse are substituted into the total transfer matrix equation. This gives the values of the reflection coefficient and the phase delay for each frequency component of the reflected pulse. Finally, a pulse compressed to its original shape for dispersion compensation as well as to nearly transform–limited pulsewidth for chirped pulse compression can be obtained directly after the standard inverse Fourier transform. In this chapter,

some demonstrations of deep linearly chirped grating filters have been carried out for applications in dispersion compensation and pulse compression; it is shown that deep chirped grating filters have good performance for ultrashort pulses in the femtosecond regime.

7.2 FORMULATION FOR THE NUMERICAL ANALYSIS

Consider a monomode linearly chirped grating waveguide with rectangular corrugation on both sides of a guide, as shown in Fig. 63, with the chirp constant defined in (106) and other parameters also listed in the inset to Fig. 63. Similar procedures as we used to treat linearly chirped gratings in Chapter 6 will be applied to the following analysis. These include dispersion compensation and pulse compression.

7.2.1 For Dispersion Compensation

The propagation characteristic of a pulse in a fibre or GVD medium can be analysed by examining the group delay for a given mode. For optical fibres the dispersion caused by group delay includes the material and waveguide dispersions, and material dispersion normally is greater than waveguide dispersion. Consider an input pulse $f_1(t)$ with Gaussian envelope $g(t)$ as

$$\begin{aligned} f_1(t) &= g(t)\exp(j\omega_0 t) \\ &= \exp(-\frac{t^2}{2\tau_0^2})\exp(j\omega_0 t) \end{aligned} \tag{107}$$

where τ_0 is a constant and ω_0 is the centre frequency. This pulse has full width half maximum pulsewidth of $2(\ln 2)^{1/2}\tau_0$ and bandwidth of $\Delta\omega_{\text{FWHM}} = 2(\ln 2)^{1/2}/\tau_0$. The Fourier transform of $g(t)$ is $G(\omega)$

$$f_1(t) = \int_{-\infty}^{\infty} G(\omega)\exp[j(\omega+\omega_0)t]d\omega \tag{108}$$

The pulse passes through a dispersive medium (*e. g.* fibre) of length L', which has dispersion $d^2\beta/d\omega^2 = 2\alpha$ at frequency ω_0. The value of $d^2\beta/d\omega^2$ can be either posi-

tive (normal dispersion) or negative (anomalous dispersion). If the fibre has normal dispersion ($\alpha > 0$), the group velocities of the Fourier components of higher frequency are smaller than those of components of lower frequency. The reverse is true for an anomalous dispersion fibre. The fibre can be modelled (approximately) as a linear, time–invariant filter with transfer function [95]

$$H(\omega) = \exp[-j\alpha L'(\omega - \omega_0)^2] \,, \quad \omega > 0 \tag{109}$$

The output pulse $f_2(t)$ is thus

$$f_2(t) = \int_{-\infty}^{\infty} H(\omega)G(\omega)\exp[j(\omega + \omega_0)t]d\omega \tag{110}$$

At the end of the fibre, the pulsewidth has been increased by a factor of C_d [95], where

$$C_d = \left[1 + (\frac{2\alpha L'}{\tau_0^2})^2\right]^{1/2} \tag{111}$$

Therefore, the transfer function of the fibre (45) is

$$H(\omega) = \exp\left[-j\frac{(C_d^2 - 1)^{1/2}}{2}\tau_0^2(\omega - \omega_0)^2\right] \,, \quad \omega > 0 \tag{112}$$

The broadened pulse $f_2(t)$ can be recompressed by a linearly chirped grating filter. According to the analysis of the mode–matching method, the complex reflection coefficient with phase delay for a given frequency can be expressed as $|R|\exp(j\phi)$, with an absolute reflection coefficient $|R|$ and phase shift ϕ. Therefore, the transfer function of the linearly chirped grating filter can be written as

$$F_g(\omega) = |R(\omega)|\exp[j\phi(\omega)] \tag{113}$$

where $|R(\omega)|$ is the absolute reflection coefficient spectrum and $\phi(\omega)$ is the phase response which depends on the propagation constant $\beta(\omega)$ and the chirped grating structure. The reflected pulse $f_3(t)$ from the chirped grating filter can be obtained by

$$\begin{aligned} f_3(t) &= \int_{-\infty}^{\infty} F_g(\omega)H(\omega)G(\omega)\exp[j(\omega + \omega_0)t]d\omega \\ &= \int_{-\infty}^{\infty} |R(\omega)|\exp(j\phi)H(\omega)G(\omega)\exp[j(\omega + \omega_0)t]d\omega \end{aligned} \tag{114}$$

The above equation can be computed very quickly by using the fast Fourier transform (FFT) technique.

7.2.2 For Pulse Compression

Optical pulses chirped by self–phase modulation in a fibre or emitted directly from a laser cavity can be compressed by several techniques. For example, *Winful* [101] proposed a method using the periodic grating filter in optical fibre for chirped pulse compression but *Ouellette* [94] had shown that the compression ratio of an unchirped Bragg grating filter is very limited, only of the order of 1.025, due to the limitation of the reflectivity and bandwidth of the high dispersion region of the spectrum. *Tomlinson* et al. [100] indicated that a grating–pair two–stage compressor can be used to compress a pulse to as short as 30 fs but this method is not suitable for on–line or on–chip implementation. *Kuhl and Heppner* [133] had shown that a femtosecond optical pulse of 210 fs can be compressed by dielectric multilayer interferometers to an almost transform–limited duration of 115 fs but its compression ratio is limited owing to the same reason as that of the unchirped grating. *Williams* et al. [102] used a linearly chirped Bragg–grating in fibres for the compression of optical pulses using self–phase modulation with the compression ratio up to 10 and a compressed pulse of 510 fs had been seen in the experimental results. As we discussed in the beginning of this chapter, ordinary linearly chirped gratings are not suitable to use for ultrashort pulse in the femtosecond regime, because the filter used in the femtosecond regime must satisfy the conditions that not only the required coupling coefficients are large but also the quadratic phase responses are board and flat over wide frequency range. In this section, we will investigate and discuss the performances and advantages of deep linearly chirped gratings for ultrashort pulse compression by virtue of the method we proposed for the analysis.

Consider that the input linearly chirped pulse is Gaussian and centred at frequency ω_0 [95][137]

$$w(t) = \exp(-\frac{t^2}{2\tau_0^2}) \exp(j\theta t^2) \exp(j\omega_0 t) \tag{115}$$

where θ is the chirp parameter. $W(\omega)$ is the Fourier transform of the above equation

given by [95]

$$W(\omega) = B \exp\left[-\frac{(\omega-\omega_0)^2\tau_0^2}{2u}\right] \exp\left[-j\frac{\theta\tau_0^4(\omega-\omega_0)^2}{u}\right] \tag{116}$$

with

$$\begin{aligned} u &= [1+4(\theta\tau_0^2)^2] \\ B &= \frac{\sqrt{2\pi}}{u^{1/4}}\tau_0 \exp\left[j\frac{1}{2}\tan^{-1}(2\theta\tau_0^2)\right] \end{aligned} \tag{117}$$

where $\theta\tau_0^2$ is the normalised chirp parameter. The input chirped pulse $w(t)$ can be expressed as

$$w(t) = \int_{-\infty}^{\infty} W(\omega)\exp(j\omega t)d\omega \tag{118}$$

An ideal quadratic filter with the transfer function

$$H_c(\omega) = \exp\left[j\frac{\theta\tau_0^4(\omega-\omega_0)^2}{u}\right] \tag{119}$$

is used to compress the chirped pulse. The phase term quadratic with frequency of (116) will be cancelled by the transfer function described above, thus the output pulse with a transform–limited pulsewidth appearing at the end of the ideal filter is given by

$$w_f(t) = \int_{-\infty}^{\infty} B\exp\left[-\frac{(\omega-\omega_0)^2\tau_0^2}{2u}\right]\exp(j\omega t)d\omega \tag{120}$$

As we mentioned before, the transfer function of a deep linearly chirped grating is

$$F_g(\omega) = |R(\omega)|\exp[j\phi(\omega)] \tag{121}$$

where $|R(\omega)|$ is the absolute reflection coefficient spectrum and $\phi(\omega)$ is the phase response which depends on the propagation constant $\beta(\omega)$ and the chirped grating structure. The resultant pulse reflected from a deep linearly chirped grating filter can be obtained from the following Fourier transform

$$w_g(t) = \int_{-\infty}^{\infty} |R(\omega)|\exp[j\phi(\omega)]W(\omega)\exp(j\omega t)d\omega \tag{122}$$

The relationship of the compression ratio C_c and the normalised chirp parameter $\theta\tau_0^2$ derived from the inverse Fourier transform of (120) is given by [95]

$$C_c = \frac{\tau_0}{\tau_f} = [1 + 4(\theta\tau_0^2)^2]^{1/2} \tag{123}$$

where τ_f is the $1/e$ intensity point of the resultant pulse compressed by the filter. Shapes of the input chirped pulse, the pulse compressed by the ideal filter, and the pulse compressed by the deep linearly chirped grating filter can be obtained from (118), (120) and (122) respectively with the help of the FFT technique.

7.3 NUMERICAL RESULTS

To apply the discrete Fourier transform, we consider a pulse function $f_1(t)$ with Gaussian profile $g(t)$ at the centre frequency ω_0. Dividing the pulse of one period into N_s samples, in which the value of period T and the N_s must be large enough in order to avoid truncation and sampling errors, the Fourier transform $G(\omega)$ of $g(t)$ can be obtained by virtue of the FFT calculation. In the following cases, a centre wavelength of $\lambda_0 = 1.55\ \mu m$, sampling period of $T = 36\tau_0$, and sampling number of $N_s = 128$ and $N_s = 180$ for dispersion compensation and pulse compression respectively, are chosen for the FFT calculation and up to 20 radiation panels as well as 20 radiation modes (for forward and backward propagation each) have been considered in the mode-matching analysis.

7.3.1 Results of the Dispersion Compensation

In Fig. 63(a), a short Gaussian pulse with $\tau_0 = 60\ fs$ and normalised bandwidth of $\Delta\omega_{\text{FWHM}}/\omega_0 = 0.02282$ (curve a), propagates through a dispersive fibre of $C_d = 2.15$, then the broadened output pulse (curve b) is recompressed by a linearly chirped grating filter with the parameters shown in the inset. The filter, which has the chirp constant $F/2\pi$ of 7.35 and a grating length $L = 69.96\ \mu m$ with $N_{chirp} = 129$, is on a slab waveguide with

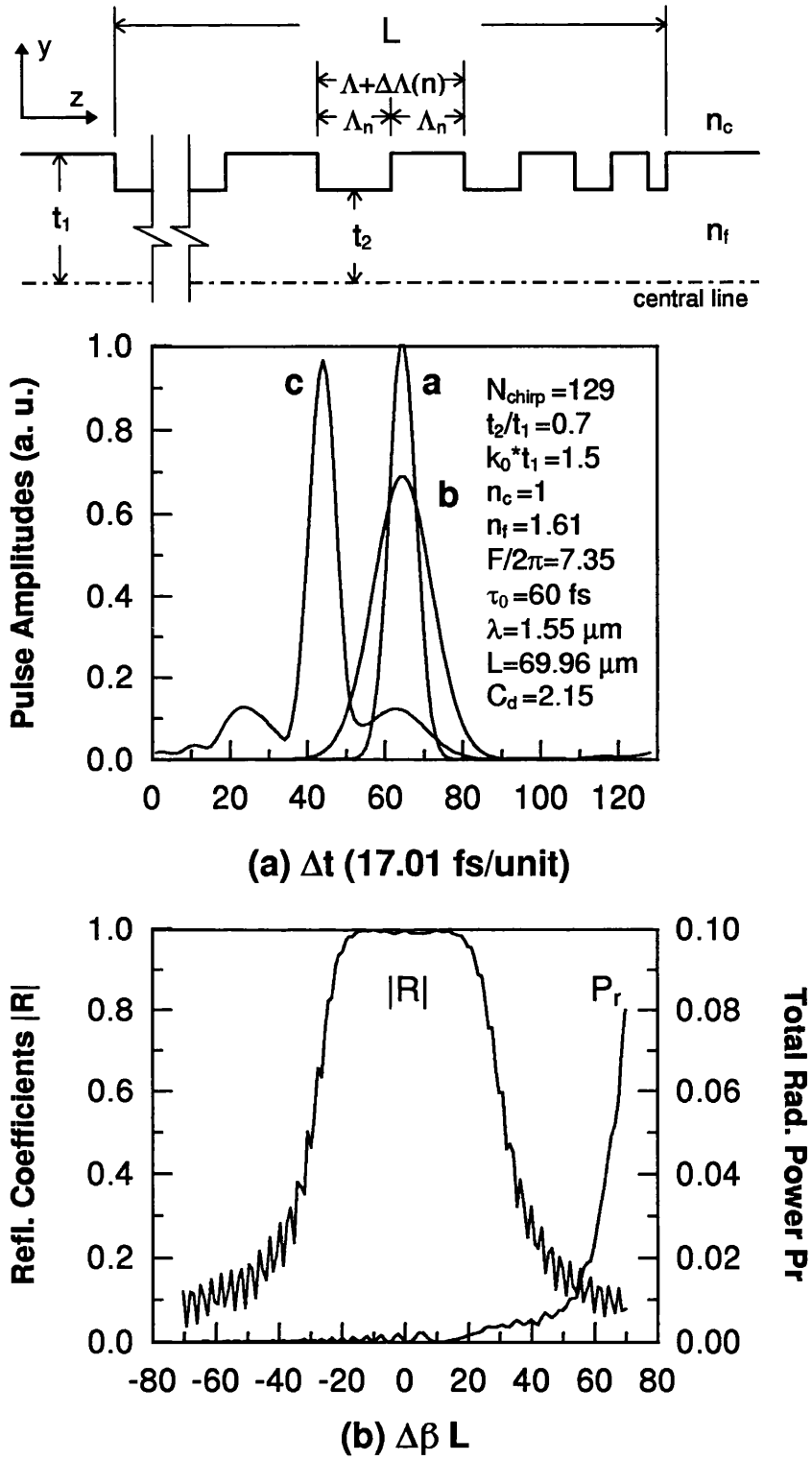

Fig. 63 *(a) Shapes of the input pulse (curve a), broadened pulse (curve b), and recompressed pulse (curve c) for a GVD fibre with C_d=2.15. (b) The reflection spectrum and total radiation power of the filter versus the detuning.*

$n_f = 1.61$ and $n_s = n_c = 1$. The resultant pulse (curve c) recompressed by the filter has the same pulsewidth as that of the original pulse. The pulse is not perfectly regenerated because of the radiation losses and the imperfect resonant frequency response of the filter. The radiation loss, as shown in Fig. 63(b), is a function of frequency and becomes very large in the high frequency region outside the filter's stopband. This also leads to the asymmetric reflection spectra. The imperfect resonant frequency response is caused by significant sidelobes in the reflection spectra and the variable resonant position of the Bragg frequency. Fig. 64(a) shows the phase responses of a dispersive fibre, an ideal compensation filter, and the deep linearly chirped grating filter (as in Fig. 63) versus the frequency deviation $(\omega - \omega_0)/\omega_0$. The response curve of the deep chirped filter is roughly quadratic in the vicinity of the centre frequency, but the curve becomes linear in lower and higher frequency regions due to a term linear with frequency which is responsible for the delay of the guided pulse (as shown in Fig. 63(a)) and does not affect the quadratic chirp. *Ouellette* [93] and *Roman and Winick* [95] have shown that the linearly chirped filter can be treated like an ideal compressor and the compression ratio C_c, the chirp constant F, and the filter length L are given by

$$\frac{L^2}{F} \approx \frac{(C_c^2 - 1)^{1/2} c^2 \tau_f^2}{4 n_{\text{eff}}^2} \tag{124}$$

where c is the light speed in free space, τ_f is the final or original pulse width, and n_{eff} is the effective index of the waveguide at the centre frequency. For an ideal compensation filter, the compression ratio C_c of the filter and the increasing factor C_d of the fibre must have the same value.

Substituting the data listed in the inset of Fig. 63(a) into (124), we get the compression ratio of $C_c = 2.83$ for the chirped grating. Comparing with our result of $C_d = 2.15$, it appears that the compression ratios of an ideal compressor and of the deep chirped filter show some discrepancy, but the relationship of the parameters in (124) still can be used to design deep chirped filters. If we use the same filter described in Fig. 63(a) to compress a broadened pulse with initial $\tau_0 = 48\ fs$, the relationship of

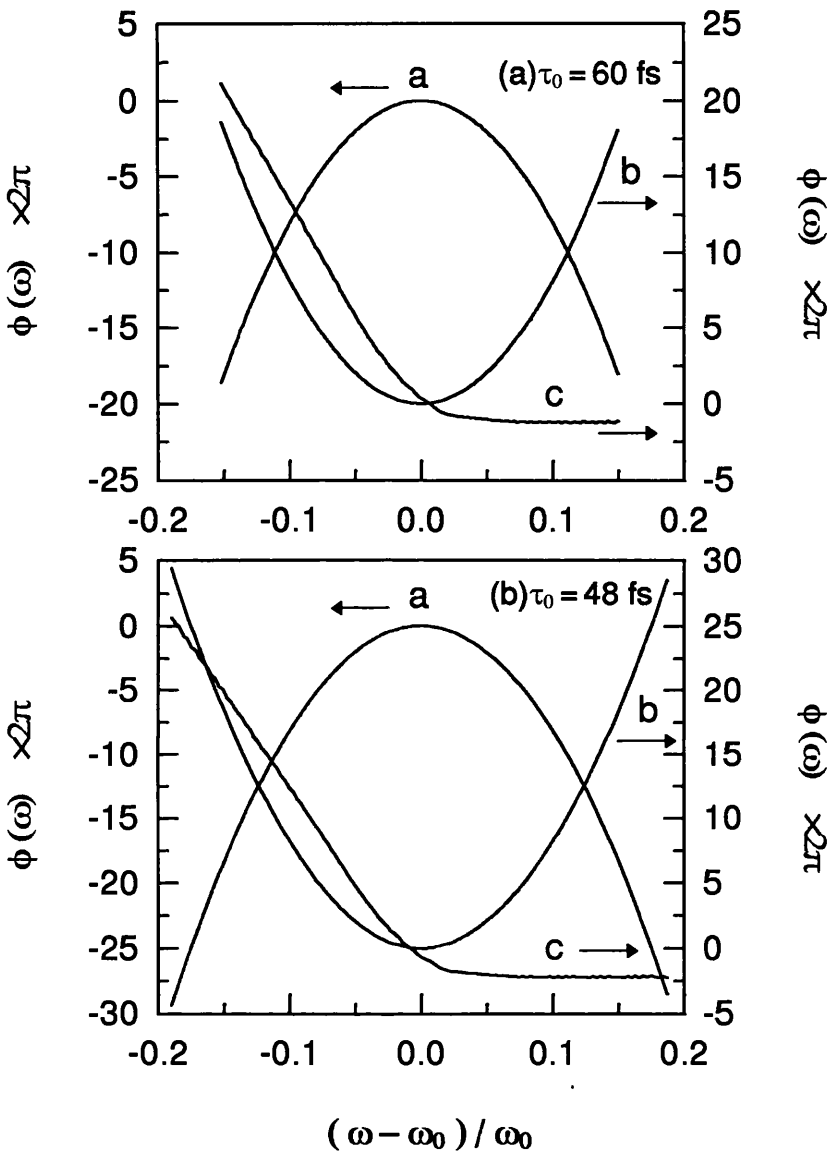

Fig. 64 *The phase responses of a dispersive fibre (curve a), an ideal compensation filter (curve b), and a deep linearly chirped grating (curve c) versus the frequency deviation. The deep chirped filter has the same parameters listed in the inset to Fig. 63 for the input pulses with (a)* τ_0 *=60 fs and (b)* τ_0 *=48 fs.*

$(C_c^2 - 1)^{1/2} \propto 1/\tau_f^2$ yields a value for C_c or C_d of 3.14. The result of $C_d = 3.17$ shown in Fig. 65 has good agreement with this prediction. Its phase responses are also shown in Fig. 64(b). Because the amplitude at the peak and the pulsewidth of the recompressed pulse can be used to judge the performance of the deep linearly chirped filter, we define the compensation efficiency of the chirped filter as

$$e = \frac{A_c^p}{A_o^p} \times 100\% \tag{125}$$

where A_c^p is the peak amplitude of the recompressed pulse and A_o^p is the peak amplitude of the original pulse. An ideal filter having 100% compensation efficiency means that the broadened pulse can be restored to its original shape perfectly. Fig. 66 shows that the efficiencies of two filters described above strongly depend on C_d. If the value of C_d is too small or too large, it indicates that the pulse is over–compensated or under–compensated respectively. In both cases, the efficiencies of the filters drop very quickly.

For a shorter pulse of $\tau_0 = 24\ fs$, its bandwidth is twice as large as that of the pulse with $\tau_0 = 48\ fs$. We choose a chirped filter with larger groove depth of $t_2/t_1 = 0.5$ and $N_{chirp} = 81$ to double the bandwidth of the filter. The results are shown in Fig. 67, in which a broadened pulse with $C_d = 2.51$ has been restored to its original shape ($e = 97.7\%$) by such a chirped filter with larger groove depth.

Fig. 68 shows that a pulse of $\tau_0 = 100\ fs$ is recompressed ($e = 95.3\%$) by a filter with $N_{chirp} = 193$, $F/2\pi = 6$, and $t_2/t_1 = 0.8$. A filter with small groove depth of $t_2/t_1 = 0.8$ is chosen to compensate this pulse with large τ_0. As τ_0 increases, the bandwidth of the pulse becomes smaller. In this case, the filter can also be designed with small bandwidth but with large dispersion to compensate the broadened pulse. Firstly, we consider a filter with small groove depth because the bandwidth of the filter strongly depends on the grating depth. Then, a long grating with a large number of periods is considered in order to get high reflectivity. Finally, a proper chirp constant is chosen to ensure that the dispersion of the filter is sufficient since the filter's dispersion is proportional to the

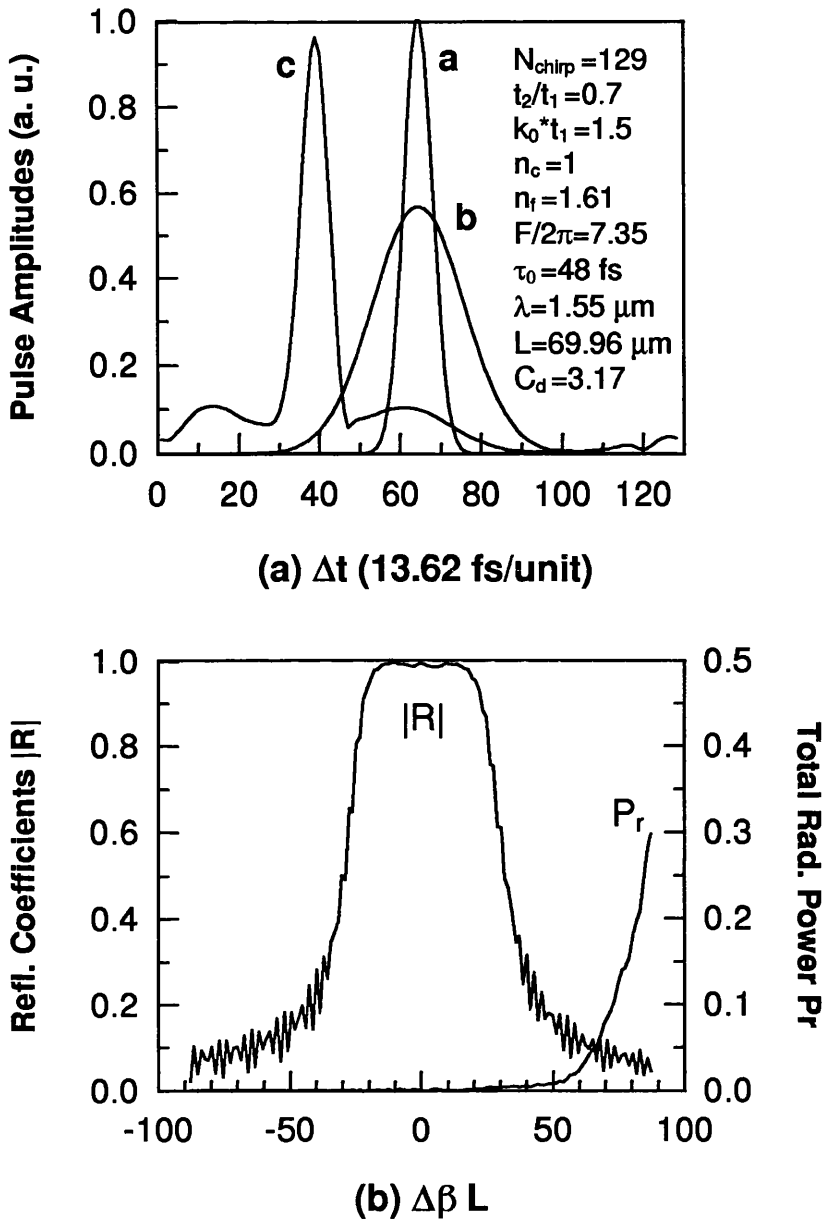

Fig. 65 *(a) Shapes of the input pulse (curve a), broadened pulse (curve b), and recompressed pulse (curve c) for a GVD fibre with C_d=3.17. (b) The reflection spectrum and total radiation power of the filter versus the detuning.*

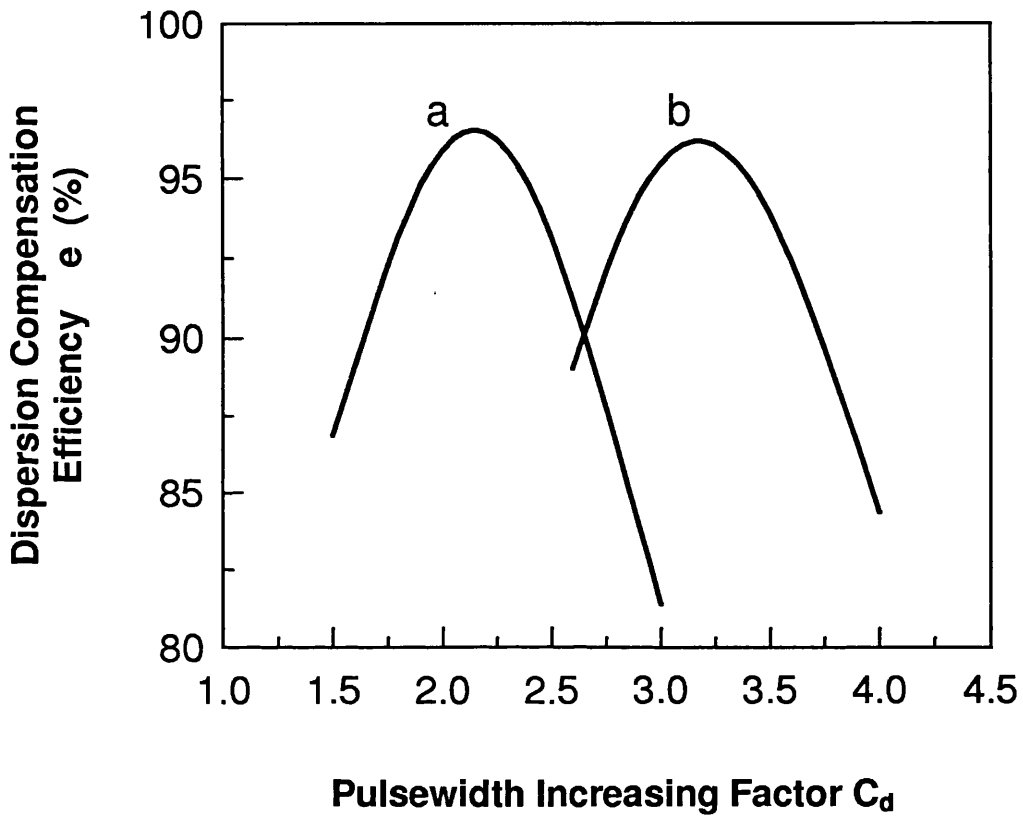

Fig. 66 *The dispersion compensation efficiency e versus the pulsewidth increasing factor C_d , for the filter with N_{chirp}=129, F/2π=7.35, and L=69.96 μm being used to compensate the broadened pulse with τ_0=60 fs (curve a) and with τ_0=48 fs (curve b).*

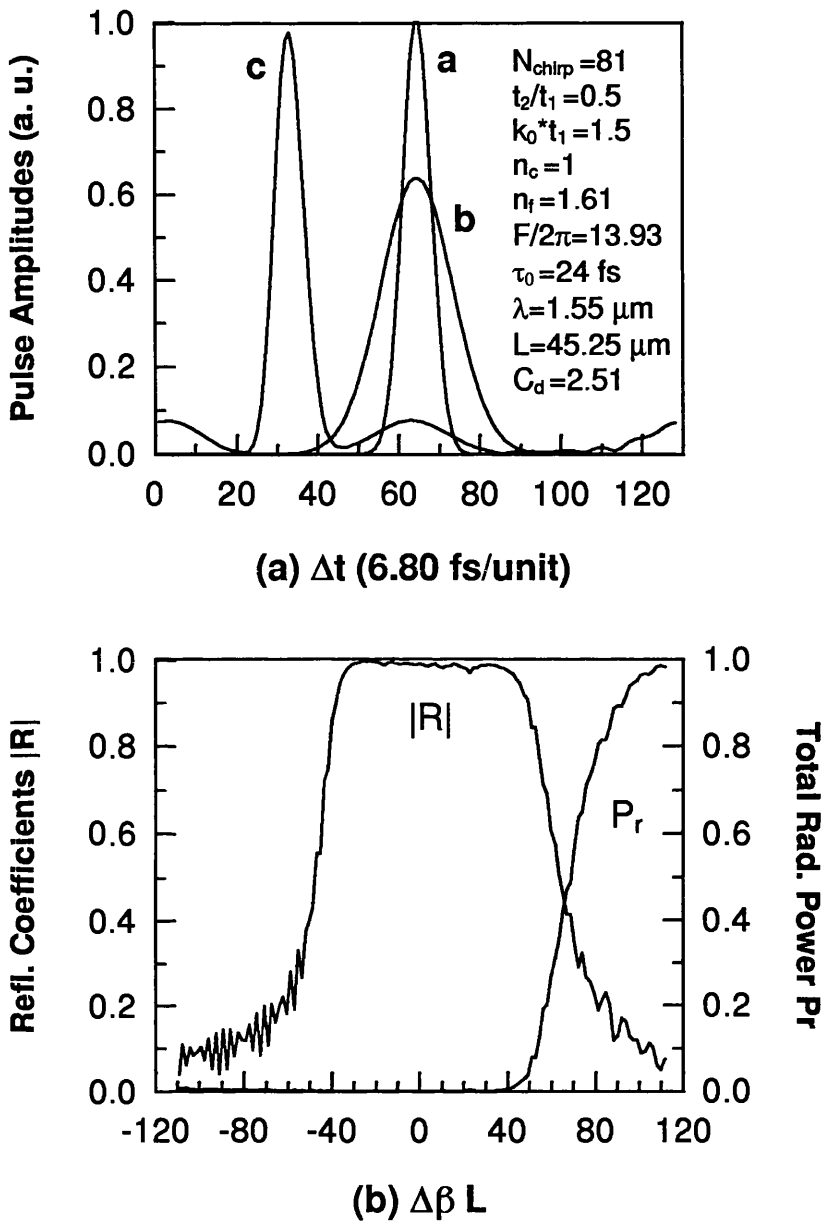

Fig. 67 *(a) Shapes of the input pulse (curve a), broadened pulse (curve b), and recompressed pulse (curve c) for a GVD fibre with C_d=2.51. (b) The reflection spectrum and total radiation power of the filter versus the detuning.*

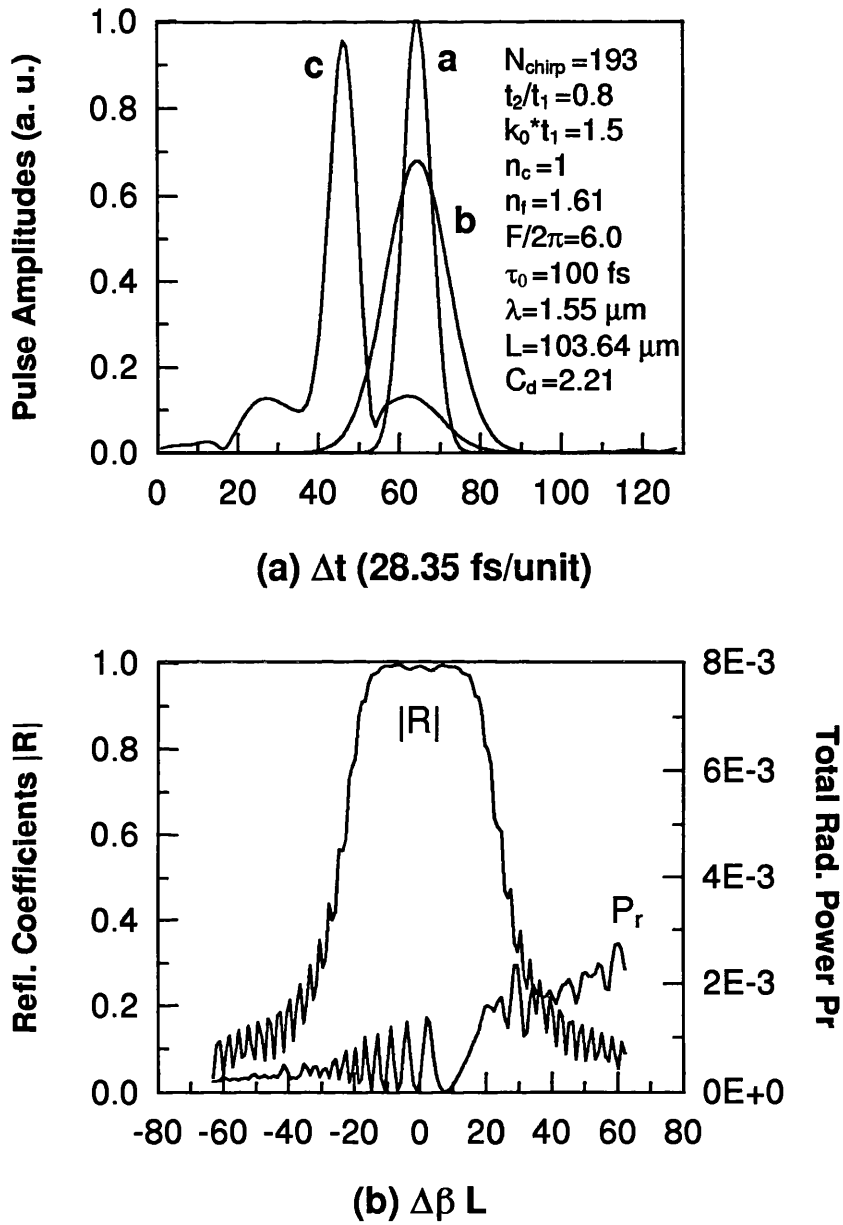

Fig. 68 *(a) Shapes of the input pulse (curve a), broadened pulse (curve b), and recompressed pulse (curve c) for a GVD fibre with C_d=2.21. (b) The reflection spectrum and total radiation power of the filter versus the detuning.*

inverse of the chirp constant [93]. If the groove depth is too small and the grating length is too long, the use of the mode–matching method described in this paper becomes too tedious and the coupled mode analysis is a better choice.

7.3.2 Results of the Pulse Compression

Fig. 69(a) shows the shape of input chirped pulse with $\tau_0 = 60\ fs$ and $\theta\tau_0^2 = 1.1837$, the shape of the pulse compressed by an ideal filter, and the shape of the pulse compressed by a deep linearly chirped grating filter with the compression ratio of $C_c = 2.57$ and the compression efficiency of $e = 89.9\%$. The compression efficiency of the deep linearly chirped grating filter is defined as:

$$e = \frac{A_g^p}{A_i^p} \times 100\% \tag{126}$$

where A_g^p is the peak amplitude of the pulse compressed by the deep chirped grating filter and A_i^p is the peak amplitude of the pulse compressed by an ideal quadratic filter. An ideal filter having 100% compression efficiency means that the duration of the input chirped pulse can be compressed to the transform–limited pulsewidth without any power loss. The compression efficiency of a deep chirped grating filter depends on the reflectivity and radiation losses of the grating and the phase response about the centre frequency.

In Fig. 69(b), the reflection spectrum and the total radiation power of the deep chirped grating filter are plotted versus the detuning $\Delta\beta L$. The reflection coefficients of the chirped grating in the vicinity of centre frequency is only about 0.9 which reflected upon the compression ratio e of only 89.9%. Fig. 69(c) shows the phase responses of the input chirped pulse and two pulses compressed by ideal and deep chirped grating filters. The response curve of the deep chirped filter appears quadratic frequency–dependent in the vicinity of the centre frequency, but the curve is tilted due to a term linear with frequency which is responsible for the delay of the guided pulse (as shown in Fig. 69(a)) and does not affect the quadratic chirp.

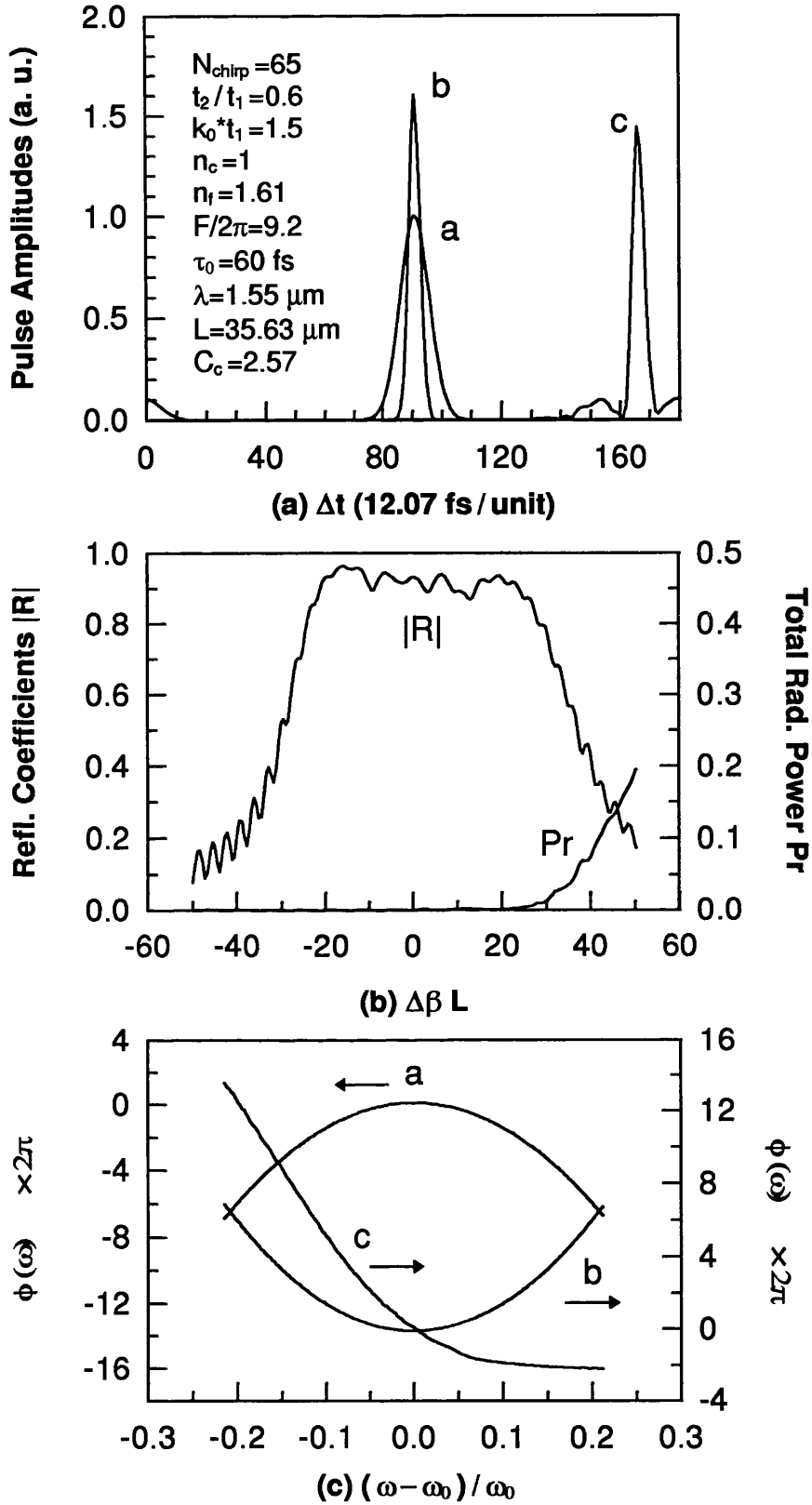

Fig. 69 *(a) Shapes of the chirped pulse (curve a), the pulse Compressed by an ideal filter (curve b), and the pulse compressed by the deep linearly chirped grating filter (curve c) with the parameters listed in inset. (b) The reflection spectrum and the total radiation power of the deep chirped grating. (c) Phase responses of curve a, b, and c shown in (a).*

Similar results also appear in Fig. 70 which shows that a shorter pulse with $\tau_0 = 48\ fs$ and $\theta\tau_0^2 = 1.553$ requires a chirped grating with large chirp constant for the pulse compression. According to (123) and (124), the relationship of the filter length L, the chirp constant F, and the compression ratio C_c is given by

$$\frac{L^2}{F} \approx \frac{(C_c^2 - 1)^{1/2}}{C_c^2} \frac{c^2\tau_0^2}{4n_{\text{eff}}^2} \tag{127}$$

or

$$\frac{(C_c^2 - 1)^{1/2}}{C_c^2} \propto \frac{L^2}{F\tau_0^2} \tag{128}$$

(128) shows that for a input chirped pulse with a small τ_0 we have to increase the chirp constant F or to decrease the length of the chirped grating filter L in order to keep the compression ratio C_c large enough. But, if the value of F becomes too large or the length of the filter L is too small, it will result a serious deterioration in the quadratic phase response and also in the reflectivity and the compression efficiency. In this case, we can increase the groove depth (or the tooth height) in order to increase not only the stopband width, which is related to the phase response, but also the reflection coefficients of the chirped grating. This is the major advantage of the use of a deep chirped grating filter for ultrashort pulse compression in the femtosecond regime. In Fig. 70(c) three phase responses of the input chirped pulse (curve a), the pulse compressed by an ideal filter (curve b), and the pulse (curve c solid line) compressed by the deep chirped grating filter (its parameters listed in the inset to Fig.70(a)) are plotted versus the frequency deviation of $(\omega - \omega_0)/\omega_0$. We use a least–squares fit to the curve c in order to avoid the tiny slope fluctuation in the curve, and the quadratic fitting curve c (dotted line) is shown in Fig. 70(c) with a very good match for the curve c (solid line) obtained from (122). Second derivatives $d^2\phi/d\omega^2$ of curves a, b, and fitting curve c (dotted line) are listed in Table 7, in which a good agreement with the value of $-2\theta\tau_0^4/u$ derived from (116) is presented.

Fig. 71 shows the ideal compression ratios C_c and the compression efficiencies of deep chirped grating filters (described in the insets) versus the normalised chirp parameter

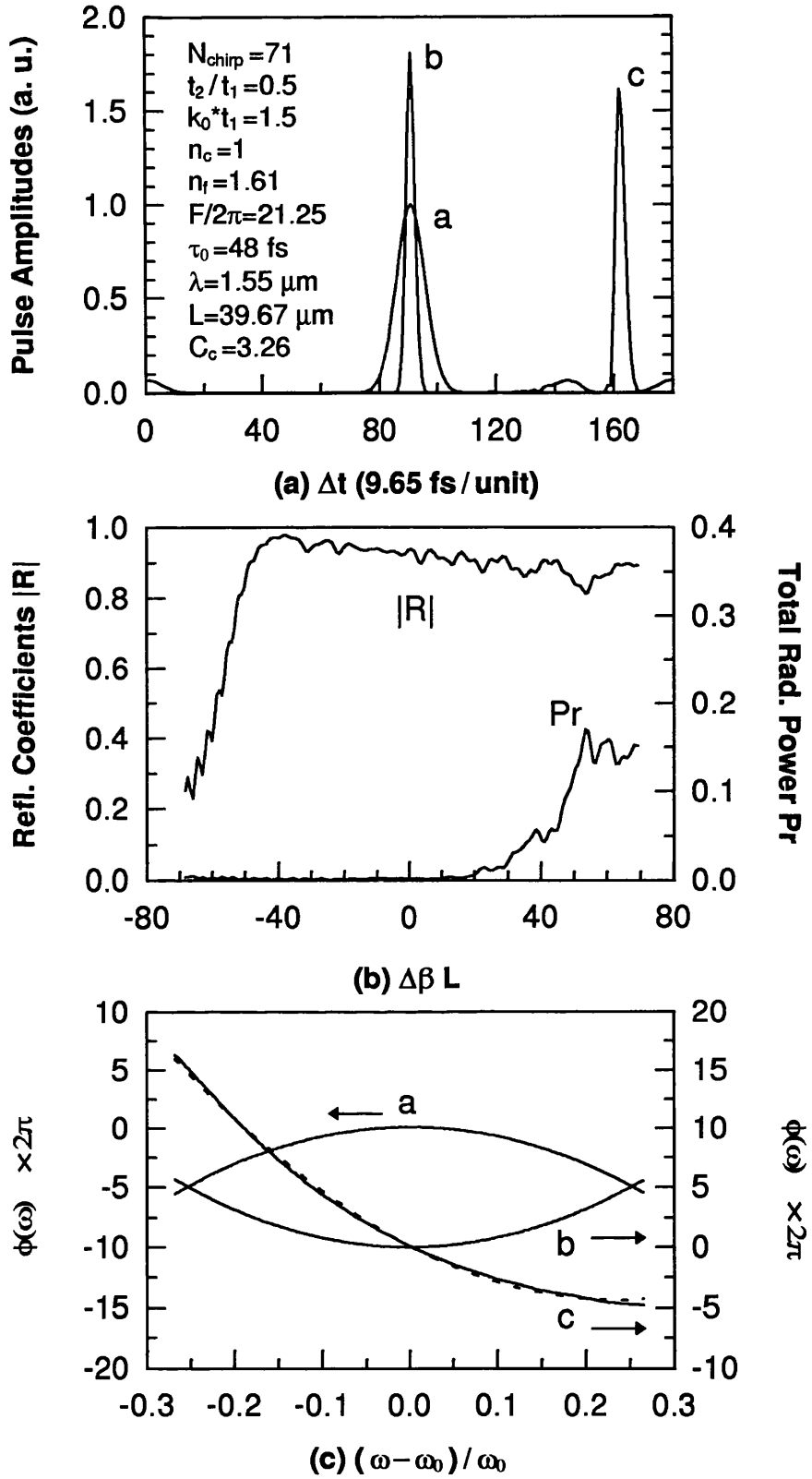

Fig. 70 *(a) Shapes of the chirped pulse (curve a), the pulse compressed by an ideal filter (curve b), and the pulse compressed by the deep linearly chirped grating filter (curve c) with the parameters listed in inset. (b) The reflection spectrum and the total radiation power of the deep chirped grating. (c) Phase responses of curve a, b, and c shown in (a). The dotted line of curve c is the quadratic fit.*

Table 7: Data of second derivative of the curve a, b, and c (dotted) in Fig. 70(c) and comparing with the value of $-2\theta\tau_0^4/u$ derived from the Fourier transform of the input chirped pulse

Data	$-2\theta\tau_0^4/u$	$d^2\phi/d\omega^2$ ($\times 10^{-27}$ s^2)			deviation
	($\times 10^{-27}$ s^2)	curve a	curve b	curve c	$(c-b)/b \times 100\%$
$\tau_0 = 48$ fs					
$C_c = 3.263$	-1.05019	-1.05019	1.05019	1.06295	1.2%
$\theta\tau_0^2 = 1.5530$					

$\theta\tau_0^2$ of the input chirped pulses with (a) $\tau_0 = 60$ fs and (b) $\tau_0 = 48$ fs. The efficiency of the deep chirped grating filter strongly depends on the normalised chirp parameter. The optimum efficiency appears as the phase response matching condition is achieved (see Table 7), and the efficiency drops as the normalised chirped parameter moves away from the phase response matching point.

In Fig. 72 an input chirped pulse with $\tau_0 = 100$ fs and $\theta\tau_0^2 = 1.7906$ compressed by an ideal filter and a deep chirped grating filter (its parameters listed in the inset) are shown, in which the compression ratio of $C_c = 3.72$ and the filter efficiency of $e = 97.1\%$ with the matching deviation of the phase response as small as 0.189% are obtained from our analysis. The pulse compressed by the deep chirped grating filter has the same profile as that from the ideal filter with a transform–limited duration.

If we increase the chirp constant of the grating, a large compression ratio of $C_c = 4.43$ is obtained with the results illustrated in Fig. 73. Table 8 contains a listing of the value of second derivative of the phase responses of the chirped grating filters described in Fig. 72 and 73 with a comparison of that derived from (116) and our results. A small degradation appears in the compression efficiency and phase response matching

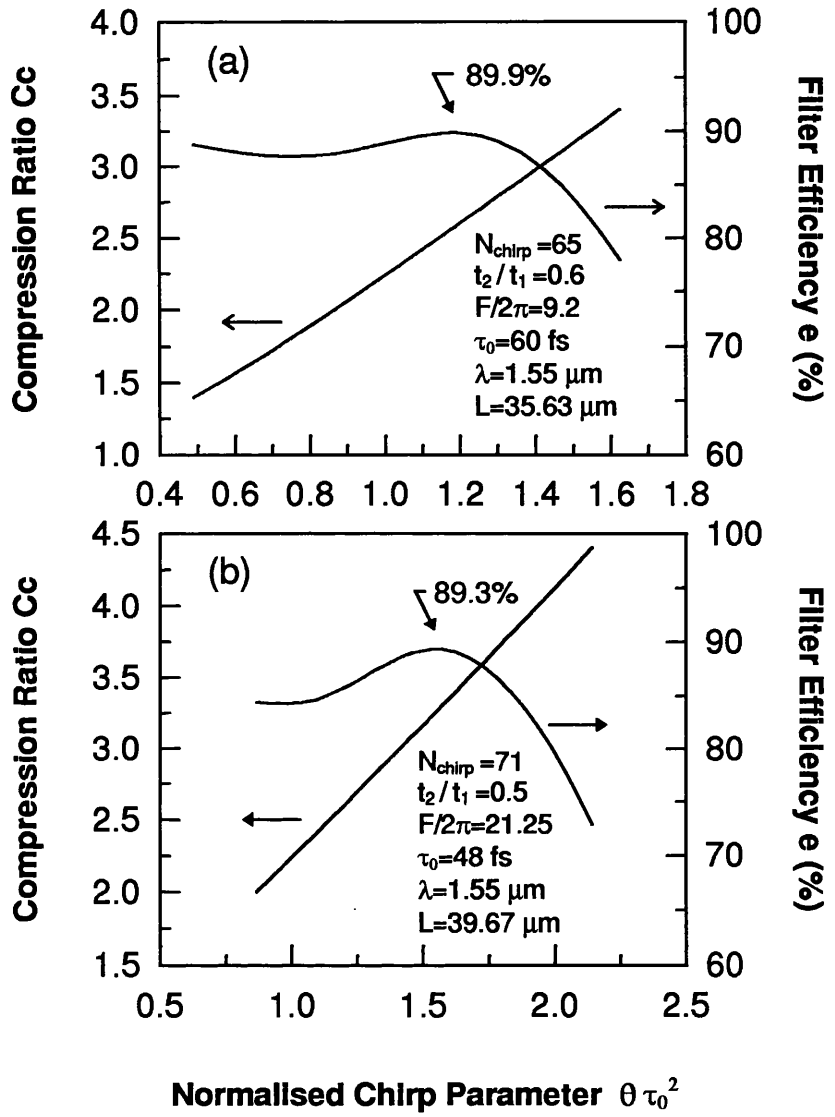

Fig. 71 *Ideal compression ratios C_c and deep linearly chirped grating filter efficiencies e versus the normalised chirp parameter $\theta\tau_0^2$ of the input pulses of (a)τ_0=60 fs and (b) τ_0=48 fs at centre wavelength of λ_0=1.55 μm, with the parameters of the grating listed in the inset of each figure.*

Table 8: Data of second derivative of the curve a, b, and c (dotted) in Fig. 72(c) and 73(c) as well as the value of $-2\theta\tau_0^4/u$ derived from the Fourier transform of the input chirped pulse

Data	$-2\theta\tau_0^4/u$	$d^2\phi/d\omega^2$ ($\times 10^{-27}$ s^2)			deviation
$\tau_0 = 100$ fs	($\times 10^{-27}$ s^2)	curve a	curve b	curve c	$\lvert(c-b)\rvert/b \times 100\%$
$C_c = 3.7182$ $\theta\tau_0^2 = 1.79060$ $F/2\pi = 30$	-2.59038	-2.59038	2.59038	2.58549	0.189%
$C_c = 4.4297$ $\theta\tau_0^2 = 2.15767$ $F/2\pi = 35$	-2.19921	-2.19921	2.19921	2.20844	0.420%

deviation of the grating with large chirp constant, as shown in Fig. 73. The performance of the chirped grating filter can be improvement, if we increase the groove depth of the chirped grating simultaneously.

7.4 CONCLUSION

We have applied the method we proposed to analyse linearly chirped grating filters with large groove depth for dispersion compensation and pulse compression. The deep linearly chirped grating filter has a high, broad, and flat frequency response, in which a nearly quadratic frequency–dependent phase response appears about the centre frequency and matches the dispersion of the GVD medium as well as the phase response of the linearly chirped pulse.

Results are presented which show that such filters have good compensation and compression performances in the femtosecond regime, and the restored pulses have very

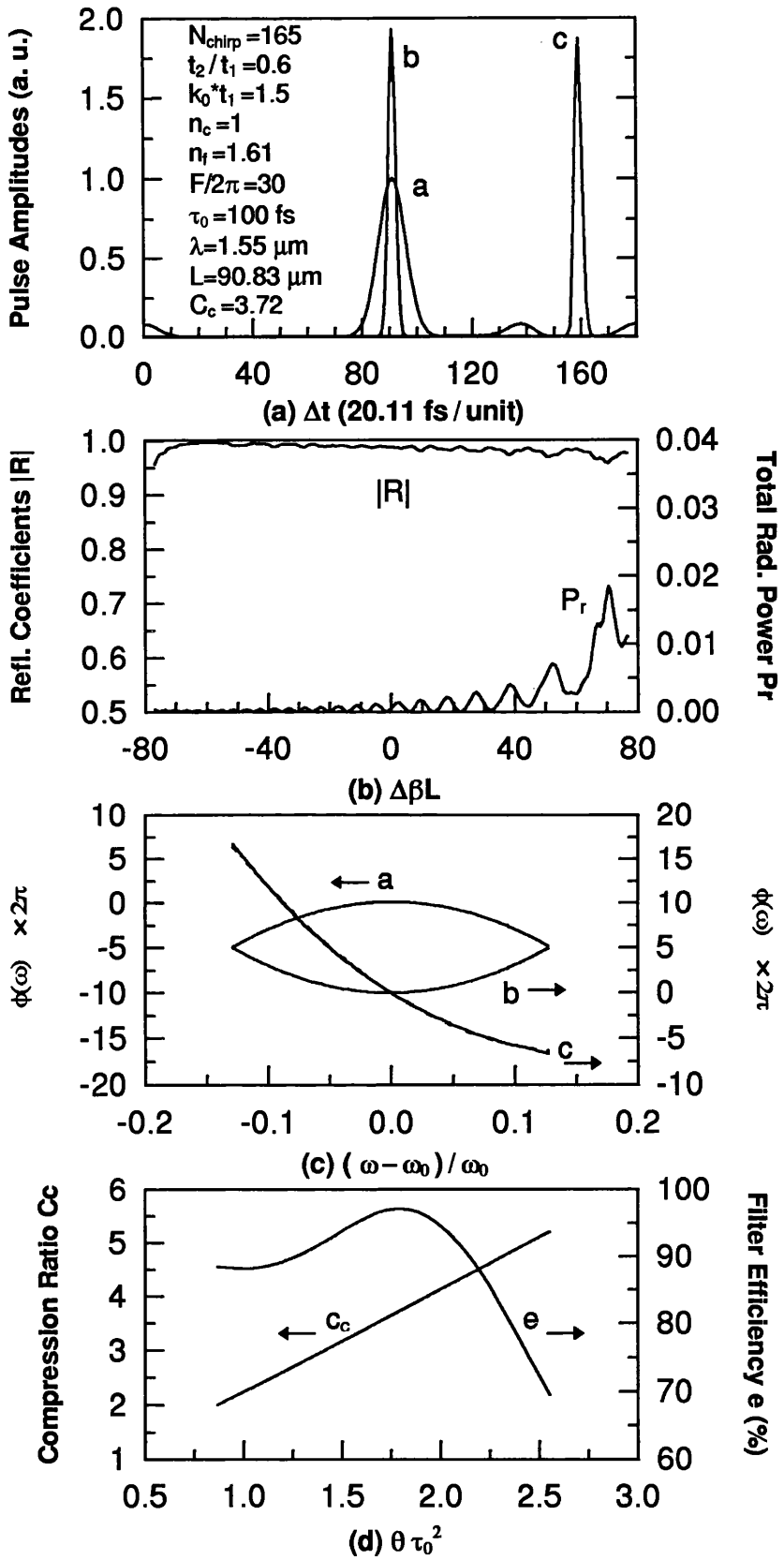

Fig. 72 *(a) Shapes of the chirped pulse (curve a), the pulse compressed by an ideal filter (curve b), and the pulse compressed by the deep linearly chirped grating (curve c) with the parameters listed in the inset. (b)* $|R|$ *and* P_r *. (c) Phase responses of curve a, b, and c. The dotted line of curve c is the quadratic fit. (d) The ideal compression ratio and the deep chirped grating filter efficiency versus the normalised chirp parameter* $\theta\tau_0^2$.

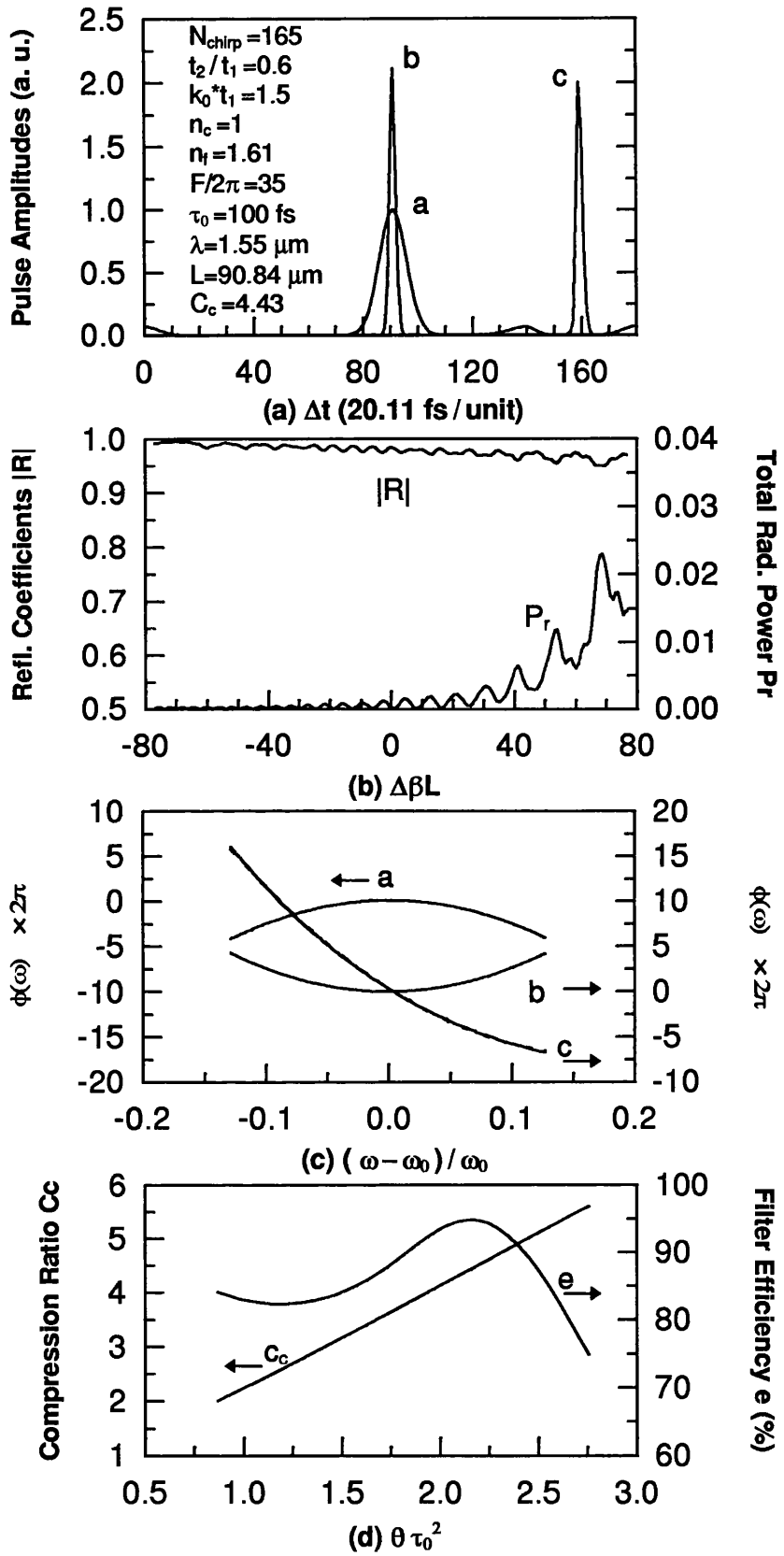

Fig. 73 *(a) Shapes of the chirped pulse (curve a), the pulse compressed by an ideal filter (curve b), and the pulse compressed by the deep linearly chirped grating (curve c) with the parameters listed in the inset. (b)* $|R|$ *and* P_r *. (c) Phase responses of curve a, b, and c. The dotted line of curve c is the quadratic fit. (d) The ideal compression ratio and the deep chirped grating filter efficiency versus the normalised chirp parameter* $\theta\tau_0^2$.

good quality with sidelobe intensity less than -17.5dB and the value of peak amplitude from 95% to 98% of its original value for the broadened pulses with the value of τ_0 ranging from 24 fs to 100 fs; the pulsewidth of the compressed pulse reaches nearly the transform–limited pulsewidth with the compression ratio of $C_c = 3.72$ and the compression efficiency up to 97.1% for the linearly chirped pulse of $\tau_0 = 100$ fs.

In particular, the filter can be fabricated compactly for on–line and on–chip applications, such as dispersion compensation for erbium–doped fibre amplifiers, for GVD materials, and intracavity chirp compensation in mode–locked lasers.

8

CHAPTER 8

CONCLUSIONS

In this thesis, we have proposed a method based on the mode–matching method associated with a transfer matrix approach to analyse rectangular waveguide gratings. All the modes produced by each step–discontinuity of the grating have been considered in detail by using the mode–matching procedure, in which we have used Simpson's rule to develop a number of linearly independent equations in terms of the same number of unknown coefficients for the forward and backward travelling modes. The linearly independent equations have been arranged in matrix form for the analysis of the multiple–step junctions and gratings; with the help of the transfer matrix approach, the phase responses of the guided and radiation modes are included in the calculation. We have applied this method to treat discontinuous structures, for example single step discontinuities, double–step discontinuities, periodic gratings, and aperiodic gratings with phase shifts. Several comparisons of our results with others obtained by existing methods are given. It is shown that our results have very good agreement with others in the cases of a step junction, double–step discontinuities, and waveguide gratings with small groove depth. However, simple approximation methods may produce erroneous results if applied to treat the gratings with large groove depth.

The method proposed in this thesis has the following advantages:

1. Very good convergence can be obtained in the computation.

2. The total power of the modes produced by discontinuous structures is equal to

the power of the incident mode, which is normalised to $1W$ per unit cross–section perpendicular to the mode propagation direction.

3. The method can be applied to both TE and TM mode incidences.

4. With minimal approximation in the formulation, this method is suitable to treat rectangular gratings with large groove depth.

5. The accuracy of the computation can be improved simply by increasing the number of radiation panels for Simpson's rule.

6. The method can be used to analyse an aperiodic grating with multiple phase shifts and special structures such as CPM and SSG.

7. The numerical algorithm of the method is suitable for computer processing.

In Chapter 4, we applied this method to a wide variety of planar waveguide discontinuities, and several characteristics of the step discontinuity for TE and TM mode incidences have been examined, including (1) the convergence of the total radiation power versus the number of panels for Simpson's rule, (2) the reflection and transmission coefficients of the step discontinuities and the total radiation power versus the relative step height, index profiles, and the thickness of the guiding layer, and (3) far–field radiation patterns of the step junctions. Several comparisons of our results and those from a simple approximation and other existing methods are presented, in which our results show good agreement with others over a large range of the step height and the refractive index profiles. But, it is shown that simple approximation methods can be used to treat discontinuous structures accurately only under the conditions of small step height and small index variation between the guide and surrounding medium.

In Chapter 5, the results of the double–step discontinuities and periodic gratings have been shown. An apparent resonance appears in the reflection coefficients as the phase–matching condition of the double–step discontinuities is achieved. The reflection

spectrum and the total radiation power of the periodic grating have been plotted versus the deviation of k'/k_0 from the Bragg wavenumber k_0 for gratings with different structures and index profiles. In addition, phase responses and radiation patterns of the radiation modes in high order gratings have been investigated. The results show that the radiation coupling angle can be steered over a wide range by properly adjusting the grating period. A deep rectangular grating may contribute a high, broad, and flat frequency response in the centre stopband and exhibit strong coupling effects, which shows that the reflected power of the backward–moving guided mode reaches saturation after passing through a small number of grating periods, in which the coupling coefficient is a function of the position along the grating. Simple approximation methods are not suitable to treat such gratings with large groove depth.

In Chapter 6, we have adjusted the total transfer matrix in our method for the analysis of aperiodic gratings. These include single phase–shifted gratings, multiple phase–shifted gratings, and linearly chirped gratings. Both the reflection spectrum and the total radiation power have been evaluated. The characteristics of the main lobe and sidelobes in the reflection spectrum and the location of the passband within the centre stopband of the single and double phase–shifted gratings strongly depend on the disposition and the degree of the phase shifts. Furthermore, a quite high, flat, and broad frequency response in the centre stopband of the deep linearly chirped grating may be obtained by appropriately choosing the number of periods and the chirp constant.

In Chapter 7, the applications of the linearly chirped grating with large groove depth for dispersion compensation and pulse compression have been investigated. This is the first time that a broadened pulse is restored to its original shape and a chirped pulse is compressed to the transform–limited pulsewidth directly obtained from the Fourier transform and mode–matching analysis. A frequency–dependent nearly–quadratic phase response appears in the vicinity of the centre frequency, and very good dispersion compensation and pulse compression performances in the femtosecond regime are realisable. Such a deep chirped grating filter having a very compact size is suitable for on–line and

on–chip implementation, for example dispersion compensation for erbium–doped fibre amplifiers, for GVD materials, and intracavity chirp compensation in mode–locked lasers.

We have presented general mode distributions in Chapter 3 for multiple–layer planar waveguides and also discussed the possibility of the application of our method to analyse multiple–layer planar waveguides. According to the conclusion and knowledge obtained from this study, we suggest that the following special topics are worth further investigating:

1. Rectangular gratings in multiple–layer planar waveguides.

2. Rectangular gratings in inhomogeneous planar optical waveguides.

3. Rectangular gratings in single–mode optical fibres.

The author has worked in the field of the inhomogeneous optical waveguides recently, and co-proposed some wave distributions using the variational analysis for slab waveguides [138][139] and for graded–index fibres [140]. These works may offer a very useful beginning for the studies described above.

APPENDIX : COMPUTER PROGRAMS

In this appendix several programs, including (a) the program for a chirped grating in the symmetric planar waveguide for TE mode incidences, (b) the program for a periodic grating on one side of the guiding layer with symmetric refractive index profile, (c) the program for a step-up and a step-down discontinuity on the asymmetric planar waveguide for TE mode incidence, (d) the program for determining the propagation constants and mode distributions of both TE and TM modes in a general multiple-layer planar waveguide, (e) the program for the analysis of the deep chirped grating filter for dispersion compensation, and (f) for pulse compression, developed from the numerical method and the algorithm described in this thesis are presented. These programs can be adjusted easily to analyse other discontinuities and gratings. A brief block diagram of the program for a deep linearly chirped grating and its applications is shown.

Block diagram of the program for a deep chirped grating (DCG)

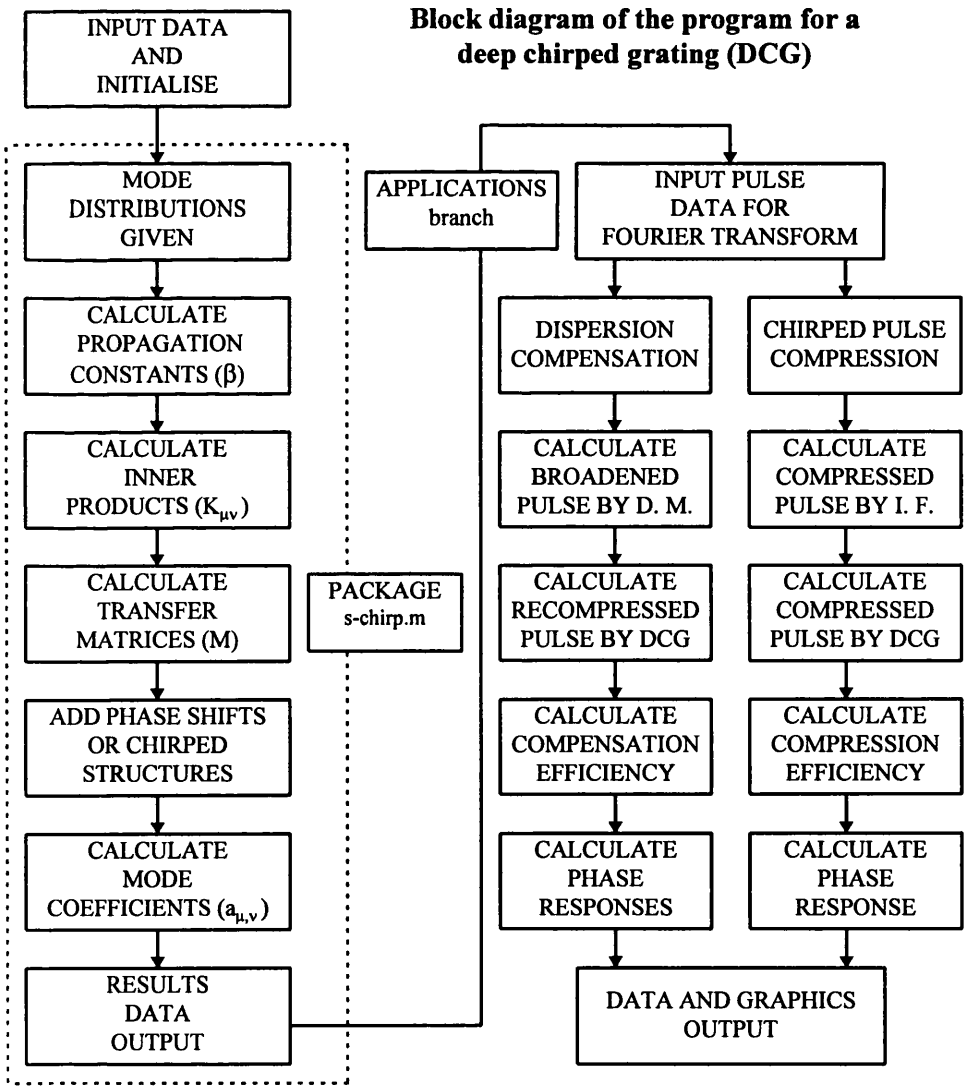

All of our computer programs shown in this appendix are written by using the *Mathematica* (Version 2.2) package, which are run on PC computers and *Sun* workstations. The calculation time of these programs on the PC (486-DX66) used was from a few minutes (for a single step discontinuity) to slightly more than twenty minutes (for a periodic waveguide grating) for each incident wavenumber k, and the computer memories require 8 megabytes RAM (random-access memory) and 25 megabytes hard disk free storage space. For chirped gratings (as shown in Fig. 61), we suggest that the program had better be run on workstations because the job demands very long calculation time and large computer memory.

Appendix A

(a) Main program for chirped gratings

```
(* Input Data *)

dfl=OpenAppend["filename.dat"]; (* Open a file for output data *)

wleng=N[8500 10^-10,20];  (* Wavelength of the incident mode *)
pi=N[Pi,20];
vk0=2*pi/wleng;  (* Free-space wavenumber of the incident mode
*)
nmod=0;    (* Mode order of the incident TE mode *)
norder=1;   (* Grating order *)
nc=N[10 10^-1,20]; nf=N[161 10^-2,20];   (* refractive indices *)
tk=N[15 10^-1,20];
(* tk = vk0*tf1 : Normalised thickness of the rib region *)
r2=N[80 10^-2,20]; r3=1;   (* The structure of the chirped grating
*)
tf1=tk/vk0;
tf2=r2*tf1;      tf3=r3*tf1;
ngr=60;      (* No. of periods of the chirped grating *)
anglimt=N[1 10^-4,20]; (* π/2 - θη *)
mmax=20;   (* Radiation panels for Simpson's rule *)
mdch=5;    (* Chirp constant *)
num=240;   (* Total points for calculating *)
noutst=1;   (* First point for the calculation *)
stopnt=num+1; (* Seting the end point in the calculation *)
nstep=1;      (* increament step *)
k0stp=N[1 10^-3,20]; (* increament in k-space k0/vk0 *)
startko=N[1-num*k0stp/2,20]; (* minimum k0/vk0 *)
k0List=Table[startk0+ist*k0stp,{ist,num}];
(* Specifying the range of the spectrum for calculating*)
<<s-chirp.m;
(* Loading in the package and starting the calculation*)
Close[dfl];      (* Close the data file *)
```

(b) Main program for periodic gratings

```
<<polarmap.m  (* Loading in the polar coordinate package *)
dfl=OpenAppend["filename.dat"]; (* Open a file for output data *)

wleng=N[6328 10^-10,20];  (* Wavelength of the incident mode *)
pi=N[Pi,20];
vk0=2*pi/wleng;  (* Free-space wavenumber of the incident mode
*)
nmod=0;    (* Mode order of the incident TE mode *)
norder=1;   (* Grating order *)
nc=N[10 10^-1,20]; nf=N[Sqrt[5],20];   (* refractive indices *)
tk=N[10 10^-1,20];
(* tk = vk0*tf1 : Normalised thickness of the rib region *)
r2=N[80 10^-2,20]; r3=1;   (* The structure of the chirped grating
*)
tf1=tk/vk0;
tf2=r2*tf1;      tf3=r3*tf1;
ngr=60;      (* No. of periods of the grating *)
anglimt=N[1 10^-4,20]; (* π/2 - θη *)
mmax=40;   (* Radiation panels for Simpson's rule *)
num=240;   (* Total points for calculating *)
noutst=1;   (* First point for the calculation *)
stopnt=num+1; (* Seting the end point in the calculation *)
nstep=1;      (* increament step *)
k0stp=N[1 10^-3,20]; (* increament in k-space k0/vk0 *)
startko=N[1-num*k0stp/2,20]; (* minimum k0/vk0 *)
k0List=Table[startk0+ist*k0stp,{ist,num}];
(* Specifying the range of the spectrum for calculating*)
<<as-dngr.m;
(* Loading in the package and starting the calculation*)
Close[dfl];      (* Close the data file *)
```

(c) Main program for asymmetric step-up and step-down discontinuities

```
<<graphics\graphics.m
(* Loading in Mathematica package graphics.m *)
dfl=OpenAppend["filename.dat"]; (* Open a file for output data *)

wleng=N[6328 10^-10,20];
pi=N[Pi,20];                vk0=2*pi/wleng;
nmod=0; (* Mode order of the incident TE mode *)
nc=N[10 10^-1,20];  nf=N[1610 10^-3,20];
ns=N[1515 10^-3,20];    (* Refractive indices *)
mmax=30; (*mmax: for S-Rad modes*)
nmax=20; (*nmax: for SC-Rad modes*)
angsc=N[ArcCos[nc/ns],20];
(* Maximum angle of the substrate radiation radiation mode *)
sanglim=N[1 10^-4,20]; (* For substrate-modes *)
canglim=N[1 10^-4,20]; (* For SC-modes *)

tf1=N[3 10^-7,20];   (* The thickness of guiding layer 1 *)
trstart=N[120 10^-2,20]; (* Thickness ratio of tf2/tf1 *)
stptr=N[2 10^-2,20];     (* Increament of the thickness ratio *)
tstep=10;                (* Total steps for calculating *)
<<a-stepup.m
(* Loading in the package and starting the calculation*)
Close[dfl];      (* Close the data file *)
```

(d) Main program for multiple planar waveguides

```
(*
 ---------------------------
  n =order of the mode,
  fl=total number of layers,
  ml=the location of the guiding layer,
  sl=the location of the substrate.
 ---------------------------
*)

<<graphics\graphics.m

(* Common constants and input data *)

npri=86;                        pi=N[Pi,npri];
ep0=N[8854187818 10^-21,npri]; vep=1.00 10^-13;
mu0=N[pi*(4 10^-7),npri];      epmu=Sqrt[ep0/mu0];
vc=Sqrt[(1/(ep0*mu0))];        wleng=N[8300 10^-10,npri];
k0=N[2*pi/wleng,npri];          omg=vc*k0;
smt=1 10^-54;                   stp=N[1 10^-12,npri];

(* Multiple-layer structure *)

n=0; fl=7; ml=4; sl=1;
na=N[36 10^-1,npri]; nb=N[34 10^-1,npri];
nc=N[34 10^-1,npri];
nl={nc, na, nb, na, nb, na, nc }; (* Index profile *)
da=N[8 10^-9,npri]; db=N[12 10^-9,npri];
dl={Infinity, da, db, da, db, da, Infinity}; (* Thickness of the each
layer *)

<<ml-te.m  (* Loading in package for TE modes incidence *)
<<ml-tm.m (* Loading in package for TM modes incidence *)
```

(e) Main program for the dispersion compensation

```
dfl=OpenAppend["filename1.dat"]; (* Open a file for output data *)

(* Common constants *)

ep0=N[8854187818 10^-21,20];
wleng=N[15500 10^-10,20];
pi=N[Pi,20];          vk0=2*pi/wleng;
mu0=N[pi*(4 10^-7),20];
vc=N[Sqrt[(1/(ep0*mu0))],20];
epmu=Sqrt[ep0/mu0]; omg=vc*vk0;

(* Data of the input pulse *)
```

```
num=128;    cd=2.15;
tau0=N[24 10^-15,20];
tstp=36*tau0/(num-1);
tini=-(num/2-1/2)*tstp;
tfin=tini+(num-1)*tstp;
wstp=(2*pi/tstp)/num;
wini=-(num/2)*wstp+omg;
wfin=wini+(num-1)*wstp;
omgList=Table[wini+(jn-1)*wstp,{jn,1,num}];
k0List=omgList/vc;
xt[t_]:=Exp[-t^2/(2 tau0^2)]*Exp[I omg t];
xw[w_]:=Sqrt[2 pi tau0^2]*Exp[-(w-omg)^2*tau0^2/2];
dw[w_]:=Exp[-I Sqrt[(cd^2-1)]*tau0^2*(w-omg)^2/2];
tList=Table[Abs[xt[t]],{t,tini,tfin,tstp}];
aa=Fourier[tList]; bb=InverseFourier[aa]; (*bb : Input pulse*)

(* for the chirped grating structure *)

mmax=20;          vep=1.00 10^-13;
nmod=0;           norder=1;
nc=N[10 10^-1,20]; nf=N[161 10^-2,20];
r2=N[80 10^-2,20]; r3=1;
tk=N[15 10^-1,20]; tf1=tk/vk0;
tf2=r2*tf1;       tf3=r3*tf1;
ngr=193;          mdch=6;
noutst=1;         nstep=1;
<<s-chirp.m; (*Loading in the package and executing *)
Close[df1];

(* Data loading in for analysing *)

df1=OpenRead["filename1.dat"];
outtab=ReadList[df1];
cgrList=Table[outtab[[i,7]],{i,1,num}];
radloss=Table[outtab[[i,5]],{i,1,num}];
dbList=Table[outtab[[i,3]],{i,1,num}];
Close[df1];

(* Calculate the recompressed pulse *)

ca={};da={};
cg=Flatten[cgrList]; (* Complex reflection coefficients *)
ch=Join[Take[cg,-num/2],Take[cg,num/2]];
dh=Join[Take[dwList,-num/2],Take[dwList,num/2]];

nout=1;Do[
      ca=Append[ca,aa[[nout]]*Abs[ch[[nout]]]*
         Exp[I Arg[ch[[nout]]]]*dh[[nout]] ];
      da=Append[da,aa[[nout]]*dh[[nout]] ];
      nout=nout+1,
      {num}
      ];

(* Calculate the compensation efficiency *)

cb=InverseFourier[ca];  db=InverseFourier[da];
cdd=Abs[cb];
(*cdd : The ecompressed pulse from the deep chirped grating*)
db=Abs[db];
(*db : The broadened pulse from the dispersive medium*)
cdmax=Max[cdd]; bbmax=Max[Abs[bb]];
ceff=100(cdmax/bbmax);
Print["Cd= ",N[cd,5]," ceff= ",ceff];
cm=Max[cdd,Abs[bb],db];

(* Shapes of the pulses *)

fi=ListPlot[Abs[bb]/cm,PlotJoined->True,PlotRange->{0,1}];
(* fi: Input pulse  *)
fd=ListPlot[Abs[db]/cm,PlotJoined->True,PlotRange->{0,1}];
(* fd: Broadened pulse *)
ff=ListPlot[cdd/cm,PlotJoined->True,PlotRange->{0,1}];
(* ff: Recompressed pulse *)
Show[fi,fd,ff,Frame->True,
   FrameLabel->"Pulse Amplitude (A.U)",
      GridLines->Automatic,
   Prolog->Thickness[0.004],
     DefaultFont->{"Helvetica-Bold",14}];

(* Saving the shapes of the above pulses *)

df2=OpenAppend["filename2.dat"];
iist=1; Do[
daout={iist,Abs[db[[iist]]]/cm,
          cdd[[iist]]/cm,
          Abs[bb[[iist]]]/cm};
Write[df2,N[daout,10]];
iist=iist+1, {num} ];
Close[df2];

(* Graphic output for |R| and Pr *)

rfllist=Table[{dbList[[m]],Abs[cgrList[[m]]]},
      {m,1,num}];
fr=ListPlot[rfllist,PlotJoined->True,
      PlotRange->{0,1},Frame->True,
      FrameLabel->"Refl. Coefficient",
      GridLines->Automatic,
      Prolog->Thickness[0.1],
      DefaultFont->{"Helvetica-Bold",14}];
radlist=Table[{dbList[[m]],Abs[radloss[[m]]]},
      {m,1,num}];
fr=ListPlot[radlist,PlotJoined->True,
      PlotRange->{0,0.1},Frame->True,
      FrameLabel->"Total Rad. Power",
      GridLines->Automatic,
      Prolog->Thickness[0.004],
      DefaultFont->{"Helvetica-Bold",14}];

(* Writing the data of the |R| and Pr into a file *)

df3=OpenAppend["filename3.dat"];
iist=1; Do[
daout={dbList[[iist]],Abs[cgrList[[iist]]],radloss[[iist]]};
Write[df3,N[daout,10]];
iist=iist+1, {num} ];
Close[df3];

(* Rearranging the data of the phase responses *)

dwarg=Arg[dwList]; cndwarg=Arg[Conjugate[dwList]];
cgrarg=Arg[cgrList];
nn=1; ln=num/2; rn=num/2+1;
rdwg=Table[0,{i,num}]; cnrdwg=Table[0,{i,num}];
rcgarg=Table[0,{i,num}];
lm=0; rm=0; ldv=0; rdv=0; cglm=0; cgrm=0;  rcadj=0.;
cnlm=0; cnrm=0; cnldv=0; cnrdv=0; cgldv=0; cgrdv=0;
rdwg[[ln]]=dwarg[[ln]]; rdwg[[rn]]=dwarg[[rn]];
cnrdwg[[ln]]=cndwarg[[ln]]; cnrdwg[[rn]]=cndwarg[[rn]];
rcgarg[[ln]]=cgrarg[[ln]]; rcgarg[[rn]]=cgrarg[[rn]];
If[rcgarg[[ln]]*rcgarg[[rn]]<0,rcadj=2*pi,rcadj=0.];
rcgarg[[rn]]=rcgarg[[rn]]-rcadj;
Do[
If[dwarg[[ln-nn]]>dwarg[[ln-nn+1]],lm=lm+1;ldv=2*lm*pi];
rdwg[[ln-nn]]=dwarg[[ln-nn]]-ldv;
If[dwarg[[rn+nn]]>dwarg[[rn+nn-1]],rm=rm+1;rdv=2*rm*pi];
rdwg[[rn+nn]]=dwarg[[rn+nn]]-rdv;

If[cndwarg[[ln-nn]]<cndwarg[[ln-nn+1]],
     cnlm=cnlm+1;cnldv=2*cnlm*pi];
cnrdwg[[ln-nn]]=cndwarg[[ln-nn]]+cnldv;
If[cndwarg[[rn+nn]]<cndwarg[[rn+nn-1]],
     cnrm=cnrm+1;cnrdv=2*cnrm*pi];
cnrdwg[[rn+nn]]=cndwarg[[rn+nn]]+cnrdv;

If[cgrarg[[ln-nn]]<cgrarg[[ln-nn+1]],
     cglm=cglm+1;cgldv=2*cglm*pi];
rcgarg[[ln-nn]]=cgrarg[[ln-nn]]+cgldv;
If[cgrarg[[rn+nn]]>cgrarg[[rn+nn-1]]+pi,
     cgrm=cgrm+1;cgrdv=2*cgrm*pi];
rcgarg[[rn+nn]]=cgrarg[[rn+nn]]-cgrdv-rcadj;

 nn=nn+1,
 {num/2-1}
];

(* Graphic output for the phase responses *)

fg=ListPlot[rdwg/(2 pi),PlotJoined->True];
cnfg=ListPlot[cnrdwg/(2 pi),PlotJoined->True];
rcgfg=ListPlot[rcgarg/(2 pi),PlotJoined->True];

(* Writing the data of the phase responses into a file *)

df4=OpenAppend["filename4.dat"];
nst=1; Do[
```

```
dat2={N[(omgList[[nst]]-omg)/omg,10],
    N[dbList[[nst]],10],
    N[rdwg[[nst]]/(2 pi),10],
    N[cnrdwg[[nst]]/(2 pi),10],
    N[rcgarg[[nst]]/(2 pi),10]};
Write[df4,dat2];
nst=nst+1, {num} ];
Close[df4];
```

(f) Main program for the linearly chirped pulse compression

```
df1=OpenAppend["filename1.dat"];

(* Common constants *)

ep0=N[8854187818 10^-21,20];
wleng=N[15500 10^-10,20];
pi=N[Pi,20];          vk0=2*pi/wleng;
mu0=N[pi*(4 10^-7),20];
vc=N[Sqrt[(1/(ep0*mu0))],20];
epmu=Sqrt[ep0/mu0]; omg=vc*vk0;

(* Preparing the data of the chirped pulse *)

num=180; cc=3.72;
tau0=N[100 10^-15,20];
tstp=36*tau0/(num-1);
theval=Sqrt[cc^2-1]/(2 tau0^2);
uval=N[1+4*(theval*tau0^2)^2,20];
bval=(Sqrt[2 pi]/uval^(1/4))tau0*
    Exp[I ArcTan[2 theval tau0^2]/2];
tini=-(num/2-1/2)*tstp;
tfin=tini+(num-1)*tstp;
wstp=(2*pi/tstp)/num;
wini=-(num/2)*wstp+omg;
wfin=wini+(num-1)*wstp;
omgList=Table[wini+(jn-1)*wstp,{jn,1,num}];
k0List=omgList/vc;

xw[w_]:=bval*Exp[-(w-omg)^2 tau0^2 /(2 uval)]*
     Exp[-I*theval*tau0^4(w-omg)^2/uval];
optxw[w_]:=bval Exp[-(w-omg)^2 tau0^2 /(2 uval)];
ifw[w_]:=Exp[I*theval*tau0^4(w-omg)^2/uval];

wList=Table[xw[w],{w,wini,wfin,wstp}];
(* Data in w-space for input pulse *)
owList=Table[optxw[w],{w,wini,wfin,wstp}];
(* Data in w-space for compressed pulse from IF *)
ifwList=Table[ifw[w],{w,wini,wfin,wstp}];
(* Data of the phase for Ideal Filter IF *)

(* for the chirped grating structure *)

mmax=20;          vep=1.00 10^-13;
nmod=0;           norder=1;
nc=N[10 10^-1,20]; nf=N[161 10^-2,20];
r2=N[60 10^-2,20]; r3=1;
tk=N[15 10^-1,20]; tf1=tk/vk0;
tf2=r2*tf1;       tf3=r3*tf1;
ngr=165;          mdch=30;
noutst=1;         nstep=1;
<<dn-chdct.m; (* Loading in the package and executing *)
Close[df1];

(* Loading in the data for analysing *)

df1=OpenRead["filename1.dat"];
outtab=ReadList[df1];
cgrList=Table[outtab[[i,7]],{i,1,num}];
radloss=Table[outtab[[i,5]],{i,1,num}];
dbList=Table[outtab[[i,3]],{i,1,num}];
Close[df1];

wl=Abs[wList];
fw=InverseFourier[wList];
gw=Flatten[{Take[fw,-num/2],Take[fw,num/2]}];
(* Input pulse in t-space *)
fw=Abs[gw]; gw=.;
ofw=InverseFourier[owList];
ogw=Flatten[{Take[ofw,-num/2],Take[ofw,num/2]}];
(* Compressed pulse in t-space IF*)
ofw=Abs[ogw]; ogw=.;
fwmax=Max[fw]; owmax=Max[ofw];
rmax=Floor[owmax/fwmax]+1;

(* Calculate the pulse compressed by deep chirped grating *)

ca={};da={};cg=Flatten[cgrList];
nout=1;Do[
      ca=Append[ca,wList[[nout]]*Abs[cg[[nout]]]*
        Exp[I Arg[cg[[nout]]]] ];
      nout=nout+1,
  {num} ];

(* Calculate the compression efficiency *)

df2=OpenAppend["filename2.dat"];
cb=InverseFourier[ca];
cb=Abs[cb]; cdmax=Max[cb];
effc=100*cdmax/owmax;
Print["ccr= ",N[cc,6]];
Print["theta*tau0^2=",N[theval*tau0^2,6]];
Print["Compression efficiency ec= ",N[effc,8],"%"];
Write[df2,{N[theval*tau0^2,8],
          N[cc,6],N[effc,8]}];

(* Graphic output for the input and compressed pulses *)

fi=ListPlot[fw/fwmax,PlotJoined->True,
  PlotRange->{0,rmax}]; (* Input pulse *)
ff=ListPlot[ofw/fwmax,PlotJoined->True,
  PlotRange->{0,rmax}]; (* Compressed pulse IF *)
fg=ListPlot[cb/fwmax,PlotJoined->True,
  PlotRange->{0,rmax}]; (* Compressed pulse DCG *)
Show[fi,ff,fg,Frame->True,
   FrameLabel->"Pulse Amplitude (Arb. Units)",
     GridLines->Automatic];

(* Writing data of the above pulses into a file *)

df3=OpenAppend["filename3.dat"];
iist=1; Do[
daout={iist,Abs[fw[[iist]]]/fwmax,
          ofw[[iist]]/fwmax,
          cb[[iist]]/fwmax};
Write[df3N[daout,10]];
iist=iist+1, {num} ];
Close[df3];

(* Graphic output for |R| and Pr *)

rfllist=Table[{dbList[[m]],Abs[cgrList[[m]]]},
      {m,1,num}];
fr=ListPlot[rfllist,PlotJoined->True,
      PlotRange->{0,1},Frame->True,
      FrameLabel->"Refl. Coefficient",
      GridLines->Automatic];
radlist=Table[{dbList[[m]],Abs[radloss[[m]]]},
      {m,1,num}];
fr=ListPlot[radlist,PlotJoined->True,
      PlotRange->{0,0.5},Frame->True,
      FrameLabel->"Total Rad. Power",
      GridLines->Automatic];

(* Writing the data of the |R| and Pr into a file *)

df4=OpenAppend["filename4.dat"];
iist=1; Do[
daout={dbList[[iist]],
    Abs[cgrList[[iist]]],
    radloss[[iist]]};
Write[df4,N[daout,10]];
iist=iist+1, {num} ];
Close[df4];

(* Rearranging the phase responses *)

dwarg=Arg[wList]; cndwarg=Arg[ifwList];
cgrarg=Arg[cgrList];
nn=1; ln=num/2; rn=num/2+1;
rdwg=Table[0,{i,num}]; cnrdwg=Table[0,{i,num}];
rcgarg=Table[0,{i,num}];
lm=0; rm=0; ldv=0; rdv=0; cglm=0; cgrm=0; rcadj=0.;
cnlm=0; cnrm=0; cnldv=0; cnrdv=0; cgldv=0; cgrdv=0;
rdwg[[ln]]=dwarg[[ln]]; rdwg[[rn]]=dwarg[[rn]];
cnrdwg[[ln]]=cndwarg[[ln]]; cnrdwg[[rn]]=cndwarg[[rn]];
rcgarg[[ln]]=cgrarg[[ln]]; rcgarg[[rn]]=cgrarg[[rn]];
If[rcgarg[[ln]]*rcgarg[[rn]]<0,rcadj=2*pi,rcadj=0.];
rcgarg[[rn]]=rcgarg[[rn]]-rcadj;
Do[
If[dwarg[[ln-nn]]>dwarg[[ln-nn+1]],lm=lm+1;ldv=2*lm*pi];
```

```
rdwg[[ln-nn]]=dwarg[[ln-nn]]-ldv;
If[dwarg[[rn+nn]]>dwarg[[rn+nn-1]],rm=rm+1;rdv=2*rm*pi];
rdwg[[rn+nn]]=dwarg[[rn+nn]]-rdv;

If[cndwarg[[ln-nn]]<cndwarg[[ln-nn+1]],
    cnlm=cnlm+1;cnldv=2*cnlm*pi];
cnrdwg[[ln-nn]]=cndwarg[[ln-nn]]+cnldv;
If[cndwarg[[rn+nn]]<cndwarg[[rn+nn-1]],
    cnrm=cnrm+1;cnrdv=2*cnrm*pi];
cnrdwg[[rn+nn]]=cndwarg[[rn+nn]]+cnrdv;

If[cgrarg[[ln-nn]]<cgrarg[[ln-nn+1]],
    cglm=cglm+1;cgldv=2*cglm*pi];
rcgarg[[ln-nn]]=cgrarg[[ln-nn]]+cgldv;
If[cgrarg[[rn+nn]]>cgrarg[[rn+nn-1]]+pi,
    cgrm=cgrm+1;cgrdv=2*cgrm*pi];
rcgarg[[rn+nn]]=cgrarg[[rn+nn]]-cgrdv-rcadj;
nn=nn+1, {num/2-1} ];

(* Graphic output for the phase responses *)

fg=ListPlot[rdwg/(2 pi),PlotJoined->True];
cnfg=ListPlot[cnrdwg/(2 pi),PlotJoined->True];
rcgfg=ListPlot[rcgarg/(2 pi),PlotJoined->True];

(* Quadratic curves fitting *)

(-theval*tau0^4/uval)
(-theval*tau0^4/uval)*wstp^2
Fit[rdwg,{1,x,x^2},x]
Fit[cnrdwg,{1,x,x^2},x]
cfit=Fit[rcgarg,{1,x,x^2},x]
Plot[cfit/(2*pi),{x,1,(wfin-wini)/wstp}]

(* Writing the data of the phase responses into a file *)

df4=OpenAppend["filename4,dat"];
cftab=Table[cfit,{x,1,num}];
nst=1; Do[
dat2={N[(omgList[[nst]]-omg)/omg,6], (* Frequency deviation *)
 N[dbList[[nst]],6], (* The detuning *)
 N[rdwg[[nst]]/(2 pi),6], (* Phase response of the input pulse *)
 N[cnrdwg[[nst]]/(2 pi),6], (* Phase resp. of the pulse comp. by IF
*)
 N[rcgarg[[nst]]/(2 pi),6], (* Phase resp. of the pulse comp. by DCG
*)
 N[cftab[[nst]]/(2 pi),6]}; (* Phase resp. of the fitting curve *)
Write[df4,dat2];
nst=nst+1, {num} ];
Close[df4];
```

Appendix B

```
(* PACKAGE FOR CHIRPED GRATINGS
   IN SYMMETRIC PLANAR WAVEGUIDES
   PROGRAM NAME: s-chirp.m          *)

(* For TE Mode Incidences *)

(*PART A*)
(* Common Constants *)

ep0=N[8854187818 10^-21,20];   vep=1.0 10^-13;
pi=N[Pi,20];                   mu0=N[pi*(4 10^-7),20];
vc=N[Sqrt[(1/(ep0*mu0))],20];  epmu=Sqrt[ep0/mu0];
omg=vc*vk0;

(*PART B*)
(* Mode Distributions *)

fv[n_,t_,b_]:=Sqrt[af^2-b^2]*t-(ArcTan[Sqrt[(b^2-ac^2)/(af^2-
b^2)]]+(n/2)*pi);
fvp[n_,t_,bp_]:=D[fv[n,t,b],b]/.b->bp;
vb[n_,t_,b_]:=b-fv[n,t,b]/fvp[n,t,b];

ef[gc_,t_,b_]:=Sqrt[(2*omg*mu0)/(b*t+b/gc)];
ec[gc_,kf_,t_,b_]:=ef[gc,t,b]*Cos[kf*t];
e1[gc_,kf_,y_,t_,b_]:=ec[gc,kf,t,b]*Exp[-gc(y-t)];
pe1[gc_,kf_,vy_,t_,b_]:=D[e1[gc,kf,y,t,b],y]/.y->vy;
e2[gc_,kf_,y_,t_,b_]:=ef[gc,t,b]*Cos[kf*y];
pe2[gc_,kf_,vy_,t_,b_]:=D[e2[gc,kf,y,t,b],y]/.y->vy;

rephc[kc_,kf_,t_]:=ArcTan[kf*Tan[kf*t]/kc];
vec[kc_,b_]:=1/Sqrt[pi*Abs[b]/(2*omg*mu0)];
reef[kc_,kf_,t_,phc_,b_]:=Abs[vec[kc,b]*Cos[phc]/Cos[kf*t]];
reec[kc_,kf_,t_,phc_,b_]:=reef[kc,kf,t,phc,b]*Cos[kf*t]/Cos[phc];
ree1[kc_,kf_,y_,t_,phc_,b_]:=reec[kc,kf,t,phc,b]*Cos[kc*(y-t)+phc];
pree1[kc_,kf_,vy_,t_,phc_,b_]:=D[ree1[kc,kf,y,t,phc,b],y]/.y->vy;
ree2[kc_,kf_,y_,t_,phc_,b_]:=reef[kc,kf,t,phc,b]*Cos[kf*y];
pree2[kc_,kf_,vy_,t_,phc_,b_]:=D[ree2[kc,kf,y,t,phc,b],y]/.y->vy;

(*PART C*)
(* For Propagation Constants *)

k0=vk0; ac=nc*k0; af=nf*k0;
 vnf=Sqrt[nf^2-nc^2]*k0;
 tcut=Table[m*(pi/vnf),{m,10}];
 m=0; nt1=1; sbe=ac+(af-ac)/2;
   Do[
     If[nt1>10,m=5; Break[] ];
     vbe=vb[nmod,tf1,sbe]; bett=vbe;
     If[vbe<af&&vbe>ac,Break[] ];
     If[vbe>=af,
       sbe=af-(1 10^-2)*(af-ac),sbe=ac+(1 10^-2)*(af-ac)];
     ++nt1,
     {20}
    ];
  Do[
     vbe=vb[nmod,tf1,vbe];
     If[Abs[vbe-bett]<(1 10^-24),Break[] ];
     bett=vbe,
    {20}
   ];
 be1=bett;
egc1=Sqrt[be1^2-ac^2];ekf1=Sqrt[af^2-be1^2];

 m=0; nt1=1; sbe=ac+(af-ac)/2;
  Do[
    If[nt1>10,m=5;Break[] ];
    vbe=vb[nmod,tf2,sbe];bett=vbe;
    If[vbe<af && vbe>ac,Break[] ];
    If[vbe>=af,
      sbe=af-(1 10^-2)*(af-ac),sbe=ac+(1 10^-2)*(af-ac)];
    ++nt1,
   {20}
  ];
  Do[
    vbe=vb[nmod,tf2,vbe];
    If[Abs[vbe-bett]<(1 10^-24),Break[] ];
    bett=vbe,
   {20}
  ];
  be2=bett;
  egc2=Sqrt[be2^2-ac^2];ekf2=Sqrt[af^2-be2^2];

  be3=be1; egc3=egc1; ekf3=ekf1;
  lmda2=norder*pi/(be2+be3); lmda3=lmda2;
  be0=(be2+be3)/2;

cgrList={};
nout=noutst;
Do[
    k0=k0List[[nout]];
   ac=nc*k0; af=nf*k0;

   m=0; nt1=1; sbe=ac+(af-ac)/2;
   Do[
     If[nt1>10,m=5; Break[] ];
     vbe=vb[nmod,tf1,sbe]; bett=vbe;
     If[vbe<af&&vbe>ac,Break[] ];
     If[vbe>=af,
       sbe=af-(1 10^-2)*(af-ac),sbe=ac+(1 10^-2)*(af-ac)];
     ++nt1,
    {20}
   ];
   Do[
     vbe=vb[nmod,tf1,vbe];
     If[Abs[vbe-bett]<(1 10^-24),Break[] ];
     bett=vbe,
    {20}
   ];
 be1=bett;
 egc1=Sqrt[be1^2-ac^2];ekf1=Sqrt[af^2-be1^2];

 m=0; nt1=1; sbe=ac+(af-ac)/2;
  Do[
    If[nt1>10,m=5;Break[] ];
    vbe=vb[nmod,tf2,sbe];bett=vbe;
    If[vbe<af && vbe>ac,Break[] ];
    If[vbe>=af,
      sbe=af-(1 10^-2)*(af-ac),sbe=ac+(1 10^-2)*(af-ac)];
    ++nt1,
   {20}
  ];
  Do[
    vbe=vb[nmod,tf2,vbe];
    If[Abs[vbe-bett]<(1 10^-24),Break[] ];
    bett=vbe,
   {20}
  ];
  be2=bett;
  egc2=Sqrt[be2^2-ac^2];ekf2=Sqrt[af^2-be2^2];

  be3=be1;    egc3=egc1;    ekf3=ekf1;
  detk0=k0-vk0; detb=(be2+be3)/2-be0;

(*PART D*)
(* For Inner Products *)

fk[b2_,gc2_,gc3_,kf2_,kf3_]:=(b2/(omg*mu0))*((af^2-
ac^2)/((kf3^2-kf2^2)(gc2^2+kf3^2)));

pu2=pe1[egc2,ekf2,tf2,tf2,be2];
v2=e2[egc3,ekf3,tf2,tf3,be3];
u2=e1[egc2,ekf2,tf2,tf2,be2];
pv2=pe2[egc3,ekf3,tf2,tf3,be3];
pu3=pe1[egc2,ekf2,tf3,tf2,be2];
v3=e2[egc3,ekf3,tf3,tf3,be3];
u3=e1[egc2,ekf2,tf3,tf2,be2];
pv3=pe2[egc3,ekf3,tf3,tf3,be3];
kuv=fk[be2,egc2,egc3,ekf2,ekf3]*((pu2*v2-u2*pv2)-(pu3*v3-
u3*pv3));

angmax=N[pi/2-anglimt*pi/180,20];
dang=angmax/(mmax); tang=Table[stm*dang,{stm,mmax}];
dtb=Table[ac*Cos[tang[[stm]]]*dang,{stm,mmax}];
tb=Table[ac*Sin[tang[[stm]]],{stm,mmax}];

m=1; akueList={}; bkueList={};
   akevList={}; bkevList={};
   kdList={};  tebe={};

Do[
```

```
  kc3=tb[[m]];       b3=Sqrt[ac^2-kc3^2];
  tebe=Append[tebe,b3];
  kf3=Sqrt[af^2-b3^2]; gc3=I kc3;
  phc3=rephc[kc3,kf3,tf3];
  ev2=ree2[kc3,kf3,tf2,tf3,phc3,b3];
  pev2=pree2[kc3,kf3,tf2,tf3,phc3,b3];
  ev3=ree2[kc3,kf3,tf3,tf3,phc3,b3];
  pev3=pree2[kc3,kf3,tf3,tf3,phc3,b3];
  vk=fk[be2,egc2,gc3,ekf2,kf3]*((pu2*ev2-u2*pev2)-(pu3*ev3-
u3*pev3));
  If[EvenQ[m],kd=(2/3)*dtb[[m]],kd=(4/3)*dtb[[m]]];
  If[m==mmax,kd=(1/3)*dtb[[m]]];
  kdList=Append[kdList,kd];
  akueList=Append[akueList,kd*vk];
  bkueList=Append[bkueList,vk];

  kc2=tb[[m]];       b2=tebe[[m]];
  kf2=Sqrt[af^2-b2^2];   gc2=I kc2;
  phc2=rephc[kc2,kf2,tf2];
  peu2=pree1[kc2,kf2,tf2,tf2,phc2,b2];
  eu2=ree1[kc2,kf2,tf2,tf2,phc2,b2];
  peu3=pree1[kc2,kf2,tf3,tf2,phc2,b2];
  eu3=ree1[kc2,kf2,tf3,tf2,phc2,b2];
  vk=fk[b2,gc2,egc3,kf2,ekf3]*((peu2*v2-eu2*pv2)-(peu3*v3-
eu3*pv3));
  akevList=Append[akevList,kd*vk];
  bkevList=Append[bkevList,vk];

  m=m+1,
 {mmax}
 ];

(*PART E*)
(* For Transfer Matrices *)

m0=Table[0,{mmax}]; mm0=Table[0,{mmax+1},{mmax+1}];
ilist=Table[1,{1+mmax}]; mi=DiagonalMatrix[ilist];

akevList=Prepend[akevList,kuv];
akueList=Prepend[akueList,kuv];

mcList={};
alist=akevList;
mcList=Append[mcList,alist];
m=1; Do[
 alist=Flatten[{bkueList[[m]],ReplacePart[m0,1,m]}];
 mcList=Append[mcList,alist];
 m=m+1,
 {mmax}
    ];
ma1=mcList; mb1=-1 mcList;

mcList={};
alist=akueList;
mcList=Append[mcList,alist];

m=1; Do[
 alist=Flatten[{bkevList[[m]],ReplacePart[m0,1,m]}];
 mcList=Append[mcList,alist];
 m=m+1,
 {mmax}
    ];
ma2=mcList; mb2=mcList;
mcList=.;  alist=.;
akueList=.; bkueList=.; akevList=.; bkevList=.;

me={}; mf={}; mg={}; mh={};
m=1; Do[
 me=Append[me,Flatten[{mi[[m]],mi[[m]]}] ];
 mf=Append[mf,Flatten[{ma1[[m]],mb1[[m]]}] ];
 mg=Append[mg,Flatten[{ma2[[m]],mb2[[m]]}] ];
 mh=Append[mh,Flatten[{mi[[m]],-1 mi[[m]]}] ];
 m=m+1,
 {mmax+1}
    ];
ma=Join[me,mf]; mb=Join[mg,mh];

ma1=.; mb1=.; ma2=.; mb2=.;
me=.;  mf=.;  mg=.;  mh=.;

ms23=Inverse[ma].mb;
ms12=Inverse[ms23];
ma=.; mb=.;

(*msr1=ms12.Inverse[mt2].ms23.Inverse[mt3];*)
(*ms12 for step-down and ms23 for step-up*)

(*PART F*)
(* For Chirp Constants and Grating Structures *)

lmda=lmda2+lmda3;    dslp=2*mdch*lmda/(ngr-1)^2;
leng=0;              lm0=lmda+(ngr+1)*dslp/2;
nsg=1; Do[
     lmphi=(lm0-nsg*dslp)/2;
     leng=leng+2*lmphi;
     ph2list={Exp[-I be2*lmphi]};
     ph3list={Exp[-I be3*lmphi]};
     m=1; Do[
          ph2list=Append[ph2list,Exp[-I tebe[[m]]*lmphi]];
          ph3list=Append[ph3list,Exp[-I tebe[[m]]*lmphi]];
          m=m+1,
          {mmax}
         ];
     mpha=Join[Conjugate[ph2list],ph2list];
     imph2=DiagonalMatrix[mpha]; mpha=.;
     mphb=Join[Conjugate[ph3list],ph3list];
     imph3=DiagonalMatrix[mphb]; mphb=.;
     msr=ms12.imph2.ms23.imph3;
     If[nsg==1,msr1=msr,msr1=msr.msr1];
     nsg=nsg+1,
    {ngr}
   ];

msr=msr1; msr1=.; ms12=.; ns23=.;
leng=leng-lmphi;
ph2list=.; mpha=.; mphb=.;
ph2list=.; imph2=.; imph3=.;

(*PART G*)
(* For Coefficients *)

m11={}; m12={}; m21={}; m22={};
m=1; Do[
 m11=Append[m11,Drop[msr[[m]],-(mmax+1)] ];
 m12=Append[m12,Drop[msr[[m]],(mmax+1)] ];
 m21=Append[m21,Drop[msr[[m+(1+mmax)]],-(mmax+1)] ];
 m22=Append[m22,Drop[msr[[m+(1+mmax)]],(mmax+1)] ];
 m=m+1,
 {mmax+1}
 ];
msr=.;

mp={}; mq={}; mr={}; ms={};
m=1; Do[
 mp=Append[mp,Flatten[{-1 m11[[m]],mm0[[m]]}] ];
 mq=Append[mq,Flatten[{-1 m21[[m]],mi[[m]]}] ];
 mr=Append[mr,Flatten[{-1 mi[[m]],m12[[m]]}] ];
 ms=Append[ms,Flatten[{-1 mm0[[m]],m22[[m]]}] ];
 m=m+1,
 {mmax+1}
    ];

m11=.; m12=.; m21=.; m22=.;

ma3=Join[mp,mq]; mb3=Join[mr,ms];
mp=.; mq=.; mr=.; ms=.;
minp=Flatten[{1,m0,0,m0}];
ms3=Inverse[ma3].mb3;
mcc=ms3.minp;
ma3=.; mb3=.;

cgt=mcc[[1]]; cgr=mcc[[2+mmax]];
cet=Take[mcc,{2,1+mmax}];
cer=Take[mcc,-mmax];
pgr=Abs[cgr]^2;pgt=Abs[cgt]^2;
cgrList=Append[cgrList,cgr];

(*PART H*)
(* For Data Output *)

per=0; pet=0;
intList={}; inrList={};
m=1; Do[
  int=ac*Cos[tang[[m]]]*Abs[mcc[[1+m]]]^2;
  inr=ac*Abs[Cos[tang[[m]]]]*Abs[mcc[[2+mmax+m]]]^2;
  intList=Append[intList,{tang[[m]]*180/pi,int}];
  inrList=Append[inrList,{180-tang[[m]]*180/pi,inr}];
```

```
  per=per+kdList[[m]]*Abs[cer[[m]]]^2;
  pet=pet+kdList[[m]]*Abs[cet[[m]]]^2;
  m=m+1, {mmax} ];
pt=pgr+pgt+per+pet;
rph=Arg[cgr]*180/pi; If[rph<0,rph=rph+360];
tph=Arg[cgt]*180/pi; If[tph<0,tph=tph+360];

m0=.; mm0=.; iList=.; mi=.;

da1=N[da1=k0/vk0,8]; da2=N[Sqrt[pgr],10];
da3=N[detb*leng,10]; da4=N[Sqrt[pgt],10];
da5=N[per+pet,10];  da6=N[rph,8];
da7=cgr;            da8=N[aa[[nout]],10];
da={da1,da2,da3,da4,da5,da6,da7,da8};
Write[df1,da];

  Print["TE modes"];
  Print["nout=",nout];
  Print["t3/t1=",N[r3,4]," t3=",N[tf3,6]," slope=",N[mdch/(ngr-
1)^2,8]];
  Print["k0*t1=",N[k0*tf1,4]," k0*t2=",N[k0*tf2,4],"
        k0*t3=",N[k0*tf3,4]];
  Print["k0'/k0=",N[k0/vk0,8]," db*L=",N[detb*leng,8],
        " k0'*b=",N[k0*lmda2,8]];
  Print["Lambda2/tf1=",N[lmda2/tf1,10],"
k0*b=",N[vk0*lmda2,8]];
  Print["Lambda2=",N[lmda2,10],
        "  beta2*Lambda2=",N[be2*lmda2,10]];
  Print["Lambda3/tf1=",N[lmda3/tf1,10]," mdch=",N[mdch,4]];
  Print["Lambda3=",N[lmda3,10],
        " beta3*Lambda3=",N[be3*lmda3,10]];
  Print["No pds=",ngr," Total corrugated length",N[leng,8]];
  Print["t2/t1=",N[r2,4]," t1*k0=",N[tf1*k0,6],"
t2*k0=",N[tf2*k0,6]];
  Print["ch const.=",N[mdch,4]," DLmda=",N[lmda*mdch/(ngr-
2),8]];
  Print["nc=",N[nc,8],",    nf=",N[nf,8]];
  Print["Cutoff thickness (tc/2) of m=2   =",N[tcut[[2]]/2,10]];
  Print["The number of panels in Rad- angles=",mmax];Print[" "];
  Print["TE(beta1)=",N[be1,10] ];
  Print["TE(beta2)=",N[be2,10] ];
  Print["TE(beta3)=",N[be3,10] ];Print[" "];
  Print["Kuv=",N[kuv,10]];
  Print[" "];
  Print["Cutoff (tc/2)*vk0 of m=2  =",N[tcut[[2]]*vk0/2,10]];
  Print["a1- =",N[cgr,10]];Print["a2+ =",N[cgt,10]];
  Print[" "];
  Print["G-mode   refl. power=",N[pgr,10]];
  Print["G-mode   refl. coeff=",N[Sqrt[pgr],10]];
  Print["G-mode   Arg[R]   =",N[rph,10]];
  Print["G-mode   tran. power=",N[pgt,10]];
  Print["G-mode   tran. coeff=",N[Sqrt[pgt],10]];
  Print["G-mode   Arg[T]   =",N[tph,10]];
  Print["Rad-modes refl. power=",N[per,10]];
  Print["Rad-modes tran. power=",N[pet,10]];
  Print["Rad-modes total power=",N[per+pet,10]];
  Print["Total Power      =",N[pt,10]];
  Print[" "];

If[nout==stopnt, Break[] ];
nout=nout+nstep,
{(num-noutst+1)/nstep} ];

Print[" END OF JOB "];
```

Appendix C

```
(*FOR PERIODIC GRATINGS ON ONE SIDE OF
   THE SYMMETRIC PLANAR WAVEGUIDE
   PROGRAM NAME: as-dngr.m                    *)

(* For TE Mode Incidences *)

(*PART A*)
(* Common Constants *)

ep0=N[8854187818 10^-21,20];    vep=1.00 10^-13;
pi=N[Pi,20];                    mu0=N[pi*(4 10^-7),20];
vc=N[Sqrt[(1/(ep0*mu0))],20];   epmu=Sqrt[ep0/mu0];
omg=vc*vk0;

(*PART B*)
(* Mode Distributions *)

fv[n_,t_,b_]:=Sqrt[af^2-b^2]*t-(ArcTan[Sqrt[(b^2-ac^2)/(af^2-
b^2)]]+(n/2)*pi);
fvp[n_,t_,bp_]:=D[fv[n,t,b],b]/.b->bp;
vb[n_,t_,b_]:=b-fv[n,t,b]/fvp[n,t,b];

ef[gc_,t_,b_]:=Sqrt[(2*omg*mu0)/(b*t/2+b/gc)];
ec[gc_,kf_,t_,b_]:=ef[gc,t,b]*Cos[kf*t/2];
e1[gc_,kf_,y_,t_,b_]:=ec[gc,kf,t,b]*Exp[-gc(y-t)];
pe1[gc_,kf_,vy_,t_,b_]:=D[e1[gc,kf,y,t,b],y]/.y->vy;
e2[gc_,kf_,y_,t_,b_]:=ef[gc,t,b]*Cos[kf*(y-t/2)];
pe2[gc_,kf_,vy_,t_,b_]:=D[e2[gc,kf,y,t,b],y]/.y->vy;
e3[gc_,kf_,y_,t_,b_]:=ec[gc,kf,t,b]*Exp[gc*y];
pe3[gc_,kf_,vy_,t_,b_]:=D[e3[gc,kf,y,t,b],y]/.y->vy;

vrph[kf_,t_]:=kf*t/2;

rephc[kc_,kf_,t_]:=ArcTan[kf*Tan[kf*t/2]/kc];
veec[kc_,b_]:=1/Sqrt[pi*Abs[b]/(2*omg*mu0)];
reef[kc_,kf_,t_,phc_,b_]:=Abs[veec[kc,b]/Sqrt[(Cos[vrph[kf,t]])^2+
                (kf^2/kc^2)*(Sin[vrph[kf,t]])^2]];
reec[kc_,kf_,t_,phc_,b_]:=reef[kc,kf,t,phc,b]*Cos[kf*t/2]/Cos[phc];
ree1[kc_,kf_,y_,t_,phc_,b_]:=reec[kc,kf,t,phc,b]*Cos[kc*(y-t)+phc];
pree1[kc_,kf_,vy_,t_,phc_,b_]:=D[ree1[kc,kf,y,t,phc,b],y]/.y->vy;
ree2[kc_,kf_,y_,t_,phc_,b_]:=reef[kc,kf,t,phc,b]*Cos[kf*(y-t/2)];
pree2[kc_,kf_,vy_,t_,phc_,b_]:=D[ree2[kc,kf,y,t,phc,b],y]/.y->vy;
ree3[kc_,kf_,y_,t_,phc_,b_]:=reec[kc,kf,t,phc,b]*Cos[kc*y-phc];
pree3[kc_,kf_,vy_,t_,phc_,b_]:=D[ree3[kc,kf,y,t,phc,b],y]/.y->vy;

rophc[kc_,kf_,t_]:=ArcCot[kf*Cot[kf*t/2]/kc];
voec[kc_,b_]:=1/Sqrt[pi*Abs[b]/(2*omg*mu0)];
roef[kc_,kf_,t_,phc_,b_]:=Abs[voec[kc,b]/Sqrt[(Sin[vrph[kf,t]])^2+
                (kf^2/kc^2)*(Cos[vrph[kf,t]])^2]];
roec[kc_,kf_,t_,phc_,b_]:=roef[kc,kf,t,phc,b]*Sin[kf*t/2]/Sin[phc];
roe1[kc_,kf_,y_,t_,phc_,b_]:=roec[kc,kf,t,phc,b]*Sin[kc*(y-t)+phc];
proe1[kc_,kf_,vy_,t_,phc_,b_]:=D[roe1[kc,kf,y,t,phc,b],y]/.y->vy;
roe2[kc_,kf_,y_,t_,phc_,b_]:=roef[kc,kf,t,phc,b]*Sin[kf*(y-t/2)];
proe2[kc_,kf_,vy_,t_,phc_,b_]:=D[roe2[kc,kf,y,t,phc,b],y]/.y->vy;
roe3[kc_,kf_,y_,t_,phc_,b_]:=roec[kc,kf,t,phc,b]*Sin[kc*y-phc];
proe3[kc_,kf_,vy_,t_,phc_,b_]:=D[roe3[kc,kf,y,t,phc,b],y]/.y->vy;

(*PART C*)
(* For Propagation Constants *)

k0=vk0; ac=nc*k0; af=nf*k0; as=ac;
vnf=Sqrt[nf^2-nc^2]*k0;
tcut=Table[m*(pi/vnf),{m,10}];
 m=0; nt1=1; sbe=ac+(af-ac)/2;
  Do[
    If[nt1>10,m=5; Break[] ];
    vbe=vb[nmod,tf1/2,sbe]; bett=vbe;
    If[vbe<af&&vbe>ac,Break[] ];
    If[vbe>=af,
      sbe=af-(1 10^-2)*(af-ac),sbe=ac+(1 10^-2)*(af-ac)];
    ++nt1,
   {20}
   ];
  Do[
    vbe=vb[nmod,tf1/2,vbe];
    If[Abs[vbe-bett]<(1 10^-24),Break[] ];
    bett=vbe,
   {20}
   ];
  be1=bett;
  egc1=Sqrt[be1^2-ac^2];ekf1=Sqrt[af^2-be1^2];

  m=0; nt1=1; sbe=ac+(af-ac)/2;
   Do[
     If[nt1>10,m=5;Break[] ];
     vbe=vb[nmod,tf2/2,sbe];bett=vbe;
     If[vbe<af && vbe>ac,Break[] ];
     If[vbe>=af,
       sbe=af-(1 10^-2)*(af-ac),sbe=ac+(1 10^-2)*(af-ac)];
     ++nt1,
    {20}
    ];
   Do[
     vbe=vb[nmod,tf2/2,vbe];
     If[Abs[vbe-bett]<(1 10^-24),Break[] ];
     bett=vbe,
    {20}
    ];
   be2=bett;
   egc2=Sqrt[be2^2-ac^2];ekf2=Sqrt[af^2-be2^2];

   be3=be1; egc3=egc1; ekf3=ekf1;
   be0=(be2+be3)/2;

 nout=noutst;
 Do[
     k0=k0List[[nout]];
    ac=nc*k0; af=nf*k0; as=ac;


  m=0; nt1=1; sbe=ac+(af-ac)/2;
   Do[
     If[nt1>10,m=5; Break[] ];
     vbe=vb[nmod,tf1/2,sbe]; bett=vbe;
     If[vbe<af&&vbe>ac,Break[] ];
     If[vbe>=af,
       sbe=af-(1 10^-2)*(af-ac),sbe=ac+(1 10^-2)*(af-ac)];
     ++nt1,
     {20}
    ];
   Do[
     vbe=vb[nmod,tf1/2,vbe];
     If[Abs[vbe-bett]<(1 10^-24),Break[] ];
     bett=vbe,
     {20}
    ];
  be1=bett;
  egc1=Sqrt[be1^2-ac^2];ekf1=Sqrt[af^2-be1^2];

  m=0; nt1=1; sbe=ac+(af-ac)/2;
   Do[
     If[nt1>10,m=5;Break[] ];
     vbe=vb[nmod,tf2/2,sbe];bett=vbe;
     If[vbe<af && vbe>ac,Break[] ];
     If[vbe>=af,
       sbe=af-(1 10^-2)*(af-ac),sbe=ac+(1 10^-2)*(af-ac)];
     ++nt1,
    {20}
    ];
   Do[
     vbe=vb[nmod,tf2/2,vbe];
     If[Abs[vbe-bett]<(1 10^-24),Break[] ];
     bett=vbe,
    {20}
    ];
   be2=bett;
   egc2=Sqrt[be2^2-ac^2];ekf2=Sqrt[af^2-be2^2];

   be3=be1; egc3=egc1; ekf3=ekf1;
   detk0=k0-vk0; detb=(be2+be3)/2-be0;

lmda2=norder*pi/(be2+be3); (*norder: grating orders*)
lmda3=lmda2;
lmda1=lmda3; lmda=lmda2+lmda3;
leng=ngr*lmda-lmda3; (*leng: grating length*)

 (*PART D*)
(* For Inner Products *)
fk[b2_,gc2_,gc3_,kf2_,kf3_]:=(b2/(2*omg*mu0))*((af^2-
ac^2)/((kf3^2-kf2^2)(gc2^2+kf3^2)));

pu2=pe1[egc2,ekf2,tf2,tf2,be2];
```

```
v2=e2[egc3,ekf3,tf2,tf3,be3];
u2=e1[egc2,ekf2,tf2,tf2,be2];
pv2=pe2[egc3,ekf3,tf2,tf3,be3];
pu3=pe1[egc2,ekf2,tf3,tf2,be2];
v3=e2[egc3,ekf3,tf3,tf3,be3];
u3=e1[egc2,ekf2,tf3,tf2,be2];
pv3=pe2[egc3,ekf3,tf3,tf3,be3];
kuv=fk[be2,egc2,egc3,ekf2,ekf3]*((pu2*v2-u2*pv2)-(pu3*v3-
u3*pv3));

angmax=N[pi/2-anglimt*pi/180,20];
dang=angmax/(mmax); tang=Table[stm*dang,{stm,mmax}];
dtb=Table[ac*Cos[tang[[stm]]]*dang,{stm,mmax}];
tb=Table[ac*Sin[tang[[stm]]],{stm,mmax}];

m=1; akueList={}; bkueList={}; akevList={}; bkevList={};
    akuoList={}; bkuoList={}; akovList={}; bkovList={};
    kdList={};  tebe={};

Do[
  kc3=tb[[m]];        b3=Sqrt[ac^2-kc3^2];
  tebe=Append[tebe,b3];
  kf3=Sqrt[af^2-b3^2];  gc3=I kc3;

  ephc3=rephc[kc3,kf3,tf3];
  eev2=ree2[kc3,kf3,tf2,tf3,ephc3,b3];
  peev2=pree2[kc3,kf3,tf2,tf3,ephc3,b3];
  eev3=ree2[kc3,kf3,tf3,tf3,ephc3,b3];
  peev3=pree2[kc3,kf3,tf3,tf3,ephc3,b3];
  vk=fk[be2,egc2,gc3,ekf2,kf3]*((pu2*eev2-u2*peev2)-
        (pu3*eev3-u3*peev3));
  If[EvenQ[m],kd=(2/3)*dtb[[m]],kd=(4/3)*dtb[[m]]];
  If[m==mmax,kd=(1/3)*dtb[[m]]];
  kdList=Append[kdList,kd];
  akueList=Append[akueList,kd*vk];
  bkueList=Append[bkueList,vk];

  ophc3=rophc[kc3,kf3,tf3];
  oev2=roe2[kc3,kf3,tf2,tf3,ophc3,b3];
  poev2=proe2[kc3,kf3,tf2,tf3,ophc3,b3];
  oev3=roe2[kc3,kf3,tf3,tf3,ophc3,b3];
  poev3=proe2[kc3,kf3,tf3,tf3,ophc3,b3];
  vk=fk[be2,egc2,gc3,ekf2,kf3]*((pu2*oev2-u2*poev2)-
        (pu3*oev3-u3*poev3));
  akuoList=Append[akuoList,kd*vk];
  bkuoList=Append[bkuoList,vk];

  kc2=tb[[m]];        b2=tebe[[m]];
  kf2=Sqrt[af^2-b2^2];  gc2=I kc2;

  ephc2=rephc[kc2,kf2,tf2];
  peeu2=pree1[kc2,kf2,tf2,tf2,ephc2,b2];
  eeu2=ree1[kc2,kf2,tf2,tf2,ephc2,b2];
  peeu3=pree1[kc2,kf2,tf3,tf2,ephc2,b2];
  eeu3=ree1[kc2,kf2,tf3,tf2,ephc2,b2];
  vk=fk[b2,gc2,egc3,kf2,ekf3]*((peeu2*v2-eeu2*pv2)-
        (peeu3*v3-eeu3*pv3));
  akevList=Append[akevList,kd*vk];
  bkevList=Append[bkevList,vk];

  ophc2=rophc[kc2,kf2,tf2];
  poeu2=proe1[kc2,kf2,tf2,tf2,ophc2,b2];
  oeu2=roe1[kc2,kf2,tf2,tf2,ophc2,b2];
  poeu3=proe1[kc2,kf2,tf3,tf2,ophc2,b2];
  oeu3=roe1[kc2,kf2,tf3,tf2,ophc2,b2];
  vk=fk[b2,gc2,egc3,kf2,ekf3]*((poeu2*v2-oeu2*pv2)-
        (poeu3*v3-oeu3*pv3));
  akovList=Append[akovList,kd*vk];
  bkovList=Append[bkovList,vk];

  m=m+1,
  {mmax}
 ];

(*PART E*)
(* For Transfer Matrices *)

m0=Table[0,{2*mmax}];
mm0=Table[0,{2*mmax+1},{2*mmax+1}];
ilist=Table[1,{1+2*mmax}]; mi=DiagonalMatrix[ilist];

akevList=Prepend[akevList,kuv];
akueList=Prepend[akueList,kuv];

mc={};
alist=Join[akevList,akovList];
blist=Join[bkueList,bkuoList];
tbelist=Join[tebe,tebe];
mc=Append[mc,alist];
f2List={Exp[-I be2*lmda2]};
f3List={Exp[-I be3*lmda3]};
m=1; Do[
 alist=Flatten[{blist[[m]],ReplacePart[m0,1,m]}];
 mc=Append[mc,alist];
 f2List=Append[f2List,Exp[-I tbelist[[m]]*lmda2]];
 f3List=Append[f3List,Exp[-I tbelist[[m]]*lmda3]];
 m=m+1,
 {2*mmax}
    ];
ma1=mc; mb1=-1 mc;

mc={};
alist=Join[akueList,akuoList];
blist=Join[bkevList,bkovList];
mc=Append[mc,alist];

m=1; Do[
 alist=Flatten[{blist[[m]],ReplacePart[m0,1,m]}];
 mc=Append[mc,alist];
 m=m+1,
 {2*mmax}
    ];
ma2=mc; mb2=mc;

mc=.; alist=.; blist=.; tbelist=.;
akueList=.; bkueList=.; akevList=.; bkevList=.;
akuoList=.; bkuoList=.; akovList=.; bkovList=.;

mpa2=DiagonalMatrix[f2List]; mpb2=Inverse[mpa2];
mpa3=DiagonalMatrix[f3List]; mpb3=Inverse[mpa3];
f2List=.; f3List=.;

me={}; mf={}; mg={}; mh={};
mpc2={}; mpd2={}; mpc3={}; mpd3={};
m=1; Do[
 me=Append[me,Flatten[{mi[[m]],mi[[m]]}] ];
 mf=Append[mf,Flatten[{ma1[[m]],mb1[[m]]}] ];
 mg=Append[mg,Flatten[{ma2[[m]],mb2[[m]]}] ];
 mh=Append[mh,Flatten[{mi[[m]],-1 mi[[m]]}] ];
 mpc2=Append[mpc2,Flatten[{mpa2[[m]],mm0[[m]]}] ];
 mpd2=Append[mpd2,Flatten[{mm0[[m]],mpb2[[m]]}] ];
 mpc3=Append[mpc3,Flatten[{mpa3[[m]],mm0[[m]]}] ];
 mpd3=Append[mpd3,Flatten[{mm0[[m]],mpb3[[m]]}] ];
 m=m+1,
 {2*mmax+1}
    ];
mpa2=.; mpa3=.; mpb2=.; mpb3=.;
ma=Join[me,mf]; mb=Join[mg,mh];

mt2=Join[mpc2,mpd2];
mt3=Join[mpc3,mpd3];

mpc2=.; mpc3=.; mpd2=.; mpd3=.;
ma1=.; mb1=.; ma2=.; mb2=.;
me=.; mf=.; mg=.; mh=.;

(*PART F*)
(* For Periodic Gratings *)

ms23=Inverse[ma].mb;
ma=.; mb=.;
msr=Inverse[ms23].Inverse[mt2].ms23.Inverse[mt3];
ms23=.; mt2=.; mt3=.;
(*ms23^-1 for step-down and ms23 for step-up*)
msrp=MatrixPower[msr,ngr];
msr=msrp; msrp=.;

(*PART G*)
(* For Coefficients *)

m11={}; m12={}; m21={}; m22={};
m=1; Do[
 m11=Append[m11,Drop[msr[[m]],-(2*mmax+1)] ];
 m12=Append[m12,Drop[msr[[m]],(2*mmax+1)] ];
 m21=Append[m21,Drop[msr[[m+(1+2*mmax)]],-(2*mmax+1)] ];
 m22=Append[m22,Drop[msr[[m+(1+2*mmax)]],(2*mmax+1)] ];
```

```
 m=m+1,
 {2*mmax+1}
 ];
msr=.;
mp={}; mq={}; mr={}; ms={};
m=1; Do[
 mp=Append[mp,Flatten[{-1 m11[[m]],mm0[[m]]}] ];
 mq=Append[mq,Flatten[{-1 m21[[m]],mi[[m]]}] ];
 mr=Append[mr,Flatten[{-1 mi[[m]],m12[[m]]}] ];
 ms=Append[ms,Flatten[{-1 mm0[[m]],m22[[m]]}] ];
 m=m+1,
 {2*mmax+1}
    ];

m11=.; m12=.; m21=.; m22=.;

ma3=Join[mp,mq]; mb3=Join[mr,ms];
mp=.; mq=.; mr=.; ms=.;
minp=Flatten[{1,m0,0,m0}];
ms3=Inverse[ma3].mb3;
mcc=ms3.minp;
ma3=.; mb3=.; ms3=.;

cgt=mcc[[1]]; cgr=mcc[[2+2*mmax]];
ecet=Take[mcc,{2,1+mmax}];
ocet=Take[mcc,{2+mmax,1+2*mmax}];
ecer=Take[mcc,{3+2*mmax,2+3*mmax}];
ocer=Take[mcc,-mmax];
pgr=Abs[cgr]^2;pgt=Abs[cgt]^2;

(*PART H*)
(* For Data Output *)

per=0; pet=0;
intList={}; inrList={};
pot1List={}; por2List={};
pot3List={}; por4List={};
m=1; Do[
  int=ac*Cos[tang[[m]]]*(Abs[ecet[[m]]]^2+Abs[ocet[[m]]]^2);
  inr=ac*Cos[tang[[m]]]*(Abs[ecer[[m]]]^2+Abs[ocer[[m]]]^2);
  intList=Append[intList,{tang[[m]]*180/pi,int}];
  inrList=Prepend[inrList,{180-tang[[m]]*180/pi,inr}];
  pot1List=Append[pot1List,int];  por2List=Prepend[por2List,inr];
  pot3List=Prepend[pot3List,int];  por4List=Append[por4List,inr];
  per=per+kdList[[m]]*(Abs[ecer[[m]]]^2+Abs[ocer[[m]]]^2);
  pet=pet+kdList[[m]]*(Abs[ecet[[m]]]^2+Abs[ocet[[m]]]^2);
  m=m+1, {mmax} ];
pt=pgr+pgt+per+pet;
rph=Arg[cgr]*180/pi; If[rph<0,rph=rph+360];
tph=Arg[cgt]*180/pi; If[tph<0,tph=tph+360];
por2List=Drop[por2List,{1}];por4List=Drop[por4List,{mmax}];
pouList=Flatten[{{0},pot1List,por2List,{0},por4List,pot3List}];
maxpo=Max[pouList]; pouList=(1/maxpo) pouList;

m0=.; mm0=.; iList=.; mi=.; mcc=.;
da1=N[da1=k0/vk0,8]; da2=N[Sqrt[pgr],10];
da3=N[detb*leng,10]; da4=N[Sqrt[pgt],10];
da5=N[per+pet,10];  da6={da1,da2,da3,da4,da5};
Write[df1,da6];

  Print[" "];
  Print["TE modes"];
  Print["t2/t1=",N[r2,4]," t1=",N[tf1,6]," t2=",N[tf2,6]];
  Print["t3/t1=",N[r3,4]," t3=",N[tf3,6]," Lt=",N[leng,8]];
  Print["k0*t1=",N[k0*tf1,4]," k0*t2=",N[k0*tf2,4],
        " k0*t3=",N[k0*tf3,4]];
  Print["No pds=",ngr,"  mmax=",N[mmax,6]];
  Print["k0'/k0=",N[k0/vk0,8]," db*L=",N[detb*leng,8],
        " k0'*b=",N[k0*lmda2,8]];
  Print["Lambda2/tf1=",N[lmda2/tf1,10],"
k0*b=",N[vk0*lmda2,8]];
  Print["Lambda2=",N[lmda2,10],
        " beta2*Lambda2=",N[be2*lmda2,10]];
  Print["Lambda3/tf1=",N[lmda3/tf1,10] ];
  Print["Lambda3=",N[lmda3,10],
        " beta3*Lambda3=",N[be3*lmda3,10]];
  Print["nc=",N[nc,8],",     nf=",N[nf,8]];
  Print["Cutoff thickness (tc) of m=1    =",N[tcut[[1]],10]];
  Print["Cutoff (tc)*k0 of m=1          =",N[tcut[[1]]*k0,10]];
  Print["The number of panels in Rad-angle=",mmax];Print[" "];
  Print["TE(beta1)=",N[be1,10] ];
  Print["TE(beta2)=",N[be2,10] ];
  Print["TE(beta3)=",N[be3,10] ];Print[" "];
  Print["Kuv=",N[kuv,10]];
  Print[" "];
  Print["a1- =",N[cgr,10]];Print["a2+ =",N[cgt,10]];
  Print[" "];
  Print["G-mode   refl. power=",N[pgr,10]];
  Print["G-mode   refl. coeff=",N[Sqrt[pgr],10]];
  Print["G-mode   Arg[R]    =",N[rph,10]];
  Print["G-mode   tran. power=",N[pgt,10]];
  Print["G-mode   tran. coeff=",N[Sqrt[pgt],10]];
  Print["G-mode   Arg[T]    =",N[tph,10]];
  Print["Rad-modes refl. power=",N[per,10]];
  Print["Rad-modes tran. power=",N[pet,10]];
  Print["Rad-modes total power=",N[per+pet,10]];
  Print["Total Power        =",N[pt,10]];
  Print[" "];

(*Part I*)
(* For Radiation Pattern *)
(* Graphic Output *)

  fg=PolarListPlot[pouList,PlotJoined->True,Axes->True,
        PlotRange->{{-1,1},{-1,1}}];

  stf=Join[intList,inrList];
  stf=Map[{#[[1]],#[[2]]/maxpo}&,stf];

  fe=LogListPlot[stf,PlotJoined->True,
         Ticks->Automatic,Frame->True,Axes->True];

If[nout==stopnt, Break[] ];
nout=nout+nstep,
{(num-noutst+1)/nstep}  ];

Print[" END OF JOB "];
```

Appendix D

```
(*FOR STEP-UP AND STEP-DOWN DISCONTINUiTIES
  ON ONE SIDE OF THE ASYMMETRIC
  THREE-LAYER PLANAR WAVEGUIDE
  PROGRAM NAME: a-stepup.m                    *)

(*For TE mode incidences*)

(*PART A*)
(* Common Constants *)

ep0=N[8854187818 10^-21,20];  vep=1.00 10^-13;
mu0=N[pi*(4 10^-7),20];       pi=N[Pi,20];
vc=Sqrt[(1/(ep0*mu0))];       epmu=Sqrt[ep0/mu0];
omg=vc*vk0;

(*PART B*)
(* Mode Distributions *)

vkc[n_,t_,e_]:=(1/t)*(ArcTan[e Sqrt[(ns^2-nc^2)/(nf^2-
ns^2)]]+n*pi);
fv[n_,t_,b_,s_,c_]:=Sqrt[af^2-b^2]*t-(ArcTan[c*Sqrt[(b^2-
ac^2)/(af^2-b^2)]]+ArcTan[s*Sqrt[(b^2-as^2)/(af^2-b^2)]]+n*pi);
fvp[n_,t_,bp_,s_,c_]:=D[fv[n,t,b,s,c],b]/.b->bp;
vb[n_,t_,b_,s_,c_]:=b-fv[n,t,b,s,c]/fvp[n,t,b,s,c];

etef[t_,gs_,gc_]:=t+1/gs+1/gc;
ef[t_,gs_,gc_,en_]:=2/Sqrt[en*epmu*etef[t,gs,gc] ];
es[t_,gs_,gc_,en_]:=ef[t,gs,gc,en]*Sqrt[(nf^2-en^2)/(nf^2-ns^2)];
ec[t_,gs_,gc_,en_]:=ef[t,gs,gc,en]*Sqrt[(nf^2-en^2)/(nf^2-nc^2)];
ephs[gs_,kf_]:=ArcTan[gs/kf];
e1[gs_,gc_,y_,t_,en_]:=ec[t,gs,gc,en]*Exp[-gc(y-t)];
pe1[gs_,gc_,vy_,t_,en_]:=D[e1[gs,gc,y,t,en],y]/.y->vy;
e2[gs_,gc_,kf_,y_,t_,en_]:=ef[t,gs,gc,en]*Cos[kf*y-ephs[gs,kf]];
pe2[gs_,gc_,kf_,vy_,t_,en_]:=D[e2[gs,gc,kf,y,t,en],y]/.y->vy;
e3[gs_,gc_,y_,t_,en_]:=es[t,gs,gc,en]*Exp[gs y];
pe3[gs_,gc_,vy_,t_,en_]:=D[e3[gs,gc,y,t,en],y]/.y->vy;

vses[b_]=2/Sqrt[pi*Abs[b]/(omg*mu0)];
rsephc[gc_,kf_]:=ArcTan[gc/kf];
rseph[gc_,kf_,ks_,t_]:=ArcTan[kf*Tan[rsephc[gc,kf]-kf*t]/ks];
rsef[phc_,kf_,t_,en_,b_]:=Abs[vses[b]/Sqrt[1+(nf^2-ns^2)*
                Sin[phc-kf*t]^2/(ns^2-en^2)]];
rsec[phc_,kf_,t_,en_,b_]:=rsef[phc,kf,t,en,b]*Cos[phc];
rses[ph_,phc_,kf_,t_,en_,b_]:=rsef[phc,kf,t,en,b]*
                Cos[kf*t-phc]/Cos[ph];
rse1[gc_,kf_,en_,y_,t_,phc_,b_]:=rsec[phc,kf,t,en,b]*Exp[-gc(y-t)];
prse1[gc_,kf_,en_,vy_,t_,phc_,b_]:=D[rse1[gc,kf,en,y,t,phc,b],y]/.y-
>vy;
rse2[kf_,en_,y_,t_,phc_,b_]:=rsef[phc,kf,t,en,b]*Cos[kf(y-t)+phc];
prse2[kf_,en_,vy_,t_,phc_,b_]:=D[rse2[kf,en,y,t,phc,b],y]/.y->vy;
rse3[ks_,y_,ph_,phc_,b_]:=rses[ph,phc,kf,t,en,b]*Cos[ks*y+ph];
prse3[ks_,vy_,ph_,phc_,b_]:=D[rse3[ks,y,ph,phc,b],y]/.y->vy;

rcph[kc_,kf_,ks_,t_]:=(1/2)*ArcTan[Sin[2 kf*t]/
                (Cos[2 kf*t]+(ks/kc)*((1-kf^2/ks^2)/
                (1-kf^2/kc^2)))];

rophs[kf_,ks_,ph_]:=ArcCot[kf*Cot[ph]/ks];
rophc[kc_,kf_,t_,ph_]:=ArcCot[kf*Cot[kf*t-ph]/kc];
roef[kc_,kf_,ks_,t_,ph_,b_]:=Abs[1/Sqrt[(pi*Abs[b]/(4*omg*mu0))
*
                ((kc/ks)*((Sin[kf*t-ph])^2+
                (kf^2/kc^2)*(Cos[kf*t-ph])^2)+
                ((Sin[ph])^2+(kf^2/ks^2)*(Cos[ph])^2))]];
roes[kc_,kf_,ks_,t_,ph_,b_]:=roef[kc,kf,ks,t,ph,b]*
                Sin[ph]/Sin[rophs[kf,ks,ph]];
roec[kc_,kf_,ks_,t_,ph_,b_]:=roef[kc,kf,ks,t,ph,b]*
                Sin[kf*t-ph]/Sin[rophc[kc,kf,t,ph]];
roe1[kc_,kf_,ks_,y_,t_,ph_,b_]:=roec[kc,kf,ks,t,ph,b]*
                Sin[kc*(y-t)+rophc[kc,kf,t,ph]];
proe1[kc_,kf_,ks_,vy_,t_,ph_,b_]:=D[roe1[kc,kf,ks,y,t,ph,b],y]/.y-
>vy;
roe2[kc_,kf_,ks_,y_,t_,ph_,b_]:=roef[kc,kf,ks,t,ph,b]*Sin[kf*y-ph];
proe2[kc_,kf_,ks_,vy_,t_,ph_,b_]:=D[roe2[kc,kf,ks,y,t,ph,b],y]/.y-
>vy;
roe3[kc_,kf_,ks_,y_,t_,ph_,b_]:=roes[kc,kf,ks,t,ph,b]*
                Sin[ks*y-rophs[kf,ks,ph]];
proe3[kc_,kf_,ks_,vy_,t_,ph_,b_]:=D[roe3[kc,kf,ks,y,t,ph,b],y]/.y-
>vy;

rephs[kf_,ks_,ph_]:=ArcTan[kf*Tan[ph]/ks];
rephc[kc_,kf_,t_,ph_]:=ArcTan[kf*Tan[kf*t-ph]/kc];
reef[kc_,kf_,ks_,t_,ph_,b_]:=Abs[1/Sqrt[(pi*Abs[b]/(4*omg*mu0))
*
                ((kc/ks)*((Cos[kf*t-ph])^2+
                (kf^2/kc^2)*(Sin[kf*t-ph])^2)+
                ((Cos[ph])^2+(kf^2/ks^2)*(Sin[ph])^2))]];
rees[kc_,kf_,ks_,t_,ph_,b_]:=reef[kc,kf,ks,t,ph,b]*
                Cos[ph]/Cos[rephs[kf,ks,ph]];
reec[kc_,kf_,ks_,t_,ph_,b_]:=reef[kc,kf,ks,t,ph,b]*
                Cos[kf*t-ph]/Cos[rephc[kc,kf,t,ph]];
ree1[kc_,kf_,ks_,y_,t_,ph_,b_]:=reec[kc,kf,ks,t,ph,b]*
                Cos[kc*(y-t)+rephc[kc,kf,t,ph]];
pree1[kc_,kf_,ks_,vy_,t_,ph_,b_]:=D[ree1[kc,kf,ks,y,t,ph,b],y]/.y-
>vy;
ree2[kc_,kf_,ks_,y_,t_,ph_,b_]:=reef[kc,kf,ks,t,ph,b]*Cos[kf*y-ph];
pree2[kc_,kf_,ks_,vy_,t_,ph_,b_]:=D[ree2[kc,kf,ks,y,t,ph,b],y]/.y-
>vy;
ree3[kc_,kf_,ks_,y_,t_,ph_,b_]:=rees[kc,kf,ks,t,ph,b]*
                Cos[ks*y-rephs[kf,ks,ph]];
pree3[kc_,kf_,ks_,vy_,t_,ph_,b_]:=D[ree3[kc,kf,ks,y,t,ph,b],y]/.y-
>vy;

(*PART C*)
(* For Propagation Constants *)

i=1; tcList={};
Do[
  vc=ArcTan[Sqrt[(ns^2-nc^2)/(nf^2-ns^2)]]+(i-1)*pi;
  ktc=vc/Sqrt[nf^2-ns^2];
  tcList=Append[tcList,ktc];
  i=i+1, {2}
 ];

k0=vk0; af=nf*vk0; as=ns*vk0; ac=nc*ck0;
js=1;Do[
tr=trstart+js*stptr;   tf2=tf1*tr;

m=0; nt1=1; sbe=as+(af-as)/2; rfs=rfc=1;
Do[
  If[nt1>10,m=5; Break[] ];
  vbe=vb[nmod,tf1,sbe,rfs,rfc]; bett=vbe;
  If[vbe<af&&vbe>as,Break[] ];
  If[vbe>=af,
    sbe=af-(1 10^-2)*(af-as),
    sbe=as+(1 10^-2)*(af-as) ];
    ++nt1,
    {20}
   ];
  Do[
    vbe=vb[nmod,tf1,vbe,rfs,rfc];
    If[Abs[vbe-bett]<(1 10^-24),Break[] ];
    bett=vbe,
    {20}
   ];
 be1=bett;ene1=be1/k0;
 egs1=Sqrt[be1^2-as^2];egc1=Sqrt[be1^2-ac^2];ekf1=Sqrt[af^2-
be1^2];

 m=0; nt1=1; sbe=as+(af-as)/2;
  Do[
    If[nt1>10,m=5;Break[] ];
    vbe=vb[nmod,tf2,sbe,rfs,rfc];bett=vbe;
    If[vbe<af && vbe>as,Break[] ];
    If[vbe>=af,
      sbe=af-(1 10^-2)*(af-as),sbe=as+(1 10^-2)*(af-as)];
    ++nt1,
    {20}
   ];
  Do[
    vbe=vb[nmod,tf2,vbe,rfs,rfc];
    If[Abs[vbe-bett]<(1 10^-24),Break[] ];
    bett=vbe,
    {20}
   ];
  be2=bett;ene2=be2/k0; egs2=Sqrt[be2^2-as^2];
  egc2=Sqrt[be2^2-ac^2];ekf2=Sqrt[af^2-be2^2];

(*PART D*)
(* Inner Products *)
```

```
fk[b1_,gc1_,gc2_,kf1_,kf2_]:=(b1/(2*omg*mu0))*
    ((af^2-ac^2)/((kf2^2-kf1^2)(gc1^2+kf2^2)));

pu1=pe1[egs1,egc1,tf1,tf1,ene1];
v1=e2[egs2,egc2,ekf2,tf1,tf2,ene2];
u1=e1[egs1,egc1,tf1,tf1,ene1];
pv1=pe2[egs2,egc2,ekf2,tf1,tf2,ene2];
pu2=pe1[egs1,egc1,tf2,tf1,ene1];
v2=e2[egs2,egc2,ekf2,tf2,tf2,ene2];
u2=e1[egs1,egc1,tf2,tf1,ene1];
pv2=pe2[egs2,egc2,ekf2,tf2,tf2,ene2];
kuv=fk[be1,egc1,egc2,ekf1,ekf2]*
    ((pu1*v1-u1*pv1)-(pu2*v2-u2*pv2));

sangmax=N[angsc-sanglim*pi/180,20];
dang=sangmax/mmax;
sang=Table[stn*dang,{stn,mmax}];
dsb=Table[as*Cos[sang[[stn]]]*dang,{stn,mmax}];
sb=Table[as*Sin[sang[[stn]]],{stn,mmax}];

cangmax=N[pi/2-canglim*pi/180,20];
dang=(cangmax-angsc)/nmax;
tang=Table[(angsc+stm*dang),{stm,nmax}];
dtb=Table[as*Cos[tang[[stm]]]*dang,{stm,nmax}];
tb=Table[as*Sin[tang[[stm]]],{stm,nmax}];

m=1;akusList={};bkusList={};aksvList={};bksvList={};
  mkdList={}; nkdList={};
Do[
  sks2=sb[[m]];          sb2=Sqrt[as^2-sks2^2];
  skf2=Sqrt[af^2-sb2^2];   sgc2=Sqrt[sb2^2-ac^2];
  sgs2=I sks2;           sen2=Abs[sb2]/k0;
  sphc2=rsephc[sgc2,skf2]; sphc1=sphc2;
  sks1=sks2;  sb1=sb2;    skf1=skf2;
  sgc1=sgc2;  sgs1=sgs2;  sen1=sen2;
  If[EvenQ[m],kd=(2/3)*dsb[[m]],kd=(4/3)*dsb[[m]]];
  If[m==mmax,kd=(1/3)*dsb[[m]] ];
  mkdList=Append[mkdList,kd];

  sev1=rse2[skf2,sen2,tf1,tf2,sphc2,sb2];
  psev1=prse2[skf2,sen2,tf1,tf2,sphc2,sb2];
  sev2=rse2[skf2,sen2,tf2,tf2,sphc2,sb2];
  psev2=prse2[skf2,sen2,tf2,tf2,sphc2,sb2];
  vk=fk[be1,egc1,sgc2,ekf1,skf2]*
      ((pu1*sev1-u1*psev1)-(pu2*sev2-u2*psev2));
  akusList=Append[akusList,kd*vk];
  bkusList=Append[bkusList,vk];

  seu1=rse1[sgc1,skf1,sen1,tf1,tf1,sphc1,sb1];
  pseu1=prse1[sgc1,skf1,sen1,tf1,tf1,sphc1,sb1];
  seu2=rse1[sgc1,skf1,sen1,tf2,tf1,sphc1,sb1];
  pseu2=prse1[sgc1,skf1,sen1,tf2,tf1,sphc1,sb1];
  vk=fk[sb1,sgc1,egc2,skf1,ekf2]*
      ((pseu1*v1-seu1*pv1)-(pseu2*v2-seu2*pv2));
  aksvList=Append[aksvList,kd*vk];
  bksvList=Append[bksvList,vk];

  m=m+1, {mmax}
  ];

n=1;akuoList={};akueList={};bkuoList={};bkueList={};
  akovList={};akevList={};bkovList={};bkevList={};
  ros1List={};res1List={};ros2List={};res2List={};
Do[
    cks2=tb[[n]];              cb2=Sqrt[as^2-cks2^2];
    ckc2=Sqrt[ac^2-cb2^2];      cgc2=Sqrt[cb2^2-ac^2];
    ckf2=Sqrt[af^2-cb2^2];      cgs2=I cks2;
    cph2=rcph[ckc2,ckf2,cks2,tf2];
    cks1=cks2;   ckc1=ckc2;   ckf1=ckf2;
    cgc1=cgc2;   cgs1=cgs2;   cb1=cb2;
    cph1=rcph[ckc1,ckf1,cks1,tf1];
    If[EvenQ[n],kd=(2/3)*dtb[[n]],kd=(4/3)*dtb[[n]]];
    If[n==nmax,kd=(1/3)*dtb[[n]] ];
    nkdList=Append[nkdList,kd];

    oeu1=roe1[ckc1,ckf1,cks1,tf1,tf1,cph1,cb1];
    poeu1=proe1[ckc1,ckf1,cks1,tf1,tf1,cph1,cb1];
    oeu2=roe1[ckc1,ckf1,cks1,tf2,tf1,cph1,cb1];
    poeu2=proe1[ckc1,ckf1,cks1,tf2,tf1,cph1,cb1];

    eeu1=ree1[ckc1,ckf1,cks1,tf1,tf1,cph1,cb1];
    peeu1=pree1[ckc1,ckf1,cks1,tf1,tf1,cph1,cb1];
    eeu2=ree1[ckc1,ckf1,cks1,tf2,tf1,cph1,cb1];
    peeu2=pree1[ckc1,ckf1,cks1,tf2,tf1,cph1,cb1];

    oev1=roe2[ckc2,ckf2,cks2,tf1,tf2,cph2,cb2];
    poev1=proe2[ckc2,ckf2,cks2,tf1,tf2,cph2,cb2];
    oev2=roe2[ckc2,ckf2,cks2,tf2,tf2,cph2,cb2];
    poev2=proe2[ckc2,ckf2,cks2,tf2,tf2,cph2,cb2];

    eev1=ree2[ckc2,ckf2,cks2,tf1,tf2,cph2,cb2];
    peev1=pree2[ckc2,ckf2,cks2,tf1,tf2,cph2,cb2];
    eev2=ree2[ckc2,ckf2,cks2,tf2,tf2,cph2,cb2];
    peev2=pree2[ckc2,ckf2,cks2,tf2,tf2,cph2,cb2];

    vk=fk[be1,egc1,cgc2,ekf1,ckf2]*
        ((pu1*oev1-u1*poev1)-(pu2*oev2-u2*poev2));
    akuoList=Append[akuoList,kd*vk];
    bkuoList=Append[bkuoList,vk];

    vk=fk[be1,egc1,cgc2,ekf1,ckf2]*
        ((pu1*eev1-u1*peev1)-(pu2*eev2-u2*peev2));
    akueList=Append[akueList,kd*vk];
    bkueList=Append[bkueList,vk];

    vk=fk[cb1,cgc1,egc2,ckf1,ekf2]*
        ((poeu1*v1-oeu1*pv1)-(poeu2*v2-oeu2*pv2));
    akovList=Append[akovList,kd*vk];
    bkovList=Append[bkovList,vk];

    vk=fk[cb1,cgc1,egc2,ckf1,ekf2]*
        ((peeu1*v1-eeu1*pv1)-(peeu2*v2-eeu2*pv2));
    akevList=Append[akevList,kd*vk];
    bkevList=Append[bkevList,vk];

    ros=roes[ckc1,ckf1,cks1,tf1,cph1,cb1];
    roc=roec[ckc1,ckf1,cks1,tf1,cph1,cb1];
    ros1List=Append[ros1List,ros^2/(ros^2+(ckc1/cks1)*roc^2)];
    ros=roes[ckc2,ckf2,cks2,tf2,cph2,cb2];
    roc=roec[ckc2,ckf2,cks2,tf2,cph2,cb2];
    ros2List=Append[ros2List,ros^2/(ros^2+(ckc2/cks2)*roc^2)];
    res=rees[ckc1,ckf1,cks1,tf1,cph1,cb1];
    rec=reec[ckc1,ckf1,cks1,tf1,cph1,cb1];
    res1List=Append[res1List,res^2/(res^2+(ckc1/cks1)*rec^2)];
    res=rees[ckc2,ckf2,cks2,tf2,cph2,cb2];
    rec=reec[ckc2,ckf2,cks2,tf2,cph2,cb2];
    res2List=Append[res2List,res^2/(res^2+(ckc2/cks2)*rec^2)];

    n=n+1,
    {nmax}
  ];

(*PART E*)
(* For Transfer Matrices *)

m0=Table[0,{mmax}]; n0=Table[0,{nmax}];
nn0=Table[0,{1+mmax+2 nmax},{1+mmax+2 nmax}];
ilist=Table[1,{1+mmax+2 nmax}];
mi=DiagonalMatrix[ilist];
akurList=Flatten[{kuv,akusList,akuoList,akueList}];
akrvList=Flatten[{kuv,aksvList,akovList,akevList}];

mc={};
alist=akrvList;
mc=Append[mc,alist];
m=1; Do[
  alist=Flatten[{bkusList[[m]],ReplacePart[m0,1,m],n0,n0}];
  mc=Append[mc,alist];
  m=m+1,
  {mmax}
     ];
na1=mc;

mc={}; md={};
n=1; Do[
  alist=Flatten[{bkuoList[[n]],m0,ReplacePart[n0,1,n],n0}];
  mc=Append[mc,alist];
  alist=Flatten[{bkueList[[n]],m0,n0,ReplacePart[n0,1,n]}];
  md=Append[md,alist];
  n=n+1,
  {nmax}
     ];
na2=mc;
na3=md;
```

```
na1=Join[na1,na2,na3]; nb1=-1 na1;
na2=.; na3=.;

mc={};
alist=akurList;
mc=Append[mc,alist];

m=1; Do[
 alist=Flatten[{bksvList[[m]],ReplacePart[m0,1,m],n0,n0}];
 mc=Append[mc,alist];
 m=m+1,
 {mmax}
    ];
ma1=mc;

mc={}; md={};
n=1; Do[
 alist=Flatten[{bkovList[[n]],m0,ReplacePart[n0,1,n],n0}];
 mc=Append[mc,alist];
 alist=Flatten[{bkevList[[n]],m0,n0,ReplacePart[n0,1,n]}];
 md=Append[md,alist];
 n=n+1,
 {nmax}
    ];
ma2=mc;
ma3=md;

ma1=Join[ma1,ma2,ma3]; mb1=ma1;
ma2=.; ma3=.;
mc=.; md=.; alist=.;

(*
akusList=.; akuoList=.; akueList=.;
bkusList=.; bkuoList=.; bkueList=.;
aksvList=.; akovList=.; akevList=.;
bksvList=.; bkovList=.; bkevList=.;
*)

me={}; mf={}; mg={}; mh={};
m=1; Do[
 me=Append[me,Flatten[{mi[[m]],mi[[m]]}] ];
 mf=Append[mf,Flatten[{na1[[m]],nb1[[m]]}] ];
 mg=Append[mg,Flatten[{ma1[[m]],mb1[[m]]}] ];
 mh=Append[mh,Flatten[{mi[[m]],-1 mi[[m]]}] ];
 m=m+1,
 {mmax+2 nmax+1}
    ];
ma=Join[me,mf]; mb=Join[mg,mh];

na1=.; nb1=.; ma1=.; mb1=.;
me=.; mf=.; mg=.; mh=.;

(*PART F*)
(* For Step-Up Structures *)
ms1=Inverse[ma].mb;
(*  ms1=Inverse[mb].ma : for step-down *)
ma=.; mb=.;

(*PART G*)
(* For Coefficients *)

m11={}; m12={}; m21={}; m22={};
m=1; Do[
 m11=Append[m11,Drop[ms1[[m]],-(mmax+2 nmax+1)] ];
 m12=Append[m12,Drop[ms1[[m]],(mmax+2 nmax+1)] ];
 m21=Append[m21,Drop[ms1[[m+(1+mmax+2 nmax)]],-(mmax+2
nmax+1)] ];
 m22=Append[m22,Drop[ms1[[m+(1+mmax+2 nmax)]],(mmax+2
nmax+1)] ];
 m=m+1,
 {mmax+2 nmax+1}
 ];
ms1=.;

mp={}; mq={}; mr={}; ms={};
m=1; Do[
 mp=Append[mp,Flatten[{-1 m11[[m]],nn0[[m]]}] ];
 mq=Append[mq,Flatten[{-1 m21[[m]],mi[[m]]}] ];
 mr=Append[mr,Flatten[{-1 mi[[m]],m12[[m]]}] ];
 ms=Append[ms,Flatten[{-1 nn0[[m]],m22[[m]]}] ];
 m=m+1,
 {mmax+2 nmax+1}
    ];

m11=.; m12=.; m21=.; m22=.;

ma3=Join[mp,mq]; mb3=Join[mr,ms];
mp=.; mq=.; mr=.; ms=.;
minp=Flatten[{1,m0,n0,n0,0,m0,n0,n0}];
ms3=Inverse[ma3].mb3;
mcc=ms3.minp;
ma3=.; mb3=.; ms3=.;

cgt=mcc[[1]]; cgr=mcc[[2+mmax+2 nmax]];
cst=Take[mcc,{2,1+mmax}];
cot=Take[mcc,{2+mmax,1+mmax+nmax}];
cet=Take[mcc,{2+mmax+nmax,1+mmax+2 nmax}];
csr=Take[mcc,{3+mmax+2 nmax,2(1+mmax+nmax)}];
cor=Take[mcc,{1+2(1+mmax+nmax),nmax+2(1+mmax+nmax)}];
cer=Take[mcc,-nmax];
pgr=Abs[cgr]^2;pgt=Abs[cgt]^2;

(*PART H*)
(* For Data Output *)

m=1; psr=0; pst=0; isrList={}; istList={}; normList={};
Do[
  vsr=Abs[csr[[m]] ]^2; vst=Abs[cst[[m]] ]^2;
  kd=mkdList[[m]];
  psr=psr+kd*vsr;      pst=pst+kd*vst;
  k1=as*Cos[sang[[m]]]; k2=sang[[m]]*180/pi;
  k3=k1*vsr;          k4=k1*vst;
  normList=Append[normList,{k3,k4}];
  istList=Append[istList,{k2,k4}];
  isrList=Prepend[isrList,{180-k2,k3}];
 m=m+1, {mmax}
 ];

n=1; psro=0; psto=0; psre=0; pste=0;
      pcro=0; pcto=0; pcre=0; pcte=0;
otsrList={}; otstList={}; etsrList={}; etstList={};
otcrList={}; otctList={}; etcrList={}; etctList={};
tsrList={}; tstList={};
tcrList={}; tctList={};
Do[
  vot=Abs[cot[[n]] ]^2;     vet=Abs[cet[[n]] ]^2;
  vor=Abs[cor[[n]] ]^2;     ver=Abs[cer[[n]] ]^2;
  kd=nkdList[[n]];
  rop1=ros1List[[n]];       rep1=res1List[[n]];
  rop2=ros2List[[n]];       rep2=res2List[[n]];
  psro=psro+kd*vor*rop1;    psre=psre+kd*ver*rep1;
  psto=psto+kd*vot*rop2;    pste=pste+kd*vet*rep2;
  k1=as*Cos[tang[[n]]];     k2=tang[[n]]*180/pi;
  k3=k1*vor*rop1;          k4=k1*vot*rop2;
  otsrList=Prepend[otsrList,{180-k2,k3}];
  otstList=Append[otstList,{k2,k4}];
  k5=k1*ver*rep1;          k6=k1*vet*rep2;
  etsrList=Prepend[etsrList,{180-k2,k5}];
  etstList=Append[etstList,{k2,k6}];
  tsrList=Prepend[tsrList,{180-k2,k3+k5}];
  tstList=Append[tstList,{k2,k4+k6}];
  normList=Append[normList,{k3+k5,k4+k6}];

  angc=ArcCos[ns*Cos[tang[[n]]]/nc];
  ka=ac*Cos[angc]*(nc/ns)*(Sin[angc]/Sin[tang[[n]]]);
  kb=angc*180/pi;
  pcro=pcro+kd*vor*(1-rop1); pcre=pcre+kd*ver*(1-rep1);
  pcto=pcto+kd*vot*(1-rop2); pcte=pcte+kd*vet*(1-rep2);
  kc=ka*vor*(1-rop1);       ke=ka*ver*(1-rep1);
  kd=ka*vot*(1-rop2);       kf=ka*vet*(1-rep2);
  normList=Append[normList,{kc,kd,ke,kf}];
  otcrList=Prepend[otcrList,{180-kb,kc}];
  otctList=Append[otctList,{kb,kd}];
  etcrList=Prepend[etcrList,{180-kb,ke}];
  etctList=Append[etctList,{kb,kf}];

  tcrList=Prepend[tcrList,{180-kb,kc+ke}];
  tctList=Append[tctList,{kb,kd+kf}];
  normList=Append[normList,{kc+ke,kd+kf}];

 n=n+1, {nmax}
 ];
tpsr=psro+psre; tpst=psto+pste;
tpcr=pcro+pcre; tpct=pcto+pcte;
tps=tpsr+tpst;  tpc=tpcr+tpct;
pt=pgr+pgt+psr+pst+tps+tpc;
```

```
da1=N[Abs[(tf2-tf1)]/wleng,6];          da2=N[tf2/tf1,8];
da3=N[Abs[cgr],8];          da4=N[Abs[cgt],8];
da5=N[psr+pst+tps,8];       da6=N[tpc,8];
da7=N[da5+da6,8];           da8=N[tk,6];
da9=N[Abs[(be1-be2)]/(be2+be1),10];
da10=N[2be2*kuv/(be2+be1),10];
da11={da1,da2,da3,da4,da5,da6,da7,da8,da9,da10};
Write[df1,da11];

m0=.; mm0=.; iList=.; mi=.;

  Print[" "];
  Print["r(tf2/tf1)=",N[tf2/tf1,4],",       wleng=",N[wleng,8]];
  Print["tkc(n=0)=",N[tcList[[1]],10],",
tkc(n=1)=",N[tcList[[2]],10]];
  Print["tk1=",N[tf1*k0,10],",       tk2=",N[tf2*k0,10]];
  Print["nc=",N[nc,5]];Print["nf=",N[nf,5]];Print["ns=",N[ns,5]];
  Print["The number of panels in Sub-Rad angle=",mmax];
  Print["The number of panels in C-S Rad angle=",nmax];Print[" "];
  Print["tf1=",N[tf1,4]," TE(beta1)=",N[be1,10] ];
  Print["tf2=",N[tf2,4]," TE(beta2)=",N[be2,10] ];
  Print["Kuv=",N[kuv,10]];
  Print[" "];
  Print["a1- =",N[cgr,10]];Print["a2+ =",N[cgt,10]];
  Print["a1-(appr) (b1-b2)/(b2+b1)=",N[(be1-be2)/(be2+be1),10]];
  Print["a2+(appr) (2*be2*kuv)/(be2+be1)=",
        N[2be2*kuv/(be2+be1),10]];
  Print[" "];
  Print["G-mode refl. power =",N[pgr,10]];
  Print["G-mode tran. power =",N[pgt,10]];
  Print["S-rad. refl. power =",N[psr,10]];
  Print["S-rad. tran. power =",N[pst,10]];
  Print["Total S-rad. power =",N[psr+pst,10]];Print[" "];
  Print["Total SC(refl)-S power=",N[tpsr,10]];
  Print["Total SC(Tran)-S power=",N[tpst,10]];
  Print["Total SC(refl)-C power=",N[tpcr,10]];
  Print["Total SC(Tran)-C power=",N[tpct,10]];
  Print["Total SC(Sub) power=",N[tps,10]];
  Print["Total SC(Cov) power=",N[tpc,10]];Print[" "];
  Print["Total rad. power  =",N[psr+pst+tps+tpc,10]];
  Print["Total Power       =",N[pt,10]];

(*Part 1*)
(* For Radiation Pattern *)
(* Graphic Output *)

  ListPlot[isrList,PlotJoined->True,GridLines->Automatic,
      Ticks->Automatic,Frame->True,Axes->True];
  ListPlot[istList,PlotJoined->True,GridLines->Automatic,
      Ticks->Automatic,Frame->True,Axes->True];
  ListPlot[otsrList,PlotJoined->True,GridLines->Automatic,
      Ticks->Automatic,Frame->True,Axes->True];
  ListPlot[otstList,PlotJoined->True,GridLines->Automatic,
      Ticks->Automatic,Frame->True,Axes->True];
  ListPlot[etsrList,PlotJoined->True,GridLines->Automatic,
      Ticks->Automatic,Frame->True,Axes->True];
  ListPlot[etstList,PlotJoined->True,GridLines->Automatic,
      Ticks->Automatic,Frame->True,Axes->True];
  ListPlot[otcrList,PlotJoined->True,GridLines->Automatic,
      Ticks->Automatic,Frame->True,Axes->True];
  ListPlot[otctList,PlotJoined->True,GridLines->Automatic,
      Ticks->Automatic,Frame->True,Axes->True];
  ListPlot[etcrList,PlotJoined->True,GridLines->Automatic,
      Ticks->Automatic,Frame->True,Axes->True];
  ListPlot[etctList,PlotJoined->True,GridLines->Automatic,
      Ticks->Automatic,Frame->True,Axes->True];
  ListPlot[tsrList,PlotJoined->True,GridLines->Automatic,
      Ticks->Automatic,Frame->True,Axes->True];
  ListPlot[tstList,PlotJoined->True,GridLines->Automatic,
      Ticks->Automatic,Frame->True,Axes->True];
  ListPlot[tcrList,PlotJoined->True,GridLines->Automatic,
      Ticks->Automatic,Frame->True,Axes->True];
  ListPlot[tctList,PlotJoined->True,GridLines->Automatic,
      Ticks->Automatic,Frame->True,Axes->True];

  LogListPlot[isrList,PlotJoined->True,
      Ticks->Automatic,Frame->True,Axes->True];
  LogListPlot[istList,PlotJoined->True,
      Ticks->Automatic,Frame->True,Axes->True];
  LogListPlot[tsrList,PlotJoined->True,
      Ticks->Automatic,Frame->True,Axes->True];
  LogListPlot[tstList,PlotJoined->True,
      Ticks->Automatic,Frame->True,Axes->True];
  LogListPlot[tcrList,PlotJoined->True,
      Ticks->Automatic,Frame->True,Axes->True];
  LogListPlot[tctList,PlotJoined->True,
      Ticks->Automatic,Frame->True,Axes->True];

  stf=Join[istList,tstList,tsrList,isrList];
  ctf=Join[tctList,tcrList];
  norm=Max[normList];
  stf=Map[{#[[1]],#[[2]]/norm}&,stf];
  ctf=Map[{#[[1]],#[[2]]/norm}&,ctf];
  LogListPlot[stf,PlotJoined->True,
      FrameLabel->{"Angle(degrees)","P/Pmax"},
      Ticks->Automatic,Frame->True,Axes->True];
  LogListPlot[ctf,PlotJoined->True,
      FrameLabel->{"Angle(degrees)","P/Pmax"},
      Ticks->Automatic,Frame->True,Axes->True];
  ListPlot[stf,PlotJoined->True,GridLines->Automatic,
      FrameLabel->{"Angle(degrees)","P/Pmax"},
      Ticks->Automatic,Frame->True,Axes->True];
  ListPlot[ctf,PlotJoined->True,GridLines->Automatic,
      FrameLabel->{"Angle(degrees)","P/Pmax"},
      Ticks->Automatic,Frame->True,Axes->True];

js=js+1,
{tstep}
];

Print[" END OF JOB "];
```

Appendix E

(a) Polar-coordinate package

```
(*PROGRAM NAME: polarmap.m *)

<<graphics\graphics.m
g05=Graphics[Circle[{0,0},0.5]];
g1=Graphics[Circle[{0,0},1]];
g2=Line[{{N[0.96Cos[10*Pi/180],8],N[0.96Sin[10*Pi/180],8]},
    {N[Cos[10*Pi/180],8],N[Sin[10*Pi/180],8]}}];
g3=Line[{{N[0.96Cos[20*Pi/180],8],N[0.96Sin[20*Pi/180],8]},
    {N[Cos[20*Pi/180],8],N[Sin[20*Pi/180],8]}}];
g4=Line[{{0,0},{N[Cos[30*Pi/180],8],N[Sin[30*Pi/180],8]}}];
g5=Line[{{N[0.96Cos[40*Pi/180],8],N[0.96Sin[40*Pi/180],8]},
    {N[Cos[40*Pi/180],8],N[Sin[40*Pi/180],8]}}];
g6=Line[{{N[0.96Cos[50*Pi/180],8],N[0.96Sin[50*Pi/180],8]},
    {N[Cos[50*Pi/180],8],N[Sin[50*Pi/180],8]}}];
g7=Line[{{0,0},{N[Cos[60*Pi/180],8],N[Sin[60*Pi/180],8]}}];
g8=Line[{{N[0.96Cos[70*Pi/180],8],N[0.96Sin[70*Pi/180],8]},
    {N[Cos[70*Pi/180],8],N[Sin[70*Pi/180],8]}}];
g9=Line[{{N[0.96Cos[80*Pi/180],8],N[0.96Sin[80*Pi/180],8]},
    {N[Cos[80*Pi/180],8],N[Sin[80*Pi/180],8]}}];
g10=Line[{{N[0.96Cos[100*Pi/180],8],N[0.96Sin[100*Pi/180],8]},
    {N[Cos[100*Pi/180],8],N[Sin[100*Pi/180],8]}}];
g11=Line[{{N[0.96Cos[110*Pi/180],8],N[0.96Sin[110*Pi/180],8]},
    {N[Cos[110*Pi/180],8],N[Sin[110*Pi/180],8]}}];
g12=Line[{{0,0},{N[Cos[120*Pi/180],8],N[Sin[120*Pi/180],8]}}];
g13=Line[{{N[0.96Cos[130*Pi/180],8],N[0.96Sin[130*Pi/180],8]},
    {N[Cos[130*Pi/180],8],N[Sin[130*Pi/180],8]}}];
g14=Line[{{N[0.96Cos[140*Pi/180],8],N[0.96Sin[140*Pi/180],8]},
    {N[Cos[140*Pi/180],8],N[Sin[140*Pi/180],8]}}];
g15=Line[{{0,0},{N[Cos[150*Pi/180],8],N[Sin[150*Pi/180],8]}}];
g16=Line[{{N[0.96Cos[160*Pi/180],8],N[0.96Sin[160*Pi/180],8]},
    {N[Cos[160*Pi/180],8],N[Sin[160*Pi/180],8]}}];
g17=Line[{{N[0.96Cos[170*Pi/180],8],N[0.96Sin[170*Pi/180],8]},
    {N[Cos[170*Pi/180],8],N[Sin[170*Pi/180],8]}}];
g18=Line[{{N[0.96Cos[-170*Pi/180],8],N[0.96Sin[-
170*Pi/180],8]},
    {N[Cos[-170*Pi/180],8],N[Sin[-170*Pi/180],8]}}];
g19=Line[{{N[0.96Cos[-160*Pi/180],8],N[0.96Sin[-
160*Pi/180],8]},
    {N[Cos[-160*Pi/180],8],N[Sin[-160*Pi/180],8]}}];
g20=Line[{{0,0},{N[Cos[-150*Pi/180],8],N[Sin[-
150*Pi/180],8]}}];
g21=Line[{{N[0.96Cos[-140*Pi/180],8],N[0.96Sin[-
140*Pi/180],8]},
    {N[Cos[-140*Pi/180],8],N[Sin[-140*Pi/180],8]}}];
g22=Line[{{N[0.96Cos[-130*Pi/180],8],N[0.96Sin[-
130*Pi/180],8]},
    {N[Cos[-130*Pi/180],8],N[Sin[-130*Pi/180],8]}}];
g23=Line[{{0,0},{N[Cos[-120*Pi/180],8],N[Sin[-
120*Pi/180],8]}}];
g24=Line[{{N[0.96Cos[-110*Pi/180],8],N[0.96Sin[-
110*Pi/180],8]},
    {N[Cos[-110*Pi/180],8],N[Sin[-110*Pi/180],8]}}];
g25=Line[{{N[0.96Cos[-100*Pi/180],8],N[0.96Sin[-
100*Pi/180],8]},
    {N[Cos[-100*Pi/180],8],N[Sin[-100*Pi/180],8]}}];
g26=Line[{{N[0.96Cos[-80*Pi/180],8],N[0.96Sin[-80*Pi/180],8]},
    {N[Cos[-80*Pi/180],8],N[Sin[-80*Pi/180],8]}}];
g27=Line[{{N[0.96Cos[-70*Pi/180],8],N[0.96Sin[-70*Pi/180],8]},
    {N[Cos[-70*Pi/180],8],N[Sin[-70*Pi/180],8]}}];
g28=Line[{{0,0},{N[Cos[-60*Pi/180],8],N[Sin[-60*Pi/180],8]}}];
g29=Line[{{N[0.96Cos[-50*Pi/180],8],N[0.96Sin[-50*Pi/180],8]},
    {N[Cos[-50*Pi/180],8],N[Sin[-50*Pi/180],8]}}];
g30=Line[{{N[0.96Cos[-40*Pi/180],8],N[0.96Sin[-40*Pi/180],8]},
    {N[Cos[-40*Pi/180],8],N[Sin[-40*Pi/180],8]}}];
g31=Line[{{0,0},{N[Cos[-30*Pi/180],8],N[Sin[-30*Pi/180],8]}}];
g32=Line[{{N[0.96Cos[-20*Pi/180],8],N[0.96Sin[-20*Pi/180],8]},
    {N[Cos[-20*Pi/180],8],N[Sin[-20*Pi/180],8]}}];
g33=Line[{{N[0.96Cos[-10*Pi/180],8],N[0.96Sin[-10*Pi/180],8]},
    {N[Cos[-10*Pi/180],8],N[Sin[-10*Pi/180],8]}}];
gaa=Show[Graphics[g1],Graphics[g2],Graphics[g3],
    Graphics[g4],Graphics[g5],Graphics[g6],
    Graphics[g7],Graphics[g8],Graphics[g9],
    Graphics[g10],Graphics[g11],Graphics[g05],
    Graphics[g12],Graphics[g13],
    Graphics[g13],Graphics[g14],Graphics[g15],
    Graphics[g16],Graphics[g17],Graphics[g18],
    Graphics[g19],Graphics[g20],Graphics[g21],
    Graphics[g22],Graphics[g23],Graphics[g24],
    Graphics[g25],Graphics[g26],Graphics[g27],
    Graphics[g28],Graphics[g29],Graphics[g30],
    Graphics[g31],Graphics[g32],Graphics[g33],
    AspectRatio->Automatic];
```

(b) Multiple-layer planar waveguide package for TE modes incidence

```
(*PROGRAM NAME: ml-te.m *)

(*
 ------------------------------
  n =order of the mode,
  fl=total number of layers,
  ml=the location of the guiding layer,
  sl=the location of the substrate.
 ------------------------------
 *)

gam[n1_,n2_]:=n1^2/n2^2;
tanfunc[k1_,k2_,d1_,tnf_]:=-(k1/k2)(Tan[k1*d1]-tnf)/
                (1+tnf*Tan[k1*d1]);
avfunc[k1_,d1_,kph1_,e1_]:=Re[(1/2)*(d1+(Sin[k1*d1]/k1)*Cos[k1
*d1-2*kph1])*e1^2];

i=1; alList={}; bList={}; biList={}; tv={0};
Do[ al=nl[[i]]*k0;
   alList=Append[alList,al];
   If[i>1,tv=Append[tv,tv[[i-1]]+dl[[i]]]];
   i=i+1,
 {fl}
 ];
 tv[[fl]]=0;

j=0; nt1=1; klList={};
sbe=alList[[sl]]+(alList[[ml]]-alList[[sl]])/4;
bList=Append[bList,{1,sbe}];
biList=Append[biList,{1,Im[sbe]}];

Do[
  i=1; klList={};
  Do[ kl=Sqrt[alList[[i]]^2-sbe^2];
    klList=Append[klList,kl];
    i=i+1,
   {fl}
   ];

   i=3; tnfsList={};
   tnfs=-I klList[[1]]/klList[[2]];
   tnfsList={0,tnfs};
   Do[ di=dl[[i-1]];
     tnfi=tanfunc[klList[[i-1]],klList[[i]],di,tnfsList[[i-1]]];
     tnfsList=Append[tnfsList,tnfi],
     {i,3,ml} ];

   i=fl-2; tnfcList=Table[0,{fl}];
   tnfc=-I klList[[fl]]/klList[[fl-1]];
   tnfcList=ReplacePart[tnfcList,tnfc,i+1];
   Do[ If[i<ml,Break[] ];
     di=dl[[i+1]];
     tnfi=tanfunc[klList[[i+1]],klList[[i]],di,tnfcList[[i+1]]];
     tnfcList=ReplacePart[tnfcList,tnfi,i],
     {i,fl-2,ml,-1} ];
   fl=klList[[ml]]*dl[[ml]]-(ArcTan[tnfsList[[ml]]]+
     ArcTan[tnfcList[[ml]]]+n*pi);
   vbe2=Sqrt[alList[[ml]]^2-(klList[[ml]]*(1+stp))^2];
   i=1;
   Do[ kl=Sqrt[alList[[i]]^2-vbe2^2];
     klList=ReplacePart[klList,kl,i];
     i=i+1, {fl} ];
   i=3;
   tnfs=-I klList[[1]]/klList[[2]];
   tnfsList=ReplacePart[tnfsList,tnfs,i-1];
   Do[ If[3>ml,Break[]];
     di=dl[[i-1]];
```

```
    tnfi=tanfunc[klList[[i-1]],klList[[i]],di,tnfsList[[i-1]]];
    tnfsList=ReplacePart[tnfsList,tnfi,i],
    {i,3,ml} ];

  i=fl-2;
  tnfc=-I klList[[fl]]/klList[[fl-1]];
  tnfcList=ReplacePart[tnfcList,tnfc,i+1];
  Do[ If[i<ml,Break[] ];
    di=dl[[i+1]];
    tnfi=tanfunc[klList[[i+1]],klList[[i]],di,tnfcList[[i+1]]];
    tnfcList=ReplacePart[tnfcList,tnfi,i],
    {i,fl-2,ml,-1} ];
  f2=klList[[ml]]*dl[[ml]]-(ArcTan[tnfsList[[ml]]]+
    ArcTan[tnfcList[[ml]]]+n*pi);
  If[f2==f1,Break[] ];
  km=klList[[ml]](1-stp*f1/(f2-f1));
  vbe=Sqrt[alList[[ml]]^2-km^2];
  If[Abs[vbe]<Abs[alList[[ml]]]&&Abs[vbe]>Abs[alList[[1]]]
    ,Break[]];
  bList=Append[bList,{nt1+1,vbe}];
  biList=Append[biList,{nt1+1,Im[vbe]}];
  If[Abs[vbe]<=Abs[alList[[sl]]],
   sbe=alList[[sl]]+(alList[[ml]]-alList[[sl]])/(4+nt1*2),
   sbe=alList[[ml]]-(alList[[ml]]-alList[[sl]])/(4+nt1*2)];
  nt1=nt1+1;
  bList=Append[bList,{nt1,sbe}];
  biList=Append[biList,{nt1,Im[sbe]}],
{30}
];
bList=Append[bList,{nt1+1,bett}];
biList=Append[biList,{nt1+1,Im[bett]}];

j2=nt1+1; bett=vbe;
Do[ i=1; j2=j2+1;
   Do[ kl=Sqrt[alList[[i]]^2-vbe^2];
     klList=ReplacePart[klList,kl,i];
     i=i+1, {fl} ];
   i=3;
   tnfs=-I klList[[1]]/klList[[2]];
   tnfsList=ReplacePart[tnfsList,tnfs,i-1];
   Do[ If[3>ml,Break[]];
     di=dl[[i-1]];
     tnfi=tanfunc[klList[[i-1]],klList[[i]],di,tnfsList[[i-1]]];
     tnfsList=ReplacePart[tnfsList,tnfi,i],
     {i,3,ml} ];

   i=fl-2;
   tnfc=-I klList[[fl]]/klList[[fl-1]];
   tnfcList=ReplacePart[tnfcList,tnfc,i+1];
   Do[ If[i<ml,Break[] ];
     di=dl[[i+1]];
     tnfi=tanfunc[klList[[i+1]],klList[[i]],di,tnfcList[[i+1]]];
     tnfcList=ReplacePart[tnfcList,tnfi,i],
     {i,fl-2,ml,-1} ];
   f1=klList[[ml]]*dl[[ml]]-(ArcTan[tnfsList[[ml]]]+
     ArcTan[tnfcList[[ml]]]+n*pi);
   vbe2=Sqrt[alList[[ml]]^2-(klList[[ml]]*(1+stp))^2];
   i=1;
   Do[ kl=Sqrt[alList[[i]]^2-vbe2^2];
     klList=ReplacePart[klList,kl,i];
     i=i+1, {fl} ];

   i=3;
   tnfs=-I klList[[1]]/klList[[2]];
   tnfsList=ReplacePart[tnfsList,tnfs,i-1];
   Do[ If[3>ml,Break[]];
     If[3>ml,Break[]];
     di=dl[[i-1]];
     tnfi=tanfunc[klList[[i-1]],klList[[i]],di,tnfsList[[i-1]]];
     tnfsList=ReplacePart[tnfsList,tnfi,i],
     {i,3,ml} ];

   i=fl-2;
   tnfc=-I klList[[fl]]/klList[[fl-1]];
   tnfcList=ReplacePart[tnfcList,tnfc,i+1];
   Do[ If[i<ml,Break[] ];
     di=dl[[i+1]];
     tnfi=tanfunc[klList[[i+1]],klList[[i]],di,tnfcList[[i+1]]];
     tnfcList=ReplacePart[tnfcList,tnfi,i],
     {i,fl-2,ml,-1} ];
   f2=klList[[ml]]*dl[[ml]]-(ArcTan[tnfsList[[ml]]]+
     ArcTan[tnfcList[[ml]]])-n*pi;
   If[f2==f1,Break[] ];
     km=klList[[ml]](1-stp*f1/(f2-f1));
     vbe=Sqrt[alList[[ml]]^2-km^2];

     If[Abs[vbe-bett]/vbe<smt,bett=vbe;Break[] ];
     bList=Append[bList,{j2,vbe}];
     biList=Append[biList,{j2,Im[vbe]}];
     bett=vbe;
     If[Re[vbe]>Re[alList[[ml]]] || Re[vbe]<Re[alList[[1]]],Break[]
],
   {20}
  ];
bList=Append[bList,{j2,vbe}];
biList=Append[biList,{j2,Im[vbe]}];

Print["n(order of the mode)= ",n];
Print["nt1=",N[nt1+1,5],",  j2=",N[j2-nt1-1,5]];
Print["fl(total layers)=",fl];
Print["ml(location of the guiding-layer)=",ml];
Print["sl(location of the substrate)=",sl];
Print["n(indices of layers)="];
Print[N[nl,8]];
Print["d(thickness of layers)="];
Print[N[dl,20]];
Print["beta=",N[bett,20]];
Print["Neff=",N[bett/k0,20]];
Print["kf*d/2=",N[klList[[ml]]*dl[[ml]]/2,20]];
Print["b*d/2=",N[bett*dl[[ml]]/2,20]];
ListPlot[Re[bList],PlotJoined->True,Frame->True];

klList=.; tnfsList=.; tnfcList=.;
nout=2; vkiList={Sqrt[bett^2-alList[[1]]^2]};
Do[
 vkiList=Append[vkiList,Sqrt[alList[[nout]]^2-bett^2]];
 nout=nout+1,
 {fl-2}
 ];
vkiList=Append[vkiList,Sqrt[bett^2-alList[[fl]]^2]];

phiList={0,ArcTan[vkiList[[1]]/vkiList[[2]]]/vkiList[[2]]};
nout=3;
Do[
  ph=ArcTan[-(vkiList[[nout-1]]/vkiList[[nout]])*
    Tan[vkiList[[nout-1]]*(dl[[nout-1]]-
    phiList[[nout-1]])]]/vkiList[[nout]];
  phiList=Append[phiList,ph];
  nout=nout+1,
  {nout,3,ml}
  ];

pht=dl[[fl-1]]-ArcTan[vkiList[[fl]]/vkiList[[fl-1]]]/vkiList[[fl-1]];
phcList={pht};
nout=fl-2;
 Do[
   ph=N[dl[[nout]]-ArcTan[-(vkiList[[nout+1]]/
     vkiList[[nout]])*Tan[vkiList[[nout+1]]*
     pht]/vkiList[[nout]],86];
   phcList=Prepend[phcList,ph];
   pht=ph,
  {nout,fl-2,ml+1,-1}
  ];
phiList=Flatten[{phiList,phcList}];
phcList=.;

eiej={1/Sqrt[1+(vkiList[[1]]/vkiList[[2]])^2]};
nout=2;
Do[
  eij=1/Sqrt[(Cos[vkiList[[nout]](dl[[nout]]-phiList[[nout]]))^2
    +(vkiList[[nout]]/vkiList[[nout+1]])^2*(Sin[vkiList[[nout]]
    (dl[[nout]]-phiList[[nout]]))^2];
  eiej=Append[eiej,eij];
  nout=nout+1,
  {fl-2}
  ];

gList={0,dl[[2]]+1/vkiList[[1]]};
nout=3;
Do[
  vg=dl[[nout]]+(1-(vkiList[[nout]]/vkiList[[nout-1]])^2)*
    Sin[2*vkiList[[nout]]*phiList[[nout]]]/(2*vkiList[[nout]]);
  gList=Append[gList,vg];
  nout=nout+1,
  {ml-3}
  ];
```

```
gList=Append[gList,1];

nout=ml+1;
Do[
  vg=dl[[nout]]+(1-(vkiList[[nout]]/vkiList[[nout+1]])^2)*
    Sin[2*vkiList[[nout]]*(dl[[nout]]-phiList[[nout]])]/
    (2*vkiList[[nout]]);
  gList=Append[gList,vg];
  nout=nout+1,
  {fl-ml-1}
 ];

nout=2; earv1=0;
Do[
  earv1=(earv1+gList[[nout]])*eiej[[nout]]^2;
  nout=nout+1,
  {ml-2}
 ];
nout=ml; earv2=0;
Do[
  earv2=(earv2+gList[[nout+1]])/eiej[[nout]]^2;
  nout=nout+1,
  {fl-ml-1}
 ];

eaml=1/Sqrt[(bett/(4*omg*mu0))*(earv1+earv2+dl[[ml]]+
   (1-(vkiList[[ml]]/vkiList[[ml-1]])^2)*Sin[2*vkiList[[ml]]*
   phiList[[ml]]]/(2*vkiList[[ml]])+(1-(vkiList[[ml]]/
   vkiList[[ml+1]])^2)*Sin[2*vkiList[[ml]]*(dl[[ml]]-
   phiList[[ml]])]/(2*vkiList[[ml]]))];
eaml=eaml*Conjugate[eaml];
eaml=eaml/Sqrt[Abs[eaml]];

nout=1; amp1=eaml; eaList=Table[0,{ml}];
Do[
  amp1=amp1*Cos[vkiList[[ml-nout+1]]phiList[[ml-nout+1]]]/
     Cos[vkiList[[ml-nout]]*(dl[[ml-nout]]-
     phiList[[ml-nout]])];
  eaList=ReplacePart[eaList,amp1,ml-nout];
  nout=nout+1,
  {ml-2}
 ];
eaList=ReplacePart[eaList,eaml,ml];
amp1=eaList[[2]]Cos[vkiList[[2]]phiList[[2]]];
eaList=ReplacePart[eaList,amp1,1];

nout=ml+1; amp2=eaml;
Do[
  amp2=amp2*Cos[vkiList[[nout-1]](dl[[nout-1]]-
     phiList[[nout-1]])]/Cos[vkiList[[nout]]*phiList[[nout]]];
  eaList=Append[eaList,amp2];
  nout=nout+1,
  {fl-ml-1}
 ];
eaList=Append[eaList,eaList[[fl-1]]Cos[vkiList[[fl-1]]*
     (dl[[fl-1]]-phiList[[fl-1]])]];

areast={Abs[eaList[[1]]]^2/(2*vkiList[[1]])};
areafl=Abs[eaList[[fl]]]^2/(2*vkiList[[fl]]);
totar=areast[[1]]+areafl;
nout=2; Do[
 area=(dl[[nout]]/2+Sin[2*vkiList[[nout]]*(dl[[nout]]-
    phiList[[nout]])]/(4*vkiList[[nout]])+
    Sin[2*vkiList[[nout]]*phiList[[nout]]]/
    (4*vkiList[[nout]]))*eaList[[nout]]^2;
 totar=totar+area;
 areast=Append[areast,area];
 nout=nout+1,
 {fl-2}
 ];
areast=Append[areast,areafl];

Print["bett/k0=",N[Chop[bett/k0],10]];
Print["areast/totar=",N[Chop[areast/totar],10]];
(*Print["confirm=",N[Sum[areast[[i]],{i,2,fl,2}]/totar,10]];*)

pkd=Sum[dl[[i]],{i,2,fl-1}]*k0;
If[pkd<1,pkd=2];

ampmax=Max[Table[Abs[eaList[[1]]*Exp[vkiList[[1]]*y/k0]],
          {y,-pkd,0,pkd/50}]];
nout=2;
Do[
  tgra=Table[Abs[eaList[[nout]]*Cos[vkiList[[nout]]*
     (y/k0-tv[[nout-1]]-phiList[[nout]])]],
     {y,tv[[nout-1]]*k0,tv[[nout]]*k0,pkd/50}];
  amp2=Max[tgra]; If[amp2>ampmax,ampmax=amp2];
  nout=nout+1,
 {fl-2}
 ];
tgra=Table[Abs[eaList[[fl]]*Exp[-vkiList[[fl]]*(y/k0-tv[[fl-1]])]],
          {y,tv[[fl-1]]*k0,tv[[fl-1]]*k0+pkd,pkd/50}];
amp2=Max[tgra]; If[amp2>ampmax,ampmax=amp2];

graph={{Plot[eaList[[1]]*Exp[vkiList[[1]]*y/k0]/ampmax,
           {y,-pkd,0}]}};

nout=2;
Do[
  xv=tv[[nout]]*k0;
  gra=Plot[eaList[[nout]]*Cos[vkiList[[nout]]*
     (y/k0-tv[[nout-1]]-phiList[[nout]])]/ampmax,
     {y,tv[[nout-1]]*k0,tv[[nout]]*k0}];
  graph=Append[graph,{gra,Graphics[Line[{{xv,-1},{xv,1}}]]}];
  nout=nout+1,
 {fl-2}
 ];
gra=Plot[eaList[[fl]]*Exp[-vkiList[[fl]]*(y/k0-tv[[fl-1]])]/
        ampmax,{y,tv[[fl-1]]*k0,2pkd}];
graph=Append[graph,gra];

gph=Flatten[graph];
Show[gph,Frame->True,FrameLabel->
   {"y*k0","Relative Amplitude"},PlotRange->{{-pkd,2pkd},{-
1,1}}];
```

(c) Multiple-layer planar waveguide package for TM modes incidence

```
(*PROGRAM NAME: ml-tm.m *)

(*
 ------------------------------------
  n =order of the mode,
  fl=total number of layers,
  ml=the location of the guiding layer,
  sl=the location of the substrate.
 ------------------------------------
*)

gam[n1_,n2_]:=n1^2/n2^2;
tanfunc[k1_,k2_,d1_,tnf_,gm_]:=-gm*(k1/k2)(Tan[k1*d1]-tnf)/
                    (1+tnf*Tan[k1*d1]);
avfunc[k1_,d1_,kph1_,e1_]:=(1/2)*(d1+(Sin[k1*d1]/k1)*Cos[k1*d1
-2*kph1])*e1^2;

i=1; alList={}; bList={}; biList={}; tv={0};
Do[ al=nl[[i]]*k0;
   alList=Append[alList,al];
   If[i>1,tv=Append[tv,tv[[i-1]]+dl[[i]]]];
   i=i+1,
 {fl}
 ];
tv[[fl]]=0;

j=0; nt1=1; klList={};
sbe=alList[[ml]]-(alList[[ml]]-alList[[sl]])/4;
bList=Append[bList,{1,sbe}];
biList=Append[biList,{1,Im[sbe]}];

Do[
  i=1; klList={};
  Do[ kl=Sqrt[alList[[i]]^2-sbe^2];
    klList=Append[klList,kl];
    i=i+1,
   {fl}
   ];

   i=3; tnfsList={};
   tnfs=-I gam[nl[[2]],nl[[1]]]*klList[[1]]/klList[[2]];
   tnfsList={0,tnfs};
   Do[ di=dl[[i-1]];
      gm=gam[nl[[i]],nl[[i-1]]];
      tnfi=tanfunc[klList[[i-1]],klList[[i]],di,tnfsList[[i-1]],gm];
      tnfsList=Append[tnfsList,tnfi],
      {i,3,ml} ];

   i=fl-2; tnfcList=Table[0,{fl}];
   tnfc=-I gam[nl[[fl-1]],nl[[fl]]]*klList[[fl]]/klList[[fl-1]];
   tnfcList=ReplacePart[tnfcList,tnfc,fl-1];
   Do[ If[i<ml,Break[] ];
      di=dl[[i+1]];
      gm=gam[nl[[i]],nl[[i+1]]];
      tnfi=tanfunc[klList[[i+1]],klList[[i]],di,tnfcList[[i+1]],gm];
      tnfcList=ReplacePart[tnfcList,tnfi,i],
      {i,fl-2,ml,-1} ];
   f1=klList[[ml]]*dl[[ml]]-(ArcTan[tnfsList[[ml]]]+
     ArcTan[tnfcList[[ml]]]+n*pi);
   vbe2=Sqrt[alList[[ml]]^2-(klList[[ml]]*(1+stp))^2];
   i=1;
   Do[ kl=Sqrt[alList[[i]]^2-vbe2^2];
      klList=ReplacePart[klList,kl,i];
      i=i+1, {fl} ];
   i=3;
   tnfs=-I gam[nl[[2]],nl[[1]]]*klList[[1]]/klList[[2]];
   tnfsList=ReplacePart[tnfsList,tnfs,2];
   Do[ If[3>ml,Break[]];
      di=dl[[i-1]];
      gm=gam[nl[[i]],nl[[i-1]]];
      tnfi=tanfunc[klList[[i-1]],klList[[i]],di,tnfsList[[i-1]],gm];
      tnfsList=ReplacePart[tnfsList,tnfi,i],
      {i,3,ml} ];

   i=fl-2;
   tnfc=-I gam[nl[[fl-1]],nl[[fl]]]*klList[[fl]]/klList[[fl-1]];
   tnfcList=ReplacePart[tnfcList,tnfc,fl-1];
   Do[ If[i<ml,Break[] ];
      di=dl[[i+1]];
      gm=gam[nl[[i]],nl[[i+1]]];
      tnfi=tanfunc[klList[[i+1]],klList[[i]],di,tnfcList[[i+1]],gm];
      tnfcList=ReplacePart[tnfcList,tnfi,i],
      {i,fl-2,ml,-1} ];
   f2=klList[[ml]]*dl[[ml]]-(ArcTan[tnfsList[[ml]]]+
     ArcTan[tnfcList[[ml]]]+n*pi);
   If[f2==f1,Break[] ];
   km=N[klList[[ml]](1-stp*f1/(f2-f1)),86];
   vbe=Sqrt[alList[[ml]]^2-km^2];
   If[Abs[vbe]<Abs[alList[[ml]]]&&Abs[vbe]>Abs[alList[[1]]]
     ,Break[]];
   bList=Append[bList,{nt1+1,vbe}];
   biList=Append[biList,{nt1+1,Im[vbe]}];
   If[Abs[vbe]<=Abs[alList[[sl]]],
     sbe=alList[[sl]]+(alList[[ml]]-alList[[sl]])/(4+nt1*2),
     sbe=alList[[ml]]-(alList[[ml]]-alList[[sl]])/(4+nt1*2)];
   nt1=nt1+1;
   bList=Append[bList,{nt1,sbe}];
   biList=Append[biList,{nt1,Im[sbe]}],
 {30}
 ];
 bList=Append[bList,{nt1+1,bett}];
 biList=Append[biList,{nt1+1,Im[bett]}];

 j2=nt1+1; bett=vbe;
 Do[ i=1; j2=j2+1;
    Do[ kl=Sqrt[alList[[i]]^2-vbe^2];
       klList=ReplacePart[klList,kl,i];
       i=i+1, {fl} ];
    i=3;
    tnfs=-I gam[nl[[2]],nl[[1]]]*klList[[1]]/klList[[2]];
    tnfsList=ReplacePart[tnfsList,tnfs,2];
    Do[ If[3>ml,Break[]];
       di=dl[[i-1]];
       gm=gam[nl[[i]],nl[[i-1]]];
       tnfi=tanfunc[klList[[i-1]],klList[[i]],di,tnfsList[[i-1]],gm];
       tnfsList=ReplacePart[tnfsList,tnfi,i],
       {i,3,ml} ];

    i=fl-2;
    tnfc=-I gam[nl[[fl-1]],nl[[fl]]]*klList[[fl]]/klList[[fl-1]];
    tnfcList=ReplacePart[tnfcList,tnfc,fl-1];
    Do[ If[i<ml,Break[] ];
       di=dl[[i+1]];
       gm=gam[nl[[i]],nl[[i+1]]];
       tnfi=tanfunc[klList[[i+1]],klList[[i]],di,tnfcList[[i+1]],gm];
       tnfcList=ReplacePart[tnfcList,tnfi,i],
       {i,fl-2,ml,-1} ];
    f1=klList[[ml]]*dl[[ml]]-(ArcTan[tnfsList[[ml]]]+
      ArcTan[tnfcList[[ml]]]+n*pi);
    vbe2=Sqrt[alList[[ml]]^2-(klList[[ml]]*(1+stp))^2];
    i=1;
    Do[ kl=Sqrt[alList[[i]]^2-vbe2^2];
       klList=ReplacePart[klList,kl,i];
       i=i+1, {fl} ];

    i=3;
    tnfs=-I gam[nl[[2]],nl[[1]]]*klList[[1]]/klList[[2]];
    tnfsList=ReplacePart[tnfsList,tnfs,2];
    Do[
       If[3>ml,Break[]];
       di=dl[[i-1]];
       gm=gam[nl[[i]],nl[[i-1]]];
       tnfi=tanfunc[klList[[i-1]],klList[[i]],di,tnfsList[[i-1]],gm];
       tnfsList=ReplacePart[tnfsList,tnfi,i],
       {i,3,ml} ];

    i=fl-2;
    tnfc=-I gam[nl[[fl-1]],nl[[fl]]]*klList[[fl]]/klList[[fl-1]];
    tnfcList=ReplacePart[tnfcList,tnfc,fl-1];
    Do[ If[i<ml,Break[] ];
       di=dl[[i+1]];
       gm=gam[nl[[i]],nl[[i+1]]];
       tnfi=tanfunc[klList[[i+1]],klList[[i]],di,tnfcList[[i+1]],gm];
       tnfcList=ReplacePart[tnfcList,tnfi,i],
       {i,fl-2,ml,-1} ];
    f2=klList[[ml]]*dl[[ml]]-(ArcTan[tnfsList[[ml]]]+
      ArcTan[tnfcList[[ml]]]+n*pi);
    If[f2==f1,Break[] ];
    km=N[klList[[ml]](1-stp*f1/(f2-f1)),86];
    vbe=Sqrt[alList[[ml]]^2-km^2];
```

```
    If[Abs[vbe-bett]/vbe<smt,bett=vbe;Break[] ];
    bList=Append[bList,{j2,vbe}];
    biList=Append[biList,{j2,Im[vbe]}];
    bett=vbe;
    If[Re[vbe]>Re[alList[[ml]]] || Re[vbe]<Re[alList[[1]]],Break[]
],
   {20}
  ];
bList=Append[bList,{j2,vbe}];
biList=Append[biList,{j2,Im[vbe]}];

Print["n(order of the mode)= ",n];
Print["nt1=",N[nt1+1,5],",  j2=",N[j2-nt1-1,5]];
Print["fl(total layers)=",fl];
Print["ml(location of the guiding-layer)=",ml];
Print["sl(location of the substrate)=",sl];
Print["n(indices of layers)="];
Print[N[nl,8]];
Print["d(thickness of layers)="];
Print[N[dl,20]];
Print["beta=",N[bett,20]];
Print["Neff=",N[bett/k0,20]];
Print["kf*d/2=",N[klList[[ml]]*dl[[ml]]/2,20]];
Print["b*d/2=",N[bett*dl[[ml]]/2,20]];
ListPlot[Re[bList],PlotJoined->True,Frame->True];

nout=2; vkiList={Sqrt[bett^2-alList[[1]]^2]};
Do[
 vkiList=Append[vkiList,Sqrt[alList[[nout]]^2-bett^2]];
 nout=nout+1,
 {fl-2}
 ];
vkiList=Append[vkiList,Sqrt[bett^2-alList[[fl]]^2]];

phiList={0,ArcTan[gam[nl[[2]],nl[[1]]]*vkiList[[1]]/
      vkiList[[2]]]/vkiList[[2]]};
nout=3;
Do[
  ph=ArcTan[-gam[nl[[nout]],nl[[nout-1]]]*(vkiList[[nout-1]]/
    vkiList[[nout]])*Tan[vkiList[[nout-1]]*(dl[[nout-1]]-
    phiList[[nout-1]])]]/vkiList[[nout]];
  phiList=Append[phiList,ph];
  nout=nout+1,
  {nout,3,ml}
 ];

pht=dl[[fl-1]]-ArcTan[gam[nl[[fl-1]],nl[[fl]]]*vkiList[[fl]]/
            vkiList[[fl-1]]]/vkiList[[fl-1]];
phcList={pht};
nout=fl-2;
 Do[
   ph=N[dl[[nout]]-ArcTan[-gam[nl[[nout]],nl[[nout+1]]]*
   (vkiList[[nout+1]]/vkiList[[nout]])*Tan[vkiList[[nout+1]]*
   pht]]/vkiList[[nout]],86];
   phcList=Prepend[phcList,ph];
   pht=ph,
  {nout,fl-2,ml+1,-1}
  ];
phiList=Flatten[{phiList,phcList}];

hihj={1/Sqrt[1+(vkiList[[1]]/vkiList[[2]])^2*gam[nl[[2]],nl[[1]]]^2]
};
nout=2;
Do[
  hij=1/Sqrt[(Cos[vkiList[[nout]](N[dl[[nout]]-
phiList[[nout]],86])])^2+

(vkiList[[nout]]/vkiList[[nout+1]])^2*gam[nl[[nout+1]],nl[[nout]]]^
2*
   (Sin[vkiList[[nout]](N[dl[[nout]]-phiList[[nout]],86])])^2];
  hihj=Append[hihj,hij];
  nout=nout+1,
  {fl-2}
 ];

gList={0,dl[[2]]+(1/(nl[[1]]^2*vkiList[[1]]))*(1+vkiList[[1]]^2/
    vkiList[[2]]^2)*hihj[[1]]^2};
nout=3;
Do[
  vg=dl[[nout]]+(1-(vkiList[[nout]]/vkiList[[nout-
1]])^2/nl[[nout]]^2)
    *Sin[2*vkiList[[nout]]*phiList[[nout]]]/(2*vkiList[[nout]]);
  gList=Append[gList,vg];
  nout=nout+1,
  {ml-3}
 ];

gList=Append[gList,1];

nout=ml+1;
Do[
  vg=dl[[nout]]+(1-
(vkiList[[nout]]/vkiList[[nout+1]])^2/nl[[nout]]^2)
    *Sin[2*vkiList[[nout]]*(dl[[nout]]-phiList[[nout]])]/
    (2*vkiList[[nout]]);
  gList=Append[gList,vg];
  nout=nout+1,
  {fl-ml-1}
 ];

nout=2; earv1=0;
Do[
  earv1=(earv1+gList[[nout]])*hihj[[nout]]^2;
  nout=nout+1,
  {ml-2}
 ];
nout=ml; earv2=0;
Do[
  earv2=(earv2+gList[[nout+1]])/hihj[[nout]]^2;
  nout=nout+1,
  {fl-ml-1}
 ];

eaml=1/Sqrt[(bett/(4*omg*ep0))*(earv1+earv2+dl[[ml]]+
   (1/nl[[ml]]^2)*(1-(vkiList[[ml]]/vkiList[[ml-1]])^2)*
   Sin[2*vkiList[[ml]]*phiList[[ml]]]/(2*vkiList[[ml]])+
   (1/nl[[ml]]^2)*(1-(vkiList[[ml]]/vkiList[[ml+1]])^2)*
   Sin[2*vkiList[[ml]]*(dl[[ml]]-phiList[[ml]])]/
   (2*vkiList[[ml]]))];

eaml=eaml*Conjugate[eaml];
eaml=eaml/Sqrt[Abs[eaml]];

nout=1; amp1=eaml; eaList=Table[0,{ml}];
Do[
  amp1=amp1*Cos[vkiList[[ml-nout+1]]phiList[[ml-nout+1]]]/
      Cos[vkiList[[ml-nout]]*(dl[[ml-nout]]-
      phiList[[ml-nout]])];
eaList=ReplacePart[eaList,amp1,ml-nout];
  nout=nout+1,
  {ml-2}
 ];
eaList=ReplacePart[eaList,eaml,ml];
amp1=eaList[[2]]Cos[vkiList[[2]]phiList[[2]]];
eaList=ReplacePart[eaList,amp1,1];

nout=ml+1; amp2=eaml;
Do[
  amp2=amp2*Cos[vkiList[[nout-1]](dl[[nout-1]]-
      phiList[[nout-1]])]/Cos[vkiList[[nout]]*phiList[[nout]]];
  eaList=Append[eaList,amp2];
  nout=nout+1,
  {fl-ml-1}
 ];
eaList=Append[eaList,eaList[[fl-1]]Cos[vkiList[[fl-1]]*
      (dl[[fl-1]]-phiList[[fl-1]])]];

areast={Abs[eaList[[1]]]^2/(2*nl[[1]]^2*vkiList[[1]])};
areafl=Abs[eaList[[fl]]]^2/(2*nl[[fl]]^2*vkiList[[fl]]);
totar=areast[[1]]+areafl;
nout=2; Do[
 area=Re[(1/nl[[nout]]^2)*(dl[[nout]]/2+Sin[2*vkiList[[nout]]*
    (dl[[nout]]-phiList[[nout]])]/(4*vkiList[[nout]])+
     Sin[2*vkiList[[nout]]*phiList[[nout]]]/
     (4*vkiList[[nout]]))*eaList[[nout]]^2];
 totar=totar+area;
 areast=Append[areast,area];
 nout=nout+1,
 {fl-2}
 ];
areast=Append[areast,areafl];

Print["bett/k0=",N[Chop[bett/k0],10]];
Print["areast/totar=",N[Chop[areast/totar],10]];
N[Sum[areast[[i]],{i,2,fl,2}]/totar,10];
```

```
pkd=Sum[dl[[i]],{i,2,fl-1}]*k0;
If[pkd<1,pkd=2];
(*pkd=5;*)

ampmax=Max[Table[Abs[eaList[[1]]*Exp[vkiList[[1]]*y/k0]],
            {y,-pkd,0,pkd/50}]];
nout=2;
Do[
  tgra=Table[Abs[eaList[[nout]]*Cos[vkiList[[nout]]*
     (y/k0-tv[[nout-1]]-phiList[[nout]])]],
     {y,tv[[nout-1]]*k0,tv[[nout]]*k0,pkd/50}];
  amp2=Max[tgra]; If[amp2>ampmax,ampmax=amp2];
  nout=nout+1,
 {fl-2}
 ];
tgra=Table[Abs[eaList[[fl]]*Exp[-vkiList[[fl]]*(y/k0-tv[[fl-1]])]],
          {y,tv[[fl-1]]*k0,tv[[fl-1]]*k0+pkd,pkd/50}];
amp2=Max[tgra]; If[amp2>ampmax,ampmax=amp2];

graph={{Plot[eaList[[1]]*Exp[vkiList[[1]]*y/k0]/ampmax,
            {y,-pkd,0}]}};

nout=2;
Do[
  xv=tv[[nout]]*k0;
  gra=Plot[eaList[[nout]]*Cos[vkiList[[nout]]*
     (y/k0-tv[[nout-1]]-phiList[[nout]])]/ampmax,
     {y,tv[[nout-1]]*k0,tv[[nout]]*k0}];
  graph=Append[graph,{gra,Graphics[Line[{{xv,-1},{xv,1}}]]}];
  nout=nout+1,
 {fl-2}
 ];
gra=Plot[eaList[[fl]]*Exp[-vkiList[[fl]]*(y/k0-tv[[fl-1]])]/
          ampmax,{y,tv[[fl-1]]*k0,2pkd}];
graph=Append[graph,gra];

gph=Flatten[graph];
Show[gph,Frame->True,FrameLabel->
   {"y*k0","Relative Amplitude"},PlotRange->{{-pkd,2pkd},{-
1,1}}];
```

References

[1] H. Kogelnik, "An introduction to integrated optics," *IEEE Tran. Microwave Theory Tech.*, Vol.MTT–23, No.1, pp.2–20, 1975.

[2] C. Elachi, "Waves in the active and passive periodic structures: a review," *Proc. IEEE*, Vol.64, No.12, pp.1666–1698, 1976.

[3] A. Yariv and M Nakamura, "Periodic structures for integrated optics," *IEEE J. Quantum Electron.*, Vol.QE–13, No.4, pp.233–253, 1977.

[4] T. Suhara and H. Nishihara, "Integrated optics components and devices using periodic structures," *IEEE J. Quantum Electron.*, Vol.QE–22, No.6, pp.845–866, 1986.

[5] H. Kogelnik and C. V. Shank, "Coupled wave theory of distributed feedback lasers," *J. Appl. Phys.*, Vol.43, No.5, pp.2327–2335, 1972.

[6] W. Streifer, D. R. Scifres, and R. D. Burnham, "Coupling coefficients for distributed feedback single– and double–heterostructure diode lasers," *IEEE J. Quantum Electron.*, Vol.QE–11, No.11, pp.867–873, 1975.

[7] Y. Itaya, T. Matsuoka, K. Kuroiwa, and T Ikegami, "Longitudinal mode behaviour of 1.5 μm range GaInAs/InP distributed feedback lasers," *IEEE J. Quantum Electron.*, Vol.QE–20, No.3, pp.230–235, 1984.

[8] S. Wang, "Principle of distributed feedback and distributed Bragg reflector lasers," *IEEE J. Quantum Electron.*, Vol.QE–10, No.4, pp.413–426, 1974.

[9] H. M. Stoll, "Optimally coupled, GaAs–distributed Bragg reflection lasers," *IEEE Trans. Circuits Sys.*, Vol.CAS–26, No.12, pp.1065–1071, 1979.

[10] G. I. Stegeman and C. J. Seaton, "Nonlinear integrated optics," *J. Appl. Phys.*, Vol.58, pp.R57–R78, 1985.

[11] D. C. Flanders, H. Kogelnik, R. V. Schmidt, and C. V. Shank, "Grating filters for thin–film optical waveguides," *Appl. Phys. Lett.*, Vol.24, No.4, pp.194–196, 1974.

[12] C. S. Hong, J. B. Shellan, A. C. Livanos, A. Yariv, and A. Katzir, "Broad–band grating filters for thin–film optical waveguides," *Appl. Phys. Lett.*, Vol.31, No.4, pp.276–278, 1977.

[13] R. V. Schmidt, D. C. Flenders, C. V. Shank, and R. D. Standley, "Narrow–band grating filters for thin–film optical waveguides," *Appl. Phys. Lett.*, Vol.25, pp.651–652, 1974.

[14] A. Yi-Yan, C. D. W. Wilkinson, and P. J. R. Laybourn, "Two–dimensional grating unit cell demultiplexer for thin-film optical waveguides," IEEE J. Quantum Electron., Vol.QE–16, No.16, pp.1089–1092, 1980.

[15] A. Yi–Yan, J. A. H. Wilkinson, and C. D. W. Wilkinson, "Optical waveguide filters for the visible spectrum," *IEE PROC.*, Vol.127, Pt. H, No.6, pp.335–341, 1980.

[16] K. A. Winick and J. E. Roman, "Design of corrugated waveguide filter by Fourier–transform techniques," *IEEE J. Quantum Electron.*, Vol.26, No.11, pp.1918–1928, 1990.

[17] M. L. Dakss, L. Kuhn, P. F. Heidrich, and B. A. Scott, "Grating coupler for efficient excitation of optical guided waves in thin films," *Appl. Phys. Lett.*, Vol.16, No.12, pp.523–525, 1970.

[18] C. C. Ghizoni, B. –U. Chen, and C. L. Tang, "Theory and experiments on grating couplers for thin–film waveguides," *IEEE J. Quantum Electron.*, Vol.QE–12, No.2, pp.69–73, 1976.

[19] M. T. Wlodarczyle and S. R. Seshadri, "Analysis of grating couplers for planar dielectric waveguides," *J. Appl. Phys.*, Vol.58, No.1, pp.69–83, 1985.

[20] W. S. Park and S. R. Seshadri, "comparisons of the different configurations of the second–order reflection grating," *J. Appl. Phys.*, Vol.60, No.12, pp.4046–4076, 1986.

[21] W. P. Huang, B. E. Little, and C. L. Xu, "On phase matching and power coupling in grating–assisted coupler," *IEEE Photon. Technol. Lett.*, Vol.4, No.2, pp.151–153, 1992.

[22] Z. M. Chuang and L. A. Coldren, "On the spectral properties of widely tunable lasers using grating–assisted codirectional coupling," *IEEE Photon. Technol. Lett.*, Vol.5, No.1, pp.7–9, 1993.

[23] S. Zhang and T. Tamir, "Analysis and design of broadband grating couplers," *IEEE J. Quantum Electron.*, Vol.29, No.11, pp.2813–2824, 1993.

[24] S. Somekh and A. Yariv, "Phase matching by periodic modulation of the nonlinear optical properties," *Opt. Commun.*, Vol.6, No.4, pp.301–304, 1972.

[25] N. Bloembergen and A. J. Sievers, "Nonlinear optical properties of periodic laminar structures," *Appl. Phys. Lett.*, Vol.17, No.11, pp.483–485, 1970.

[26] B. U. Chen, C. C. Ghizoni and C. L. Tang, "Phase-matched second– harmonic generation in solid thin film using modulation of the nonlinear susceptibilities," *Appl. Phys. Lett.*, Vol.28, No.11, pp.651–653, 1976.

[27] D. Marcuse, *Theory of Dielectric Optical Waveguide.* New York: Academic Press 2nd Edition, 1991, Chapter 1–3.

[28] H. Kogelnik, *Guided–Wave Optoelectronics, Vol.26, edited by T. Tamir.* Berlin, Heidelberg, New York: Springer–Verlag 2nd Edition, 1990, Chapter 2.

[29] S. R. Seshadri, "Coupling of guided modes in the thin films with surface corrugation," *J. Appl. Phys.*, Vol.63, No.10, pp.R115–R146, 1988.

[30] K. Wagatsuma, H. Sakaki and S. Saito, "Mode Conversion and optical filtering of obliquely incident waves in corrugated waveguide filters," *IEEE J. Quantum Electron.*, Vol.QE–15, No.7, pp.1497–1507, 1979.

[31] S. R. Seshadri and M. –C. Tsai, "Mode conversion of obliquely incident guided magnetic waves by a grating on a yttrium iron garnet film for the normal magnetization," *J. Appl. Phys.*, Vol.56, No.2, pp.501–510, 1984.

[32] E. Popov and L. Mashev, "Analysis of mode coupling in planar optical waveguides," *OPTICA ACTA*, Vol.32, No.3, pp.265–280, 1985.

[33] J. Van Roey and P. E. Lagasse, "Coupled wave analysis of obliquely incident waves in thin film gratings," *Appl. Optics*, Vol.20, No.3, pp.423–429, 1981.

[34] G. L. Matthael, "A note concerning modes in dielectric waveguide for filter applications," *IEEE Trans. Microwave Theory Tech.*, Vol.MTT–31, No.3, pp.309–312, 1983.

[35] G. I. Stegeman, D. Sarid, J. J. Burke, and D. G. Hall, "Scattering of guided waves by surface periodic gratings for arbitrary angles of incidence: perturbation field theory and implications to normal–mode analysis," *J. Opt. Soc. Am.*, Vol.71, No.12, pp.1497–1507, 1981.

[36] L. A. Weller–Brophy and D. G. Hall, "Local normal mode analysis of guided mode interactions with waveguide gratings," *IEEE J. Lightwave Technol.*, Vol.6, No.6, pp.1069–1082, 1988.

[37] H. M. Stoll, "Distributed Bragg deflector: a multifunctional integrated optical device," *Appl. Opt.*, Vol.17, No.16, pp.2562–2569, 1978.

[38] A. C. Livanos, A. Katzir, A. Yariv, and C. S. Hong, "Chirped–grating demultiplexers in dielectric waveguides," *Appl. Phys. Lett.*, Vol.30, No.10, pp.519–521, 1977.

[39] T. Fukuzawa and M. Nakamura, "Mode coupling in thin–film chirped gratings," *Opt. Lett.*, Vol.4, No.11, pp.343–345, 1979.

[40] M. A. Diforte, M. Papuchon, C. Puech, P. Lallemand, and D. B. Ostrowsky, "Tuneable optically pumped GaAs–GaAlAs distributed–feedback lasers," *IEEE J. Quantum Electron.*, Vol.QE–14, No.8, pp.560-562, 1978.

[41] W. Streifer, D. R. Scifres, and R. D. Burnham, "Analysis of grating–coupled radiation in GaAs:GaAlAs lasers and waveguides," *IEEE J. Quantum Electron.*, Vol.QE–12, No.7, pp.422–428, 1976.

[42] T. Nobuyoshi, N. Morita, N. Kumagai, "Scattering and Mode conversion of guided modes by an arbitray cross–sectional cylindrical object in an optical slab waveguide," *IEEE J. Lightwave Technol.*, Vol.LT–1, No.2, pp.374–380, 1983.

[43] S. L. Chuang and J. A. Kong, "Wave scattering and guidance by dielectric waveguides with periodic surfaces," *J. Opt. Soc. Am.*, Vol.73, No.5, pp.669–679, 1983.

[44] J. H. Harris, R. K. Winn, and D. G. Dalgontte, "Theory and design of periodic couplers," *Appl. Opt.*, Vol.11, No.10, pp.2234–2241, 1972.

[45] K. Ogawa, W. S. C. Cheng, B. L. Sopori, and F. J. Rosenbaum, "A theoretical analysis of etched grating couplers for integrated optics," *IEEE J. Quantum Electron.*, Vol.QE–9, No.1, pp.29–42, 1973.

[46] H. Stoll and A. Yariv, "Coupled–mode analysis of periodic dielectric waveguides," *Opt. Commun.*, Vol.8, No.1, pp.5–8, 1973.

[47] C. Elachi and C. Yeh, "Periodic structures in integrated optics," *J. Appl. Phys.*, Vol.44, No.7, pp.3146–3152, 1973.

[48] K. Ogawa and W. S. C. Cheng, "Analysis of holographic thin film grating coupler," *Appl. Opt.*, Vol.12, No.9, pp.2167–2171, 1973.

[49] S. T. Peng, H. L. Bertoni, and T. Tamir, "Analysis of periodic thin–film structures with rectangular profile," *Opt. Commun.*, Vol.10, No.1, pp.91–94, 1974.

[50] S. T. Peng, T. Tamir, H. L. Bertoni, "Theory of periodic dielectric waveguides," *IEEE Trans. Microwave Theory Tech.*, Vol.MTT-23, No.1, pp.123–133, 1975.

[51] L. L. Hope, "Theory of optical grating couplers," *Opt. Commun.*, Vol.5, pp.179–182, 1972.

[52] F. W. Dabby, A. Kestenbaum, and U. C. Peak, "Periodic dielectric waveguides," *Opt. Commun.*, Vol.6, pp.125–130, 1972.

[53] K. Sakuda and A. Yariv, "Analysis of optical propagation in a corrugated dielectric waveguide," *Opt. Commun.*, Vol.8, pp.1–4, 1973.

[54] M. Neviere, R. Petit, and M. Cadilhac, "About the theory of optical grating coupler–waveguide systems," *Opt. Commun.*, Vol.8, pp.113–117, 1973.

[55] J. E. Sipe and G. I. Stegeman, "Comparison of normal mode and total field analysis techniques in planar integrated optics," *J. Opt. Soc. Am.*, Vol.69, No.12, pp.1676–1683, 1979.

[56] J. Marcou, N. Gremillet, and G. Thomin, "Polarization conversion by Bragg deflection in isotopic planar integrated optics waveguides part I, theoretical study," *Opt. Commun.*, Vol.32, No.1, pp.63–68, 1980.

[57] K. Morishita, S.–I. Inagaki, and N. Kumagai, "Analysis of discontinuities in dielectric waveguides by means of the least squares boundary residual method," *IEEE Trans. Microw. Theory Tech.*, Vol.MTT–27, No.4, pp.310–315, 1979.

[58] S. T. Peng and A. A. Oliner, "Guidance and leakage properties of a glass of open dielectric waveguides: part I—mathematical formulations," *IEEE Trans. Microw. Theory Tech.*, Vol.MTT–29, No.9, pp.843–854, 1981.

[59] A. A. Oliner, S. –T. Peng, T. –I. Hsu, and A. Sanchez, "Guidance and leakage properties of a class of open dielectric waveguides: Park II — new physical effects," *IEEE Trans. Microw. Theory Tech.* Vol.MTT–29, No.9, pp.855–869, 1981.

[60] M. Suzuki and M. Koshiba, "Finite element analysis of discontinuity problems in a planar dielectric waveguide," *Radio Sci.*, Vol.17, pp. 85–91, 1982.

[61] M. Koshiba and K. Hirayama, "Application of finite–element method to arbitrarily shaped discontinuities in a dielectric slab waveguide," *IEE PROCEEDINGS H*, Vol.135, pp.8–12, 1988.

[62] M. Koshiba and M. Kuzuki, "Boundary–element analysis of dielectric slab waveguide discontinuities," *Appl. Opt.*, Vol.25, No.6, pp.828–829, 1986.

[63] J. K. Butler, W. E. Ferguson Jr., G. A. Evans, P. J. Stabile, and A. Rosen, "A boundary element technique applied to the analysis of waveguides with periodic surface corrugations," *IEEE J. Quantum Electron.*, Vol.28, No.7, pp.1701–1709, 1992.

[64] K. Hirayama and M. Koshiba, "Numerical analysis of arbitrarily shaped discontinuities between planar dielectric waveguides with different thicknesses," *IEEE Trans. Microw. Theory Tech.*, Vol.38, No.3, pp.260–264, 1990.

[65] A. Ittipiboon and M. Hamid, "Scattering of surface wave at a slab waveguide discontinuity," *PROC. IEE*, Vol.126, No.9, pp.798–804, 1979.

[66] E. Nishimura, N. Morita, and N. Kumagai, "An integral equation approach to electromagnetic scattering from arbitrarily shaped junctions between multilayered dielectric planar waveguides," *IEEE J. Lightwave Technol.*, Vol.LT–3, No.4, pp.887–894, 1985.

[67] L. R. Gomaa, "Beam propagation method applied to a step discontinuity in dielectric planar waveguides," *IEEE Trans. Microw. Theory Tech.*, Vol.36, No.4, pp.791–792, 1988.

[68] B. M. Nyman and P.R. Prucnal, "The modified beam propagation method," *IEEE J. Lightwave Technol.*, Vol.7, No.6, pp.931–936, 1989.

[69] E. Popov and L. Mashev, "The determination of mode coupling coefficients," *OPTICA ACTA*, Vol.32, No.6, pp.635–637, 1985.

[70] T. E. Rozzi, "Rigorous analysis of the step discontinuity in a planar dielectric waveguide," *IEEE Trans. Microw. Theory Tech.*, Vol.MTT–26, No.7, pp.738–809, 1978.

[71] H. Shigesawa and M. Tsuji, "mode propagation through a step discontinuity in dielectric planar waveguide," *IEEE Trans. Microw. Theory Tech.*, Vol. MTT–34, No.2, pp.205–212, 1986.

[72] T. E. Rozzi and G. H. In't Veld, "Field and network analysis of interacting step discontinuities in planar dielectric waveguides," *IEEE Trans. Microw. Theory Tech.*, Vol.MTT–27, No.4, pp.303–309, 1979.

[73] T. Hosono, T. Hinata, and A. Inoue, "Numerical analysis of the discontinuities in slab dielectric waveguides," *Radio Sci.*, Vol.17, No.1, pp.75–83, 1982.

[74] P. G. Suchoski, Jr., and V.Ramaswamy, "Exact numerical technique for the analysis of step discontinuities and tapers in optical dielectric waveguides," *J. Opt. Soc. Am. A*, Vol.3, No.2, pp.194–203, 1986.

[75] I. Orfanos, T. Sphicopoulos, A. Tsigopoulos, and C. Caroubalos, "A tractable above–threshold model for the design of DFB and phase–shifted DFB lasers," *IEEE J. Quantum Electron.*, Vol.27, No.4, pp.946–956, 1991.

[76] G. Bjork and O. Nilsson, "A new exact and efficient numerical matrix theory of complicated laser structures: Properties of asymmetric phase–shifted DFB lasers," *IEEE J. Lightwave Technol.*, Vol.LT–5, No.1, pp.140–146, 1987.

[77] W. Huang and J. Hong, "A transfer matrix approach based on local normal modes for coupled waveguides with periodic perturbations," *IEEE J. Lightwave Technol.*, Vol.10, No.10, pp.1367–1375, 1992.

[78] K. Sekartedjo, N. Eda, K. Furuya, Y. Suematsu, F. Koyama, and T. Tanbun–Ek, "1.5μm phase–shifted DFB lasers for single–mode operation," *Electron. Lett.*, 25th year publication, pp.S48–S49, 1989.

[79] H. Hilmer, S. Hansmann, and H. Burkhand, "1.53 μm InGaAsP–InP first–order $\lambda/4$–shifted distributed feedback lasers with high coupling coefficients," *IEEE J. Quantum Electron.*, Vol.27, No.6, pp.1753–1758, 1991.

[80] T. Makino, "Analysis of below–threshold spectrum and linewidth of surface–emitting $\lambda/4$–shifted DFB lasers with DBR mirror," *Electron. Lett.*, Vol.27, No.13, pp.1120–1121, 1991.

[81] K. Uomi, T. Tsuchiya, H. Nakano, M. Aoki, M. Suzuki, and N. Chinone, "High–speed and ultralow–chirp 1.55 μm multiquantum well $\lambda/4$–shifted DFB lasers," *IEEE J. Quantum Electron.*, Vol.27, No.6, pp.1705–1713, 1991.

[82] J. E. A. Whiteaway, B. Garrrett, G. H. B. Thompson, A. J. Collar, C. J. Armistead, and M. J. Fice, "The static and dynamic charateristics of single and multiple phase–shifted DFB laser structures," *IEEE J. Quantum Electron.*, Vol.28, No.5, pp.1277–1293, 1992.

[83] H. Ishii, Y. Tohmori, Y. Yoshikuni, T. Tamamura, and Y. Kondo, "Multiple-phase-shift, super structure grating DBR lasers for broad wavelength tuning," *IEEE Photonics Tech. Lett.*, Vol.5, No.6, pp.613–615, 1993.

[84] M. Okai, T. Tsuchiya, K. Uomi, N. Chinone, and T. Harada, "Corrugation-pitch modulated MQW-DFB lasers with narrow spectral linewidth," *IEEE J.Quantum Electron.*, Vol.27, No.6, pp.1767–1772, 1991.

—, "Corrugation-pitch-modulated MQW-DFB laser with narrow spectral linewidth (170 kHz)," *IEEE Photonics Tech. Lett.*, Vol.2, No.8, pp.529–530, 1990.

—, "Effect of $1/f$ noise on the spectral linewidth of corrugation-pitch-modulated multiquantum-well distributed feedback lasers at high output power," *IEEE Photonics Tech. Lett.*, Vol.3, No.5, pp.427–429, 1991.

[85] P. Zhou and G. S. Lee, "Chirped grating $\lambda/4$ shifted DFB laser with uniform longitudinal field distribution," *Electron. Lett.*, Vol.26, No.20, pp.1660–1661, 1990.

[86] K. Uomi, S. Sasaki, T. Tsuchiya, H. Nakano, and N. Chinone, "Ultralow chirp and high-speed 1.55 μm multiquantum well $\lambda/4$-shifted DFB lasers," *IEEE Photonics Tech. Lett.*, Vol.2, No.4, pp.229–230, 1990.

[87] H. Hilmer, K. Magari, and Y. Suzuki, "Chirped gratings for DFB laser diodes using bent waveguides," *IEEE Photonics Tech. Lett.*, Vol.5, No.1, pp.10–12, 1993.

[88] S. Ogita, Y. Kotaki, M. Matsuda, Y. Kuwahara, and H. Ishihawa, "Long-cavity, multiple-phase-shift, distributed feedback laser for linewidth narrowing," *Electron. Lett.*, Vol.25, No.10, pp.629–630, 1989.

[89] F. Kano, H. Ishii, Y. Tohmori, and Y. Yoshikuni, "Characteristics of super structure grating (SSR) DBR lasers under broad range wavelength tuning," *IEEE Photon. Tech. Lett.*, Vol.5, No.6, pp.611–613, 1993.

[90] H. Ishii, Y. Tohmori, T. Tamamura, and Y. Yoshikuni, "Super structure grating (SSG) for Broadly tunable DBR lasers," *IEEE Photonics Tech. Lett.*, Vol.4, No.4, pp.393–395, 1993.

[91] H. Ishii, Y. Tohmori, M. Yamamoto, T. Tamamura, and Y. Yoshikuni, "Modified multiple-phase-shift super-structure-grating DBR lasers for broad wavelength tuning," *Electron. Lett.*, Vol.30, No.14, 1994.

[92] M. Aoki, K. Uomi, T. Tsuchiya, S. Sasaki, and N. Chinone, "Stabilization of the longitudinal mode against spatial hole burning in $\lambda/4$–shifted DFB lasers by quantum size effect," *IEEE Photonics Tech. Lett.*, Vol.2, No.9, pp.617–619, 1990.

[93] F. Ouellette, "Dispersion cancellation using linearly chirped Bragg grating filters in optical waveguides," *Opt. Lett.*, Vol.12, No.10, pp.847–849, 1987.

[94] F. Ouellette, "Limits of chirped pulse compression with an unchirped Bragg grating filter," *Appl. Opt.*, Vol.29, No.32, pp.4826–4829, 1990.

[95] J. E. Roman and K. A. Winick, "Waveguide grating filters for dispersion compensation and pulse compression," *J Quantum Electron.*, Vol.29, No.3, pp.975–982, 1993.

[96] R. Kashyap, S. V. Chernikov, P. F. Mckee, and J. R. Taylor, "30ps chromatic dispersion compensation of 400fs pulses at 100Gbite/s in fibres using an all fibre photoinduced chirped reflection graitng," *Electron. Lett.*, Vol.30, No.13, pp.1078–1080, 1994.

[97] J. A. R. Williams, I. Bennion, K. Sugden, and N. J. Doran, "Fibre dispersion compensation using a chirped in–fibre Bragg grating," *Electron. Lett.*, Vol.30, No.12, pp.985–987, 1994.

[98] K. Sugden, I. Bennion, A. Molony, and N. J. Copner, "Chirped gratings produced in photosensitive optical fibres by fibre deformation during exposure," *Electron. Lett.*, Vol.30, No.5, pp.440–442, 1994.

[99] K. O. Hill, F. Bilodeau, B. Malo, T. Kitagawa, S. Thériault, D. C. Johnson, J. Albert, and K. Takiguchi, "Chirped in–fiber Bragg gratings for compensation of optical–fiber dispersion," *Opt. Lett.*, Vol.19, No.17, pp.1314–1316, 1994.

[100] W. J. Tomlinson, R. H. Stolen, and C. V. Shank, "Compression of optical pulses chirped by self–phase modulation fibers," *J. Opt. Soc. Am. B,* Vol.1, No.2, pp.139–149, 1984.

[101] H. G. Winful, "Pulse compression in optical fiber filters," *Appl. Phys. Lett.*, Vol.46, No.6, pp.527–529, 1985.

[102] J. A. R. Williams, I. Bennion, and L. Zhang, "The compression of optical pulses using self–phase–modulation and linearly chirped Bragg–gratings in fibers," *IEEE Photonics Technol. Lett.*, Vol.7, No.5, pp.491–493, 1995.

[103] N. K. Uzunoglu, C. N. Capsalis, and C. P. Chronopoulos, "Frequency–dependent analysis of a shielded microstrip step discontinuity using an efficient mode–matching technique," *IEEE Trans. Microwave Theory Tech.*, Vol.36, No.6, pp.976–984, 1988.

[104] A. Weisshaar and V. K. Tripathi, "Modal analysis of step discontinuities in graded–index dielectric slab waveguides," *IEEE J. Lightwave Technol.*, Vol.10, No.5, pp.593–602, 1992.

[105] G. A. Gesell and I. R. Ciric, "Recurrence modal analysis for multiple waveguide discontinuities and its application to circular structures," *IEEE Trans. Microwave Theory Tech.*, Vol.41, No.3, pp.484–490, 1993.

[106] D. P. Nyquist, D. R. Johnson, and S. V. Hsu, "Orthogonality and amplitude spectrum of radiation modes along open–boundary waveguides," *J. Opt. Soc. Am.*, Vol.71, No.1, pp.49–54, 1981.

[107] J. Seligson, "The orthogonality relation for TE– and TM–modes in guided–wave optics," *IEEE J. Lightwave Technol.*, Vol.6, No.8, pp.1260–1264, 1988.

[108] H. M. Barlow and J. Brown, *Radio Surface Waves*, Oxford: Clarendon Press. 1962.

[109] F. Erdogan and G. D. Gupta, "On the numerical solution of singular integral equations," *Quarterly Appl. Math.*, Vol.30, No.1, pp.525–534, 1972.

[110] B. Rulf and N. Kedem, "Surface wave diffraction by means of singular integral equations," *J. Sound Vibration*, Vol.45, No.1, pp.15–28, 1976.

[111] B. Rulf, "On the matching of two optical waveguides," *Radio Sci.*, Vol.12, No.4, pp.593–601, 1977.

[112] P. Gelin, M. Petenzi, and J. Citerne, "Rigorous analysis of the scattering of surface waves in an abruptly ended slab dielectric waveguide," *IEEE Trans. Microwave Theory Tech.*, Vol.MTT-29, No.2, pp.107–114, 1981.

[113] V. Ramaswamy, P.G. Suchoski, Jr., "Power loss at a step discontinuity in an asymmetrical dielectric slab waveguide," *J. Opt. Soc. Am. A*, Vol.1, No.7, pp.754–759, 1984.

[114] A. Hardy, "Exact derivation of the coupling coefficients in corrugated waveguides with rectangular tooth shape," *IEEE J. Quantum Electron.*, Vol.OE–20, No.10, pp.1132–1139, 1984.

[115] S.–J. Chung and C. H. Chen, "A partial variational approach for arbitrary discontinuities in planar dielectric waveguides," *IEEE Trans. Microwave Theory Tech.*, Vol.37, No.1, pp.208–214, 1989.

[116] M. Yamada and K. Sakuda, "Analysis of almost–periodic distributed feedback slab waveguides via a fundamental matrix approack," *Appl. Opt.*, Vol.26, No.16, pp.3474–3478, 1987.

[117] M. Usami, S. Akiba, and K. Utaka, "Asymmetric $\lambda/4$–shifted InGaAsP/InP DFB lasers," *IEEE J. Quantum Electron.*, Vol.QE–23, No.6, pp.815–821, 1987.

[118] H. Kogelnik, "Filter response of nonuniform almost–periodic structures," *Bell Sys. Tech. J.*, Vol.55, No.1, pp.109–128, 1976.

[119] W. Streifer, D. R. Scifres, and R. D. Burnham, "Optical analysis of multiple-quantum-well lasers," *Appl. Opt.*, Vol.18, No.21, pp.3547-3548, 1979.

[120] J. Chilwell and I. Hodgkinson, "Thin-films field-transfer matrix theory of planar multilayer waveguides and reflection from prism-loaded waveguides," *J. Opt. Soc. Am. A*, Vol.1, No.7, pp.742-753, 1984.

[121] L. M. Walpita, "Solutions for planar optical waveguide equations by selecting zero elements in a characteristic matrix," *J. Opt. Soc. Am. A* Vol.2, No.4, pp.595–602, 1985.

[122] A. K. Ghatak, K. Thyagarajan, and M. R. Shenoy, "Numerical analysis of planar optical waveguides using matrix approach," *J. Lightwave Technol.*, Vol.LT-5, No.5, pp.660–667, 1987.

[123] T. J. M. Boyd, I. moshkun, and I. M. Stephenson, "Radiation losses due to discontinuities in asymmetric three-layer optical waveguides," *Opt. Quantum Electron.*, Vol.12, pp.143–158, 1980.

[124] J. Salzman and G. Lenz, "The Bragg reflection waveguide directional coupler," *IEEE Photon. Technol. Lett.*, Vol.1, No.10, pp.319–322, 1989.

[125] R. M. Emmons and D. G. Hall, "Comparison of film thickness tolerances in waveguide grating couplers," *Opt. Lett.*, Vol.16, No.13, pp.998–1000, 1991.

[126] D. Marcuse, "Radiation loss of grating–assisted directional coupler," *IEEE J Quantum Electron.*, Vol.26, No.4, pp.675–684, 1990.

[127] A. Hardy, D. F. Welch, and W. Streifer, "Analysis of second–order gratings," *IEEE J Quantum Electron.*, Vol.25, No.10, pp.2096–2105, 1989.

[128] A. Hardy, "Exact derivation of the coupling coefficient in corrugated waveguides with arbitrary cross–section: application to optical fibers," *IEEE J Quantum Electron.*, Vol.31, No.3, pp.505–511, 1995.

[129] K. A. Winick, "Effective–index method and coupled–mode theory for almost–periodic waveguide gratings: a comparison," *Appl. Opt.*, Vol.31, No.6, pp.757–764, 1992.

[130] J. L. Frolik and A. E. Yagle, "An asymmetric discrete–time approach for the design and analysis of periodic waveguide gratings," *J Lightwave Technol.*, Vol.13, No.2, pp.175–185, 1995.

[131] S.-H. Kim and C. G. Fonstad, "Tunable narrow–band thin–film waveguide grating filters," *IEEE J Quantum Electron.*, Vol.OE-15, No.12, pp.1405–1408, 1979.

[132] S. Radic, N. George, and G. P. Agrawal, "Analysis of nonuniform nonlinear distributed feedback structures: generalized transfer matrix method," *IEEE J Quantum Electron.*, Vol.31, No.7, pp.1326–1336, 1995.

[133] J. Kuhl and J. Heppner, "Compression of femtosecond optical pulse with dielectric multilayer interferometers," *IEEE Trans. Quantum Electron.*, Vol.QE–22, No.1, pp.182–185, 1986.

[134] A. Stingl, C. Spielmann, and F. Krausz, "Generation of 11–fs pulse from a Ti:sapphire laser without the use of prisms," *Opt. Lett.*, Vol.19, No.3, pp.204–206, 1993.

[135] B. Proctor, E. Westwig, and F. Wise, "Characterization of a Kerr–lens mode–locked Ti:sapphire laser with positive group–velocity dispersion," *Opt. Lett.*, Vol.18, No.19, pp.1654–1656, 1993.

[136] K. Tamura, C. R. Doerr, L. E. Nelson, H. A. Haus, and E. P. Ippen, "Technique for obtaining high-energy ultrashort pulses from an additive–pulse mode–locked erbium–doped fiber ring laser," *Opt. Lett.*, Vol.19, No.1, pp.46–48, 1994.

[137] J. Goodberlet and P. L. Hagelstein, "Chirp–compensated autocorrelation of optical pulses," *Opt. Lett.*, Vol.18, No.19, pp.1648–1650, 1993.

[138] W.–H. Tsai, S.–C. Chao, and M.–S. Wu, "Variational analysis of single–mode inhomogeneous planar optical waveguide," *J Lightwave Technol.*, Vol.10, No.6, pp.747–752, 1992.

[139] S.–C. Chao, M.–S. Wu, and W.–H. Tsai, "Variational analysis of modal-coupling efficiency between graded–index waveguides," *J Lightwave Technol.*, Vol.12, No.9, pp.1543–1549, 1994.

[140] S.–C. Chao, W.–H. Tsai, and M.–S. Wu, "Extended Gaussian approximation for single–mode graded–index fibers," *J Lightwave Technol.*, Vol.12, No.3, pp.392–395, 1994.